

Design and Implementation of Adaptive OFDM in a Software Defined Radio Framework

Von der Fakultät für Elektrotechnik und Informationstechnik
der Rheinisch-Westfälischen Technischen Hochschule Aachen
zur Erlangung des akademischen Grades eines Doktors
der Ingenieurwissenschaften genehmigte Dissertation

vorgelegt von

Diplom-Ingenieur
Milan Zivkovic

aus Nis, Serbien

Berichter: Universitätsprofessor Dr. rer. nat. Rudolf Mathar
Universitätsprofessor Dr.-Ing. Gerd Ascheid

Tag der mündlichen Prüfung: 09. September 2013

Diese Dissertation ist auf den Internetseiten
der Hochschulbibliothek online verfügbar.

Berichte aus der Kommunikationstechnik

Milan Zivkovic

**Design and Implementation of Adaptive OFDM
in a Software Defined Radio Framework**

Shaker Verlag
Aachen 2014

Bibliographic information published by the Deutsche Nationalbibliothek

The Deutsche Nationalbibliothek lists this publication in the Deutsche Nationalbibliografie; detailed bibliographic data are available in the Internet at <http://dnb.d-nb.de>.

Zugl.: D 82 (Diss. RWTH Aachen University, 2013)

Copyright Shaker Verlag 2014

All rights reserved. No part of this publication may be reproduced, stored in a retrieval system, or transmitted, in any form or by any means, electronic, mechanical, photocopying, recording or otherwise, without the prior permission of the publishers.

Printed in Germany.

ISBN 978-3-8440-2924-6

ISSN 0945-0823

Shaker Verlag GmbH • P.O. BOX 101818 • D-52018 Aachen

Phone: 0049/2407/9596-0 • Telefax: 0049/2407/9596-9

Internet: www.shaker.de • e-mail: info@shaker.de

Preface

This thesis was written during my time at the Institute for Theoretical Information Technology of RWTH Aachen University.

I would like to thank Univ.-Prof. Dr. rer. nat. Rudolf Mathar for giving me the opportunity to work on my dissertation under his supervision and to be a part of his highly qualified and productive research team. I am particularly grateful to Prof. Mathar for motivating me and giving me the continuous support and freedom to pursue my own ideas.

Many thanks belong to Univ.-Prof. Dr.-Ing. Gerd Ascheid for acting as the second referee for this thesis. His precious technical and conceptual comments have motivated me to arise new questions and establish different angles regarding my present and future work.

The great part of the presented work has originated from the collaboration with the students through the joint work and supervision of master and bachelor theses. A special thankyou goes to Dominik Auras for spending numerous hours unconditionally contributing to the development of TIGR, starting from the first lines of code up to the Demo Award in Beijing. I would also like to thank Jonas Börner, Martin Harries, Jan Willem Jansen, Benedikt Koppers, Karu Ramiah, Natalia Revuelto, Christian Rohlfing, and Johannes Schmitz for their support and valuable contributions.

Another special thankyou goes to Dr.-Ing. Daniel Bielefeld and Dr.-Ing. Gernot Fabeck for helping me to shape and develop some of the ideas during our collaboration. I would also like to thank Dr.-Ing. Chunhui Liu for having a great courage and strong nerves to spend (usually more than) 40 hours per week sharing the office with me for five years.

I would like to express my deepest gratitude to all my present and former colleagues at the Institute for Theoretical Information Technology of RWTH Aachen University for fruitful discussions. Thank you for sharing your time and my slivovitz with me and for teaching me valuable scientific and life lessons.

A deep emotional thankyou goes to Floriane for being present during possibly the hardest moments of my life. Thank you for your patience, love, and for encouraging me to keep my pace.

Finally, I would like to thank my parents, Slavica and Velibor, and my brother Marko for their unconditional love, support, and encouragement throughout the years. A great deal of my achievements, both professional and private, could not have been possible without them being around. This dissertation is dedicated to them.

Contents

Preface	iii
1. Introduction	1
2. OFDM Basics	5
2.1. Wireless Channel Propagation	5
2.1.1. Time-Invariant Frequency-Selective Channels	5
2.1.2. Time-Invariant Flat Fading Channels	8
2.1.3. Time-Variant Fading Channels	9
2.2. OFDM Technology	12
2.3. Discrete-Time OFDM System Model	15
2.4. Digital Modulations Used in OFDM Systems	18
2.4.1. Phase Shift Keying (PSK)	19
2.4.2. Quadrature Amplitude Modulation (QAM)	21
2.5. OFDM System Impairments	22
2.5.1. Effects of Timing Offset	25
2.5.2. Joint Effect of Frequency and Sampling Offset	27
2.6. Equalization	28
2.7. Performance of OFDM systems	30
3. Resource Allocation Basics	33
3.1. Water-Filling Optimization	34
3.1.1. SNR Gap Analysis	34
3.1.2. Water-Filling Optimization in OFDM Systems	35
3.2. Discrete Rate Optimization	38
3.2.1. Loading with Discrete Information Units	38
3.2.2. Levin-Campello Algorithm (LC)	40
3.2.3. Uniform Power Allocation (UP)	42
3.2.4. Subband Resource Allocation (SB, SB-UP)	43
3.2.5. Band Resource Allocation (BA)	43
3.3. Simulation Results	44
4. SNR Estimation in OFDM Systems	49
4.1. SNR Estimators	50
4.1.1. MMSE Estimator	50
4.1.2. Boumard's Estimator	51
4.1.3. Ren's Estimators	52
4.2. Periodic Sequence (PS) Estimator	53
4.2.1. Computational Complexity Analysis	57

4.2.2. Statistical Properties	57
4.2.3. Numerical Results	65
4.3. Improved PS (IPS) Estimator	73
4.3.1. Numerical Results	74
5. SNR Estimation in MIMO OFDM Systems	79
5.1. MIMO System Model	79
5.2. MIMO-PS Estimator	81
5.3. Improved MIMO-PS (MIMO-IPS) Estimator	84
5.4. Simulation Results	85
6. Joint Synchronization and Spectrum Characterization in OFDM-based Cognitive Radio Systems	91
6.1. Fractional Bandwidth (FBW) Scenario	92
6.1.1. Preamble Design	95
6.2. Fractional CFO Estimation	96
6.3. Joint Integer CFO and FBW Mode Estimation	97
6.4. SNR and Interference Power Estimation	97
6.5. Simulation Results	99
7. Resource Allocation in the Presence of Synchronization Errors	105
7.1. SNR Degradation	106
7.2. Estimation of Synchronization Impairments	111
7.2.1. CFO Estimation	112
7.2.2. Residual CFO and SFO Compensation	114
7.3. SNR Estimation in the Presence of Synchronization Errors	120
7.3.1. Numerical Results	124
7.4. Resource Allocation in the Presence of Receiver Imperfections	128
8. Implementing Adaptive OFDM by Software Defined Radio	133
8.1. The Basics of Software Defined Radios	134
8.2. GNU Radio Architecture	136
8.2.1. An Example: Wireless Channel Simulation	142
8.3. TIGR System Overview	143
8.3.1. CORBA Integration	145
8.3.2. Resource Manager	147
8.3.3. Graphical User Interface (GUI)	147
8.3.4. The Transmitter	149
8.3.5. The Receiver	151
8.4. Experimental Results	156
8.4.1. TIGR Receiver Performance	158
8.4.2. Resource Allocation Performance	165
9. Conclusions	173
9.1. Summary	173
9.2. Outlook	174
A. Simulation Setup	175

B. OFDM Based Wireless Standards	177
B.1. Wireless LAN (IEEE 802.11 Series of Standards)	177
B.2. WiMAX (IEEE 802.16 Series of Standards)	179
B.3. LTE	182
B.4. WRAN (IEEE 802.22 Standard)	184
C. The Impact of the Constant Gap Assumption	187
D. The TIGR Transceiver Benchmark	189
Bibliography	207

1. Introduction

Current broadband wireless standards are based on Orthogonal frequency division multiplexing (OFDM), a multicarrier modulation scheme that provides strong robustness against inter-symbol interference (ISI). OFDM divides the broadband channel into many orthogonal narrowband subchannels in such a way that attenuation across each subchannel stays flat [1]. Orthogonalization of subchannels is performed with low complexity by using the Inverse Fast Fourier Transform (IFFT), an efficient implementation of the Inverse Discrete Fourier Transform (IDFT). In this way, the serial high-rate data stream is converted into multiple parallel low-rate streams, each modulated on a different subcarrier. Due to its robustness to multipath propagation at high data rates, OFDM has been successfully used as physical layer (PHY) technology in numerous wireless standards. This includes European terrestrial digital audio and video broadcasting (DAB and DVB-T), the IEEE 802.11 series of standards for wireless local area network (WLAN), and the IEEE 802.16 series of standards (WiMAX) for wireless metropolitan area network (WMAN). Moreover, OFDM is incorporated in the Long Term Evolution (LTE) standard for 4G cellular mobile networks as well as in the recently ratified cognitive radio IEEE 802.22 standard for wireless regional area networks (WRAN).

The increasing demand for new high data rate services requires future OFDM systems to better exploit frequency diversity offered by broadband channels. The energy and capacity efficiency of an OFDM system in a particular wireless environment can be preserved by adaptable transmission parameters, such as bandwidth, data rate, and power. For given Quality of Service (QoS) demands, usually determined by the target bit error rate (BER), this can be formulated as an optimization problem. Within the last two decades, extensive theoretical research work has resulted in the development of optimal and suboptimal solutions for an efficient resource allocation in OFDM wireless networks [2, 3, 4, 5].

However, the investigation and assessment of information theoretic concepts in a radio frequency (RF) environment is limited in the literature. This is mostly due to the lack of commercial hardware that can support adaptable transmission parameters. Currently, these functionalities are only offered by Software Defined Radio (SDR) technology supported by general purpose hardware.

The main issue in assessing resource allocation algorithms by radio testbeds is the presence of hardware imperfections at the radio frequency (RF) frontend. Moreover, the applicability of the given theoretical model associated with specific impairment should also be considered during implementation. In most cases, the performance degradation depends on specific synchronization procedures applied for timing and frequency estimation. Additionally, in order to compensate the effects of multipath propagation, equalization requires the estimation of the channel frequency response. The influence of a certain channel estimation method on the system performance should also be taken into account.

Another very important issue for adaptive OFDM systems is the accurate and computationally efficient estimation of the signal-to-noise ratio (SNR). Representing the measure of signal quality, SNR is used as an input parameter for any resource allocation algorithm that produces specific power and/or rate allocation. Most of the SNR estimators from the literature are related to a single carrier transmission and can be directly applied to OFDM systems in the presence of additive white Gaussian noise (AWGN) [6]. However, the SNR estimation in frequency-selective channels additionally requires the estimation of the channel frequency response, inherently required for equalization. Several recently proposed SNR estimators for OFDM systems [7, 8] have shown relatively poor performance for frequency-selective channels. Therefore, there is a need for a robust SNR estimator which provides accurate input to a resource allocation algorithm.

The main goal of this thesis is to identify and address the important challenges that arise from the implementation of an adaptive OFDM communication system. This comprises the presence of a real radio frequency (RF) channel, as well as the critical influence of the SNR estimation and hardware imperfections on the system performance. The contributions in this theses are of **theoretical** and **practical** nature. The main **theoretical** contribution of the thesis is an efficient algorithm for the SNR estimation in wireless OFDM systems. The proposed estimator is based on second-order moments of preamble samples received in the frequency domain. Furthermore, the thesis contains the study of the rate adaptive resource allocation algorithms in a synchronization mismatch scenario with the proposed SNR estimator. This discussion provides information about performance degradation of a real implementable transceiver with respect to an ideal transmission system with perfectly estimated parameters. The main **practical** contribution of the thesis is the design and implementation of an SDR-based reconfigurable framework for testing the capacity-achieving adaptive OFDM transmission in a real RF environment. The implemented framework contains a large set of reconfigurable parameters, which are normally static in real systems. Moreover, high flexibility of the setup enables the implementation and assessment of different signal processing and resource allocation algorithms for various classes of system requirements.

This thesis is organized as follows. After a short overview of wireless channels and basic foundations of general multicarrier and OFDM transmission technology, Chapter 2 introduces the discrete-time OFDM system model, defining the SNR as a measure of signal quality. Furthermore, the performance degradation in the presence of synchronization errors is characterized with the SNR loss.

In Chapter 3, the basic concepts of optimization for multicarrier systems are given. Water-filling is introduced as an optimal solution for infinite granulation of transmitted information, thus presenting theoretical limit for the achievable rate. Furthermore, the concept of rate-power function is presented as the link between performance requirements and subchannel conditions expressed through the SNR per subcarrier. Since realizable systems can support only a finite granulation of transmitted bits, several optimal and suboptimal algorithms for resource allocation are introduced while their performance is compared with the water-filling solution.

The preamble-based method for SNR estimation in OFDM systems is introduced in Chapter 4. The proposed method, named PS estimator, utilizes the time-periodic preamble structure of the synchronization preamble. In the frequency domain, this structure

contains non-used (nulled) subcarriers to estimate the average noise power. Combined with the average signal plus noise power estimation obtained on the used (loaded) subcarriers, the average noise power estimate is utilized for the average SNR estimation. Moreover, the statistical properties of the PS estimator are given in order to provide an analytical model for the analysis of performance degradation by certain resource allocation algorithms. Furthermore, an improved version of the PS estimator, named IPS, is proposed. The IPS estimator adaptively selects the most significant channel impulse response (CIR) paths. As a result, its performance in a low SNR region is significantly improved over the PS estimator.

Initially proposed for single input single output (SISO) antenna systems, the PS estimator is further extended to a multiple input multiple output (MIMO) antenna scenario in Chapter 5. Furthermore, a preamble-based method for joint frequency synchronization and spectrum characterization in OFDM cognitive radio systems is introduced in Chapter 6. In particular, the synchronization preamble is properly adjusted to an interference scenario such that the proposed method enables frequency synchronization and detection of interference within the considered band. Finally, the method provides the SNR and interference power estimates as reliable quantitative indicators of spectrum occupancy.

In Chapter 7, resource allocation algorithms in a synchronization mismatch scenario are studied. The influence of the variance of synchronization algorithms and the SNR estimation onto system performance degradation is further discussed. Hardware impairments are simulated and an appropriate model is proposed by including estimation noise into the rate-power function.

The applicability of adaptive OFDM transmission in a real RF link is examined through the experiments using a reconfigurable testbed. In Chapter 8, as the main practical contribution of this thesis, an SDR-based real-time reconfigurable framework for adaptive OFDM transmission, named TIGR (TI GNU Radio), is introduced. The implementation comprises a complete reconfigurable physical layer transceiver. This framework enables adaptivity of individual subcarriers such that practical evaluation of resource allocation algorithms can be performed. The transceiver performance is characterized and analyzed through the concept of SNR loss and corresponding rate-power function. Furthermore, the performance evaluation of the resource allocation algorithms in real RF conditions using the TIGR framework is presented. The results are compared with the simulation results obtained in Chapter 7, showing the applicability of hardware imperfections models and robustness of the proposed SNR estimator to the design of efficient resource allocation algorithms.

Finally, we conclude with a summary of our work and a brief outlook in Chapter 9.

Most of the contributions in this thesis have already been published in [9, 10, 11, 12, 13, 14, 15, 16, 17]. Related material was published in [18, 19, 20, 21, 22, 23, 24]. Further publications based on this work are in preparation.

2. OFDM Basics

2.1. Wireless Channel Propagation

Many advantages of wireless communication systems such as mobility, high scalability, easy access and installation, can be limited by the nature of radio communication channel. Transmitted signals are typically reflected, diffracted, and scattered from the surrounding objects arriving at the receiver along multiple paths, each with different delay, amplitude, and phase, as illustrated in Figure 2.1. Additionally, each multiple path undergoes time variations due to mutual movements between transmitter, receiver, and/or surrounding objects that contribute to the varying conditions of the wireless channel. This effect is known as multipath propagation, or multipath fading, because the received signal presents a constructive or destructive superposition of a possibly large number of time-variant, attenuated, delayed, and phase-shifted copies of the transmitted signal.

A common model to describe the time-varying multipath wireless channel uses the channel impulse response, denoted by $h(\tau, t)$. The channel impulse response represents a time-limited pulse train that corresponds to a response of the channel at time t to a Dirac delta function applied at time $t - \tau$. It can be written as [25]

$$h(\tau, t) = \sum_{l=0}^{L-1} \alpha_l(t) e^{j\theta_l(t)} \delta(\tau - \tau_l(t)), \quad (2.1)$$

where $\delta(\tau - \tau_l(t))$ denotes the Dirac delta function defined to be zero everywhere except at $\tau = \tau_l(t)$, where it equals ∞ with $\int_{-\infty}^{\infty} \delta(\tau) d\tau = 1$. Here, L presents the total number of received signal paths. The functions $\alpha_l(t)$, $\theta_l(t)$, and $\tau_l(t)$ denote the time-variant attenuation, phase shift, and time delay, associated with the l th path.

Moreover, the time-varying multipath channel is characterized in the frequency domain by the channel frequency response, denoted as $H(f, t)$, which represents the Fourier transform of the channel impulse response, $h(\tau, t)$, with respect to τ , at time instant t , thus giving

$$\begin{aligned} H(f, t) &= \int_{-\infty}^{\infty} h(\tau, t) e^{-j2\pi f\tau} d\tau \\ &= \sum_{l=0}^{L-1} \alpha_l(t) e^{j\theta_l(t)} e^{-j2\pi f\tau_l(t)}. \end{aligned} \quad (2.2)$$

2.1.1. Time-Invariant Frequency-Selective Channels

In fixed wireless communications environments, characterized by the absence of mutual movements among transmitter, receiver, and surrounding objects during certain transmission period, the multipath channel can be considered as time-invariant and classified

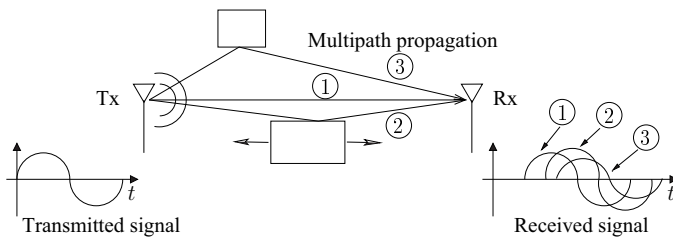


Figure 2.1.: The basic principle of multipath propagation.

as a slow-fading channel. As a result, the channel impulse response in (2.1) and channel frequency response in (2.2) can be denoted as $h(\tau) \triangleq h(\tau, t)$ and $H(f) \triangleq H(f, t)$, respectively.

The time distribution of the average received signal power associated with a given multipath delay in time-invariant frequency-selective channels is characterized by the power delay profile, or multipath intensity profile, denoted as $P_D(\tau)$, and defined as

$$P_D(\tau) \equiv E\{|h(\tau)|^2\} = \sum_{l=0}^{L-1} \Omega(l) \delta(\tau - \tau_l). \quad (2.3)$$

Here, $\Omega(l) = E\{|h(l, t)|^2\}$ is the statistical expectation of the received power associated with the l th multipath component. In many practical applications, due to normalization purposes, the sum of individual average multipath powers is normalized to 1, i.e., $\sum_{l=0}^{L-1} \Omega(l) = 1$. A tabular representation of the power delay profile of extended ITU channel models [26], adopted for large bandwidth transmission scenarios in LTE, is given in Appendix A. The amount of signal dispersion transmitted over a multipath channel is usually characterized by the root mean square (RMS) delay spread, denoted as τ_{RMS} , and defined as [27]

$$\tau_{RMS} = \sqrt{\tau^2 - (\bar{\tau})^2}, \quad (2.4)$$

where

$$\bar{\tau} = \frac{\sum_{l=0}^{L-1} \tau_l \Omega_l}{\sum_{l=0}^{L-1} \Omega_l} = \sum_{l=0}^{L-1} \tau_l \Omega_l \quad (2.5)$$

is the mean excess delay, and

$$\bar{\tau}^2 = \frac{\sum_{l=0}^{L-1} \tau_l^2 \Omega_l}{\sum_{l=0}^{L-1} \Omega_l} = \sum_{l=0}^{L-1} \tau_l^2(l) \Omega_l. \quad (2.6)$$

The channel impulse response and channel frequency response determine the behavior of the slowly-fading frequency-selective channel for the given transmitted signal. On the other hand, τ_{RMS} provides a rough indication of the maximum data rate that can be reliably transported over the channel, when no additional processing, such as equalization, is performed. Figures 2.2 and 2.3 show the power delay profile and channel frequency response, respectively, of the Extended Pedestrian A (EPA) channel model whose parameters are given in Table A.1.

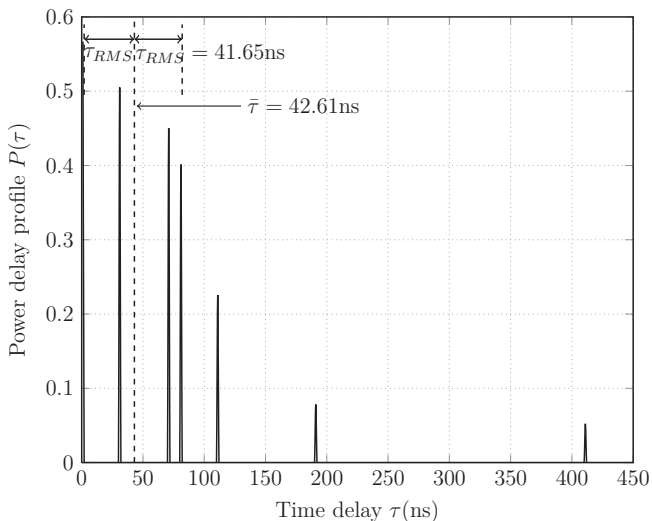


Figure 2.2.: Power delay profile of the EPA channel given in Table A.1.

The variations of $H(f)$ with respect to f is characterized by the channel coherence bandwidth B_c , which can be also considered as the frequency-domain dual of the τ_{RMS} . Therefore, B_c gives a rough measure for the range of frequencies over which the channel frequency response is correlated. For two frequencies, f_1 and f_2 , it holds [27]

$$\begin{aligned} |f_1 - f_2| \leq B_c &\Rightarrow H(f_1, t) \approx H(f_2, t) \\ |f_1 - f_2| > B_c &\Rightarrow H(f_1, t) \text{ and } H(f_2, t) \text{ are uncorrelated.} \end{aligned}$$

The exact expression for the B_c depends inversely on the τ_{RMS} and on a constant K that determines the level of correlation. That is

$$B_c = \frac{1}{K\tau_{RMS}}, \quad (2.7)$$

where K ranges from 5 to 50 for the bandwidths over which channel correlation exceeds from 0.5 to 0.9 [28].

Therefore, wireless communication channels can be classified as flat fading and frequency-selective fading according to the relation between the B_c and the signal bandwidth B . Flat fading refers to the case when the signal bandwidth B is much smaller than B_c , i.e., $B \ll B_c$, thus, resulting in highly correlated fading across the entire signal bandwidth. On the other hand, the frequency-selective fading corresponds to the scenario when the signal bandwidth B is larger than the B_c , i.e., $B > B_c$. This results in a large variation of the frequency components separated by more than the coherence bandwidth B_c , thus introducing performance degradation to the signal detector.

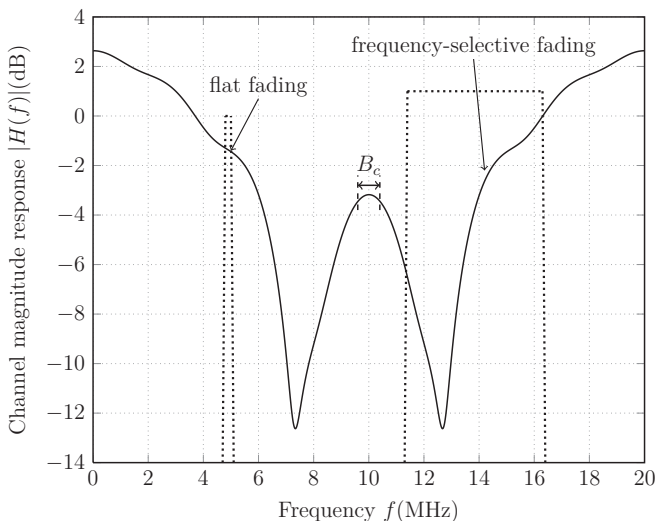


Figure 2.3.: Frequency response of the EPA channel given in Table A.1.

Since in linearly modulated systems the signal bandwidth B is inversely proportional to the symbol time T_s , i.e., $T_s = 1/B$, the frequency-flat and frequency-selective fading can be also classified according to the relation between the T_s and the τ_{RMS} . Having (2.7), it yields that $T_s \gg \tau_{RMS}$ corresponds to frequency-flat channels, while $T_s < \tau_{RMS}$ characterizes frequency-selective channels. For the EPA channel, given in Table A.1, with the power delay profile shown in Figure 2.2, it can be found that $\tau_{RMS} = 41.65$ ns, while $B_c = 480.23$ kHz for $K = 50$. The corresponding scenarios for signals that undergoes flat and selective fading are shown in Figure 2.3.

2.1.2. Time-Invariant Flat Fading Channels

For frequency-flat channels, the path delays are much smaller than the symbol duration, i.e., $\tau_l \approx 0$. The channel impulse response in (2.1) and channel frequency response in (2.2) can be written as

$$h(\tau) \approx \tilde{\alpha} \delta(\tau) \quad (2.8)$$

and

$$H(f) \approx \tilde{\alpha}, \quad (2.9)$$

respectively, where

$$\tilde{\alpha} = \alpha e^{j\theta} = \sum_{l=0}^{L-1} \alpha_l e^{j\theta_l}. \quad (2.10)$$

As it can be seen from (2.9) and (2.10), the magnitude of the channel frequency response $|H(f)|$ is constant over the whole signal bandwidth, while the value of $\tilde{\alpha}$ presents the

sum of L statistically independent multipath elements. Thus, according to the central limit theorem [27], the real and the imaginary component of $\tilde{\alpha}$ can be considered as two statistically independent Gaussian random variables with the same variance σ^2 and mean values μ_R and μ_I , respectively.

For some types of wireless environments, such as isotropic scattering, there is an absence of a direct or line-of-sight (LOS) path between the transmitter and receiver, thus giving $\mu_R = \mu_I = 0$. In this case, the magnitude α has a Rayleigh distribution with the probability density distribution (pdf)

$$f_\alpha(\alpha) = \frac{2\alpha}{\Omega_\alpha} \exp\left(-\frac{\alpha^2}{\Omega_\alpha}\right), \quad \alpha \geq 0, \quad (2.11)$$

where $\Omega_\alpha = 2\sigma^2 = \sum_{l=0}^{L-1} |\alpha_l|^2$ is the total average multipath channel power. Total power of frequency-flat channel, $\alpha^2 = |\tilde{\alpha}|^2$, has the Exponential distribution, given by

$$f_{\alpha^2}(x) = \frac{1}{\Omega_\alpha} \exp\left(-\frac{x}{\Omega_\alpha}\right), \quad \alpha \geq 0. \quad (2.12)$$

However, in some applications, such as satellite or mobile radio systems, the strong LOS path is present jointly with scattered paths. In this case, the amplitude α follows a Rice distribution with the pdf given by

$$f_\alpha(\alpha) = \frac{2\alpha(K+1)}{\Omega_\alpha} \exp\left(-\left(K + \frac{(K+1)\alpha^2}{\Omega_\alpha}\right)\right) I_0\left(2\alpha\sqrt{\frac{K(K+1)}{\Omega_\alpha}}\right), \quad \alpha \geq 0, \quad (2.13)$$

where $\mu_R^2 + \mu_I^2 = \alpha_0$ is the average power of the LOS component, $2\sigma^2 = \sum_{l=1}^{L-1} |\alpha_l|^2$ is the average power of the scattered components, and $\Omega_\alpha = 2\sigma^2 + \mu_R^2 + \mu_I^2$ is the total average power of the LOS multipath channel. Moreover, $K = (\mu_R^2 + \mu_I^2)/(2\sigma^2)$ is the Ricean factor, which defines the ratio between the power of the LOS and scattered component, while $I_0(u)$ presents the modified Bessel function of the first kind of the order 0 [29], defined as

$$I_0(u) = \frac{1}{2\pi} \int_0^{2\pi} e^{u \cos \theta} d\theta. \quad (2.14)$$

The corresponding total power of the LOS multipath channel, $\alpha^2 = |\tilde{\alpha}|^2 = 2$, follows a Noncentral Chi-square distribution with two degrees of freedom, given by

$$f_{\alpha^2}(x) = \frac{(K+1)}{\Omega_\alpha} \exp\left(-\left(K + \frac{(K+1)x}{\Omega_\alpha}\right)\right) I_0\left(2\sqrt{\frac{K(K+1)x}{\Omega_\alpha}}\right), \quad \alpha \geq 0. \quad (2.15)$$

2.1.3. Time-Variant Fading Channels

Without the loss of generality, the time-variant fading channel introduces the time-variant component into the flat channel model in (2.8). This is extended to the frequency-selective multipath channel, given by

$$h(\tau, t) \approx \tilde{\alpha}(t)\delta(\tau), \quad (2.16)$$

where

$$\tilde{\alpha}(t) = \alpha(t)e^{j\theta(t)} = \sum_{l=0}^{L-1} \alpha_l(t)e^{j\theta_l(t)} \quad (2.17)$$

is defined. The corresponding channel frequency response $H(f, t)$ becomes

$$H(f, t) \approx \tilde{\alpha}(t), \quad (2.18)$$

where time-variant phase shift $\theta_l(t)$ is given by

$$\theta_l(t) = 2\pi f_{D,l}t + \varphi_l. \quad (2.19)$$

Here, φ_l is an arbitrary random phase uniformly distributed on the interval $[-\pi, \pi]$ while $f_{D,l}$ presents a frequency domain dispersion of the l th path caused by the Doppler effect. Moreover,

$$f_{D,l} = f_D \cos(\psi_l) \quad (2.20)$$

is also known as the Doppler frequency at the l th propagation path associated with the angle of arrival ψ_l . The maximum Doppler frequency f_D occurs for the angle of arrival equal to zero, i.e., $\psi_l = 0$, and is given by

$$f_D = f_c \frac{\nu}{c}, \quad (2.21)$$

which depends on the velocity ν of the terminal station, the speed of light c , and the carrier frequency f_c .

As shown in (2.17) and (2.18), the time-varying channel can be considered as a superposition of many distinct scatterers, each with an unpredictable frequency shift due to random nature of the angle ψ_l . This effect induces a spectral broadening of the received spectrum, known as Doppler spread, and physically presents frequency interval $[f_c - f_D, f_c + f_D]$, known as Doppler spectrum. Jakes [30] proposed a statistical characterization of time-varying channel as a superposition of zero-mean Gaussian processes $\tilde{\alpha}(t)$ with power σ^2 and autocorrelation function

$$R(\Delta t) = \sigma^2 J_0(1\pi f_D \Delta t), \quad (2.22)$$

where $J_0(u)$ is the Bessel function of the first kind of the order 0. In this case, $\alpha(t)$ follows a Rayleigh distribution, while the corresponding Doppler spectrum, defined as the Fourier transform of $2R(\Delta t)$, is given by

$$S_D(f) = \begin{cases} \frac{2\sigma^2}{\pi\sqrt{f_D^2 - f^2}}, & |f| \leq f_D \\ 0, & \text{otherwise.} \end{cases} \quad (2.23)$$

Similar to frequency-selective channels, for which coherence bandwidth B_c characterizes the channel variations with respect to the frequency, coherence time T_c characterizes the time variation of the channel. It presents a time interval during which the channel impulse response and channel frequency response are highly correlated or $R(\Delta t)$ stays above a certain threshold. For a correlation threshold of 0.5, T_c is approximated as

$$T_c = \frac{9}{16\pi f_D}. \quad (2.24)$$

Consequently, depending on the relation between symbol time T_s and coherence time T_c , the channel is classified as slow and fast fading. The slow fading refers to case when

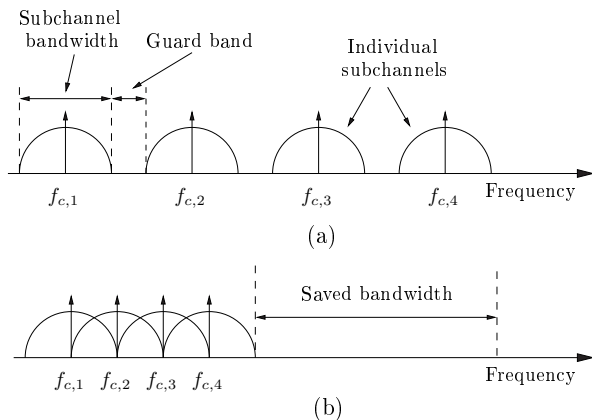


Figure 2.4.: (a) Conventional non-overlapping multicarrier modulation; (b) OFDM modulation.

$T_s \ll T_c$, for which the channel impulse response remains unchanged during the symbol time. On the other hand, if $T_s > T_c$, the signal undergoes fast fading with varying channel during symbol time. The real wireless communication systems, such as mobile cellular networks, however, may be affected by both frequency-selective and time-variant fading, known as double-selective fading.

Furthermore, the increased need for higher data rates requires short symbol duration. For linearly modulated systems this leads to increased bandwidth, often larger than coherence bandwidth, i.e., $B > B_c$. The resulting frequency-selective fading introduces inter-symbol interference (ISI) that affects the system performance. In conventional single-carrier systems, a standard method to combat frequency-selective fading uses a properly designed complex linear filter, called channel equalizer, which, ideally, has a frequency response that is the exact inverse of the channel frequency response $H(f)$. The number of channel paths defines the number of equalizer taps, which can be very large for highly selective channels. Moreover, in the presence of deep fades, equalizer introduces noise enhancement.

One effective method to combat frequency-selective channel, avoiding complex equalizers, is to parallelize data transmission by transferring data chunks at a lower rate. Each of those chunks, thus, occupies smaller bandwidth, known as subchannel, that are narrower than the coherence bandwidth B_c . Early parallel transmission systems [31] consist of non-overlapping subchannels that share the whole frequency band as shown in Figure 2.4a, where independent data is frequency multiplexed. The potential interference among adjacent subchannels, also known as inter-channel interference (ICI), is eliminated by the guard bands introduced between non-overlapping bands. To overcome the problem of wasting the spectrum, the concept of Orthogonal frequency division multiplexing (OFDM) is proposed in [32] by involving overlapped subchannels, realized by the Discrete Fourier

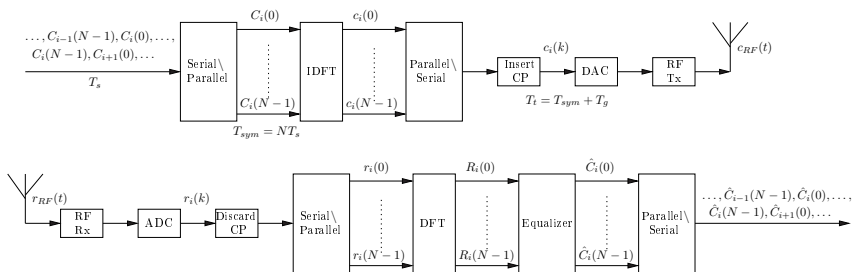


Figure 2.5.: Block diagram of a typical OFDM system.

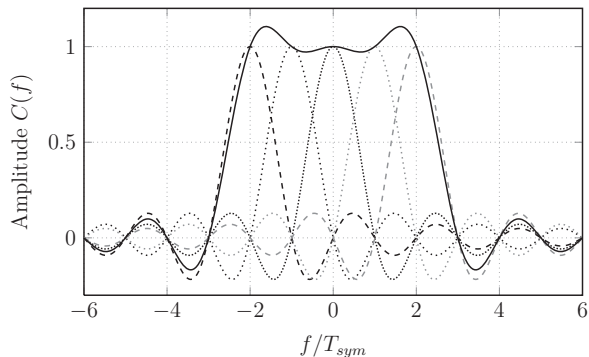
Transform (DFT) and a cyclic prefix. In such a way, bandwidth is saved, as shown in Figure 2.4b.

Due to its robustness to multipath propagation at high data rates, OFDM has been successfully used as the PHY layer technology in numerous wireless standards, such as European terrestrial digital audio and video broadcasting (DAB and DVB-T), IEEE 802.11 series of standards for wireless local area network (WLAN), and IEEE 802.16 series of standards (WiMAX) for wireless metropolitan area network (WMAN). Moreover, OFDM is incorporated in the Long Term Evolution (LTE) standard for 4G cellular mobile networks, as well as in the recently ratified cognitive radio based IEEE 802.22 standard for wireless regional area networks (WRAN). The basic principles of OFDM are given in the following section.

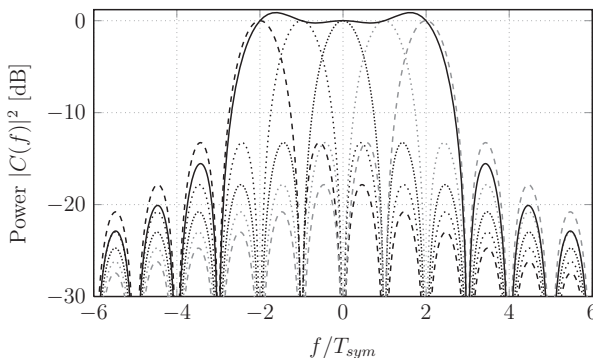
2.2. OFDM Technology

OFDM is a multicarrier modulation scheme that is widely adopted in many recently standardized broadband communication systems due to its ability to cope with frequency-selective fading [25]. The block diagram of a typical OFDM system is shown in Figure 2.5. The main idea behind OFDM is to divide a high-rate encoded data stream, with symbol time T_s and bandwidth B , into N parallel substreams, each with symbol time $T_{sym} = NT_s$ and bandwidth $\Delta f = 1/T_{sym} = 1/(NT_s)$, which are modulated onto N orthogonal carriers, $f_n = n/T_{sym} = 1/(NT_s)$, also referred as subcarriers. This operation is easily implemented in the discrete-time domain through an N -point Inverse Discrete Fourier Transform (IDFT) unit. It provides orthogonality among subchannels under ideal propagating conditions. The number of subchannels is chosen to ensure that each of them has a bandwidth less than the coherence bandwidth of the channel, thus undergoing relatively flat fading. OFDM systems accomplish the data transmission in a symbolwise fashion, for which each OFDM symbol conveys N complex data symbols. At the receiver, the information is recovered by performing a DFT on the received block of signal samples.

Due to the time-limited nature of each symbol, i.e., due to the finite duration T_{sym} of all subcarriers, the spectrum of the OFDM signal can be considered as the sum of the frequency shifted sinc functions in the frequency domain. The subcarriers are spaced directly proportional to the symbol rate T_{sym} , such that the peak of each subcarrier



(a) The amplitude of the OFDM signal (linear scale).



(b) Power spectrum of the OFDM signal [dB].

Figure 2.6.: Spectral characteristic of OFDM signal with five subcarriers.

coincides with the nulls of other subcarriers, thus avoiding the mutual interference, as illustrated in Figure 2.6.

Moreover, OFDM signal may incur out-of-band radiation, which causes non-negligible adjacent-channel interference (ACI). Figure 2.6b shows that the first sidelobe is not so small as compared to the main lobe in the spectra. Therefore, OFDM scheme places a guard band at outer subcarriers, called virtual carriers (VC), to prevent transmitted power from leaking into neighboring channels. In such a way, the spectrum shaping requirements at the transmitter are simplified, although, at the cost of decreased spectral efficiency. The virtual carriers are also used because of the non-ideal characteristics of low-pass filters required for the analog-to-digital (ADC) and digital-to-analog (DAC) conversion of the baseband signals, thus suppressing the use of all N subcarriers, if an N -point IDFT is applied for modulation. The subcarriers close to the Nyquist frequency $f_s/2 = 1/(2T_s)$ are attenuated by these filters and, thus, cannot be used for data transmission. The direct

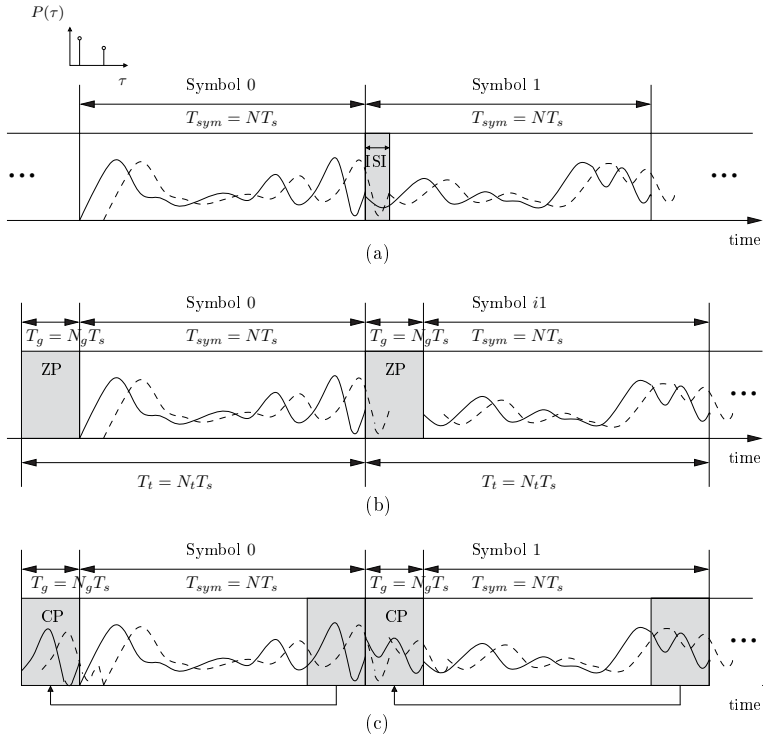


Figure 2.7.: Structure of an OFDM symbol (a) Without GI; (b) With ZP; (c) With CP.

current (DC) subcarrier is usually avoided for transmission, because DC offsets at the ADC and DAC may introduce heavy distortion by carrier feedthrough. A more detailed discussion on the implementation issues is given in Chapter 7.

Furthermore, due to the time dispersion associated with the frequency-selective channel, adjacent OFDM symbols may partially overlap in the time domain. This effect introduces ISI that limits the system performance, as shown in Figure 2.7a. The common approach to mitigate the ISI is to introduce a guard interval (GI) among adjacent symbols, as shown in Figure 2.7b,c. By extending the total symbol duration to $N_t = N + N_g$ samples, the length of the guard interval is made to be longer than the delay spread of the wireless channel. It also contains an additionally reserved part for synchronization margins, due to timing estimation issues and sampling frequency offsets between the transmitter and receiver. As a result, the maximum delay spread and hardware specification requirements must be considered during the design of an OFDM system. One way to realize GI is a zero padding (ZP) transmission where a null waveform is sent during GI, as shown in Figure 2.7b.

This approach, however, introduces inter-carrier interference (ICI), because the superposition of multiple copies of the transmitted signal destroys the orthogonality among subcarriers. Therefore, in practice, the guard interval is obtained by replicating the last N_g samples of each IDFT output from back to the front, thus forming the cyclic prefix (CP). As illustrated in Figure 2.7, the CP is appended to the front of the corresponding IDFT output. As guard interval carries no information and actually reduces bandwidth efficiency, the ratio of the GI length to the effective OFDM symbol is usually kept below one quarter. Nevertheless, it is shown that the redundancy and cyclic correlation features introduced by CP can be efficiently exploited for the synchronization [33] and signal identification [34] purposes.

As shown in Figure 2.5, after prepending the CP, an OFDM symbol, consisting of N_t complex (in-phase/quadrature) samples, is fed to the DAC and then filtered to remove baseband replicas. Finally, the analog signal is upconverted to be transmitted over a radio frequency (RF) carrier. The reverse steps are performed by the receiver. Therefore, after the downconversion, filtering, and ADC, the CP is removed from the received complex symbols by discarding the first N_g samples of the considered symbol. The remaining N samples are fed to a DFT and the corresponding output is subsequently passed to the channel equalizer. Assuming that the synchronization has already been established and that the CP is sufficiently long to eliminate the ISI, only a one-tap complex-valued multiplier is required to compensate for the channel distortion over each subcarrier. The equalization is further described in Subsection 2.6. However, to better understand this fundamental property and related implementation issues of an OFDM system, in the following section we introduce the mathematical model of the OFDM communication scheme, depicted in Figure 2.5.

2.3. Discrete-Time OFDM System Model

Because OFDM is a block-based communication model, a serial data stream is converted into parallel blocks of size N^1 while the IDFT is applied to obtain the time domain OFDM symbols. Complex data symbols within the i th OFDM symbol, denoted as $C_i(n)$, for $n = -\frac{N}{2}, \dots, \frac{N}{2} - 1$, are taken either from a PSK or from a QAM constellation, having the average power $E\{|C_i(n)|^2\} = \sigma_S^2$. The time domain representation of the i th OFDM symbol after the IDFT and CP insertion is then given by

$$c_i(t) = \begin{cases} \frac{1}{\sqrt{N}} \sum_{n=-\frac{N}{2}}^{\frac{N}{2}-1} C_i(n) e^{j2\pi f_n t}, & -T_g \leq t \leq T_{sym} \\ 0, & \text{otherwise} \end{cases}. \quad (2.25)$$

As described earlier, due to the digital implementation of an OFDM system, having T_s as a sampling interval, and k as a time sampling index, the sampled version of the continuous-time t can be written as $t = kT_s$. The subcarrier frequency f_n becomes

¹Usually, N takes a value of a power of two, which allows for the efficient implementation of the (I)FFT, having complexity of $\mathcal{O}(N \log_2 N)$ [35].

$f_n = n\Delta f = n/(NT_s)$, thus giving the discrete-time model of the transmitted OFDM signal

$$c_i(k) \triangleq c_i(kT_s) = \begin{cases} \frac{1}{\sqrt{N}} \sum_{n=-\frac{N}{2}}^{\frac{N}{2}-1} C_i(n) e^{j2\pi kn/N}, & -N_g \leq k \leq N-1 \\ 0, & \text{otherwise} \end{cases}. \quad (2.26)$$

By concatenating OFDM symbols in the time domain, the transmitted signal becomes

$$c(k) = \sum_i c_i(k - iT_s). \quad (2.27)$$

As mentioned in Section 2.1, the multipath propagation in wireless channels introduces time dispersion of the transmitted signal. To model this effects, we assume that the channel is quasi-static during the transmission of the i th OFDM symbol. The discrete-time model for the channel impulse response at the time instant k , sampled at the rate T_s , can be written as

$$h(k) = \sum_{l=0}^{L-1} \alpha_l e^{j\theta_l} \delta(k-l). \quad (2.28)$$

We further assume that the channel is sample-spaced, i.e., the channel impulse response paths are integer multiples of the system sampling rate T_s , thus giving $h(l) \triangleq h(lT_s) = h(\tau_l)$, for $l = 0, \dots, L-1$. The received signal $y(k)$ presents the linear convolution of the channel impulse response $h(k)$ and the transmitted signal $c(k)$, given by

$$y(k) = h(k) * c(k) = c(k) * h(k) = \sum_{l=0}^{L-1} h(l)c(k-l). \quad (2.29)$$

A CP consisting of $N_g \geq L$ samples is appended to each OFDM symbol to remove the ISI between two successive OFDM symbols. Because this operation inserts periodicity into the transmitted signal, the linear convolution in (2.29) becomes the circular convolution within the N -point time window, thus yielding

$$y(k) = h(k) \circledast c(k) = c(k) \circledast h(k) = \sum_{l=0}^{L-1} h(l)c(k-l)_N, \quad (2.30)$$

where $(k-l)_N$ denotes $(k-l) \bmod N$, i.e., $c(k-l)_N$ is a periodic version of $c(k-l)$ with the period N . Consequently, $y(k)$ becomes periodic with the period N .

Besides the multipath effect, additive noise is introduced to the transmitted signal. The main sources of additive noise are thermal background noise, electrical noise in the receiver equipment (such as flicker and shot noise), and interference [36]. The total effective noise at the receiver of an OFDM system can be modeled as additive white Gaussian noise (AWGN) having a uniform spectral density and zero-mean circularly symmetric complex Gaussian probability distribution with variance σ_W^2 , i.e., the time domain noise samples are given by $w(k) \sim SCN(0, \sigma_W^2)$. Therefore, the discrete-time model of the received OFDM signal can be written as

$$y(k) = \sum_{l=0}^{L-1} h(l)c(k-l)_N + w(k). \quad (2.31)$$

Multipath propagation and additive noise may significantly corrupt the signal and often place limitations on the system performance.

At the receiver, the DFT output for the i th OFDM symbol is computed as

$$Y_i(n) = \frac{1}{\sqrt{N}} \sum_{k=0}^{N-1} y(k + iN_t) e^{-j2\pi kn/N}, \quad -\frac{N}{2} \leq n \leq \frac{N}{2} - 1. \quad (2.32)$$

By substituting (2.31) into (2.32), it yields

$$\begin{aligned} Y_i(n) &= \frac{1}{\sqrt{N}} \sum_{k=0}^{N-1} \left[\sum_{l=0}^{L-1} h(l) c_i(k-l)_N + w_i(k) \right] e^{-j2\pi kn/N} \\ &= \frac{1}{N} \sum_{k=0}^{N-1} \sum_{l=0}^{L-1} h(l) \sum_{m=-\frac{N}{2}}^{\frac{N}{2}-1} C_i(m) e^{j2\pi(k-l)m/N} e^{-j2\pi kn/N} + W_i(n) \\ &= \frac{1}{N} \sum_{m=-\frac{N}{2}}^{\frac{N}{2}-1} \left[\sum_{l=0}^{L-1} h(l) e^{-j2\pi lm/N} \right] C_i(m) \left[\sum_{k=0}^{N-1} e^{-j2\pi k(m-n)/N} \right] + W_i(n) \\ &= \sum_{m=-\frac{N}{2}}^{\frac{N}{2}-1} H(m) C_i(m) \delta(m-n) + W_i(n), \end{aligned} \quad (2.33)$$

where $W_i(n) \sim SCN(0, \sigma_W^2)$ is given by

$$W_i(n) = \frac{1}{N} \sum_{k=0}^{N-1} w(k) e^{-j2\pi kn/N}, \quad -\frac{N}{2} \leq n \leq \frac{N}{2} - 1, \quad (2.34)$$

and $H(m)$ presents the complex channel frequency response, defined as the DFT of the channel impulse response, such that

$$H(m) = \sum_{l=0}^{L-1} h(l) e^{-j2\pi lm/N}, \quad -\frac{N}{2} \leq n \leq \frac{N}{2} - 1. \quad (2.35)$$

Because $\delta(m-n)$ presents the Kronecker delta, defined as

$$\delta(m-n) = \frac{1}{N} \sum_{k=0}^{N-1} e^{-j2\pi k(m-n)/N} = \begin{cases} 1, & m = n \\ 0, & m \neq n \end{cases}, \quad (2.36)$$

the received OFDM symbol in (2.33) becomes

$$Y_i(n) = H(n) C_i(n) + W_i(n). \quad (2.37)$$

From (2.37), it follows that an ideal (perfectly synchronized) OFDM system can be considered as a set of parallel Gaussian channels, each with different complex-valued attenuations/amplifications $H(n)$, as shown in Figure 2.8. This is the direct consequence of the DFT operation, which transforms the circular convolution in time from (2.30) to the multiplication in the frequency domain, i.e., $DFT^T[c(k) \otimes h(k)] = C(n)H(n)$, for $n = -N/2, \dots, N/2 - 1$.

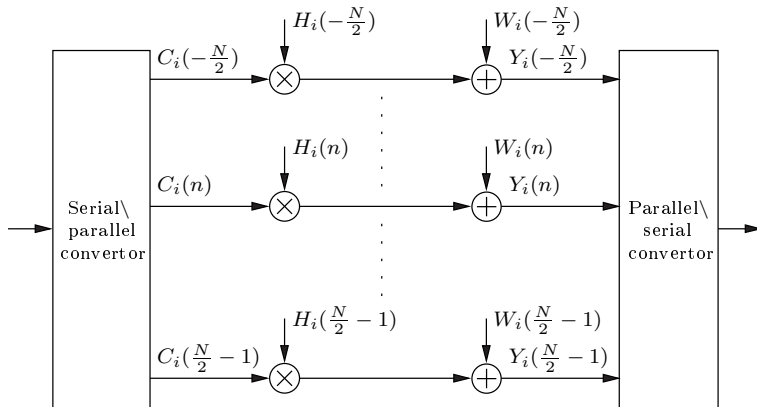


Figure 2.8.: An ideal OFDM transmission model considered as a set of N parallel Gaussian channels.

In order to recover the transmitted symbols correctly, an appropriate channel estimation is required. Having different attenuations, each distinct subcarrier is characterized with its individual signal-to-noise ratio (SNR), further referred as the SNR per subcarrier. It represents a standard measure of signal quality for communications systems, and is defined as

$$\begin{aligned}
 \rho(n) &= \frac{\mathbb{E}\{|C_i(n)H(n)|^2\}}{\mathbb{E}\{|W_i(n)|^2\}} \\
 &= \frac{\mathbb{E}\{|C_i(n)|^2\} |H(n)|^2}{\mathbb{E}\{|W_i(n)|^2\}} \\
 &= \frac{\sigma_S^2 |H(n)|^2}{\sigma_W^2} \\
 &= \rho_{av} \cdot |H(n)|^2,
 \end{aligned} \tag{2.38}$$

where ρ_{av} is the average SNR given by

$$\begin{aligned}
 \rho_{av} &= \frac{\mathbb{E}\{\sum_{n=0}^{N-1} |C_i(n)H(n)|^2\}}{\mathbb{E}\{\sum_{n=0}^{N-1} |W_i(n)|^2\}} \\
 &= \frac{\sigma_S^2}{\sigma_W^2}.
 \end{aligned} \tag{2.39}$$

as derived in [7]. Here, $|\cdot|^2$ denotes the squared magnitude of the complex data and $\mathbb{E}\{\cdot\}$ denotes the expectation over the time index i .

2.4. Digital Modulations Used in OFDM Systems

We consider some digital information that is represented by a finite bit sequence. To transmit this information over a physical analog channel, we need a mapping rule between

the set of bit sequences and the set of possible signals or constellation points in the complex plane, as shown in Figure 2.9. Such mapping rule is called a digital modulation scheme. A linear digital modulation scheme is characterized by the complex baseband signal [37], given by

$$C(t) = \sum_i C_i g(t - kT), \quad (2.40)$$

where C_i is a given constellation point and $g(t)$ is a pulse shape used for transmission. Because the mapping is usually performed in the digital domain we further consider the discrete domain representation of modulated complex symbols. In the following, we resume some of the coherent modulation schemes, typically used in OFDM systems within the current standards.

2.4.1. Phase Shift Keying (PSK)

Phase Shift Keying (PSK) modulation or Multiple PSK modulation (M-PSK) modulation, where M denotes the number of constellation points, puts all signal information into the phase of the transmitted signal, thus preserving constant envelope property. The M-PSK complex symbol C_i can be written as

$$C_i = \sigma_S \cdot e^{j(\frac{2\pi m}{M} + \theta_0)}, \quad m = 0, 1, \dots, M - 1, \quad (2.41)$$

where σ_S^2 is the average signal power and θ_0 is an arbitrary constant phase. Figure 2.9 shows the constellation diagrams for $M = 2, 4$, and 8 , i.e., Binary Phase Shift Keying (BPSK), Quadrature Phase Shift Keying (QPSK or 4-PSK), and 8-PSK, for $\theta_0 = 0$.

The simplest PSK modulation format is BPSK, for which a logical „1“ is encoded as a zero phase, while a logical „0“ is coded as a phase of π . The modulated symbol, defined in (2.41), is given by

$$C_i = \pm \sigma_S, \quad (2.42)$$

having the constellation diagram shown in Figure 2.9a. The M-PSK constellation diagrams for 4-PSK constellation (2 bits mapped into $4 = 2^2$ phases) and 8-PSK constellation (3 bits mapped into $8 = 2^3$ phases), are shown in Figure 2.9b and Figure 2.9c, respectively. They are optimized to minimize the bit error rate (BER), resulting in the Gray-coded M-PSK constellation, i.e., the adjacent constellation points differ in one bit as in Figure 2.9.

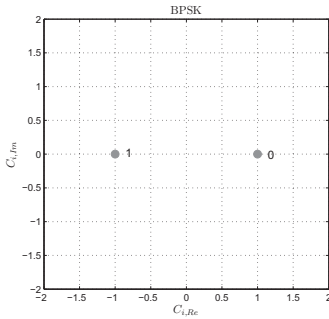
The BER is defined as the ratio between the number of erroneous bits to the number of total transmitted bits. It is usually taken as a measure of modulation quality in the presence of the noise. Due to statistical nature of the additive noise, the BER is approximated with its expectation, named bit error probability p_b . This estimate is accurate for a long time interval and a high number of bit errors. In this thesis, during the performance analysis, we denote the bit error probability p_b as the BER.

The BER of BPSK modulation in an AWGN channel can be expressed as [38]

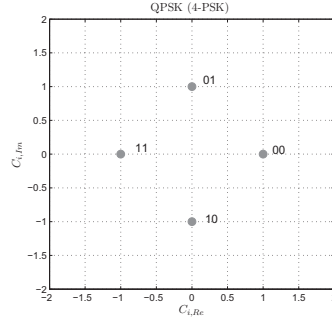
$$BER_{BPSK} = Q\left(\sqrt{2\rho}\right), \quad (2.43)$$

where ρ is the average SNR per symbol, defined in (2.39), and $Q(x)$ is given by

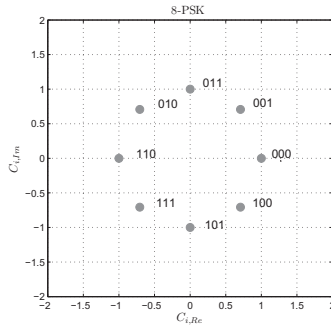
$$Q(x) = \frac{1}{2} \operatorname{erfc}\left(\frac{x}{\sqrt{2}}\right), \quad (2.44)$$



(a) BPSK constellation diagram



(b) QPSK(4-PSK) constellation diagram



(c) 8-PSK constellation diagram

Figure 2.9.: Gray-coded M-PSK constellation diagrams.

where

$$\operatorname{erfc}(x) = \frac{2}{\sqrt{\pi}} \int_x^{\infty} e^{-y^2} dy \quad (2.45)$$

is the complementary error function (erfc). For higher order M-PSK modulations, where $M > 4$, the symbol error rate SER can be expressed as

$$SER_{M-PSK} = 2Q\left(\sqrt{2\rho} \sin\left(\frac{\pi}{M}\right)\right). \quad (2.46)$$

For Gray-coded modulations, the BER in the high SNR regime is given approximately as

$$BER_{M-PSK} \approx \frac{SER_{M-PSK}}{\log_2 M}.$$

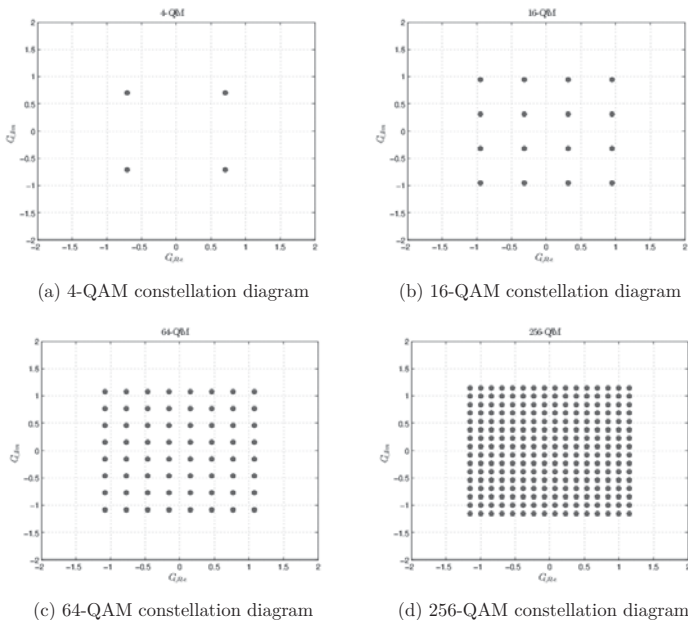


Figure 2.10.: QAM constellation diagrams.

2.4.2. Quadrature Amplitude Modulation (QAM)

Quadrature Amplitude Modulation (QAM) is a bandwidth efficient signaling scheme that, unlike M-PSK, is characterized with the non-constant envelope. This property enables more bits per second (bps) to be transmitted in a given frequency bandwidth [39]. QAM modulated symbols with M constellation points can be written as

$$C_i = \sigma_S \cdot K \cdot (C_{i,Re} + jC_{i,Im}),$$

where $C_{i,Re}, C_{i,Im} \in \{\pm 1, \pm 3, \dots, \sqrt{M} - 1\}$ while K is a scaling factor that normalizes the average power to σ_S^2 . Table 2.1 shows the values of K for different QAM constellations. The corresponding QAM constellation diagrams for 4-QAM (2 bits mapped into $4 = 2^2$ points), 16-QAM (4 bits mapped into $16 = 2^4$ points), 64-QAM (6 bits mapped into $64 = 2^6$ points), and 256-QAM (8 bits mapped into $256 = 2^8$ points), are shown in Figure 2.10. It can be noticed that 4-QAM corresponds to QPSK with the constant phase shift $\theta_0 = \pi/4$. The SER of QAM modulation is given by

$$SER_{M-QAM} = 1 - \left(1 - 2 \left(1 - \frac{1}{\sqrt{M}}\right) Q \left(\sqrt{3 \frac{E_b \log_2 M}{(M-1)N_0}}\right)\right)^2,$$

Table 2.1.: Modulation dependent parameters.

Modulation	Number of bits m	K
4-QAM	2	$1/\sqrt{2}$
16-QAM	4	$1/\sqrt{10}$
64-QAM	6	$1/\sqrt{42}$
256-QAM	8	$1/\sqrt{170}$

where $Q(x)$ is defined in (2.44). For Gray-coded QAM constellations, the BER in the high SNR regime is, similar to M-PSK, given approximately by

$$BER_{M-QAM} \approx \frac{SER_{M-QAM}}{\log_2 M}. \quad (2.47)$$

QAM modulation schemes, such as 4-QAM (QPSK), 16-QAM, and 64-QAM, are used in current digital wireless communications standards, such as Wireless Local Area Network (WLAN), Worldwide Interoperability for Microwave Access (WiMAX), and Long Term Evolution (LTE) [40].

2.5. OFDM System Impairments

As previously mentioned, OFDM transmission is based on the orthogonality among subcarriers. This allows for parallel transmission that mitigates the ISI distortion caused by the multipath fading channel. However, due to hardware imperfections and multipath channel effects, required orthogonality can not be warranted. This introduces the ISI and ICI that result in a large performance degradation. Therefore, synchronization inevitably plays an important role in the design of OFDM systems. The basic task of synchronization is to recover some reference parameters from the received signal that are further required for reliable data detection. The basic impairments that affect the orthogonality of subcarriers in an OFDM system can be classified in the following way [25]:

- *symbol timing offset (STO)*: In order to correctly perform the N -point DFT at the receiver, the exact samples of the transmitted signal during the OFDM symbol duration must be "caught" inside the DFT window. However, as shown in Figure 2.14, the starting point of the DFT window may be estimated correctly, a little earlier, too early, or a little later than the exact timing instance. The goal of timing estimation is to identify the starting point of each received OFDM symbol to find the correct position of the DFT window. It is also used to locate the start of the frame (a sequence of OFDM symbols) in the burst-mode transmissions. This refers to frame synchronization. STO causes a linear phase rotation of the subcarriers, which can be easily corrected during channel estimation. The timing synchronization errors should be kept small compared to the GI, with respect to the available margin, as described in Subsection 2.5.1.

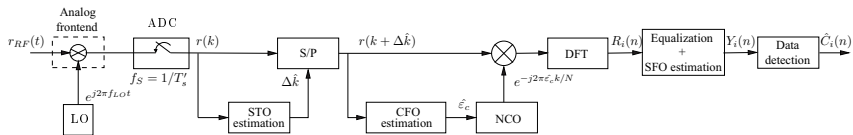


Figure 2.11.: Block diagram of a basic OFDM receiver.

- carrier frequency offset (CFO):** There are two main sources that cause this phenomenon: the frequency error between the local oscillators at the transmitter and receiver; and common Doppler shift due to movement of the transmitter and receiver, as discussed in Section 2.1. As shown in Figure 2.12, CFO causes attenuation and phase shift of the particular subcarrier while introducing the ICI. In standard communication systems, such as IEEE 802.11 WLAN, the oscillator precision tolerance is specified to be less than ± 20 . This results into the CFO range of -40 ppm to $+40$ ppm, e.g., at the carrier frequency $f_c = 5$ GHz, the resulting CFO is up to ± 200 kHz. This causes 2π phase rotation of the received baseband signal every $5\mu\text{s}$, resulting in the complete loss of information unless appropriate synchronization is performed. Additionally, the Doppler spread, originated from the movement of the transmitter and/or receiver, introduces some additional hundreds of hertz, which is relatively minor to the CFO caused by the mismatch of local oscillators, as discussed in [41]. The orthogonality of subcarriers is restored by performing frequency synchronization and compensating for any frequency offset.
- sampling frequency offset (SFO):** Similar to CFO, in practical systems, there is a frequency mismatch between the oscillator used to drive sampling clock of the DAC at the transmitter and the sampling clock frequency of the ADC at the receiver. As shown in Figure 2.13, this effect causes the received waveform to be sampled at the time-varying time instants. This introduces the subcarrier dependent attenuation and phase shift, as well as the ICI at the output of the receiver Discrete Fourier Transform (DFT). Moreover, SFO causes a periodic insertion or loss of one sample, thus introducing additional degradation of the system performance. The sampling clock synchronization limits those impairments to a tolerable level.

We further introduce the individual and joint effects of each of the abovementioned system impairments in the discrete-time model. Figure 2.11 depicts the block diagram of the receiver. In the analog frontend, the incoming waveform $r_{RF}(t)$ is filtered and down-converted to the baseband using the two quadrature sinusoids generated by a local oscillator (LO). The baseband signal is then passed to the ADC, where it is sampled with the frequency $f'_s = 1/T'_s$. Due to the presence of the SFO between the sampling oscillators, the sampling time at the receiver ADC, T'_s , is different from the sampling time T_s used at the transmitter [42], as shown in Figure 2.13. This impairment can be expressed as $T'_s = T_s(1 + \epsilon_s)$, thus defining the normalized SFO ϵ_s as

$$\epsilon_s = \frac{T'_s - T_s}{T_s}. \quad (2.48)$$

The received baseband signal, sampled at T'_s , can be further written as

$$r(k) \triangleq r(kT'_s) = y(k(1 + \epsilon_s)T_s). \quad (2.49)$$

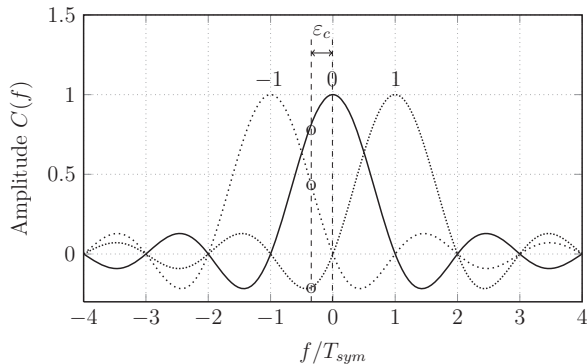


Figure 2.12.: Inter-carrier interference (ICI) subject to the CFO.

The presence of Doppler shifts and/or RF oscillator instabilities, additionally causes the difference between the receiver frequency f_{LO} and the transmitter carrier frequency f_c , as shown in Figure 2.12. The difference $f_d = f_c - f_{LO}$ is referred to as the CFO, or shorter, frequency offset. Therefore, the received baseband signal, sampled at T'_s in the presence of the CFO, can be expressed as

$$r(k) = y(k(1 + \varepsilon_s))e^{j\theta(k)} + w(k), \quad (2.50)$$

where phase shift (rotation) influenced by the CFO and SFO is given by

$$\theta(k) = 2\pi k f_d T'_s. \quad (2.51)$$

The frequency offset f_d normalized to the subcarrier spacing $\Delta f = 1/(NT_s)$ is defined as

$$\varepsilon_c = \frac{f_d}{\Delta f} = N f_d T_s. \quad (2.52)$$

By substituting (2.48) and (2.52) in (2.50), the received signal in the presence of hardware impairments is given by

$$r(k) = y(k(1 + \varepsilon_s))e^{j2\pi k f_d T'_s} = y(k(1 + \varepsilon_s))e^{j2\pi \varepsilon_c (1 + \varepsilon_s) k / N}. \quad (2.53)$$

When the signal reception starts, the beginning of the OFDM symbols is unknown to the receiver, because the time scales at the transmitter and receiver are misaligned, as shown in Figure 2.14. Let Δk denote the number of samples by which the receive time scale is shifted from its ideal setting. The samples from the ADC are thus expressed by

$$r(k) = e^{j2\pi \varepsilon_c (1 + \varepsilon_s) k / N} y((k - \Delta k)(1 + \varepsilon_s)) + w(k). \quad (2.54)$$

By replacing (2.27) and (2.31) in (2.54), it becomes

$$r(k) = e^{j2\pi \varepsilon_c (1 + \varepsilon_s) k / N} \sum_i \sum_{l=0}^{L-1} h(l) c_i((k - \Delta k)(1 + \varepsilon_s) - l - iN_t)_N + w(k). \quad (2.55)$$

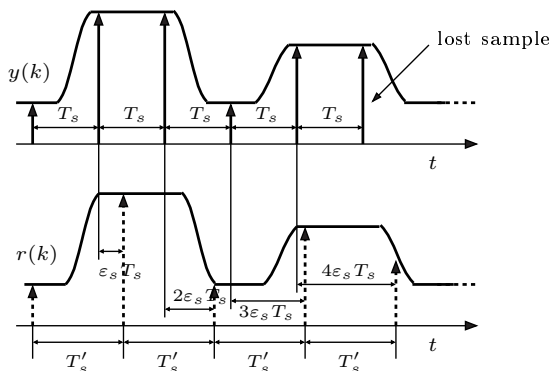


Figure 2.13.: An illustration of the SFO.

The individual effects of the abovementioned system impairments to the received signal in the frequency domain can be derived by taking the DFT of the time domain received samples (2.55), i.e., the received signal in frequency domain becomes

$$R_i(n) = \frac{1}{N} \sum_{k=0}^{N-1} r(k + iN_i) e^{-j2\pi kn/N}, \quad -\frac{N}{2} \leq n \leq \frac{N}{2} - 1. \quad (2.56)$$

The frequency and timing synchronization units shown in Figure 2.11 employ the received samples $r(k)$ to compute the estimates of ε_c and Δk , denoted as $\hat{\varepsilon}_c$ and $\hat{\Delta k}$, respectively. The former is used to counter-rotate $r(k)$ at an angular speed $2\pi\hat{\varepsilon}_c k/N$ (frequency correction) using a numerically controlled oscillator (NCO). On the other hand, the timing estimate, $\hat{\Delta k}$, is exploited to achieve the correct position of the received signal within the DFT window (timing correction). More specifically, the samples $r(k)$ with the indices $iN_i + \Delta k \leq k \leq iN_i + \Delta k + N - 1$ are fed to the DFT device. The corresponding output of the DFT is used to detect the data symbols conveyed by the i th OFDM block. The specific implementation of the synchronization stages within the TIGR framework is discussed in Section 8.

2.5.1. Effects of Timing Offset

To assess the performance of the OFDM system in the presence of a small STO, let assume the absence of SFO and CFO, i.e., $\varepsilon_s, \varepsilon_c = 0$, respectively. As shown in Figure 2.14, there are four different cases of the STO: the DFT window position is exact, a little earlier, too early, or a little later than the DFT window of the received OFDM signal. For the first case, the estimated starting point of OFDM symbol coincides with the exact timing, thus preserving the orthogonality among subcarrier frequency components. Therefore, the OFDM symbol can be perfectly recovered without any type of interference.

The second case refers to the situation when the estimated starting point of the OFDM symbol is located before the exact point, but after the uncorrupted part of the CP, i.e.,

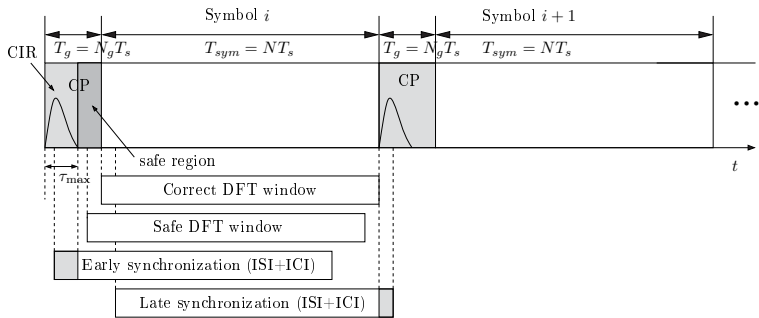


Figure 2.14.: Different cases of the DFT window location.

$-N_g + L - 1 \leq \Delta k \leq 0$. There is no ISI because two adjacent symbols do not overlap. The effects of STO on the received signal can be derived from (2.56) as

$$\begin{aligned}
 R_i(n) &= \frac{1}{N} \sum_{k=0}^{N-1} \left[\sum_{l=0}^{L-1} h(l) c_i(k-l-\Delta k)_N + w_i(k) \right] e^{-j2\pi kn/N} \\
 &= \frac{1}{N} \sum_{k=0}^{N-1} \sum_{l=0}^{L-1} h(l) \sum_{m=-\frac{N}{2}}^{\frac{N}{2}-1} C_i(m) e^{j2\pi(k-l-\Delta k)m/N} e^{-j2\pi kn/N} + W_i(n) \\
 &= \frac{1}{N} \sum_{m=-\frac{N}{2}}^{\frac{N}{2}-1} \left[\sum_{l=0}^{L-1} h(l) e^{-j2\pi lm/N} \right] C_i(m) \left[\sum_{k=0}^{N-1} e^{-j2\pi k(m-n)/N} \right] e^{-j2\pi \Delta km/N} + W_i(n) \\
 &= \sum_{m=-\frac{N}{2}}^{\frac{N}{2}-1} H(m) C_i(m) \delta(m-n) e^{-j2\pi \Delta km/N} + W_i(n) \\
 &= H(n) C_i(n) e^{-j2\pi \Delta kn/N} + W_i(n),
 \end{aligned} \tag{2.57}$$

where $W_i(n)$ and $H(m)$ are defined in (2.34) and (2.35), respectively, and $\delta(m-n)$ presents the Kronecker delta defined in (2.36).

From (2.57) it can be seen that the orthogonality among subcarriers is preserved and that the small STO causes only a linear phase offset proportional to Δk and subcarrier index n . This offset can be compensated by the channel equalizer, which treats STO-induced phase shifts as a phase rotation caused by the channel effects.

The last two cases refer to the scenario for which the STO is outside the time segment $[-N_g + L - 1, 0]$, thus causing the i th symbol to introduce interference to the $(i-1)$ th or $(i+1)$ th symbol, depending on whether $\Delta k < -N_g + L - 1$ or $\Delta k > 0$, respectively. Additionally, the orthogonality among the subcarriers within the symbol is destroyed causing the ICI. During the evaluation of the system performance, only the first two cases are considered because timing synchronization in TIGR utilizes the robust S&C method [43] based on the sufficiently long CP. This assures the timing point to belong

to the safe region. The more detailed study on STO-induced system degradation can be found in [44].

2.5.2. Joint Effect of Frequency and Sampling Offset

Because both the CFO and SFO introduce attenuation, phase shift, and ICI into the received signal, we jointly consider their influence on the system performance. The presented discrete-time characterization is based on the model given in [45], where the general case of MIMO OFDM receiver is considered. Let assume an ideal STO compensation, i.e., $\Delta k = 0$. By substituting (2.55) in (2.56), the received signal at the DFT output is given by

$$\begin{aligned}
 R_i(n) &= \frac{1}{N} \sum_{k=0}^{N-1} \left[e^{j2\pi\varepsilon_c(1+\varepsilon_s)(k+iN_t)/N} \sum_{l=0}^{L-1} h(l)c_i((k+iN_t)(1+\varepsilon_s) - l - iN_t)_N + w(k) \right] e^{-j2\pi kn/N} \\
 &= \frac{1}{N} e^{j\varphi_i} \sum_{k=0}^{N-1} e^{j2\pi k(\varepsilon_c(1+\varepsilon_s)-n)/N} \sum_{l=0}^{L-1} h(l) \sum_{m=-\frac{N}{2}}^{\frac{N}{2}-1} C_i(m) e^{j2\pi(k(1+\varepsilon_s)-l+i\varepsilon_s N_t)m/N} + W_i(n) \\
 &= \frac{1}{N} e^{j\varphi_i} \sum_{m=-\frac{N}{2}}^{\frac{N}{2}-1} \left\{ \sum_{l=0}^{L-1} h(l) e^{-j2\pi lm/N} \right\} C_i(m) e^{j2\pi i m \varepsilon_s N_t/N} \sum_{k=0}^{N-1} e^{j2\pi k((m+\varepsilon_c)(1+\varepsilon_s)-n)/N} + W_i(n) \\
 &= \frac{1}{N} e^{j\varphi_i} \sum_{m=-\frac{N}{2}}^{\frac{N}{2}-1} H(m) C_i(m) e^{j2\pi i m \varepsilon_s N_t/N} \sum_{k=0}^{N-1} e^{j2\pi k((m+\varepsilon_c)(1+\varepsilon_s)-n)/N} + W_i(n),
 \end{aligned} \tag{2.58}$$

where $\varphi_i = 2\pi i \varepsilon_c(1+\varepsilon_s)N_t/N$ is the (symbol) time dependent phase shift, while $W_i(n)$ and $H(m)$ are zero mean AWGN with the variance σ_W^2 and channel frequency response, defined in (2.34) and (2.35), respectively.

Let's define $f_N(x)$ as

$$\begin{aligned}
 f_N(x) &= \frac{1}{N} \sum_{k=0}^{N-1} e^{j\frac{2\pi kx}{N}} \\
 &= \frac{\sin(\pi x)}{N \sin(\pi x/N)} e^{j\frac{\pi(N-1)x}{N}}.
 \end{aligned} \tag{2.59}$$

Then, replacing (2.59) in (2.58), it yields

$$R_i(n) = e^{j\varphi_i} \sum_{m=-\frac{N}{2}}^{\frac{N}{2}-1} H(m) C_i(m) e^{j2\pi i m \varepsilon_s N_t/N} f_N((\varepsilon_c + m)(1+\varepsilon_s) - n) + W_i(n), \tag{2.60}$$

which can be rewritten as

$$R_i(n) = e^{j2\pi i N_t \phi_n/N} H(n) C_i(n) f_N(\phi_n) + I_i(n, \varepsilon_c, \varepsilon_s) + W_i(n). \tag{2.61}$$

Here, $I_i(n, \varepsilon_c, \varepsilon_s)$ accounts for the ICI on the n th subcarrier, given by

$$I_i(n, \varepsilon_c, \varepsilon_s) = e^{j\varphi_i} \sum_{m=-\frac{N}{2}, m \neq n}^{\frac{N}{2}-1} H(m) C_i(m) e^{j2\pi i m \varepsilon_s N_t/N} f_N(\phi_m + m - n), \tag{2.62}$$

where ϕ_m is used to denote the joint contribution of the CFO and SFO on the m th subcarrier, and is defined as

$$\begin{aligned}\phi_m &\triangleq \phi_m(\varepsilon_c, \varepsilon_s) = \varepsilon_c(1 + \varepsilon_s) + m\varepsilon_s \\ &\approx \varepsilon_c + m\varepsilon_s, \quad -\frac{N}{2} \leq m \leq \frac{N}{2} - 1.\end{aligned}\tag{2.63}$$

It follows from (2.61) that the joint effect of frequency offset ε_c and sampling offset ε_s influences the received signal on the n th subcarrier twofold. First, the subcarriers are attenuated by $|f_N(\phi_n)|^2$ and the symbol constellation on each subcarrier is phase rotated by $(\pi\phi_n(2iN_i + N - 1)/N)$. Secondly, (2.62) gives the interference contributed from other subcarriers (ICI). The subcarrier symbol rotation consists of two components that both depend on the subcarrier position, given by ϕ_n . The first component $e^{\frac{j\pi(N-1)\phi_n}{N}}$ is contained in $f_n(\phi_n)$ and is time independent. Therefore, it is the same in all symbols within the frame for the particular subcarrier, similar to the effect of the STO in (2.57). The second component $e^{\frac{j2\pi i N_i \phi_n}{N}}$ depends on the time index i . This effect requires continuous tracking and compensation of the rotated phase during the time. More on this is given in Section 7.2.

The discussion about the joint and individual impacts of the CFO ε_c and SFO ε_s on the system performance is given in Chapter 7. Those degradations are quantified through the concept of SNR loss.

2.6. Equalization

Channel equalization is the process through which a coherent receiver compensates for any distortion induced by frequency-selective fading. Let us consider the ideal timing and frequency synchronization throughout this subsection, i.e., $\varepsilon_c = 0$, $\varepsilon_s = 0$, and $\Delta k = 0$. The channel is assumed to be static over each OFDM symbol, but can vary from symbol to symbol. The output of the receiver DFT during the i th symbol can be written as

$$Y_i(n) = R_i(n) = H_i(n)C_i(n) + W_i(n), \quad -\frac{N}{2} \leq n \leq \frac{N}{2} - 1,\tag{2.64}$$

where $C_i(n)$ is the complex data symbol, while $W_i(n)$ and $H_i(m)$ are defined in (2.34) and (2.35), respectively. An important feature of OFDM is that channel equalization can be independently performed over each subcarrier using a bank of one-tap multipliers. As shown in Figure 2.15, the n th DFT output $Y_i(n)$ is weighted by a complex-valued coefficient $P_i(n)$ to compensate for the channel-induced attenuation and phase rotation. The equalized sample $Y'_i(n) = P_i(n)Y_i(n)$ is subsequently passed to the detection unit, which delivers the final decisions $\hat{C}_i(n)$ on the transmitted data.

Intuitively, the simplest method for the design of the equalizer coefficients is to perform a pure channel inversion, known as zero forcing (ZF) criterion. The equalizer coefficients are then given by

$$P_i(n) = \frac{1}{H_i(n)},\tag{2.65}$$

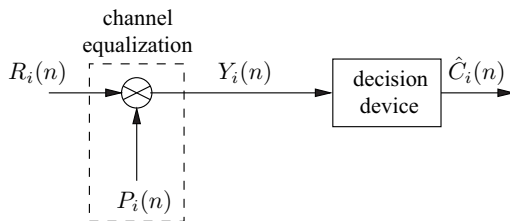
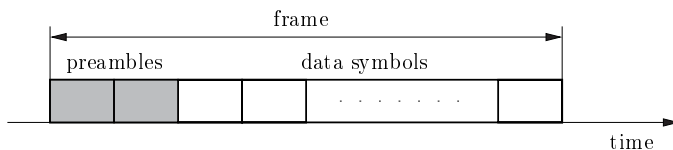
Figure 2.15.: Equalization of the n th subcarrier.

Figure 2.16.: The frame structure.

while the DFT output takes the form

$$Y'_i(n) = \frac{Y_i(n)}{H_i(n)} = C_i(n) + \frac{W_i(n)}{H_i(n)}, \quad -\frac{N}{2} \leq n \leq \frac{N}{2} - 1. \quad (2.66)$$

Observing (2.66), it can be noticed that ZF equalization totally compensates for any distortion induced by the wireless channel. However, the resulting noise power, given by $\sigma_W^2/|H_i(n)|^2$, may be excessively large over the subcarriers with low channel gains.

An inherent system requirement for the ZF equalizer is the knowledge of the channel frequency response $H_i(n)$. Therefore, in many wireless OFDM systems, the sequence of data symbols is preceded by several reference OFDM symbols (preambles) known to the receiver, forming the OFDM frame. Figure 2.16 shows a typical frame structure for which preambles are typically used for synchronization and/or channel estimation. Some of the fixed wireless standards, such as WLAN, assume that the channel remains static over the frame duration, i.e., $H_i(n) = H(n)$, for $i = 1, \dots, I$, where I is the total number of OFDM symbols within one frame. Consequently, channel estimates obtained from the preambles can be used to coherently detect the entire data payload.

Assuming that the OFDM frame has one preamble with the index $i = p = 1$, the output of the DFT block (2.64) can be written as

$$Y_p(n) = H(n)C_p(n) + W_p(n), \quad -\frac{N}{2} \leq n \leq \frac{N}{2} - 1, \quad (2.67)$$

where $C_p(n)$ is the complex data symbol known to the receiver. The estimates of the channel frequency response $\hat{H}(n)$ are then obtained as

$$\hat{H}(n) = \frac{Y_p(n)}{C_p(n)} = H(n) + \frac{W_p(n)}{C_p(n)}, \quad -\frac{N}{2} \leq n \leq \frac{N}{2} - 1. \quad (2.68)$$

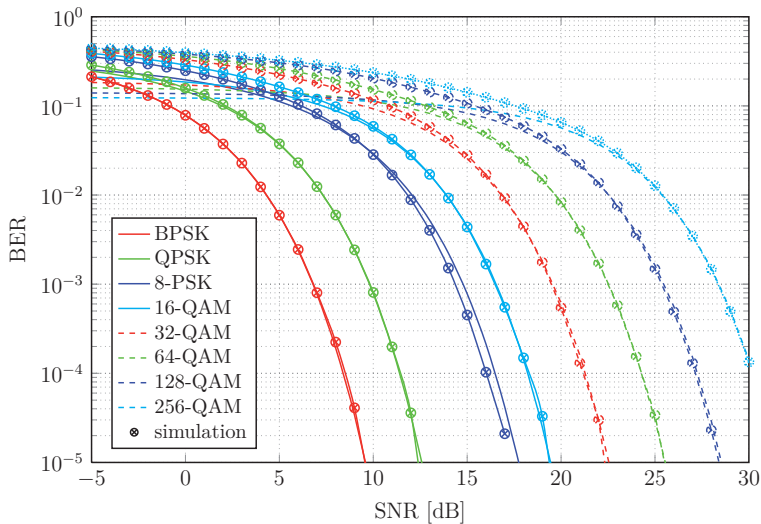


Figure 2.17.: BER performance of an OFDM system in an AWGN channel.

However, in applications characterized by relatively high mobility, such as those provided by the LTE standard, the channel response undergoes significant variations over one frame. It must be therefore continuously tracked to maintain the reliable data detection. In this case, in addition to initial reference blocks, known symbols called pilots are inserted into the payload section of the frame at some convenient positions. These pilots are scattered both in time and frequency directions, i.e., they are positioned over different blocks and different subcarriers, such that they are used as reference values for channel estimation and tracking.

2.7. Performance of OFDM systems

The performance of an ideal OFDM system in the presence of an AWGN channel is shown in Figure 2.17. It is shown that simulation results match the analytical curves derived in Section 2.4. Furthermore, Figure 2.18 shows the performance of an OFDM system applying the LS channel estimation. For a particular BER, channel estimation introduces certain SNR loss, i.e., compared to the ideal transceiver, higher SNR is required to achieve the same BER. Table 2.2 shows the required SNR values and corresponding SNR losses of considered modulations for target BER = 10^{-4} and BER = 10^{-3} .

More advanced schemes for channel estimation in OFDM system, such as Minimum Mean Square Error (MMSE) and DFT methods [46, 47, 48], assume the known statistical properties of the channel and noise variance. They can improve the mean square error (MSE) performance of the channel estimation up to 15 dB ([49]). However, the reasons

Table 2.2.: Required SNR, SNR gap, and SNR margin of an OFDM system with the LS channel estimation in an AWGN channel for $\text{BER} = 10^{-3}$.

Modulation bits r_n	Req. SNR [dB] BER = 10^{-3}	Req. SNR [dB] BER = 10^{-4}	ΔSNR [dB] (LS) BER = 10^{-3}	ΔSNR [dB] (LS) BER = 10^{-4}
1	6.79	8.4	1.1	1.19
2	9.8	11.44	2.36	2.36
3	14.42	16.1	2.94	3.27
4	16.54	18.24	2.91	3.25
5	19.56	21.26	3.05	3.15
6	22.55	24.32	3.32	3.49
7	25.41	27.19	3.23	3.5
8	28.41	30.22	3.38	3.75

for choosing an LS estimator in the following discussion and implementation within the TIGR framework are twofold. First, the simplicity and low computational requirement favor the LS channel estimator compared to other advanced methods, because it is easy implementable in an SDR testbed, such that additional processing load at the receiver is avoided. Secondly, the influence of the LS channel estimator on the system performance can be considered as a "higher bound" of how the channel estimation can affect the performance of a particular resource allocation algorithm. The utilization of other advanced channel estimation methods can bring the performance curve closer to the "ideal" curve.

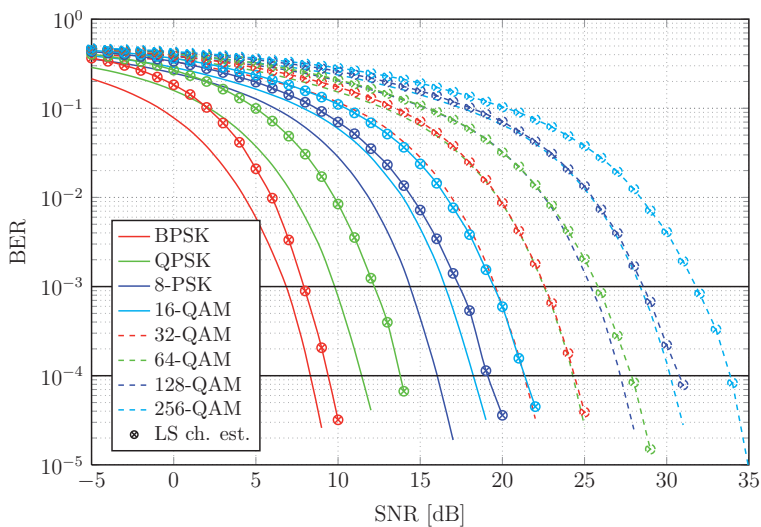


Figure 2.18.: BER performance of an OFDM system with the LS channel estimation in an AWGN channel.

3. Resource Allocation Basics

In time-dispersive environments, the performance of standard OFDM systems, which apply the same modulation over all subcarriers, is characterized by different BER values over subcarriers. While severely faded subcarriers contribute to the most of the errors, the rest of the OFDM signal spectrum may experience no bit errors. A significant performance improvement of OFDM systems can be achieved by properly adjusting allocated power and data rate over subcarriers such that the frequency diversity offered by multipath channels is exploited. This kind of spectrally efficient transmission, named *adaptive modulation* or *resource allocation*¹, aims at optimizing the transmission parameters (bandwidth, coding/data rate, power) to provide power and bandwidth efficiency.

For given Quality of Service (QoS) demands, usually determined by the target BER, this can be formulated as an optimization problem to be solved by an efficient resource allocation algorithm. There are basically two approaches of objectives, as stated in [1]:

- Rate adaptive (RA) optimization, which maximizes the overall rate given a fixed total power,
- Margin adaptive (MA) optimization, for which the total transmitted power is minimized maintaining certain service rate demands.

In both cases, a resource allocation algorithm favors subcarriers with better quality, i.e., with the higher SNR. This is achieved by allocating more information bits to them, whereas severely faded channels are either loaded by low order modulation or even left idle (nulled) due to the very poor SNR. Subcarrier adaptive modulation is an adaptive transmission that assigns the most efficient modulation supported by the subchannel at a given BER.

In the following sections, the basic concepts of adaptive modulation for single-user OFDM systems are given. The focus is given on a rate adaptive scenario characterized for data communication. We first introduce an optimal solution, named *water-filling* [50]. However, water-filling assumes infinite granularity in constellation size, which is not implementable in real systems. Therefore, the Levin-Campello (LC) algorithm [3] is recalled from the literature as an optimal method for discrete bit loading.

The initial work on resource allocation (adaptive modulation) in OFDM systems was related to digital subscriber line (DSL) systems, a technology that provides broadband wireline communication over existing public switched telephone network (PSTN) [2, 3]. In wireless channels, the signal dispersion in time is caused by multipath propagation. In DSL systems, the crosstalk among adjacent copper twisted pairs produces frequency-selective interference. Because the fading rate in DSL systems is slow, the signaling of

¹Likewise the common practice in previous works on this topic, both terms will be used interchangeable even though resource allocation is a more general term that also comprises the bandwidth adaptive transmission and scheduling.

channel states is not an issue and dynamic resource allocation was implementable. However, in wireless channels, the dynamic adaptation of the estimated SNR per subcarrier reduces bandwidth efficiency through the increased feedback information. Therefore, we present two suboptimal methods that reduce the signaling overhead. The first method assumes uniform power allocation across subcarriers, which offers a negligible performance loss compared to the Levin-Campello algorithm, but reduces the dimensionality of the optimization problem. Only bit loading is performed, while the allocated power is kept constant over subcarriers. The second method is subband adaptation for which adjacent subcarriers are grouped in blocks, named subbands, using the same modulation and power over all subcarrier in the same subband. The signaling is therefore simplified at the price of performance loss. These two suboptimal methods can be further combined such that uniform power allocation is performed over subbands.

In the following sections, rather than focusing on optimizing the computational complexity of abovementioned algorithms, we compare their performance assuming an ideal transceiver by means of the Monte-Carlo simulation.

3.1. Water-Filling Optimization

The theoretical capacity of multicarrier systems offered by frequency-selective channels can be achieved by introducing the water-filling principle. In information theory, *capacity* is defined as the largest transmission rate at which reliable communication can take place and represents the maximum mutual information between the transmitted data symbols and the received signal, where maximization is performed over the *probability density function (pdf)* of the transmitted data [51]. However, in practical systems, capacity is given by the maximum data rate that can be supported by the channel with an arbitrarily low BER [25]. In the following, we apply these concepts to an OFDM communication system.

3.1.1. SNR Gap Analysis

To further proceed with resource allocation algorithms, the SNR gap analysis is briefly presented as a convenient approach for the analysis of real implementable systems.

According to Shannon theory [52], the *spectral efficiency*, defined as a capacity normalized by channel bandwidth B , of an AWGN channel is given by

$$c = \frac{C}{B} = \log_2(1 + \rho_{av}) \frac{\text{bits}}{\text{s} \cdot \text{Hz}}, \quad (3.1)$$

where C presents the channel capacity and ρ_{av} is the average SNR. In real transmission systems, however, the achieved spectral efficiency (further referred as *data rate*² r) is always $r < c$, while achieving a certain BER. Therefore, for any given modulation scheme (data rate) r and a given target BER, the *SNR gap* Γ_r , is defined as [36]

$$\Gamma_r = \frac{2^c - 1}{2^r - 1} = \frac{\rho_{av}}{2^r - 1} \quad (3.2)$$

²The term *data rate* is interchangeably used with the terms *modulation scheme* and *constellation size*, because we assume that in the uncoded systems the data rate is equal to the number of transmitted bits per transmission unit.

and presents the measure of SNR distortion that arises due to the practical implementation. The physical interpretation for Γ_r is the amount of additional SNR that an implementable transmission system requires in order to achieve capacity at the target BER. Using (3.2), the data rate r of the real system can be written as

$$r = \log_2 \left(1 + \frac{\rho_{av}}{\Gamma_r} \right). \quad (3.3)$$

The SNR gap for each modulation can be derived from the BER dependency on the SNR, or, inversely defined, the SNR dependency requisite for achieving a certain BER. This dependency, named *rate-power function* $f(r, p_e)$, can be written as

$$\rho_{av} = f(r, BER). \quad (3.4)$$

The concept of rate-power function can be explained by observing the BER curves in Figure 2.18. The interception of the line that corresponds to a constant BER with the modulation curve on SNR axis presents the required SNR for achieving a particular BER. The corresponding inverse rate-power function for the system with an ideal receiver, that uses constellation sizes $r = 1, \dots, 8$, is shown in Figure 3.1³. It can be seen that rate-power function is actually a step function. The steps are localized at SNR values required to achieve a particular rate at the given BER. Due to the finite granularity (in this case equal to one bit), SNR values between two steps do not increase the data rate because the required BER would be violated.

From the rate-power function, the corresponding SNR gap can be derived as

$$\Gamma_r = \frac{\rho_{av}}{2^r - 1} = \frac{f(r, BER)}{2^r - 1}. \quad (3.5)$$

The values of the required SNR and corresponding Γ_r for considered modulation set at $BER = 10^{-3}$ and $BER = 10^{-4}$ are shown in Table 3.1.

It can be seen from (3.5) that SNR gap presents a function of the target BER and applied modulation scheme r . However, for the large constellations, the SNR gap can be assumed to be constant. This allows for applying different rates over subchannels characterized with the constant gap Γ , which is utilized in water-filling solution.

3.1.2. Water-Filling Optimization in OFDM Systems

The classical analysis of water-filling [1] assumes a constant SNR gap for all constellations, i.e., $\Gamma_r = \Gamma$ for $r = 1, \dots, 8$. As discussed in Section 2.3, according to (2.37), an OFDM transmission system can be considered as a set of N parallel AWGN subchannels for which the overall data rate r is the sum of individual data rates r_n , i.e.,

$$r = \sum_n r_n, \quad n = 1 \dots, N. \quad (3.6)$$

³In order to represent the concept of SNR gap and corresponding rate-power function, Figure 3.1 shows its inverse because it visualizes the “distance” between the capacity of communication system with finite granularity and theoretically achievable capacity (the solid curve).

Table 3.1.: Rate-power function, SNR gap, and LS SNR margin in an AWGN channel for BER = 10^{-3} and BER = 10^{-4} .

Modulation bits r	BER = 10^{-3}			BER = 10^{-4}		
	Required SNR [dB]	Γ_r [dB]	$\Delta\text{SNR}_{\text{LS}}$ [dB]	Required SNR [dB]	Γ_r [dB]	$\Delta\text{SNR}_{\text{LS}}$ [dB]
1	6.79	6.79	1.1	8.4	8.4	1.19
2	9.8	5.02	2.36	11.44	6.72	2.36
3	14.42	5.93	2.94	16.1	7.58	3.27
4	16.54	4.75	2.91	18.24	6.5	3.25
5	19.56	4.61	3.05	21.26	6.22	3.15
6	22.55	4.53	3.32	24.32	6.29	3.49
7	25.41	4.36	3.23	27.19	6.14	3.5
8	28.41	4.31	3.39	30.22	6.15	3.75

According to (3.3), the data rate on the n th subchannel is given by

$$r_n = \log_2 \left(1 + \frac{\rho(n)}{\Gamma} \right) = \log_2 \left(1 + \frac{P(n)G(n)}{\Gamma} \right), \quad (3.7)$$

where $P(n)$ is the power allocated to the n th subcarrier and $G(n)$ is the received channel-to-noise ratio (CNR) of the n th subcarrier, defined as

$$G(n) = \frac{|H(n)|^2}{\sigma_w^2}. \quad (3.8)$$

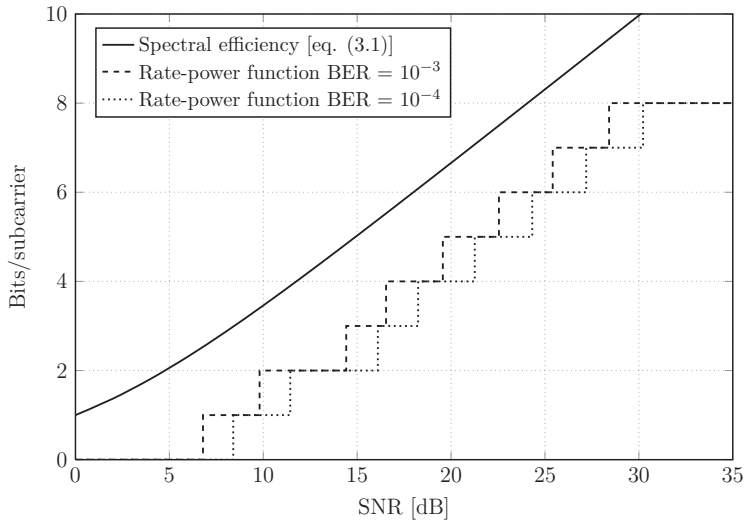


Figure 3.1.: Rate-power function for BER = 10^{-3} and BER = 10^{-4} .

Given the CNR on the n th subcarrier, $G(n)$, and SNR gap Γ , determined by the BER requirement, the goal of *rate adaptive* (RA) resource allocation is to optimally distribute available power among the subchannels such that the overall data rate r is maximized subject to a total transmit power constraint P_{tot} . Therefore, the RA maximization problem can be stated as

$$\max_{P(n)} \sum_{n=1}^N r_n \quad (3.9)$$

subject to

$$\sum_{n=1}^N P(n) \leq P_{tot}. \quad (3.10)$$

The optimal solution to this problem leads to a non-integer bit allocation. Due to the strict monotonicity of $\log(1+x)$, the optimum solution can be found with the help of Lagrange multipliers [53, pp. 215–223] by forming the cost function $\mathcal{L}(\lambda_{\mathcal{L}})$, defined as

$$\mathcal{L}(\lambda_{\mathcal{L}}) = \sum_n \log_2 \left(1 + \frac{P(n)G(n)}{\Gamma} \right) + \lambda_{\mathcal{L}} \left(P_{tot} - \sum_{n=1}^N P(n) \right). \quad (3.11)$$

Differentiating (3.11) with respect to $P(n)$ yields

$$\frac{\partial}{\partial P(n)} \mathcal{L}(\lambda_{\mathcal{L}}) = \frac{1}{\ln 2} \frac{G(n)}{G(n)P(n) + \Gamma} - \lambda_{\mathcal{L}}, \quad n = 0, \dots, N-1. \quad (3.12)$$

The optimal power allocation $P^*(n)$ is derived by setting (3.12) to zero, i.e.,

$$\frac{\partial}{\partial P(n)} \mathcal{L}(\lambda_{\mathcal{L}}) = 0,$$

thus giving

$$P^*(n) = \left(K - \frac{\Gamma}{G(n)} \right)^+, \quad (3.13)$$

where K is the constant chosen such that (3.10) holds with equality, i.e.,

$$\sum_{n=1}^N P^*(n) = \sum_{n=1}^N \left(K - \frac{\Gamma}{G(n)} \right)^+ = P_{tot}. \quad (3.14)$$

The expression (3.14) is the water-filling solution as illustrated in Figure 3.2. The colored region presents the total power P_{tot} that is allocated to a multicarrier transmission system over the subchannels. It resembles the amount of water that fills the “bowl” whose bottom is determined by the inverse CNR, i.e., by $\Gamma/G(n)$. The available amount of water P_{tot} is filled up to a constant level that is defined by the constant K in (3.13). The form of water-filling remains the same as long as Γ is constant over all subchannels. It can be also noticed that some subchannels, characterized with the low SNR, are excluded from resource allocation if the normalized inverse CNR, denoted as $\Gamma/G(n)$, exceeds the constant K . The basic idea is that water-filling takes advantage of frequency selectivity by allocating more power on better subchannels while either avoiding or putting less power on the bad subchannels. In this way, the sum of the allocated individual powers $P(n)$ and normalized inverse CNR, given by $\Gamma/G(n)$, is constant over all subcarriers (3.13).

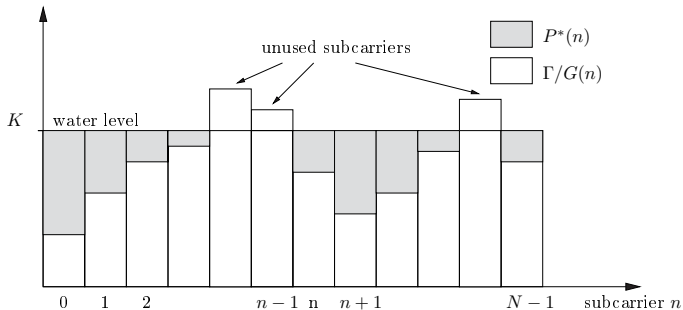


Figure 3.2.: Water-filling power allocation.

Because the rate function being maximized (3.6) is a concave, the water-filling solution is optimal. Therefore, there is a unique optimum power distribution and a corresponding rate distribution among the subchannels. Observing (3.14), it can be concluded that water-filling can not be computed in closed form due to the presence of nonlinear operator $(\cdot)^+$. This requires an iterative procedure with the complexity $\mathcal{O}(N)$. Algorithm 1, from [1], summarizes the iterative procedure for the RA resource allocation algorithm.

3.2. Discrete Rate Optimization

3.2.1. Loading with Discrete Information Units

The water-filling solution assumes infinite granularity of information units (data rates), which is given in the Step 11 of the Algorithm 1. However, because implementable OFDM systems are constrained to integer (or to multiples of finite granularity) bit assignments, specified for a finite set of allowable PSK or QAM modulations⁴, the water-filling solution has to be properly modified. There are two basic approaches to perform discrete rate loading. The first approach, named Chow's Algorithm, computes the bit distribution by rounding the water-filling results. The second approach is based on greedy methods in mathematics that utilize an iterative procedure of power increment/decrement. The most known algorithm based on the second approach is the Levin-Campello (LC) algorithm. The basic concept is that the each increment of information unit (additional bit loading) is performed on the subchannel that requires the least incremental power for the transmission. Such algorithms are optimal for loading when the information granularity β is equal for all subchannels, which is usually the case.

⁴Applying modulations without the coding provides the granularity of 1, i.e., $r_n \in \mathbb{N}_0$. However, an additional coding technique decreases granularity for the given code rate.

Algorithm 1 The rate adaptive water-filling algorithm.

Input: The CNR per subchannel $G(n)$ and the total available transmit power P_{tot} .

Output: The optimal power allocation $P(n)$ and rate allocation r_n for all N subchannels.

- 1: Sort $G(n)$ in a descending order, such that $G(1) = \max\{G(n)\}$ and $G(N) = \min\{G(n)\}$.
 - 2: Set the number of used subchannels $N^* = N$.
 - 3: $\mathcal{G} = \sum_{n=1}^N \frac{1}{G(n)}$
 - 4: $K = \frac{1}{N}(P_{tot} + \Gamma\mathcal{G})$
 - 5: **while** $P(N^*) = K - \frac{\Gamma}{G(N^*)} < 0$ **do**
 - 6: $\mathcal{G} \leftarrow \mathcal{G} - \frac{1}{G(N^*)}$
 - 7: $N^* \leftarrow N^* - 1$
 - 8: $K = \frac{1}{N^*}(P_{tot} + \Gamma\mathcal{G})$
 - 9: **end while**
 - 10: $P(n) = \begin{cases} K - \frac{\Gamma}{G(n)} & n = 1, \dots, N^* \\ 0 & n = N^* + 1, \dots, N \end{cases}$
 - 11: $r_n = \begin{cases} \log_2\left(\frac{KG(n)}{\Gamma}\right) = \log_2\left(1 + \frac{P(n)G(n)}{\Gamma}\right) & n = 1, \dots, N^* \\ 0 & n = N^* + 1, \dots, N \end{cases}$
 - 12: **return** $P(n), r_n$
-

Here, the granularity β of a multicarrier transmission system is defined as the smallest incremental unit of information that can be transmitted. Therefore, the rate distribution over N subchannels can be written as

$$r_n = \beta R_n, R_n \in \mathbb{N}_0. \quad (3.15)$$

For the simplicity of notation, we introduce a bit distribution vector \mathbf{r} , which represents the rate distribution over N subcarriers, and is defined as

$$\mathbf{r} = [r_1 \ r_2 \ \dots \ r_N]. \quad (3.16)$$

The required power for transmitting the bit distribution vector \mathbf{r} over the channel characterized by the CNR $G(n)$, according to (3.7), is given by

$$P_{r_n}(n) = \frac{\Gamma_{r_n}}{G(n)} (2^{r_n} - 1), \quad n = 0, \dots, N - 1, \quad (3.17)$$

where the SNR gap Γ_{r_n} for the subchannel n is determined by the rate-power function in (3.5), such as

$$\Gamma_{r_n} = \frac{\rho(n)}{2^{r_n} - 1} = \frac{f(r_n, p_e)}{2^{r_n} - 1}. \quad (3.18)$$

Because discrete loading algorithms are based on the monotonically increasing relation between the transmit symbol power and the number of bits transmitted on any subchannel, we introduce the concept of incremental power $\Delta P_{r_n}(n)$, which is defined as

the amount of additional power required to increase the number of information bits in subchannel n for the given β . It is defined as

$$\Delta P_{r_n}(n) = \begin{cases} P_{r_n}(n), & r_n = \beta \\ P_{r_n}(n) - P_{r_n-\beta}(n), & r_n > \beta \end{cases} \quad (3.19)$$

After replacing (3.17) in (3.19), it yields

$$\Delta P_{r_n}(n) = \begin{cases} \frac{\Gamma_{r_n}}{G(n)}, & r_n = \beta \\ \frac{\Gamma_{r_n}}{G(n)}(2^{r_n} - 1) - \frac{\Gamma_{r_n-\beta}}{G(n)}(2^{r_n-\beta} - 1), & r_n > \beta \end{cases} \quad (3.20)$$

However, it is likely that there are many different bit distributions that achieve the maximum rate, but only one is the optimum in the sense that it requires the minimum total power. This property, named efficiency, is satisfied for

$$\max_n \Delta P_{r_n}(n) \leq \min_m \Delta P_{r_m+\beta}(m), \quad n, m = 1, \dots, N. \quad (3.21)$$

The efficiency means that there is no available swapping of an information unit from one subchannel to another that reduces the total power.

3.2.2. Levin-Campello Algorithm (LC)

In practical scenarios, the Levin-Campello algorithm (LC) [3] determines the optimal power and rate distribution for a transmission system with discrete rate distribution. It can be summarized in the following steps:

1. Start with the arbitrary bit/rate distribution \mathbf{r} .
2. Calculate the efficient bit/rate distribution \mathbf{r}^* using (3.21) (Algorithm 2 (EF)).
3. The efficient bit/rate distribution \mathbf{r}^* becomes the optimal bit/rate distribution \mathbf{r}_{opt} such that power constraint (3.10) is satisfied (Algorithm 3 (ET)).
4. Power $P_{r_n}(n)$ of the n th subchannel is calculated using (3.17).

The Energy Efficientizing (EF) Algorithm 2 produces the efficient bit distribution satisfying (3.21), given the input bit distribution. First, the subchannel index m that gives the minimum incremental power for additional information unit β is determined. Then, the subchannel index n that gives the maximum incremental power required for the present bit distribution is determined. The β rate is swapped between the subchannels m and n such that current bit allocation is efficient as long as the incremental energy function monotonically increases with the number of information bits, which is always the case in practical systems. However, an additional property of *E-tightness* is necessary for the optimum solution to the discrete RA loading problem.

E-tightness, given in Algorithm 3, implies that no additional unit of information can be carried without violation of the total power constraint in (3.10), allowing the use of all total power. When algorithm starts with initial bit distribution, it is not clear if this distribution requires less or more power than given power constraint. The algorithm runs

Algorithm 2 Levin-Campello Efficientizing (EF) algorithm.

Input: \mathbf{r} , β und $\Delta P_{r_n}(n)$, for $n \in \{1, \dots, N\}$.

Output: The efficient bit distribution \mathbf{r}^* .

```

1:  $m \leftarrow \arg \min_{1 \leq i \leq N} \Delta P_{r_i+\beta}(i)$ 
2:  $n \leftarrow \arg \max_{1 \leq j \leq N} \Delta P_{r_j}(j)$ 
3: while  $(\Delta P_{r_m+\beta}(m) < \Delta P_{r_n}(n))$  do
4:    $r_m \leftarrow r_m + \beta$ 
5:    $r_n \leftarrow r_n - \beta$ 
6:    $m \leftarrow \arg \min_{1 \leq i \leq N} \Delta P_{r_i+\beta}(i)$ 
7:    $n \leftarrow \arg \max_{1 \leq j \leq N} \Delta P_{r_j}(j)$ 
8: end while
9: return  $\mathbf{r}^*$ 

```

Algorithm 3 Levin-Campello E-tightening (ET) algorithm.

Input: The efficient bit distribution \mathbf{r}^* , β and $\Delta P_{r_n}(n)$, for $n \in \{1, \dots, N\}$.

Output: The optimal bit distribution \mathbf{r}_{opt} .

```

1:  $P_{SUM} = \sum_{n=1}^N P_{r_n}(n)$ 
2: while  $(P_{tot} - P_{SUM} \geq \min_{1 \leq i \leq N} \Delta P_{r_i+\beta}(i) \text{ or } (P_{tot} - P_{SUM} < 0))$  do
3:   if  $(P_{tot} - P_{SUM} < 0)$  then
4:      $n \leftarrow \arg \max_{1 \leq i \leq N} \Delta P_{r_i}(i)$ 
5:      $P_{tot} \leftarrow P_{tot} - \Delta P_{r_n}(n)$ 
6:      $r_n \leftarrow r_n - \beta$ 
7:   else
8:      $m \leftarrow \arg \min_{1 \leq i \leq N} \Delta P_{r_i+\beta}(i)$ 
9:      $P_{tot} \leftarrow P_{tot} + \Delta P_{r_m+\beta}(m)$ 
10:     $r_m \leftarrow r_m + \beta$ 
11:   end if
12: end while
13: return  $\mathbf{r}_{\text{opt}}$ 

```

while the power constraint is violated or while the loading of additional information unit β satisfies the power constraint, thus giving the optimal bit distribution in both cases. In the first case, in each iteration, the bits are deallocated from the subchannel that requires the highest incremental power, until the power constraint is satisfied. If the power constraints are not violated, the information unit β is loaded to the subchannel that requires the least incremental power. The computational load depends on the achieved data rate r .

Algorithm 4 The suboptimal uniform power allocation algorithm.

Input: The SNR per subchannel $G(n)$ and the total available transmit power P_{tot} .

Output: The optimal power allocation $P(n)$ and rate allocation r_n for all N subchannels.

- 1: Sort $G(n)$ in a descending order, such that $G(1) = \max\{G(n)\}$ and $G(N) = \min\{G(n)\}$.
 - 2: Set the number of used subchannels $N^* = N$.
 - 3: $P(n) = P_{tot}/N^*$, for $n = 1, \dots, N^*$
 - 4: $r'_n = \log_2\left(1 + \frac{P(n)G(n)}{\Gamma_{rn}}\right)$, for $n = 1, \dots, N^*$
 - 5: $r_n = \min\{r_{\max}, \text{int}(r'_n)\}$, for $n = 1, \dots, N^*$
 - 6: **while** $r_{N^*} \leq 0$ **do**
 - 7: $N^* \leftarrow N^* - 1$
 - 8: $P(n) = P_{tot}/N^*$, for $n = 1, \dots, N^*$
 - 9: $r'_n = \log_2\left(1 + \frac{P(n)G(n)}{\Gamma_{rn}}\right)$, for $n = 1, \dots, N^*$
 - 10: $r_n = \min\{r_{\max}, \text{int}(r'_n)\}$, for $n = 1, \dots, N^*$
 - 11: **end while**
 - 12: $P(n) = \begin{cases} P_{tot}/N^* & n = 1, \dots, N^* \\ 0 & n = N^* + 1, \dots, N \end{cases}$
 - 13: $r_n = \begin{cases} r_n & n = 1, \dots, N^* \\ 0 & n = N^* + 1, \dots, N \end{cases}$
 - 14: **return** $P(n), r_n$
-

3.2.3. Uniform Power Allocation (UP)

The Levin-Campello algorithm, based on the iterative procedure for the bit loading/removing, allocates more power to subchannels with higher SNR, such that the sum of data rates in all subchannels is maximized given the total power constraint. In general, allocated powers are different, while no power is loaded to the subchannel on which the noise power exceeds a certain threshold determined by the water level. However, due to the logarithmic dependence on power, the resulting data rate becomes insensitive to the exact power allocation in the high SNR region. Therefore, several suboptimal schemes based on uniform power-variable rate allocation are proposed in the literature together with the theoretical bounds [54, 55]. Additionally, the concept of the uniform power allocation (UP) simplifies the transceiver design complexity.

The corresponding scheme for which the total available signal power is shared equally among all non-nulled subchannels [25] is given in Algorithm 4. First, the CNR values are sorted in descending order while the power is allocated uniformly to all subcarriers, i.e., $P(n) = P_{tot}/N^*$, where N^* is the index of the worst (weakest) subchannel. Using (3.7), the corresponding discrete rate distribution is calculated in the Step 5, given the maximum modulation scheme r_{\max} . If $r_{N^*} \leq 0$, the worst subchannel is removed and iterative procedure continues until this is satisfied, while the total power and rate are reallocated among the remaining subchannels.

3.2.4. Subband Resource Allocation (SB, SB-UP)

Previously presented allocation schemes assume power and/or bit allocation per subcarrier. However, the complexity of given algorithms increases with the number of subcarriers. In fast varying channels, resource allocation needs to be performed more frequently such that it introduces additional energy consumption and increased signaling overhead. To overcome these effects at the cost of reduced data rate, the subchannels can be clustered into blocks, named subbands such that each subband presents one allocation unit. This approach is used in WiMAX where each subband may either contain adjacent or distributed subcarriers (more on this is given in Appendix B.2). The Levin-Campelo algorithm and UP allocation may be performed as indicated in Algorithm 2 and Algorithm 4, respectively, by taking an individual subband as an allocation unit.

We consider the scenario of N subchannels divided into M subbands, each carrying $N_{SB} = N/M$ adjacent subchannels, where n_{SB} denote the subband index such that $n_{SB} = 1, \dots, M$. The corresponding versions of the LC and UP algorithms for the subband scenario can be derived by replacing the subcarrier index n with n_{SB} ($n \rightarrow n_{SB}$) and the number of subcarriers N with the number of subbands M ($N \rightarrow M$) in Algorithm 2, 3 and 4. Accordingly, $P(n_{SB})$ presents the allocated power at the subband n_{SB} giving the allocated power at the individual subchannels of the subband as n_{SB} is $P(n_{SB})/N_{SB}$.

Furthermore, the CNR of the subband n_{SB} , denoted as $G(n_{SB})$, can be derived in several ways. We consider two ways that differ in the margin level they impose on the BER requirement. In the conservative way, $G(n_{SB})$ is determined with the worst subcarrier from the subband n_{SB} , i.e.,

$$G(n_{SB}) = \min_{(n_{SB}-1) \cdot N_{SB} + 1 \leq n \leq n_{SB} \cdot N_{SB}} \{G(n)\}. \quad (3.22)$$

The requested BER is never violated because the subband subchannels with the SNR higher than $G(n_{SB})$ are allocated with the "lower" modulation scheme which results in reduced data rate. The second way is based on the concept of the *geometric CNR*, a reliable single performance measure that characterizes a multicarrier transmission system [36]. The CNR of the subband n_{SB} is given by

$$G(n_{SB}) = \left(\prod_{(n_{SB}-1) \cdot N_{SB} + 1}^{n_{SB} \cdot N_{SB}} G(n) \right)^{\frac{1}{N_{SB}}}. \quad (3.23)$$

In this case, the variation of the CNRs within the subband determines performance degradation, depending on the channel selectivity.

3.2.5. Band Resource Allocation (BA)

Band resource allocation (BA) assumes the uniform rate and power allocation over all subchannels, which are considered as one allocation unit. The modulation scheme is chosen according to the band CNR. It can be determined either as a minimum CNR within the band or as geometric CNR, similarly to the subband allocation, with only difference in the number of considered subcarriers. Providing the simplified signaling and

scheduling at the cost of decreased performance, BA is currently used in WLAN. More on this is given in Appendix B.1.

3.3. Simulation Results

In this section, we compare the performance of considered algorithms for the discrete resource allocation by means of computer simulations. The simulation environment is compatible with the WiMAX PHY standard specification, given in Appendix B.2. The system parameters used in the simulation are taken from WiMAX 5 MHz mode having the total of $N = 512$ subcarriers, where $N_u = 384$ subcarriers are used for data transmission. Furthermore, the CP length is 64 samples with the sampling frequency of 7.68 MHz (5 MHz bandwidth mode). We evaluate the performance for moderately selective Extended Vehicular A (EVA) and highly selective Extended Typical Urban (ETU) channels, given in Appendix A. During the simulation, the required BER is chosen to be $\text{BER} = 10^{-3}$ and the maximum transmit power is limited to $P_{\text{tot}} = 0$ dBm, while the noise power is varied from 0 dBm to -30 dBm. The x -axis denotes the ratio of the average transmit power $P_{av} = E\{P(n)\}$ to average noise power σ_W^2 , which is referred to as SNR hereafter.

Figure 3.3 shows the rate performance of discussed RA algorithms in the EVA channel. The performance of LC algorithm is close to the water-filling while other allocation strategies exhibit worse performance. To quantify the performance loss of discrete rate allocation schemes, the decrement of data rate introduced by the given strategy compared to the water-filling solution is defined as

$$\frac{r^{WF} - r}{r^{WF}} \times 100\%, \quad (3.24)$$

where r^{WF} is the data rate achieved by the water-filling algorithm, while r is the rate of the considered allocation.

The rate decrements and achieved BER of the discussed algorithms in the EVA channel are shown in Figure 3.4 and Figure 3.5, respectively. The LC allocation offers the best performance while sustaining the required BER. As it is expected, due to the logarithmic dependence of data rate to the received SNR, the performance loss of the LC algorithm is higher in the low SNR region and drops to zero at the average SNR of 20 dB. The UP and SB allocation with minimum SNR selection, denoted as UP-min and SB-min, respectively, have worse performance compared to the LC algorithm, but with the reduced BER. Other resource allocation solutions experiences worse performance than the LC algorithm but with the considerable BER violations.

The performance of discussed solutions in highly selective ETU channel is shown in Figure 3.6 and Figure 3.7. Furthermore, it is shown that LC and UP performance is robust against channel selectivity, while other solutions experience decreased performance due to the subband clustering. In the presence of the additional noise caused by the LS channel estimation, rate decrement compared to water-filling solution increases while achieved BER stays the same, as shown in Figure 3.8 and Figure 3.9. While the LC algorithm for an ideal transceiver approaches the water-filling solution as SNR increases, the rate

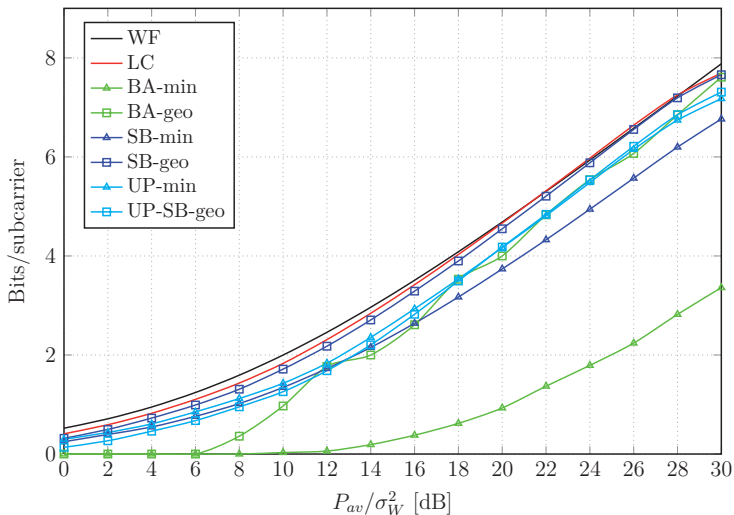


Figure 3.3.: Number of bits per subcarrier vs. SNR for an ideal transceiver in the EVA channel for $\text{BER} = 10^{-3}$.

decrement of the LC algorithm for an transceiver with the LS channel estimation goes down to 17% for the average SNR of 30 dB. As discussed in Section 2.6, the influence of the LS channel estimator on the system performance presents a "higher bound" of how the channel estimation can affect the performance of a particular resource allocation algorithm. By applying an advanced channel estimation methods, the performance curve can approach the "ideal" curve, thus reducing the gap shown in Figure 3.8.

The analysis presented in this chapter assumes the perfect information about the CNR or SNR, which is required for calculating the incremental power $\Delta P_{r_n}(n)$ in 3.20. However, in practical systems only the estimated SNR values are available. The accuracy of an SNR estimation method determines the performance of a particular resource allocation algorithm. In the following chapter, we propose an computationally efficient SNR estimation algorithm that shows robust performance in frequency-selective channels.

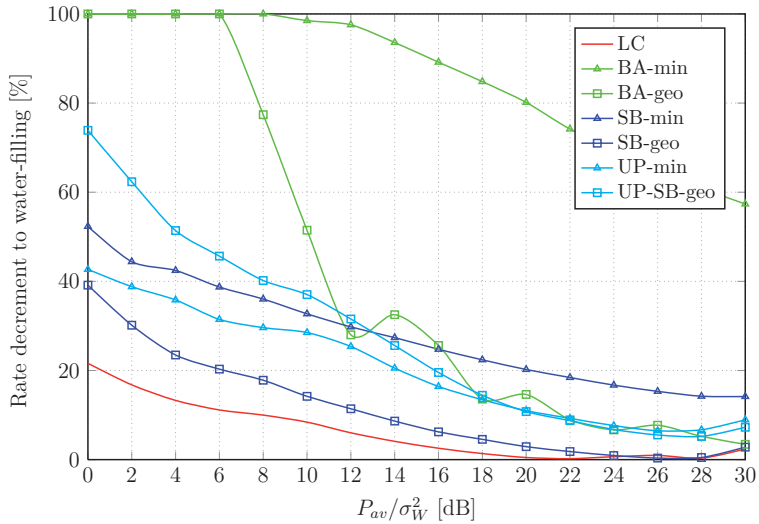


Figure 3.4.: Rate decrement compared to water-filling vs. SNR of an ideal transceiver in the EVA channel for $\text{BER} = 10^{-3}$.

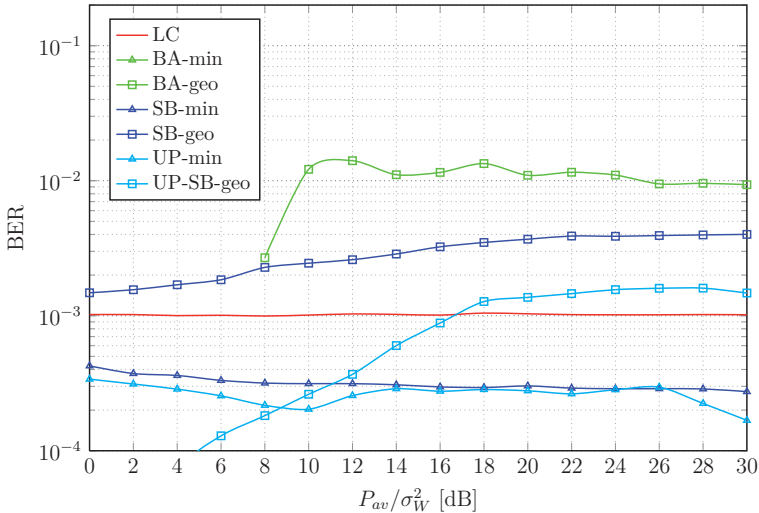


Figure 3.5.: BER vs. SNR of an ideal transceiver in the EVA channel for $\text{BER} = 10^{-3}$.

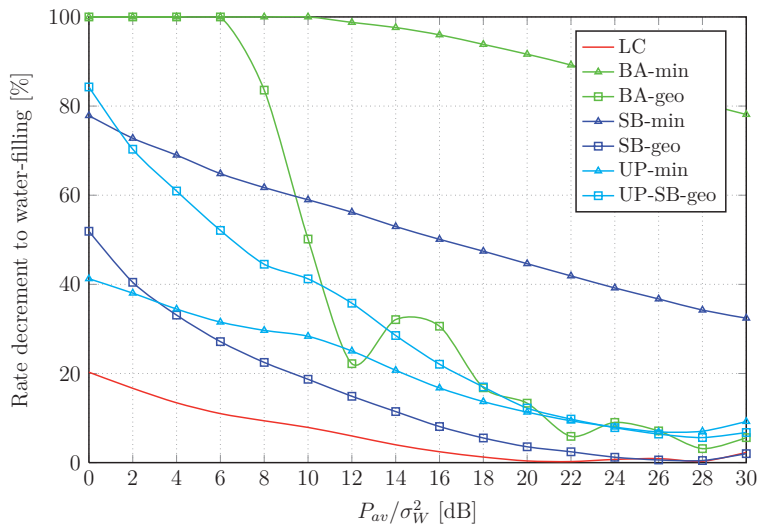


Figure 3.6.: Rate decrement compared to water-filling vs. SNR of an ideal transceiver in the ETU channel for $\text{BER} = 10^{-3}$.

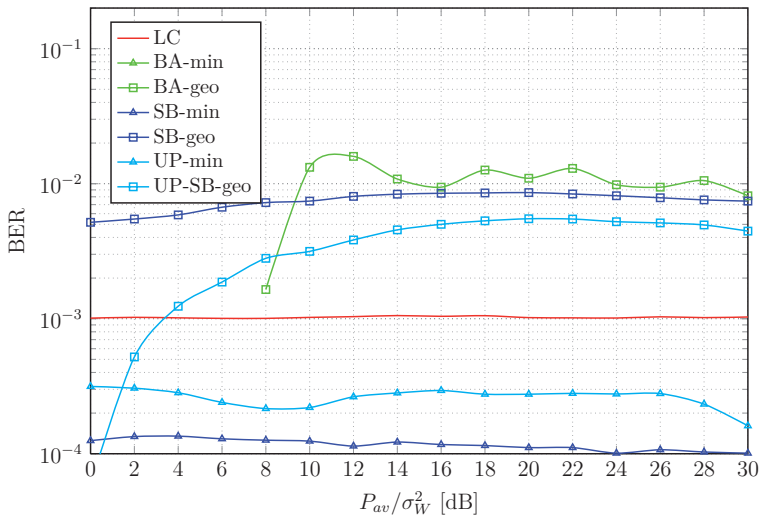


Figure 3.7.: BER vs. SNR of an ideal transceiver in the ETU channel for $\text{BER} = 10^{-3}$.

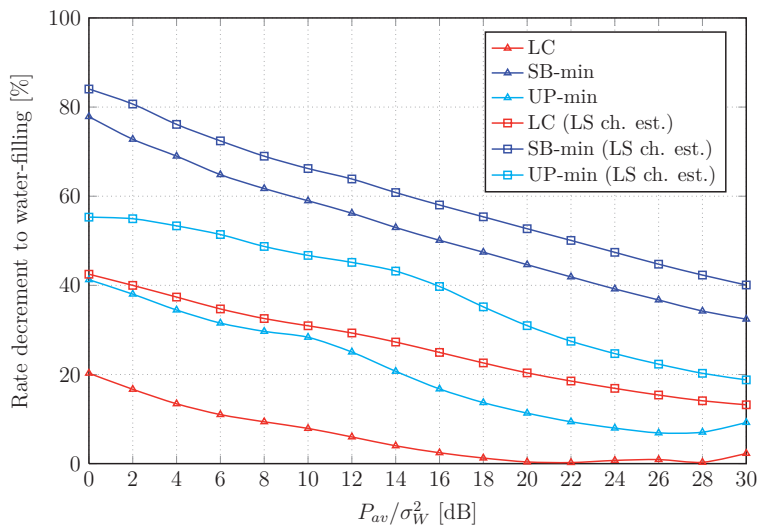


Figure 3.8.: Rate decrement compared to water-filling vs. SNR in the ETU channel for $\text{BER} = 10^{-3}$.

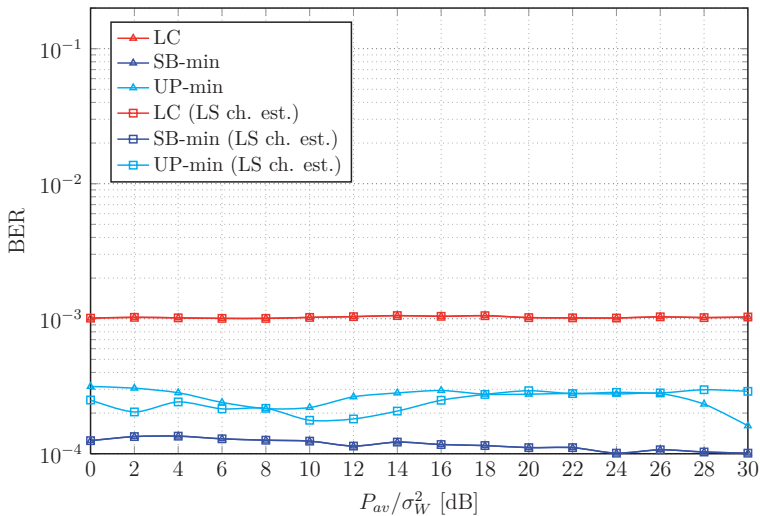


Figure 3.9.: BER vs. SNR in the ETU channel for $\text{BER} = 10^{-3}$.

4. SNR Estimation in OFDM Systems

An important task in the design of future OFDM system is to exploit frequency-selective channels. The power and bandwidth efficiency can be preserved by adapting transmission parameters (bandwidth, coding/data rate, power) to the channel conditions at the receiver. In order to achieve such improvements, an efficient and exact SNR estimation algorithm is needed. As defined in (2.39), the SNR presents the ratio of the desired signal power to the noise power and is widely used as a standard measure of signal quality for communication systems. SNR estimators derive an estimate by averaging the observable properties of the received signal over a number of symbols.

There are two general categories of average SNR estimators. *Data-aided* (DA) estimators are based on either perfect or estimated knowledge of the transmitted data. However, a certain portion of data is needed for estimation purposes, which reduces the bandwidth efficiency. Blind or *in-service* estimators derive SNR estimate from an unknown information-bearing portion of the received signal. They preserve efficiency at the cost of decreased performance. For packet based communications, a block of information data is usually preceded by several training symbols (preambles) of known data used for synchronization and equalization purposes as shown in Figure 2.16. Therefore, DA SNR estimators can utilize preambles without additional throughput reduction.

Most of the SNR estimators from the literature so far are related to single carrier transmission. In [56], a detailed comparison of various algorithms is presented, together with the derivation of the Cramer-Rao Bound (CRB). Most of these algorithms can be directly applied to OFDM systems in AWGN [6], while the SNR estimation in frequency-selective channels additionally requires efficient estimation of the channel frequency response.

In this chapter, we propose an efficient algorithm for the average SNR estimation in wireless OFDM systems, named periodic sequence (PS) estimator. Based on second-order moments of received samples in the frequency domain, the PS estimator utilizes preamble structure proposed by Morelli and Mengali in [57]. Compared to the preamble proposed by Schmidl and Cox in [43], this preamble structure allows synchronization over a wider frequency offset range with only one preamble, hence reducing the training symbol overhead. The SNR per subcarrier is estimated using the average noise power estimate and channel estimates obtained by Discrete Fourier Transform (DFT) interpolation, which is based on the fact that the channel power is concentrated on relatively small number of time domain samples [46]. Since the proposed estimation algorithm relies on the signal samples at the output of the DFT, its performance depends strongly on the preamble structure.

However, we show that PS estimator has bad performance for SNR per subcarrier estimates at low SNR values. This requires some more sophisticated mechanisms for channel estimation. In [58], the authors propose a method for adaptive selection of significant channel impulse response (CIR) paths. The rest of CIR paths, whose average power is

below the threshold determined by noise power estimates, are nulled, thus improving the performance of the channel estimation. Therefore, we further propose a modification of the PS estimator, which utilizes the method of significant CIR path selection from [58]. Average noise power estimates from the PS estimator are used to determine an appropriate threshold for significant path selection. The modified PS estimator, named improved PS (IPS) estimator, performs better when estimating the average SNR in low SNR region. Furthermore, it significantly improves the performance of the SNR per subcarrier estimation.

The performance evaluation of the proposed SNR estimators is based on the statistical characterization and calculation of the normalized mean square error (NMSE) of the average SNR and SNR per subcarrier as a function of the received SNR. Moreover, the performance comparison with existing estimation methods, such as Minimum Mean Square Error (MMSE) [6], Boumard's [8], and Ren's [7, 59] algorithms, indicates the advantage of the PS and IPS estimators in frequency-selective channels.

Parts of the following results have been presented in [9] and [11].

4.1. SNR Estimators

In the following subsections, several DA SNR estimators for OFDM systems from the literature are briefly discussed and their performance is further compared to the proposed PS and IPS estimators. The estimates are calculated based on the preambles used for synchronization and equalization. We consider general model of frame structure composed of I preambles where each preamble contains N modulated subcarriers, as shown in Figure 2.16. Let $C_i(n)$ denote the complex data symbol on the n th subcarrier in the i th preamble, where $i = 0, \dots, I - 1$ and $n = 0, \dots, N - 1$. It is assumed that modulated subcarriers within the preamble have constant magnitude $E\{|C_i(n)|\} = 1$ with equal allocated power σ_s^2 . This is a regular assumption because current OFDM standards usually contain preambles composed of QPSK and/or BPSK modulated subcarriers. At the receiver, perfect timing and frequency synchronization is assumed, i.e., $\Delta k, \varepsilon_s, \varepsilon_c = 0$. Therefore, according to (2.64), at the DFT output, the received signal on the n th subcarrier in the i th preamble can be expressed as

$$Y_i(n) = R_i(n) = \sigma_s C_i(n) H_i(n) + \sigma_w W_i(n), \quad (4.1)$$

where $W_i(n)$ is sampled complex zero-mean AWGN of unit variance, while σ_w^2 denotes the corresponding noise power.

4.1.1. MMSE Estimator

MMSE algorithm [6] for SNR estimation in OFDM system is based on the orthogonality between the estimation error and the channel frequency response estimate, given by

$$(Y(n) - \hat{H}(n)C(n))(\hat{H}(n)C(n))^* = 0, \quad n = 0, \dots, N - 1,$$

where $\hat{H}(n)$ denotes the estimate of $H(n)$ and $(\cdot)^*$ denotes the conjugate value. Here we assume that the MMSE estimator is based on one preamble and therefore we omit the time index i . The MMSE average SNR estimate is given by [6]

$$\hat{\rho}_{av,MMSE} = \frac{\hat{\sigma}_{S,MMSE}^2}{\hat{\sigma}_{W,MMSE}^2}, \quad (4.2)$$

where

$$\hat{\sigma}_{S,MMSE}^2 = \left| \frac{1}{N} \sum_{n=0}^{N-1} Y(n)C(n)^* \right|^2$$

and

$$\hat{\sigma}_{W,MMSE}^2 = \frac{1}{N} \sum_{n=0}^{N-1} |Y(n)|^2 - \hat{\sigma}_{S,MMSE}^2$$

are the MMSE estimates of σ_S^2 and σ_W^2 , respectively.

4.1.2. Boumard's Estimator

In [8], Boumard proposed a second-order moment-based SNR estimator for 2×2 MIMO OFDM system in slow varying channel in both time and frequency domain. In [7], Ren et al. derived its corresponding SISO version keeping the presumption that the channel is time-invariant and that *two* identical preambles are used for SNR estimation, i.e., $i = 0, 1$ are the time indexes for two preamble symbols and $C_0(n) = C_1(n) = C(n)$, for $n = 0, \dots, N - 1$. The average SNR estimate can be expressed as

$$\hat{\rho}_{av,Bou} = \frac{\hat{\sigma}_{S,Bou}^2}{\hat{\sigma}_{W,Bou}^2}, \quad (4.3)$$

where

$$\hat{\sigma}_{S,Bou}^2 = \frac{1}{N} \sum_{n=0}^{N-1} |\hat{H}(n)|^2$$

and

$$\hat{\sigma}_{W,Bou}^2 = \frac{1}{4(N-1)} \sum_{n=1}^{N-1} |C(n-1)(Y_0(n) + Y_1(n)) - C(n)(Y_0(n-1) + Y_1(n-1))|^2$$

are the estimates of σ_S^2 and σ_W^2 , respectively, while

$$\hat{H}(n) = \frac{\sigma_S C^*(n)}{2} (Y_0(n) + Y_1(n)) \quad (4.4)$$

is the least squares (LS) estimate of $H(n)$ averaged over two preamble symbols. Using $\hat{H}(n)$, the SNR on the n th subcarrier is estimated as

$$\hat{\rho}(n) = \frac{|\hat{H}(n)|^2}{\hat{\sigma}_{W,Bou}^2}. \quad (4.5)$$

Boumard's estimator assumes that the channel frequency responses of adjacent subchannels are the same or similar. As shown in [7], when SNR approaches infinity, the estimated average SNR (4.3) approaches

$$\lim_{\rho_{av} \rightarrow \infty} \hat{\rho}_{av, Bou} = \frac{N-1}{\sum_{n=1}^{N-1} |H(n) - H(n-1)|^2}, \quad (4.6)$$

while for low SNR values the corresponding estimate approaches

$$\lim_{\rho_{av} \rightarrow 0} \hat{\rho}_{av, Bou} = \frac{1}{2}. \quad (4.7)$$

Therefore, since Boumard's estimator is initially proposed for wireless channels characterized with slow frequency selectivity, an increasing of number of CIR paths causes decreased performance.

4.1.3. Ren's Estimators

Ren's I Estimator

The main disadvantage of the Boumard's estimator is its high sensitivity to frequency selectivity. In [7], employing the presumed preamble arrangement from Boumard's estimator, Ren et al. proposed a more accurate second-order moment-based SNR estimator, which is robust to the frequency selectivity. Derived average SNR estimate can be expressed as

$$\hat{\rho}_{av, Ren I} = \frac{\hat{\sigma}_{S, Ren I}^2}{\hat{\sigma}_{W, Ren I}^2}, \quad (4.8)$$

where

$$\hat{\sigma}_{W, Ren I}^2 = \frac{4}{N} \sum_{n=0}^{N-1} \left\{ \text{Im} \left[Y_0(n) C_0^*(n) \hat{H}^*(n) / |\hat{H}^*(n)| \right] \right\}^2 \quad (4.9)$$

and

$$\hat{\sigma}_{S, Ren I}^2 = \frac{1}{N} \sum_{n=0}^{N-1} |Y_0(n)|^2 - \hat{\sigma}_{W, Ren I}^2$$

are the estimates of σ_W^2 and σ_S^2 , respectively, while $\hat{H}(n)$ is defined in (4.4). It is shown that the performance is independent of the channel frequency response estimation although the estimated channel states are used for the average SNR estimation. Additionally, the SNR on the n th subcarrier is estimated as in (4.5) using the noise power estimate from (4.9).

Ren's II Estimator

Furthermore, Ren et al. proposed in [59] a new moment-based estimator based on two identical preambles or one preamble with two identical parts in frequency domain. Assuming the quasi-static channel condition (channel frequency response is constant over two adjacent symbols), the two identical parts (preambles) will differ only in different AWGN parts that after subtraction provide the estimate of the noise power.

From (4.1), having $C_0(n) = C_1(n)$ and $H_0(n) = H_1(n)$, the noise power can be written as the scaled expectation of the square of the difference over the received preamble's samples [59], i.e.,

$$\sigma_{W, Ren II}^2 = \frac{1}{2N} \mathbb{E} \left\{ |Y_0(n) - Y_1(n)|^2 \right\}. \quad (4.10)$$

The noise estimate is then given by

$$\hat{\sigma}_{W, Ren II}^2 = \frac{1}{2N} \sum_{n=0}^{N-1} |Y_0(n) - Y_1(n)|^2, \quad (4.11)$$

where $Y_i(n)$, $i = 0, 1$ is given by (4.1). The estimate of the signal power is derived similarly as for the Ren's I Estimator, i.e.,

$$\hat{\sigma}_{S, Ren II}^2 = \frac{1}{N} \sum_{n=0}^{N-1} |Y_0(n)|^2 + |Y_1(n)|^2 - \hat{\sigma}_{W, Ren II}^2. \quad (4.12)$$

For one preamble having two identical parts in the time domain, the $N/2$ -point DFT of each part can be taken giving the received data $Y'_0(n)$ and $Y'_1(n)$, for $n = 0, \dots, N/2 - 1$ in the frequency domain. Therefore, the estimate of noise power is given by

$$\hat{\sigma}_{W', Ren II}^2 = \frac{1}{2} \sum_{n=0}^{N/2-1} |Y'_0(n) - Y'_1(n)|^2, \quad (4.13)$$

while the estimate of the signal power can be written as

$$\hat{\sigma}_{S', Ren II}^2 = \frac{1}{N} \sum_{n=0}^{N-1} |Y_0(n)|^2 - \hat{\sigma}_{W', Ren II}^2. \quad (4.14)$$

Finally, the average SNR estimate is given by

$$\hat{\rho}_{av, Ren II} = \frac{\hat{\sigma}_{S, Ren II}^2}{\hat{\sigma}_{W, Ren II}^2}. \quad (4.15)$$

It is shown in [59] that the performance is independent of the channel frequency response estimation although the estimated channel states are used for the average SNR estimation. Similar to the Ren's I estimator, the SNR on the n th subcarrier is estimated as in (4.5) using the noise power estimate from (4.11) or (4.13), depending on the number of preambles.

4.2. Periodic Sequence (PS) Estimator

The block diagram of the PS estimator is shown in Figure 4.2. The key idea of the estimator rests upon the time domain periodic preamble structure utilized for time and frequency synchronization [60]. In order to cover a wider frequency range, a preamble of Q identical parts, each containing N/Q samples, as depicted in Figure 4.1a, is proposed in [57]. The corresponding frequency domain representation is shown in Figure 4.1b.

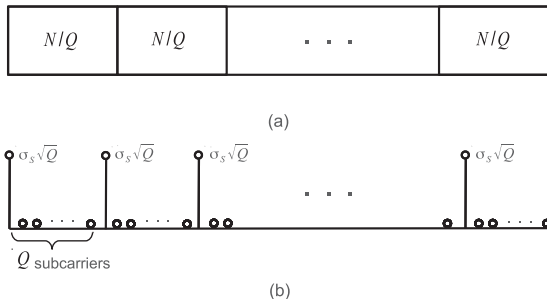


Figure 4.1.: Preamble structure in the (a) time and (b) frequency domain.

In the sequel we assume that Q divides N , such that the number of loaded subcarriers $N_p = N/Q$ is integer.

Starting from the 0th, each Q th subcarrier is modulated with a QPSK signal $C_p(m)$, $m = 0, 1, \dots, N_p - 1$ with $|C_p(m)| = 1$ and loaded with power σ_S^2 . The remainder of $N_z = N - N_p = \frac{(Q-1)}{Q}N$ subcarriers is not used (nulled). In order to maintain the total energy level over all symbols within the preamble, the power is scaled by factor Q yielding a total transmit power of $Q\sigma_S^2$ on the loaded subcarriers. Therefore, the time domain representation of the preamble with Q identical parts can be written as

$$c_p(k) = c_p(k + q\frac{N}{Q}), \quad k = 0, \dots, \frac{N}{Q} - 1, \quad q = 1, \dots, Q - 1,$$

while its representation in the frequency domain is given by

$$C(n) = C(mQ + q) = \begin{cases} \sqrt{Q}\sigma_S C_p(m), & q = 0 \\ 0, & q = 1, \dots, Q - 1 \end{cases}, \quad (4.16)$$

for $n = mQ + q$, $m = 0, \dots, N_p - 1$, $q = 0, \dots, Q - 1$. From (4.1), the received symbol on the n th subcarrier is given by

$$Y(n) = Y(mQ + q) = \begin{cases} Y_p(m), & q = 0 \\ Y_z(mQ + q), & q = 1, \dots, Q - 1 \end{cases}, \quad (4.17)$$

where

$$Y_p(m) = \sqrt{Q}\sigma_S C_p(m)H_p(m) + \sigma_W W(m) \quad (4.18)$$

denotes the received signal on the loaded subcarriers, and

$$Y_z(mQ + q) = \sigma_W W(mQ + q) \quad (4.19)$$

is the received signal on the nulled subcarriers containing only noise.

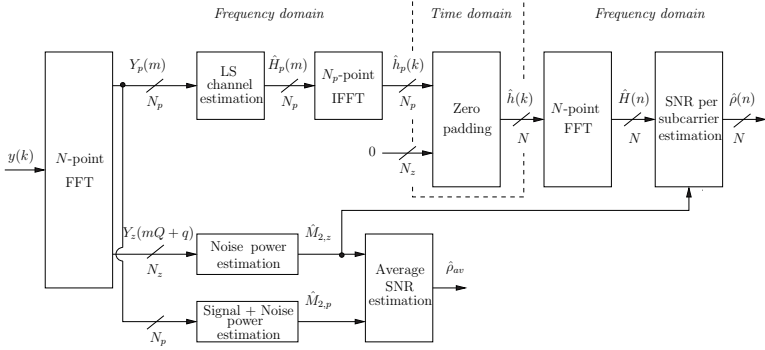


Figure 4.2.: Block diagram of the PS estimator.

The empirical second-order moment of the received signal on the loaded subcarriers can be written as

$$\hat{M}_{2,p} = \frac{1}{N_p} \sum_{m=0}^{N_p-1} |Y_p(m)|^2, \quad (4.20)$$

while its expected value is given by

$$\begin{aligned} \mathbb{E}\{\hat{M}_{2,p}\} &= \frac{1}{N_p} \mathbb{E}\left\{\sum_{m=0}^{N_p-1} |Y_p(m)|^2\right\} \\ &= \frac{1}{N_p} \sum_{m=0}^{N_p-1} \mathbb{E}\{|Y_p(m)|^2\} \\ &= \frac{Q\sigma_S^2}{N_p} \sum_{m=0}^{N_p-1} \mathbb{E}\{|H(m)|^2\} + \frac{\sigma_W^2}{N_p} \sum_{m=0}^{N_p-1} \mathbb{E}\{|W(m)|^2\} \\ &= Q\sigma_S^2 + \sigma_W^2. \end{aligned} \quad (4.21)$$

Similarly, the empirical second moment of the received signal on the nulled subcarriers,

$$\hat{M}_{2,z} = \frac{1}{N_p(Q-1)} \sum_{m=0}^{N_p-1} \sum_{q=1}^{Q-1} |Y_z(mQ+q)|^2, \quad (4.22)$$

has expectation

$$\begin{aligned} \mathbb{E}\{\hat{M}_{2,z}\} &= \frac{1}{N_p(Q-1)} \mathbb{E}\left\{\sum_{m=0}^{N_p-1} \sum_{q=1}^{Q-1} |Y_z(mQ+q)|^2\right\} \\ &= \frac{1}{N_p(Q-1)} \sum_{m=0}^{N_p-1} \sum_{q=1}^{Q-1} \mathbb{E}\{|Y_z(mQ+q)|^2\} \\ &= \frac{\sigma_W^2}{N_p(Q-1)} \sum_{m=0}^{N_p-1} \sum_{q=1}^{Q-1} \mathbb{E}\{|W(mQ+q)|^2\} \\ &= \sigma_W^2. \end{aligned}$$

In summary, the average SNR ρ_{av} can be estimated by forming

$$\begin{aligned}\hat{\rho}_{av} &= \frac{1}{Q} \frac{\hat{M}_{2,p} - \hat{M}_{2,z}}{\hat{M}_{2,z}} \\ &= \frac{1}{Q} \left(\frac{\hat{M}_{2,p}}{\hat{M}_{2,z}} - 1 \right),\end{aligned}\quad (4.23)$$

where, by the strong law of large numbers, $\hat{M}_{2,p}$ and $\hat{M}_{2,z}$ are strongly consistent unbiased estimators of $Q\sigma_S^2 + \sigma_W^2$ and average noise power σ_W^2 , respectively.

The estimate of the average SNR, $\hat{\rho}_{av}$, is obtained by inserting (4.20) and (4.22) in (4.23), thus giving

$$\hat{\rho}_{av} = \frac{1}{Q} \left((Q-1) \frac{\sum_{m=0}^{N_p-1} |Y_p(m)|^2}{\sum_{m=0}^{N_p-1} \sum_{q=1}^{Q-1} |Y_z(mQ+q)|^2} - 1 \right). \quad (4.24)$$

Note that $\hat{\rho}_{av}$ requires no knowledge of the transmitted symbols on the loaded subcarriers. Only the arrangement of the loaded and nulled subcarriers must be known to the receiver. However, channel estimates $\hat{H}(n)$ are requisite for the estimation of the SNR per subcarrier from (2.38). They are available only for the loaded subcarriers by the means of least square (LS) estimation such that

$$\begin{aligned}\hat{H}_p(m) &= \frac{1}{\sqrt{Q}} C_p^*(m) Y_p(m) \\ &= \sigma_S H_p(m) + \frac{\sigma_W}{\sqrt{Q}} \tilde{W}(m),\end{aligned}\quad (4.25)$$

where $\tilde{W}(m) = C_p^*(m) W(m)$.

As shown in Figure 4.2, channel estimates for nulled subcarriers $\hat{H}(mQ+q)$, $m = 0, \dots, N_p-1$, $q = 1, \dots, Q-1$, are obtained by the DFT interpolation. Therefore, the CIR estimates after the IDFT can be written as

$$\begin{aligned}\hat{h}_p(k) &= \text{IDFT}_{N_p} [\hat{H}_p(m)], \quad 0 \leq k \leq N_p - 1 \\ &= \sigma_S h(k) + \frac{\sigma_W}{\sqrt{Q}} \tilde{w}(k),\end{aligned}\quad (4.26)$$

where $\text{IDFT}_{N_p}[\cdot]$ presents the N_p -point IDFT and $\tilde{w}(k) = \text{IDFT}_{N_p} [\tilde{W}(m)]$. To obtain channel estimates, the rest of $N_z = N - N_p$ samples are padded with zeros giving the CIR prior to the N -point DFT as

$$\hat{h}(k) = \begin{cases} \hat{h}_p(k), & 0 \leq k \leq N_p - 1 \\ 0, & N_p \leq k \leq N - 1. \end{cases} \quad (4.27)$$

Channel estimates after the N -point DFT are obtained as

$$\begin{aligned}\hat{H}(n) &= \text{DFT}_N [\hat{h}(k)] \\ &= \sigma_S H(n) + \frac{\sigma_W}{\sqrt{Q}}(n) \tilde{W}(n), \quad 0 \leq n \leq N - 1.\end{aligned}\quad (4.28)$$

It can be easily noticed that in order to preserve CIR information, the number of the loaded subcarriers has to be larger or equal to the CIR length, i.e., $N_p \geq L$. Hence, $Q \leq N/L$ must be satisfied, which puts a constraint to the preamble design.

Similarly to (4.21), the expectation of the empirical second order moment of $\hat{H}(n)$ in (4.28), $\hat{M}_{2,p}(n) = |\hat{H}(n)|^2$, is given by

$$\begin{aligned} \mathbb{E}\{\hat{M}_{2,p}(n)\} &= \mathbb{E}\{|\hat{H}(n)|^2\} \\ &= \sigma_s^2 \mathbb{E}\{|H(n)|^2\} + \frac{1}{Q} \mathbb{E}\{|\widetilde{W}(n)|^2\} \\ &= \sigma_s^2 \mathbb{E}\{|H(n)|^2\} + \frac{\sigma_w^2}{Q}. \end{aligned} \quad (4.29)$$

Finally, using (2.38) with the noise power estimate obtained in (4.22), the SNR estimate on the n th subcarrier can be written as

$$\hat{\rho}(n) = \frac{\hat{M}_{2,p}(n)}{\hat{M}_{2,z}} - \frac{1}{Q}. \quad (4.30)$$

4.2.1. Computational Complexity Analysis

From an implementation point of view, the PS estimator has lower complexity than the Boumard's and both Rens' estimator. For the average SNR estimation Boumard's estimator requires $5N$ and $2N$ complex multiplications and complex additions per estimation, respectively, as indicated in (4.3). Ren's estimator I from (4.8) and (4.9) needs $4N$ and $3N$ complex multiplications and additions, respectively. Implementing the Ren's estimator II with two preambles as indicated in (4.11) and (4.12) requires $3N$ and $2N$ complex multiplications and complex additions per estimation, respectively, while Ren's estimator II with one preamble from (4.13) and (4.14) requires $1.5N$ and $1.5N$ complex multiplications and complex additions per estimation, respectively. The PS algorithm (4.23) requires only N multiplications and N additions per estimate. Moreover, the PS estimator is of higher bandwidth efficiency since only one preamble is needed unlike the Ren's and Boumard's estimators.

4.2.2. Statistical Properties

In order to evaluate and include the impact of SNR estimation on the BER performance and spectral efficiency of adaptive modulation, the statistical properties of the average SNR and SNR per subcarrier estimation are derived in the following.

The Average SNR Estimation

To derive the statistical properties of the average SNR $\hat{\rho}_{av}$ and SNR per subcarrier $\hat{\rho}(n)$ estimator, it can be shown that $2N_p \frac{\hat{M}_{2,p}}{\sigma_w^2}$ and $2N_z \frac{\hat{M}_{2,z}}{\sigma_w^2}$ are noncentral chi-squared (see Proposition 4.2) and central chi-squared (see Proposition 4.1) random variables, respectively.

Proposition 4.1. Let $Y_z(mQ + q)$, for $m = 0, 1, \dots, N_p - 1$ and $q = 1, \dots, Q - 1$, denote independent circular symmetric Gaussian random variables with zero means and identical variances σ_W^2 , i.e., $Y_z(mQ + q) \sim SCN(0, \sigma_W^2)$. Then, $Z = \frac{2}{\sigma_W^2} \sum_{m=0}^{N_p-1} \sum_{q=1}^{Q-1} |Y_p(mQ + q)|^2 = 2N_z \frac{\hat{M}_{2,z}}{\sigma_W^2}$ has a *central chi-squared* distribution, $\chi_{\nu_z}^2$, with $\nu_z = 2N_z$ degrees of freedom. Therefore, $Z \sim \chi_{\nu_z}^2$, with the pdf given by

$$f_Z(z) = \frac{1}{2^{\frac{\nu_z}{2}} \Gamma\left(\frac{\nu_z}{2}\right)} z^{\frac{\nu_z}{2}-1} e^{-\frac{z}{2}}, \quad z \geq 0, \quad (4.31)$$

where $\Gamma(u)$ is the Gamma function [29], defined by

$$\Gamma(u) = \int_0^{\infty} t^{u-1} e^{-t} dt. \quad (4.32)$$

As it is shown in [61], the mean and the variance of Z are given by

$$\mathbb{E}(Z) = \nu_z = 2N_z, \quad (4.33)$$

and

$$\text{Var}(Z) = 2\nu_z = 4N_z, \quad (4.34)$$

respectively.

Proposition 4.2. Let $Y_p(m)$, for $m = 0, 1, \dots, N_p - 1$, denote independent circular symmetric complex Gaussian random variables with expected values $\sqrt{Q}\sigma_S H_p(m)$ and identical variances σ_W^2 , i.e., $Y_p(m) \sim SCN(\sqrt{Q}\sigma_S H_p(m), \sigma_W^2)$. Then, $P = \frac{2}{\sigma_W^2} \sum_{m=0}^{N_p-1} |Y_p(m)|^2 = 2N_p \frac{\hat{M}_{2,p}}{\sigma_W^2}$ has a *noncentral chi-squared* distribution, $\chi_{\nu_p, \lambda}^2$, with $\nu_p = 2N_p$ degrees of freedom and noncentrality parameter $\lambda = 2Q \frac{\sigma_S^2}{\sigma_W^2} \sum_{m=0}^{N_p-1} |H_p(m)|^2 = 2Q\rho_{av}N_p$. Therefore, $P \sim \chi_{\nu_p, \lambda}^2$, with the pdf given by

$$f_P(p) = \frac{1}{2} \left(\frac{p}{\lambda}\right)^{\frac{\nu_p-2}{4}} e^{-\frac{p+\lambda}{2}} I_{\frac{\nu_p}{2}-1}(\sqrt{p\lambda}), \quad p \geq 0, \quad (4.35)$$

where $I_a(u)$ is the modified Bessel function of the first kind of the order a [29] defined as

$$I_a(u) = \frac{\left(\frac{1}{2}u\right)^a}{\sqrt{\pi}\Gamma\left(a + \frac{1}{2}\right)} \int_0^{\pi} e^{u \cos \theta} \sin^{2a}\theta d\theta. \quad (4.36)$$

As shown in [61], the mean and the variance of P are given by

$$\mathbb{E}(P) = \nu_p + \lambda = 2N_p(1 + Q\rho_{av}), \quad (4.37)$$

and

$$\text{Var}(P) = 2\nu_p + 4\lambda = 4N_p(1 + 2Q\rho_{av}), \quad (4.38)$$

respectively.

Lemma 4.3. Given $Z = 2N_z \frac{\hat{M}_{2,z}}{\sigma_W^2}$ as a *central chi-squared* random variable with $\nu_z = 2N_z$ degrees of freedom and $P = 2N_p \frac{\hat{M}_{2,p}}{\sigma_W^2}$ as a *noncentral chi-squared* random variable with $\nu_p = 2N_p$ degrees of freedom and noncentrality parameter $\lambda = 2Q\rho_{av}N_p$, the random variable $V = \frac{\hat{M}_{2,p}}{\hat{M}_{2,z}}$ is *noncentral F-distributed*, i.e., $V \sim F_{\nu_p, \nu_z}(\lambda)$.

Proof. From the empirical second order moments $\hat{M}_{2,p}$ and $\hat{M}_{2,z}$ in (4.20) and (4.22), respectively, it can be noticed that the different data (samples originating from different subcarriers $Y(n)$) are used for performing estimation. Therefore, $\hat{M}_{2,p}$ and $\hat{M}_{2,z}$ can be considered as independent random variables, thus giving random variables P and Z also as independent, respectively. According to [61], having P and Z stochastically independent, a noncentral F -distributed random variable V is obtained when dividing a noncentral chi-squared random variable $P \sim \chi_{\nu_p, \lambda}^2$ by a central chi-squared random variable $Z \sim \chi_{\nu_z}^2$,

$$V = \frac{P/\nu_p}{Z/\nu_z}. \quad (4.39)$$

Replacing P, Z, ν_p , and ν_z in (4.39) directly yields

$$\begin{aligned} V &= \frac{\left(\frac{2N_p \hat{M}_{2,p}}{\sigma_W^2}\right) / (2N_p)}{\left(\frac{2N_z \hat{M}_{2,z}}{\sigma_W^2}\right) / (2N_z)} \\ &= \frac{\hat{M}_{2,p}}{\hat{M}_{2,z}}. \end{aligned} \quad (4.40)$$

□

The F -distributed random variable V in (4.39), has a pdf given by

$$f_V(v) = e^{-\frac{\lambda}{2}} \sum_{k=0}^{\infty} \frac{(\frac{\lambda}{2})^k}{k!} \frac{(\frac{\nu_p}{\nu_z})^{\frac{1}{2}\nu_p+k}}{B\left(\frac{\nu_p+2k}{2}, \frac{\nu_z}{2}\right)} v^{\frac{\nu_p}{2}+k-1} \left(1 + \frac{\nu_p}{\nu_z}v\right)^{-\frac{1}{2}(\nu_p+\nu_z)-k}, \quad (4.41)$$

where $B(u, v)$ is the Beta function, which can be represented by Gamma functions [29] as

$$B(u, v) = \frac{\Gamma(u)\Gamma(v)}{\Gamma(u+v)}. \quad (4.42)$$

The mean and the variance of the F -distributed random variable V , defined in (4.39), are given by

$$E(V) = \frac{\nu_z(\nu_p + \lambda)}{\nu_p(\nu_z - 2)}, \quad \nu_z > 2, \quad (4.43)$$

and

$$\text{Var}(V) = 2 \cdot \left(\frac{\nu_z}{\nu_p}\right)^2 \frac{(\nu_p + \lambda)^2 + (\nu_z - 2)(\nu_p + 2\lambda)}{(\nu_z - 2)^2(\nu_z - 4)}, \quad \nu_z > 4, \quad (4.44)$$

respectively [61]. Replacing ν_p and ν_z in (4.43) and (4.44) yields

$$\begin{aligned} E(V) &= \frac{2N_z \cdot 2N_p(1 + Q\rho_{av})}{2N_p \cdot 2(N_z - 1)} \\ &= \frac{1 + Q\rho_{av}}{\left(1 - \frac{1}{N_z}\right)}, \quad N_z > 1, \end{aligned} \quad (4.45)$$

and

$$\begin{aligned} \text{Var}(V) &= 2 \cdot \frac{\left(\frac{2N_z}{2N_p}\right)^2 \frac{4N_p^2(1 + Q\rho_{av})^2 + 4N_p(N_z - 1)(1 + 2Q\rho_{av})}{4(N_z - 1)^2 \cdot 2(N_z - 2)}}{\frac{1}{N_z} \frac{(1 + Q\rho_{av})^2 + \frac{1}{N_p}(N_z - 1)(1 + 2Q\rho_{av})}{\left(1 - \frac{1}{N_z}\right)^2 \left(1 - \frac{2}{N_z}\right)}}, \quad N_z > 2, \end{aligned} \quad (4.46)$$

respectively.

Comparing (4.23) with (4.40), the estimated average SNR $\hat{\rho}_{av}$ can be obtained by transforming the random variable V

$$\begin{aligned}\hat{\rho}_{av} &= \frac{1}{Q} \left(\left(\frac{\hat{M}_{2,p}}{\hat{M}_{2,z}} \right) - 1 \right) \\ &= \frac{1}{Q} (V - 1).\end{aligned}\quad (4.47)$$

Its expectation $E(\hat{\rho}_{av})$ is given by

$$\begin{aligned}E(\hat{\rho}_{av}) &= \frac{1}{Q} \left(E \left(\frac{\hat{M}_{2,p}}{\hat{M}_{2,z}} \right) - 1 \right) \\ &= \frac{1}{Q} (E(V) - 1) \\ &= \frac{1}{Q} \left(\frac{1 + Q\rho_{av}}{1 - \frac{1}{N_z}} - 1 \right) \\ &= \frac{1}{Q} \left(Q\rho_{av} + \frac{1 + Q\rho_{av}}{N_z - 1} \right) \\ &= \rho_{av} + \frac{\frac{1}{Q} + \rho_{av}}{N_z - 1}.\end{aligned}\quad (4.48)$$

Because N_z represents the number of the nulled subcarriers, i.e., $N_z = \frac{Q-1}{Q}N$, (4.48) can be written as

$$\begin{aligned}E(\hat{\rho}_{av}) &= \rho_{av} + \frac{\frac{1}{Q} + \rho_{av}}{N \left(1 - \frac{1}{Q} \right) - 1} \\ &\approx \rho_{av},\end{aligned}\quad (4.49)$$

for $N \gg 1$, which is a regular case in real OFDM systems.

Similarly, according to the transformation (4.47), the mean square error (MSE) of the estimated average SNR is given by

$$\begin{aligned}\text{MSE}(\hat{\rho}_{av}) &= E \left((\hat{\rho}_{av} - \rho_{av})^2 \right) \\ &\approx \text{Var}(\hat{\rho}_{av}) \\ &= \frac{1}{Q^2} \text{Var}(V).\end{aligned}\quad (4.50)$$

Inserting (4.46) into (4.50), for $N_z = \frac{Q-1}{Q}N$ and $N_z = \frac{N}{Q}$ yields

$$\text{MSE}(\hat{\rho}_{av}) \approx \frac{1}{NQ(Q-1)} \frac{(1 + Q\rho_{av})^2 + (Q-1 - \frac{Q}{N})(1 + 2Q\rho_{av})}{\left(1 - \frac{Q}{(Q-1)N}\right)^2 \left(1 - \frac{2Q}{(Q-1)N}\right)}.\quad (4.51)$$

By using the transformation of the F -distributed random variable V in (4.47), the pdf of the estimated average SNR $\hat{\rho}_{av}$ can be derived as

$$\begin{aligned} f_{\hat{\rho}_{av}}(\hat{\rho}_{av}) &= Q \cdot f_V(1 + Q\hat{\rho}_{av}) \\ &= Q \cdot e^{-\frac{\lambda p}{2}} \sum_{k=0}^{\infty} \frac{\left(\frac{\lambda p}{2}\right)^k}{k!} \frac{\left(\frac{\nu_p}{\nu_z}\right)^{\frac{1}{2}\nu_p+k}}{B\left(\frac{\nu_p+2k}{2}, \frac{\nu_z}{2}\right)} (1 + Q\hat{\rho}_{av})^{\frac{\nu_p}{2}+k-1} \left(1 + \frac{\nu_p}{\nu_z}(1 + Q\hat{\rho}_{av})\right)^{-\frac{1}{2}(\nu_p+\nu_z)-k}. \end{aligned} \quad (4.52)$$

Replacing λ , ν_p , and ν_z in (4.52) and having $N_z = \frac{Q-1}{Q}N$, this yields

$$\begin{aligned} f_{\hat{\rho}_{av}}(\hat{\rho}_{av}) &= Q \cdot e^{-N\rho_{av}} \sum_{k=0}^{\infty} \frac{(N\rho_{av})^k}{k!} \frac{\left(\frac{1}{Q-1}\right)^{k+\frac{N}{Q}}}{B\left(k+\frac{N}{Q}, \frac{Q-1}{Q}N\right)} (1 + Q\hat{\rho}_{av})^{k-1+\frac{N}{Q}} \left(\frac{1}{1 + \frac{Q(1+\hat{\rho}_{av})}{(Q-1)}}\right)^{k+N} \\ &= \frac{e^{-N\rho_{av}} \cdot (Q-1)^{N(1-\frac{1}{Q})}}{Q^{N-1}} \cdot \frac{(1 + Q\hat{\rho}_{av})^{\frac{N}{Q}-1}}{(1 + \hat{\rho}_{av})^N} \cdot \sum_{k=0}^{\infty} \frac{\rho_{av}^k \cdot \left(\frac{N}{Q}\right)^k}{k! \cdot B\left(k+\frac{N}{Q}, \frac{Q-1}{Q}N\right)} \left(\frac{1 + Q\hat{\rho}_{av}}{1 + \hat{\rho}_{av}}\right)^k. \end{aligned} \quad (4.53)$$

Figure 4.3 shows the pdf of the estimated average SNR in (4.53) for true SNR = 10 dB. It can be seen that the simulation results agree with the derived analytical model. Moreover, increasing the number of periodic parts Q improves the accuracy of the SNR estimation, i.e., the pdf curve becomes more concentrated around the true SNR value for the higher Q values.

The SNR per Subcarrier Estimation

To derive the statistical properties of the SNR per subcarrier estimate (4.30), we obtain the statistical property of $\hat{M}_{2,p}(n)$ in the following. As $\hat{M}_{2,p}(n) = |\hat{H}(n)|^2$, we rewrite the channel estimate after the N -point DFT (4.28) as

$$\hat{H}(n) = \sigma_S H(n) + \frac{1}{\sqrt{Q}} H(n) \tilde{W}(n), \quad 0 \leq n \leq N-1. \quad (4.54)$$

Proposition 4.4. Let $\hat{H}(n)$, for $n = 0, 1, \dots, N-1$, denote independent circular symmetric complex Gaussian random variables with expected values $\sigma_S H(n)$ and identical variances $\frac{\sigma_W^2}{Q}$, i.e., $\hat{H}(n) \sim SCN(\sigma_S H(n), \frac{\sigma_W^2}{Q})$. Then, $P_n = 2Q \frac{|\hat{H}(n)|^2}{\sigma_W^2} = 2Q \frac{\hat{M}_{2,p}(n)}{\sigma_W^2}$ has a noncentral chi-squared distribution, $\chi_{\nu_n, \lambda}^2$, with $\nu_n = 2$ degrees of freedom and noncentrality parameter $\lambda_n = 2Q \frac{\sigma_S^2}{\sigma_W^2} |H(n)|^2 = 2Q\rho(n)$. Therefore, $P_n \sim \chi_{\nu_n, \lambda_n}^2$, with the pdf given by

$$f_{P_n}(p_n) = \frac{1}{2} \left(\frac{p_n}{\lambda}\right)^{\frac{\nu_n-2}{2}} e^{-\frac{p_n+\lambda}{2}} I_{\frac{\nu_n}{2}-1}(\sqrt{p_n\lambda}), \quad p_n \geq 0, \quad (4.55)$$

where $I_a(u)$ is the modified Bessel function of the first kind of the order a [29] given in (4.36).

Lemma 4.5. Given $Z = 2N_z \frac{\hat{M}_{2,z}}{\sigma_W^2}$ as central chi-squared random variable with $\nu_z = 2N_z$ degrees of freedom and $P_n = 2Q \frac{\hat{M}_{2,p}(n)}{\sigma_W^2}$ as a noncentral chi-squared random variable with

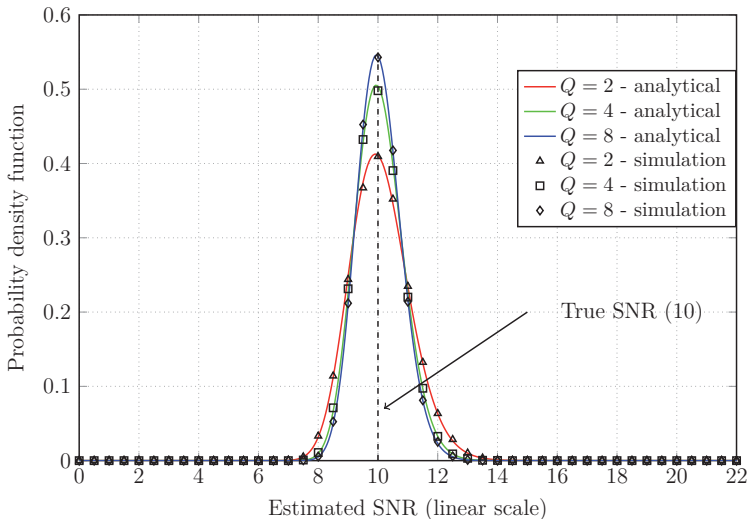


Figure 4.3.: Pdf of the average SNR estimation for true SNR = 10 dB, $N = 256$, and the number of periodic parts $Q = 2, 4, 8$.

$\nu_n = 2$ degrees of freedom and a noncentrality parameter $\lambda_n = 2Q\rho(n)$, the random variable $V_n = Q \frac{\hat{M}_{2,p}(n)}{\hat{M}_{2,z}}$ is noncentral F -distributed, i.e., $V_n \sim F_{\nu_n, \nu_z}(\lambda_n)$.

Proof. From the empirical second order moments $\hat{M}_{2,p}(n)$ and $\hat{M}_{2,z}$ in (4.29) and (4.22), respectively, it can be seen that the different data (samples originating from different subcarriers $Y(n)$) are used for performing estimation. Therefore, $\hat{M}_{2,p}(n)$ and $\hat{M}_{2,z}$ can be considered as independent random variables, thus giving random variables P_n and Z also as independent, respectively. According to [61], having P_n and Z stochastically independent, the noncentral F -distributed random variable V_n is obtained as the ratio of a noncentral chi-squared random variable $P_n \sim \chi_{\nu_n, \lambda}^2$ and a central chi-squared random variable $Z \sim \chi_{\nu_z}^2$,

$$V_n = \frac{P_n/\nu_n}{Z/\nu_z}. \quad (4.56)$$

Replacing P_n, Z, ν_p , and ν_z in (4.56) directly yields

$$\begin{aligned} V_n &= \frac{\left(\frac{2Q\hat{M}_{2,p}}{\sigma_W^2}\right)/2}{\left(\frac{2N_z\hat{M}_{2,z}}{\sigma_W^2}\right)/(2N_z)} \\ &= Q \frac{\hat{M}_{2,p}(n)}{\hat{M}_{2,z}}. \end{aligned} \quad (4.57)$$

□

Following the approach in (4.41)-(4.44), the mean and variance of the F -distributed random variables V_n in (4.56) can be written as

$$\begin{aligned} E(V_n) &= \frac{2N_z(1 + Q\rho(n))}{2(N_z - 1)} \\ &= \frac{1 + Q\rho(n)}{\left(1 - \frac{1}{N_z}\right)}, \quad N_z > 1, \end{aligned} \quad (4.58)$$

and

$$\begin{aligned} \text{Var}(V_n) &= 2 \cdot \left(\frac{2N_z}{2}\right)^2 \frac{4(1 + Q\rho(n))^2 + 4(N_z - 1)(1 + 2Q\rho(n))}{4(N_z - 1)^2 \cdot 2(N_z - 2)} \\ &= \frac{1}{N_z} \frac{(1 + Q\rho(n))^2 + (N_z - 1)(1 + 2Q\rho(n))}{\left(1 - \frac{1}{N_z}\right)^2 \left(1 - \frac{2}{N_z}\right)}, \quad N_z > 2, \end{aligned} \quad (4.59)$$

respectively.

Comparing (4.30) with (4.57), the estimated average SNR per subcarrier $\hat{\rho}_n$ can be written as a transformation of random variable V_n

$$\begin{aligned} \hat{\rho}(n) &= \frac{\hat{M}_{2,p}}{\hat{M}_{2,z}} - \frac{1}{Q} \\ &= \frac{1}{Q} \left(\left(Q \frac{\hat{M}_{2,p}(n)}{\hat{M}_{2,z}} \right) - 1 \right) \\ &= \frac{1}{Q} (V_n - 1). \end{aligned} \quad (4.60)$$

Its expectation $E(\hat{\rho}(n))$ is given by

$$\begin{aligned} E(\hat{\rho}(n)) &= \frac{1}{Q} (E(V_n) - 1) \\ &= \frac{1}{Q} \left(\frac{1 + Q\rho(n)}{1 - \frac{1}{N_z}} - 1 \right) \\ &= \frac{1}{Q} \left(Q\rho(n) + \frac{1 + Q\rho(n)}{N_z - 1} \right) \\ &= \rho(n) + \frac{\frac{1}{Q} + \rho(n)}{N_z - 1}. \end{aligned} \quad (4.61)$$

Because N_z represents the number of the nulled subcarriers, i.e., $N_z = \frac{Q-1}{Q}N$, (4.61) can be written as

$$\begin{aligned} E(\hat{\rho}(n)) &= \rho(n) + \frac{\frac{1}{Q} + \rho(n)}{N \left(1 - \frac{1}{Q}\right) - 1} \\ &\approx \rho(n), \end{aligned} \quad (4.62)$$

for $N \gg 1$, which is a regular case in real OFDM systems.

Similarly, according to the transformation (4.60), the MSE of the estimated average SNR is given by

$$\begin{aligned} \text{MSE}(\hat{\rho}(n)) &= \text{E} \left((\hat{\rho}(n) - \rho(n))^2 \right) \\ &\approx \text{Var}(\hat{\rho}(n)) \\ &= \frac{1}{Q^2} \text{Var}(V_n). \end{aligned} \quad (4.63)$$

Inserting (4.59) into (4.63), for $N_z = \frac{Q-1}{Q}N$ and $N_z = \frac{N}{Q}$, it yields

$$\text{MSE}(\hat{\rho}(n)) \approx \frac{1}{NQ(Q-1)} \frac{(1 + Q\rho(n))^2 + (N-1 - \frac{N}{Q})(1 + 2Q\rho(n))}{(1 - \frac{Q}{(Q-1)N})^2 (1 - \frac{2Q}{(Q-1)N})}. \quad (4.64)$$

Similarly to (4.41), the pdf of the F -distributed random variable V_n is given by

$$f_{V_n}(v_n) = e^{-\frac{\lambda_n}{2}} \sum_{k=0}^{\infty} \frac{(\frac{\lambda_n}{2})^k}{k!} \frac{(\frac{\nu_n}{\nu_z})^{\frac{1}{2}\nu_n+k}}{B\left(\frac{\nu_n+2k}{2}, \frac{\nu_z}{2}\right)} v_n^{\frac{\nu_n}{2}+k-1} \left(1 + \frac{\nu_n}{\nu_z} v_n\right)^{-\frac{1}{2}(\nu_n+\nu_z)-k}, \quad (4.65)$$

where $B(u, v)$ is the Beta function given in (4.42).

Having a transformation of random variable V_n (4.60), the pdf of estimated SNR per subcarrier is given by

$$\begin{aligned} f_{\hat{\rho}(n)}(\hat{\rho}(n)) &= Q \cdot f_{V_n}(1 + Q\hat{\rho}(n)) \\ &= Q \cdot e^{-\frac{\lambda_n}{2}} \sum_{k=0}^{\infty} \frac{(\frac{\lambda_n}{2})^k}{k!} \frac{(\frac{\nu_n}{\nu_z})^{\frac{1}{2}\nu_n+k}}{B\left(\frac{\nu_n+2k}{2}, \frac{\nu_z}{2}\right)} (1 + Q\hat{\rho}(n))^{\frac{\nu_n}{2}+k-1} \left(1 + \frac{\nu_n}{\nu_z}(1 + Q\hat{\rho}(n))\right)^{-\frac{1}{2}(\nu_n+\nu_z)-k}. \end{aligned} \quad (4.66)$$

Replacing λ , ν_n , and ν_z in (4.66) and having $N_z = \frac{Q-1}{Q}N$, it yields

$$\begin{aligned} f_{\hat{\rho}(n)}(\hat{\rho}(n)) &= Q \cdot e^{-Q\rho(n)} \sum_{k=0}^{\infty} \frac{(Q\rho(n))^k}{k!} \frac{\left(\frac{Q}{(Q-1)N}\right)^{k+1}}{B\left(k+1, \frac{Q-1}{Q}N\right)} (1 + Q\hat{\rho}(n))^k \left(\frac{1}{1 + \frac{Q(1+Q\hat{\rho}(n))}{(Q-1)N}}\right)^{\frac{Q-1}{Q}N+k+1} \\ &= \frac{e^{-Q\rho(n)}}{N} \cdot \sum_{k=0}^{\infty} \frac{\rho^k(n) \cdot Q^{2(k+1)} N^k}{k! \cdot B\left(k+1, \frac{Q-1}{Q}N\right)} (1 + Q\hat{\rho}(n))^k \left(\frac{1}{1 + \frac{Q(1+Q\hat{\rho}(n))}{(Q-1)N}}\right)^{\frac{Q-1}{Q}N+k+1} \\ &= \frac{e^{-Q\rho(n)}}{1 + Q\hat{\rho}(n)} \left(\frac{1}{1 + \frac{Q(1+Q\hat{\rho}(n))}{N(Q-1)}}\right)^{N(1-\frac{1}{Q})} \cdot \sum_{k=0}^{\infty} \frac{\rho^k(n) \cdot Q^{2(k+1)}}{k! \cdot B\left(k+1, \frac{Q-1}{Q}N\right)} \left(\frac{1}{Q + \frac{(Q-1)N}{1+Q\hat{\rho}(n)}}\right)^{k+1}. \end{aligned} \quad (4.67)$$

The pdf of the estimated SNR per subcarrier in (4.67) for true SNR = 10 dB, is shown in Figure 4.4. It can be seen that the simulation results agree with the derived analytical model. Similarly to the average SNR case, increasing the number of periodic parts Q improves the accuracy of SNR estimation, i.e., the pdf curve becomes more concentrated around the true SNR value for the higher Q values. Moreover, comparing with the corresponding curves related to the average SNR, shown in Figure 4.3, it can be noticed that the average SNR per subcarrier is characterized with the higher statistical uncertainty. The effect of the SNR estimation variance on adaptive modulation is further discussed in Chapter 7.

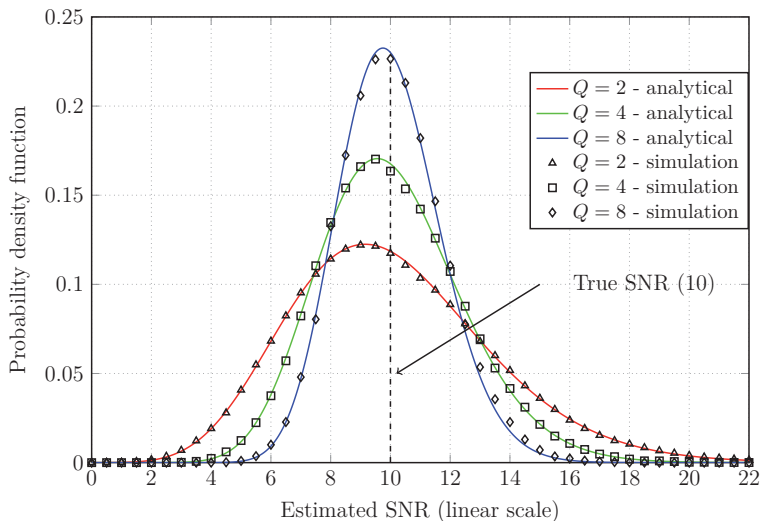


Figure 4.4.: Pdf of the SNR per subcarrier estimation for true SNR = 10 dB, $N = 256$, and the number of periodic parts $Q = 2, 4, 8$.

4.2.3. Numerical Results

First, we evaluate the performance of the PS estimator. We compare the simulation results obtained from the Monte-Carlo simulation with the analytical expressions derived from the statistical properties investigated in Subsection 4.2.2. Afterwards, we discuss the performance results of the PS estimator for a different number of preamble identical parts, i.e., $Q = 2, 4$, and 8 and compare them with the performance of the MMSE, Boumard's, and Rens' estimators. The system parameters used in the simulation are taken from the WiMAX specifications, namely $N = 512$ subcarriers, CP length of 64 samples and sampling frequency of 7.68 MHz (5 MHz bandwidth mode), see Appendix B.2. The performance is evaluated for four different channels: AWGN channel and three extended ITU channels described in Appendix A. The number of independent trials is set to $N_t = 100000$ assuring narrow confidence interval for the estimators. The performance evaluation is done in the terms of the normalized MSE (NMSE) of the estimated average SNR values following

$$\text{NMSE}_{\text{av}} = \frac{1}{N_t} \sum_{i=1}^{N_t} \left(\frac{\hat{\rho}_{\text{av},i} - \rho_{\text{av}}}{\rho_{\text{av}}} \right)^2, \quad (4.68)$$

where $\hat{\rho}_{\text{av},i}$ is the estimate of the average SNR in the i th trial, while ρ_{av} is the true value. The second considered performance measure is the NMSE of the estimated SNR per subcarrier, given by

$$\text{NMSE}_{\text{sc}} = \frac{1}{NN_t} \sum_{i=1}^{N_t} \sum_{n=0}^N \left(\frac{\hat{\rho}_i(n) - \rho(n)}{\rho(n)} \right)^2, \quad (4.69)$$

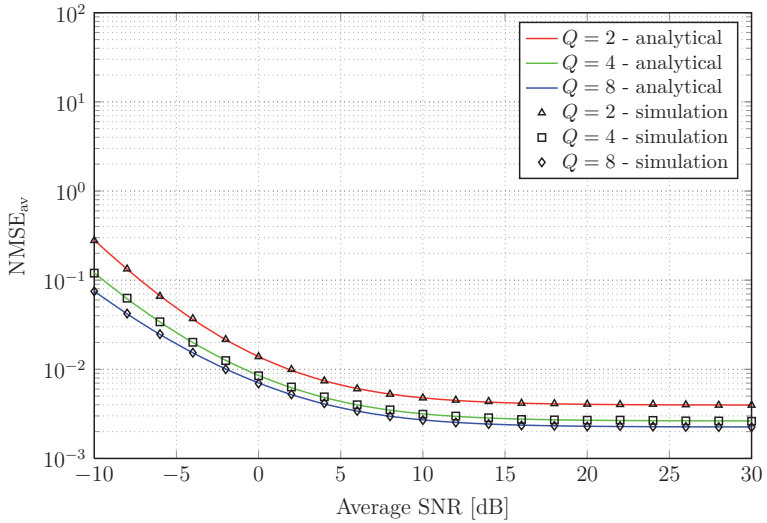


Figure 4.5.: NMSE of the average SNR estimation by PS in an AWGN channel.

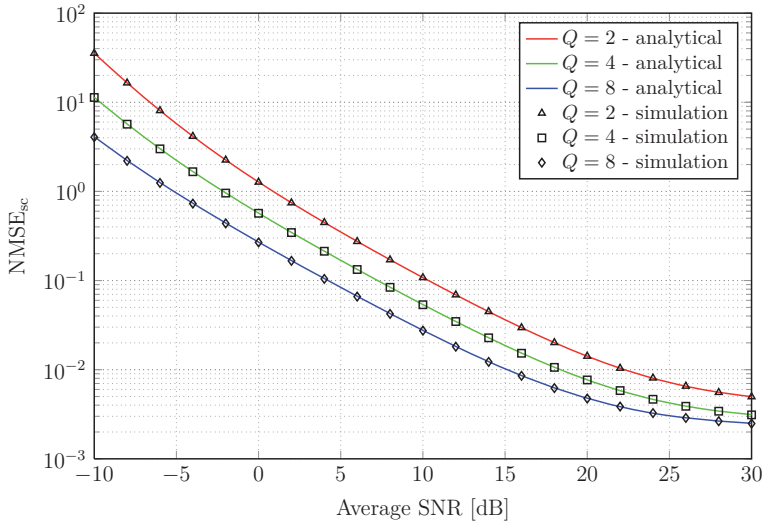


Figure 4.6.: NMSE of the SNR per subcarrier estimation by PS in an AWGN channel.

where $\hat{\rho}_i(n)$ is the estimate of the $\rho(n)$ in the i th trial.

Figure 4.5 shows the simulation results for NMSE_{av} of the PS estimator as a function of the SNR for a different number of identical parts Q in AWGN together with the analytical results derived from (4.50). It can be seen that the derived analytical model agrees with the simulation results. Similarly, it is shown in Figure 4.6 that simulation results for NMSE_{sc} correspond to analytical curves derived from (4.51). Thus, given mathematical model can be utilized for parameter selection during the design of the estimation unit at the receiver.

Furthermore, the performance of the PS estimator is compared with the performance of the existing abovementioned SNR estimators in extended ITU channels. During the comparison, the Ren's II estimator is implemented with either one or two preambles: one preamble is used for the MMSE and PS estimator, while two preambles are considered for the Boumard's and Ren's I estimator.

Figure 4.7 shows the NMSE_{av} of the considered estimators as a function of the SNR in the Extended Pedestrian A (EPA) channel with a low delay spread. To assess the absolute performance of the estimators, they are compared with the Cramer-Rao bound (CRB), which is a lower bound for the variance of any unbiased estimator [62]. The normalized CRB (NCRB) for an OFDM signal with N QPSK modulated subcarriers in an AWGN channel can be expressed as [63]

$$\text{NCRB} = \frac{1}{N} \left(\frac{2}{\rho_{\text{av}}} + 1 \right). \quad (4.70)$$

The MMSE estimator shows the best performance with the NMSE_{av} curve indistinguishable from the NCRB defined in (4.70). The Ren's II estimator with two preambles for SNR values greater than 0 dB shows no degradation with respect to the NCRB. The Ren's II estimator with one preamble performs similarly as the PS estimator for $Q = 2$. The Boumard's estimator for average SNR values smaller than 10 dB performs worse than the Ren's I and PS estimators. For average SNR values greater than 10 dB it outperforms both the Ren's I and PS estimator for $Q = 2$. Note that increasing the number of the nulled subcarriers in the preamble ($Q = 4, 8$) brings its performance closer to the NCRB. It can be explained with the notion that more subcarriers are used for the average noise power estimation (4.22) while the transmitted signals on the loaded subcarriers get more power due to the scaling by Q , thus giving the more accurate estimation in (4.20).

Figure 4.8 and Figure 4.9 compare the NMSE_{av} as a function of the SNR of the considered estimators in time-invariant Extended Vehicular A (EVA) and Extended Typical Urban (ETU) channels characterized with the medium and high delay spread, respectively. It is shown that the performance of the PS estimator and both of the Ren's estimators are robust against frequency selectivity, while the Boumard's estimator performs highly sensitive to channel selectivity.

The NMSE_{sc} performance of the considered estimators in the EPA, EVA, and ETU channels are shown in Figure 4.10, Figure 4.11, and Figure 4.12, respectively. Because all considered estimators depend on channel estimations, bad performance in the low SNR region is expected. The performance can be further improved by combining estimated average noise power with more sophisticated channel estimation algorithms using pilot subcarriers distributed within the data symbols. It can be noticed that in the high SNR

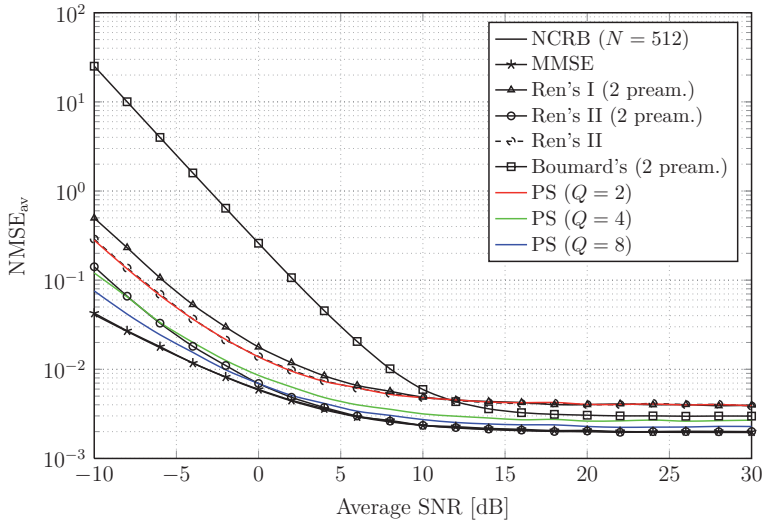


Figure 4.7.: NMSE of the average SNR estimation in the EPA channel.

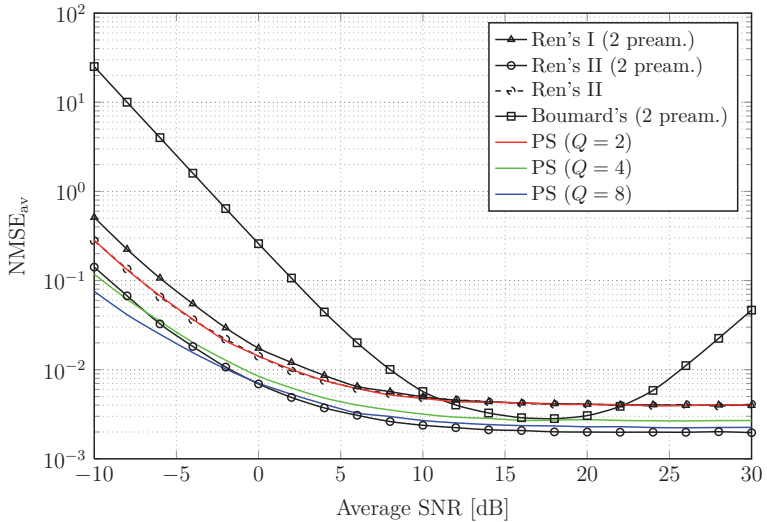


Figure 4.8.: NMSE of the average SNR estimation in the EVA channel.

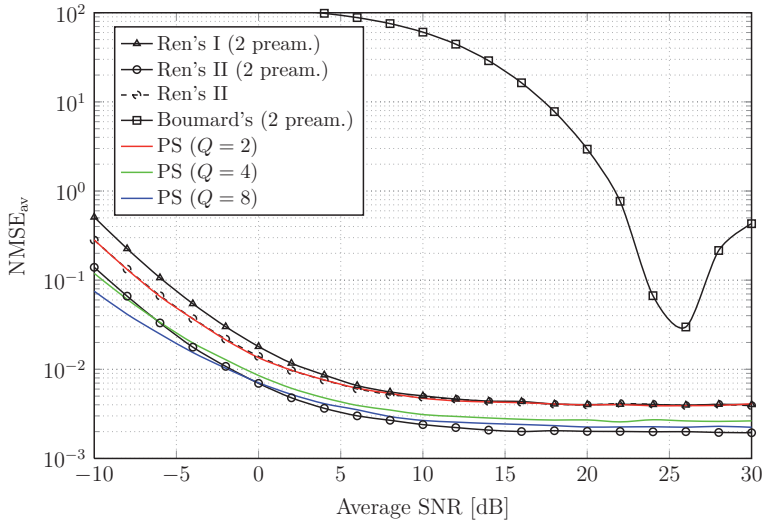


Figure 4.9.: NMSE of the average SNR estimation in the ETU channel.

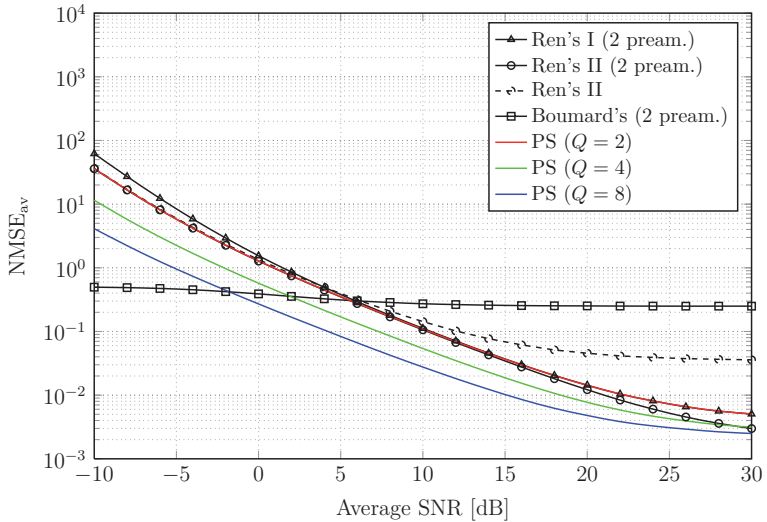


Figure 4.10.: NMSE of the SNR per subcarrier estimation in the EPA channel.

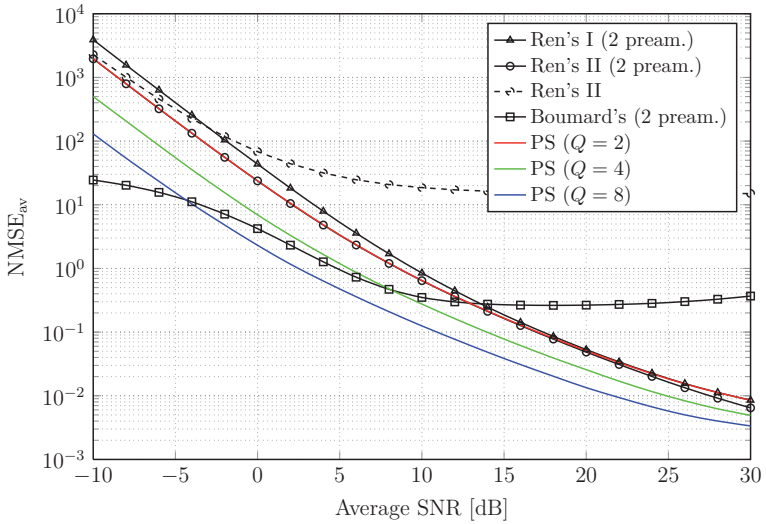


Figure 4.11.: NMSE of the SNR per subcarrier estimation in the EVA channel.

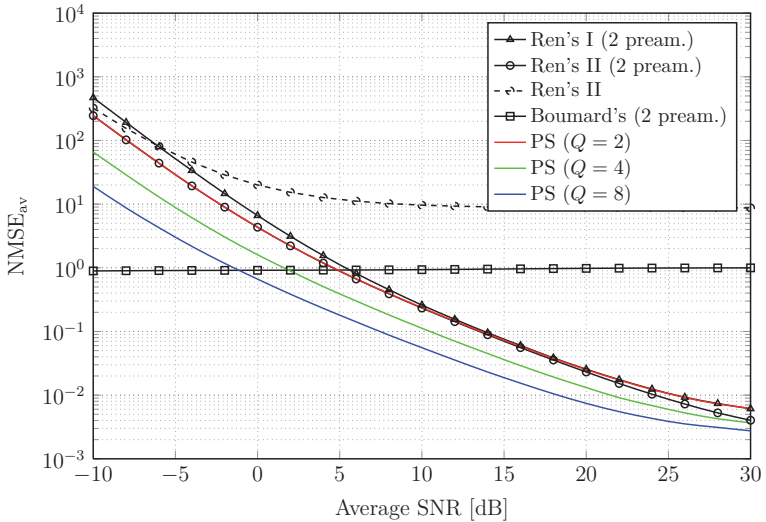


Figure 4.12.: NMSE of the SNR per subcarrier estimation in the ETU channel.

region, channel estimations stop to act as the deteriorating factor and NMSE_{sc} approaches the NMSE_{av} . The performance of the PS estimator depends on the channel selectivity, which is expected due to the performed interpolation during the channel estimation. Furthermore, it can be seen that the PS estimator for $Q = 2$ performs similarly to the Ren's II estimator with two preambles, while it outperforms the Boumard's and other Ren's estimators.

The Performance in Time-Variant Channel

Figure 4.13 and Figure 4.14 show the performance of the PS estimator in time-variant ETU channel by means of NMSE_{av} as a function of the data symbols per frame for the real $\text{SNR} = 10$ dB and $\text{SNR} = 25$ dB, respectively. The data frame is considered to consist of 50 data symbols and that the NMSE_{av} of the average SNR estimation is determined for each OFDM symbol within the frame. It is shown that the accuracy of all considered estimators is getting worse as the symbol index increases. The performance decay rate increases with the average SNR value.

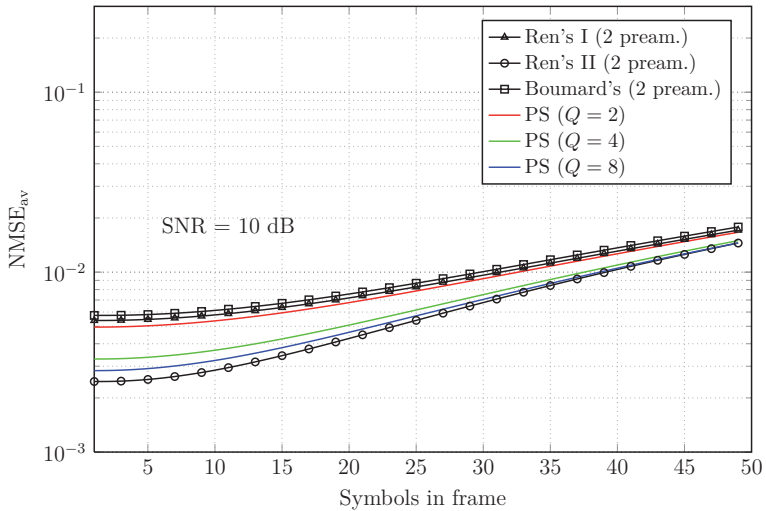


Figure 4.13.: NMSE of the average SNR estimation per OFDM symbol for $SNR = 10$ dB in the ETU channel, $\nu = 5$ km/h.

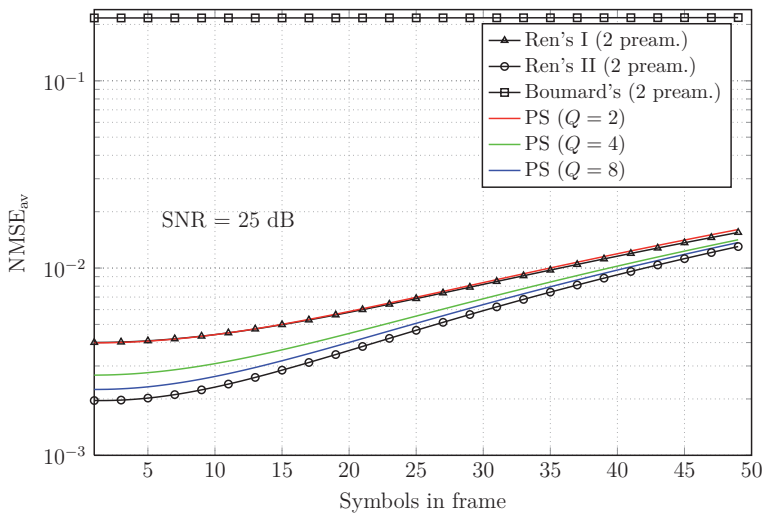


Figure 4.14.: NMSE of the average SNR estimation per OFDM symbol for $SNR = 25$ dB in the ETU channel, $\nu = 5$ km/h.

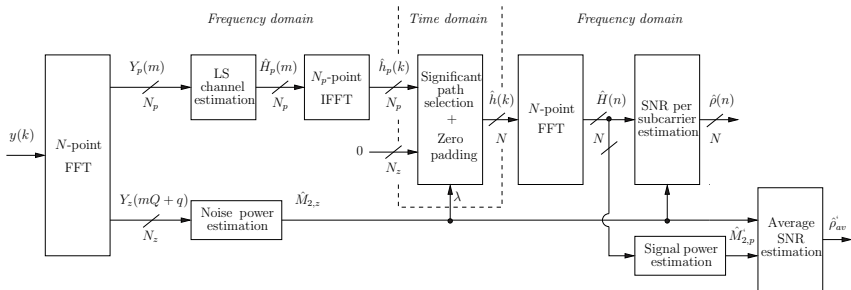


Figure 4.15.: Block diagram of the IPS estimator.

4.3. Improved PS (IPS) Estimator

As simulation results presented in Subsection 4.2.3 indicate, the PS estimator performs poorly in the low SNR regime. Therefore, we propose a modification to the PS estimator, as shown in Figure 4.15. By comparing the average power estimates of the individual CIR paths $|\hat{h}_p(k)|^2$ with the certain threshold λ , only the significant CIR paths are selected as inputs to the N -point DFT. The value of the threshold λ is determined by the average noise power estimate $\hat{M}_{2,z}$ obtained in the frequency domain. The rest of CIR paths, whose average power estimates are below the threshold, are nulled assuming that they contain only noise samples. Figure 4.16 shows one channel realization from the simulations together with the appropriate threshold value used for significant path selection. Therefore, the CIR prior to the N -point DFT can be written as

$$\hat{h}(k) = \begin{cases} \hat{h}_p(k), & |\hat{h}_p(k)|^2 > \lambda \\ 0, & \text{otherwise} \end{cases}. \quad (4.71)$$

The selection of the threshold λ is based on the reduction of the MSE of the individual channel estimates. It is shown in [58] that the MSE is reduced when

$$\sigma_{\hat{h}}^2(k) > \frac{1}{\rho_{av}}, \quad k = 0, \dots, N-1, \quad (4.72)$$

holds. Here, $\sigma_{\hat{h}}^2(k) = E\{|h(k)|^2\}$ denote the average power of the k th CIR path. According to (4.26), because only CIR estimates $\hat{h}_p(k)$ are available, $\sigma_{\hat{h}_p}^2(k)$ can be written as

$$\sigma_{\hat{h}_p}^2(k) = \sigma_S^2 \sigma_{\hat{h}}^2(k) + \frac{\sigma_W^2}{Q}. \quad (4.73)$$

By replacing (4.73) in (4.72), it can be derived that the MSE is reduced when

$$\sigma_{\hat{h}_p}^2(k) > \left(1 + \frac{1}{Q}\right) \sigma_W^2 \quad (4.74)$$

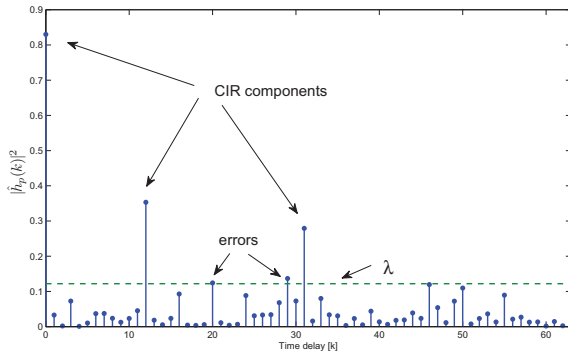


Figure 4.16.: Significant path selection for the EVA channel with $Q = 4$ and $\text{SNR} = -6$ dB.

holds.

The average power of the k th path $\sigma_{h_p}^2(k)$ and average noise power σ_W^2 in (4.74) can be replaced with available unbiased estimates, $|\hat{h}_p(k)|^2$ and $\hat{M}_{2,z}$, respectively. Therefore, the appropriate threshold can be derived as

$$|\hat{h}_p(k)|^2 > \left(1 + \frac{1}{Q}\right) \hat{M}_{2,z} = \lambda. \quad (4.75)$$

After the significant path selection and DFT, channel estimates $\hat{H}(n)$ are obtained using (4.28), while SNR per subcarrier estimates $\hat{\rho}(n)$ are derived from (4.30). Because performed CIR filtering significantly reduces the amount of noise present in channel estimates, the average power estimate can be written as

$$\hat{M}'_{2,p} = \frac{1}{N} \sum_{n=0}^{N-1} |\hat{H}(n)|^2, \quad (4.76)$$

which gives the average SNR estimate

$$\hat{\rho}_{av} = \frac{\hat{M}'_{2,p}}{\hat{M}_{2,z}} - \frac{1}{Q}. \quad (4.77)$$

4.3.1. Numerical Results

The NMSE_{av} as a function of the SNR for the PS and IPS estimators is shown in Figure 4.17. The increasing number of identical parts Q in the preamble brings the performance of both estimators closer to the NCRB because more subcarriers are used for

the average noise power estimation (4.22) while the loaded subcarriers get more power due to the scaling by Q . Both estimators show robust performance in frequency-selective channels, i.e., the corresponding accuracy is not affected by the level of channel selectivity. It can be also noticed that the IPS estimator outperforms the PS estimator in the low SNR regime because the selection of significant CIR paths filters the noise. However, the performance improvement for $Q = 8$ is slightly worse in the ETU channel compared to the corresponding improvement in an AWGN channel. For $Q = 8$, the IPS estimator reaches the NCRB at low SNR values. In the frequency-selective ETU channel, there is no improvement compared to the PS estimator while performance is slightly worse compared to $Q = 4$ at SNR values less than -7 dB.

The NMSE_{sc} performance of the IPS and PS estimators in the EPA, EVA, and ETU channels are shown in Figure 4.18, Figure 4.19, and Figure 4.20, respectively. It can be seen that the IPS outperforms the PS estimator in all considered channels for each particular value of Q . Moreover, the increasing number of periodic parts Q improves the performance of the PS estimator independently of channel selectivity. However, the IPS estimator for $Q = 8$ stops to benefit from the increase of Q and shows worse performance compared to $Q = 4$ case for SNR values less than 0 dB in the frequency-selective ETU channel.

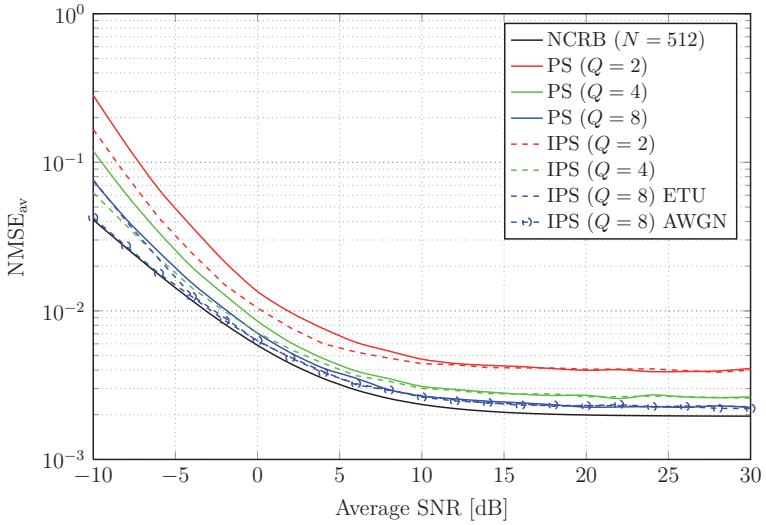


Figure 4.17.: NMSE of the average SNR estimation.

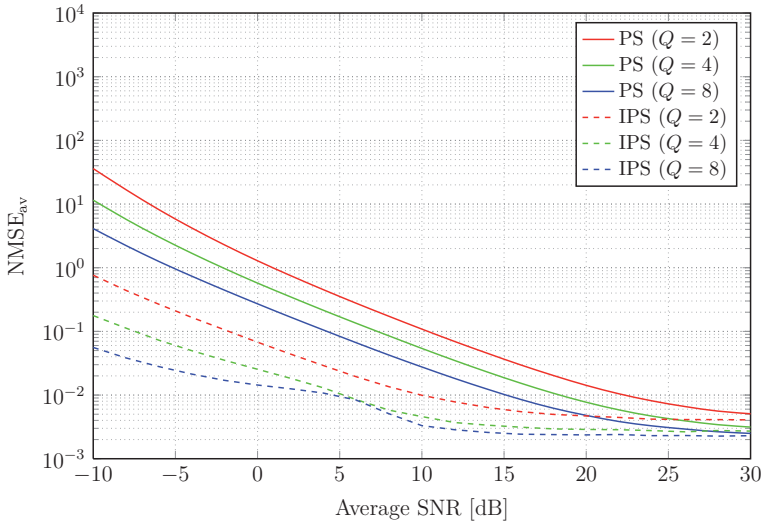


Figure 4.18.: NMSE of the SNR per subcarrier estimation in the EPA channel.

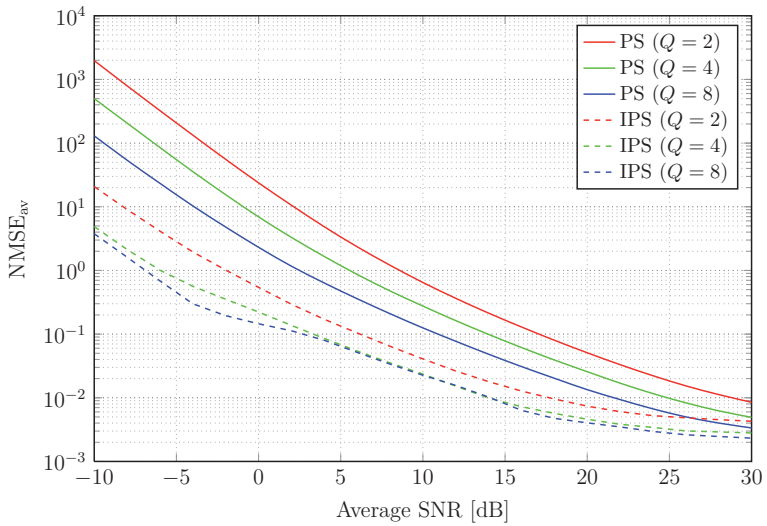


Figure 4.19.: NMSE of the SNR per subcarrier estimation in the EVA channel.

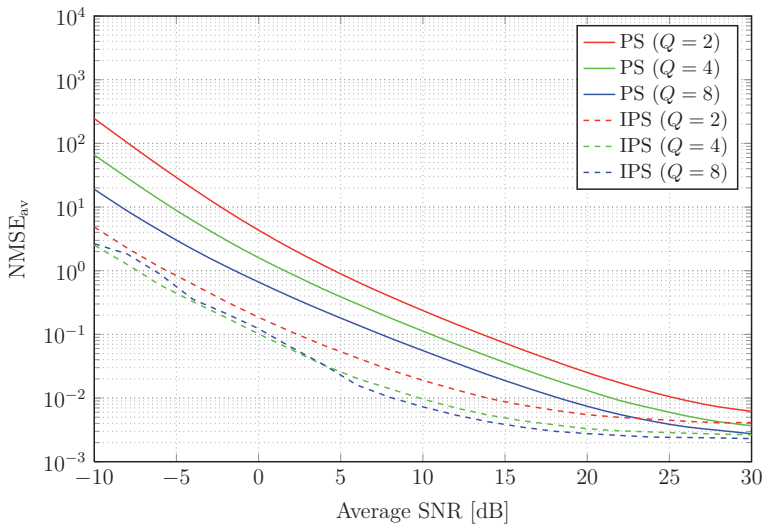


Figure 4.20.: NMSE of the SNR per subcarrier estimation in the ETU channel.

5. SNR Estimation in MIMO OFDM Systems

The transmission rate can be further increased without the need for larger signal bandwidth. By using multiple antennas, so called multiple-input multiple-output (MIMO) systems have additional parallel channels in the spatial domain. They provide improved link reliability and increased data rate through the multiplexing technique. Hence, MIMO OFDM systems offer a promising combination for the high data requirement of the present (WiMAX, WLAN, LTE) and future wireless systems. Most preamble-based SNR estimators from the literature so far are related to a single carrier single-input single-output (SISO) transmission. To the best of our knowledge only Boumard in [8] proposed a preamble-based SNR estimator for 2×2 MIMO OFDM systems.

In this chapter, we extend our work on SNR estimation for single-input single-output (SISO) systems by proposing a modification of the PS estimator for $N_T \times N_R$ MIMO OFDM systems, named MIMO-PS estimator. The proposed estimator uses one preamble and allows better bandwidth efficiency than Boumard's estimator, which inherently uses two preambles. Low complexity and robustness to frequency selectivity combined with bandwidth efficiency favors the proposed estimator over the existing preamble-based estimators available from the literature. Parts of the following results have been presented in [10] where we proposed the MIMO-PS estimator for 2×2 MIMO OFDM systems. In this chapter, we extend the existing estimator for arbitrary MIMO dimensions and give insight into implementation issues.

5.1. MIMO System Model

Similarly to the SISO OFDM systems in Section 4.2, we assume a general model for the frame structure composed of I preambles where each preamble contains N modulated subcarriers. Furthermore, we consider $N_T \times N_R$ MIMO OFDM system, where N_T and N_R denote the number of transmit and receive antennas, respectively. To illustrate the scenario, the simplified block diagram of 2×2 MIMO OFDM system in the acquisition mode is shown in Figure 5.1. Because we consider SNR estimation performed in the frequency domain, the model contains only frequency domain characterization of the received signal in frequency-selective AWGN channels. Let $C_t(i, n)$ denote the complex data symbol on the n th subcarrier in the i th preamble at the t th transmit antenna, where $i = 0, \dots, I - 1$, $n = 0, \dots, N - 1$, and $t = 1, \dots, N_T$.

We assume that the modulated subcarriers within the preambles have constant magnitude $E\{|C_t(i, n)|\} = 1$ with the same allocated power $\sigma_{S,t}^2 = \sigma_S^2$. Similarly to the SISO case in Section 4.2, this is a regular assumption because current OFDM standards usually contain preambles composed of QPSK and/or BPSK modulated subcarriers. At the

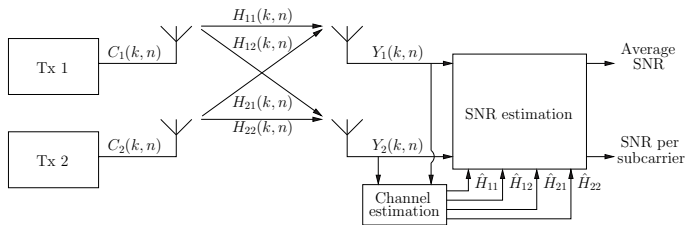


Figure 5.1.: Simplified block diagram of 2×2 MIMO OFDM system.

receiver, perfect timing and frequency synchronization is assumed, hence after the DFT, the received signal on the n th subcarrier in the i th preamble at the r th receive antenna can be expressed as

$$Y_r(i, n) = \frac{\sigma_S}{\sqrt{N_T}} \sum_{i=t}^{N_T} C_t(i, n) H_{tr}(i, n) + \sigma_{W,r} g m_{W,r} W_r(i, n), \quad r = 1, \dots, N_R. \quad (5.1)$$

Furthermore, σ_S^2/N_T is the transmitted signal power at the single antenna (giving the total transmit power of σ_S^2), $W_r(i, n)$ are complex zero-mean AWGN samples of unit variance, and $\sigma_{W,r}^2$ is the corresponding noise power at the r th receiving antenna. The channel frequency response between the t th and r th antenna, $H_{tr}(i, n)$, is given by

$$H_{tr}(i, n) = \sum_{l=1}^L h_{l,tr}(iT_s) \cdot e^{-j2\pi \frac{n\tau_{l,tr}}{NT_s}}. \quad (5.2)$$

Here, $h_{l,tr}(iT_s)$ and $\tau_{l,tr}$ denote the l th path gain and delay between the t th and r th antenna during the i th preamble, respectively, T_s is the duration of the OFDM preamble, g and L is the memory length of the channel. The channel path gains $h_{l,tr}(iT_s)$ are uncorrelated and normalized for each pair of Tx/Rx antennas, such that their expected total power is unity, i.e., $\sum_{l=1}^L |h_{l,tr}(iT_s)|^2 = 1$ is satisfied for $\forall t, r$. We assume that channel is constant during the whole frame, because we consider the SNR estimators for adaptive transmission. Therefore, the time index i is omitted during the estimation procedure, i.e., $H_{tr}(i, n)$ is replaced by $H_{tr}(n)$. We also assume that the average SNR and SNR per subcarrier estimates are valid for all information data bearing OFDM symbols within the frame.

Generalizing the result presented in [8], the received signal average SNR for an $N_T \times N_R$ MIMO OFDM system can be written as

$$\begin{aligned} \rho_{av} &= \frac{1}{N_R} \sum_{r=1}^{N_R} \frac{\sum_{t=1}^{N_T} \text{E}\{\sum_{n=0}^{N-1} |\frac{\sigma_S}{\sqrt{N_T}} C_t(i, n) H_{tr}(n)|^2\}}{\text{E}\{\sum_{n=0}^{N-1} |\sigma_{W,r} W_r(i, n)|^2\}} \\ &= \frac{\sigma_S^2}{N_T N_R} \sum_{r=1}^{N_R} \frac{\sum_{t=1}^{N_T} \sum_{n=0}^{N-1} |H_{tr}(n)|^2}{\sigma_{W,r}^2} \\ &= \frac{\sigma_S^2}{N_R} \sum_{r=1}^{N_R} \frac{1}{\sigma_{W,r}^2} = \frac{1}{N_R} \sum_{j=1}^{N_R} \rho_{av,r}, \end{aligned} \quad (5.3)$$

where $\rho_{av,r} = \sigma_S^2/\sigma_{W,r}^2$ is the average SNR at the r th antenna and $\sum_{n=0}^{N-1} |H_{tr}(n)|^2 = N$ is satisfied. For equal noise powers at the antennas, i.e., $\sigma_{W,r}^2 = \sigma_W^2$ for $r = 1, \dots, N_R$, the average SNR (5.3) can be expressed as $\rho_{av} = \sigma_S^2/\sigma_W^2$.

Furthermore, the average SNR on the n th subcarrier is given by

$$\begin{aligned} \rho(n) &= \frac{1}{N_R} \sum_{r=1}^{N_R} \frac{\sum_{t=1}^{N_T} E\{|\frac{\sigma_S}{\sqrt{N_R}} C_t(i, n) H_{tr}(n)|^2\}}{E\{|\sigma_{W,r} W_r(i, n)|^2\}} \\ &= \frac{\sigma_S^2}{N_T N_R} \sum_{r=1}^{N_R} \frac{\sum_{t=1}^{N_T} \{ |H_{tr}(n)|^2 \}}{\sigma_{W,r}^2} \\ &= \frac{1}{N_T N_R} \sum_{r=1}^{N_R} \rho_{av,r} \sum_{t=1}^{N_T} E\{ |H_{tr}(n)|^2 \}. \end{aligned} \quad (5.4)$$

From (5.4), it is clear that the SNR per subcarrier estimate depends on the average SNR (or the average noise power) estimate at each antenna and appropriate channel estimates.

5.2. MIMO-PS Estimator

The preamble structure for a 2×2 MIMO OFDM systems is shown in Figure 5.2. Different indexes for loaded subcarriers at each antenna must be introduced. The nulled subcarriers are used to estimate the noise power. Proposed estimator can be further extended for arbitrary MIMO systems. The required design condition is that the number of subcarriers which are nulled on each receive antenna must be larger or equal to $N/2$, i.e., $Q \geq 2N_T$. Figure 5.2 shows the corresponding time and frequency domain representations of the preamble structure used for the SNR estimation in MIMO systems.

At the t th antenna, starting from the $2(t-1)$ th subcarrier, each Q th subcarrier is modulated with a QPSK signal $C_{t_p}(m_t)$ with $|C_{t_p}(m_t)| = 1$ and loaded with the power σ_S^2 , where $t = 1, \dots, N_T$. For $m = 0, 1, \dots, N_p - 1$, the indexes of loaded subcarriers at the t th antenna are given by $m_t = (t-1)mQ$. The remainder of $N_z = N - N_p = \frac{(Q-1)}{Q}N$ subcarriers at each antenna is not used (nulled), thus giving $\frac{(Q-N_T)}{Q}N$ subcarriers which are nulled on both antennas. In order to maintain the total energy level over all symbols within the preamble, the transmit power is additionally scaled by factor Q . This yields a total transmit power of $\sigma_S^2 Q / N_T$ on loaded subcarriers.

Write $n = mQ + q$, $m = 0, \dots, N_p - 1$, $m_t = (t-1)mQ$, $q = 0, \dots, Q - 1$. The transmitted signal on the n th subcarrier at the t th antenna is described as

$$C_t(n) = C_t(mQ + q) = \begin{cases} \sqrt{\frac{Q}{N_T}} \sigma_S C_{t_p}(m_t), & q = 2(t-1) \\ 0, & q \neq 2(t-1), \quad t = 1, \dots, N_T \end{cases}. \quad (5.5)$$

From (5.1), the received signal on the n th subcarrier at the r th antenna is given by

$$Y_r(n) = Y(mQ + q) = \begin{cases} Y_{tr_p}(m_t), & q = 2(t-1) \\ Y_{r_z}(mQ + q), & q \neq 2(t-1), \quad t = 1, \dots, N_T \end{cases},$$

where

$$Y_{tr_p}(m_t) = \sqrt{\frac{Q}{N_T}} \sigma_S C_{t_p}(m_t) H_{tr_p}(m_t) + \sigma_{W,r} W_{r_p}(m_t) \quad (5.6)$$

denote the received signal on the loaded subcarriers, and

$$Y_{r_z}(mQ + q) = \sigma_{W,r} W_{r_z}(mQ + q) \quad (5.7)$$

is the received signal on the nulled subcarriers containing only noise.

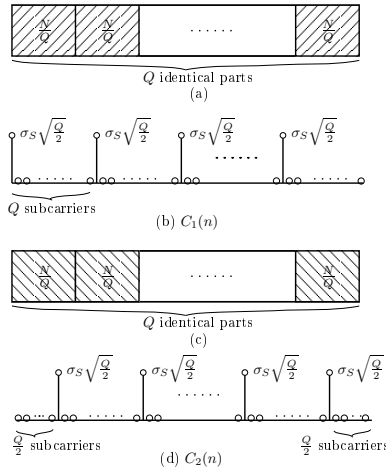


Figure 5.2.: Preamble structure in the a), c) time and b), d) frequency domain.

The empirical second-order moment of the received signal on the loaded subcarriers is

$$\hat{M}_{2,tr_p} = \frac{1}{N_p} \sum_{m_t} |Y_{tr_p}(m_t)|^2. \quad (5.8)$$

Its expected value is given by

$$\begin{aligned} \mathbb{E} \left\{ \hat{M}_{2,tr_p} \right\} &= \frac{1}{N_p} \sum_{m_t} \mathbb{E} \left\{ |Y_{tr_p}(m_t)|^2 \right\} \\ &= \frac{Q\sigma_S^2}{N_T N_p} \sum_{m_t} \mathbb{E} \left\{ |H_{tr_p}(m_t)|^2 \right\} + \frac{\sigma_{W,r}^2}{N_p} \sum_{m_t} \mathbb{E} \left\{ |W_{r_p}(m_t)|^2 \right\} \\ &= \frac{Q\sigma_S^2}{N_T} + \sigma_{W,r}^2. \end{aligned}$$

Similarly, the empirical second moment of the received signal on the nulled subcarriers can be written as

$$\hat{M}_{2,r_z} = \frac{1}{N_p(Q - N_T)} \sum_{m=0}^{N_p-1} \sum_{\substack{q=1, \\ q \neq 2(t-1), \\ t=1, \dots, N_T}}^{Q-1} |Y_{r_z}(mQ + q)|^2, \quad (5.9)$$

and has expectation

$$\begin{aligned} \mathbb{E} \left\{ \hat{M}_{2,r_z} \right\} &= \frac{1}{N_p(Q - N_T)} \sum_{m=0}^{N_p-1} \sum_{\substack{q=1, \\ q \neq 2(t-1), \\ t=1, \dots, N_T}}^{Q-1} \mathbb{E} \left\{ |Y_{r_z}(mQ + q)|^2 \right\} \\ &= \frac{\sigma_{W,r}^2}{N_p(Q - N_T)} \sum_{m=0}^{N_p-1} \sum_{\substack{q=1, \\ q \neq 2(t-1), \\ t=1, \dots, N_T}}^{Q-1} \mathbb{E} \left\{ |W_{r_z}(mQ + q)|^2 \right\} \\ &= \sigma_{W,r}^2. \end{aligned} \quad (5.10)$$

In summary, the average SNR at the r th antenna $\rho_{av,r}$ can be estimated as

$$\begin{aligned}\hat{\rho}_{av,r} &= \frac{1}{Q} \frac{\left(\sum_{t=1}^{N_T} \hat{M}_{2,tr_p} - N_T \hat{M}_{2,r_z}\right)}{\hat{M}_{2,r_z}} \\ &= \frac{1}{Q} \left((Q - N_T) \frac{\sum_{t=1}^{N_T} \sum_{m_t} |Y_{tr_p}(m_t)|^2}{\sum_{m=0}^{N_p-1} \sum_{\substack{q=1, \\ q \neq 2(t-1), \\ t=1, \dots, N_T}}^{Q-1} |Y_{r_z}(mQ+q)|^2} - N_T \right),\end{aligned}\quad (5.11)$$

where, by the strong law of large numbers, \hat{M}_{2,tr_p} and \hat{M}_{2,r_z} are strongly consistent unbiased estimators of $\frac{Q\sigma_S^2}{N_T} + \sigma_{W,r}^2$ and average noise power $\sigma_{W,r}^2$ at the r th antenna, respectively. In the case of equal noise power on antennas, i.e., $\sigma_{W,r}^2 = \sigma_W^2$, for $r = 1, \dots, N_R$, the average SNR estimate can be expressed as

$$\begin{aligned}\hat{\rho}_{av} &= \frac{1}{Q} \frac{\left(\sum_{r=1}^{N_R} \sum_{t=1}^{N_T} \hat{M}_{2,tr_p} - N_T \sum_{r=1}^{N_R} \hat{M}_{2,r_z}\right)}{\sum_{r=1}^{N_R} \hat{M}_{2,r_z}} \\ &= \frac{1}{Q} \left((Q - N_T) \frac{\sum_{r=1}^{N_R} \sum_{t=1}^{N_T} \sum_{m_t} |Y_{tr_p}(m_t)|^2}{\sum_{r=1}^{N_R} \sum_{m=0}^{N_p-1} \sum_{\substack{q=1, \\ q \neq 2(t-1), \\ t=1, \dots, N_T}}^{Q-1} |Y_{r_z}(mQ+q)|^2} - N_T \right).\end{aligned}\quad (5.12)$$

The PS estimator does not need any knowledge of the transmitted symbols or channel estimates on the loaded subcarriers for the average SNR estimation. Only the arrangement of the loaded and nulled subcarriers must be known to the receiver. However, channel estimates are requisite for the estimation of the average SNR per subcarrier (5.4). They are available only for the loaded subcarriers by the means of the least squares (LS) estimation as

$$\begin{aligned}\hat{H}_{tr_p}(m_t) &= \frac{1}{\sqrt{Q}} C_{t_p}^*(m_t) Y_{tr_p}(m_t) \\ &= \frac{\sigma_S}{\sqrt{N_T}} H_{tr_p}(m_t) + \frac{\sigma_{W,r}}{\sqrt{Q}} \tilde{W}_{r_p}(m_t),\end{aligned}\quad (5.13)$$

where $\tilde{W}(m_t) = C_{t_p}^*(m_t) W(m_t)$. Similar to the SISO case (4.26), the channel estimates for the rest of the subcarriers $\hat{H}_{tr}(mQ+q)$, $m = 0, \dots, N_p - 1$, $q = 0, \dots, Q - 1 \wedge q \neq 2(t-1)$, are obtained by the DFT interpolation. Therefore, the channel impulse response (CIR) estimates after the IDFT can be written as

$$\begin{aligned}\hat{h}_{tr_p}(k) &= \text{IDFT}_{N_p} \left[\hat{H}_{tr_p}(m_t) \right], \quad 0 \leq k \leq N_p - 1 \\ &= \frac{\sigma_S}{\sqrt{N_T}} h_{tr}(k) + \frac{\sigma_{W,r}}{\sqrt{Q}} \tilde{w}_{r_p}(k),\end{aligned}\quad (5.14)$$

where $\text{IDFT}_{N_p}[\cdot]$ presents the N_p -point IDFT and $\tilde{w}_{r_p}(k) = \text{IDFT}_{N_p} \left[\tilde{W}_{r_p}(m_t) \right]$. To obtain channel estimates, the rest of $N_z = N - N_p$ samples are padded with zeros giving the CIR prior to N -point DFT as

$$\hat{h}_{tr}(k) = \begin{cases} \hat{h}_{tr_p}(k), & 0 \leq k \leq N_p - 1 \\ 0, & N_p \leq k \leq N - 1. \end{cases}\quad (5.15)$$

Channel estimates after the N -point FFT are obtained as

$$\begin{aligned}\hat{H}_{tr}(n) &= \text{DFT}_N [\hat{h}_{tr}(k)] \\ &= \frac{\sigma_S}{\sqrt{N_T}} H_{tr}(n) + \frac{\sigma_{W,r}}{\sqrt{Q}} \bar{W}_r(n), \quad 0 \leq n \leq N-1.\end{aligned}\quad (5.16)$$

Similarly to (4.29), the expectation of the empirical second order moment of (5.16), $\hat{M}_{2,p,tr}(n) = |\hat{H}_{tr}(n)|^2$, is given by

$$\begin{aligned}\text{E} \{ \hat{M}_{2,p,tr}(n) \} &= \text{E} \{ |\hat{H}_{tr}(n)|^2 \} \\ &= \frac{\sigma_S^2}{N_T} \text{E} \{ |H_{tr}(n)|^2 \} + \frac{\sigma_{W,r}^2}{Q} \text{E} \{ |\bar{W}_r(n)|^2 \} \\ &= \frac{\sigma_S^2}{N_T} \text{E} \{ |H_{tr}(n)|^2 \} + \frac{\sigma_{W,r}^2}{Q}.\end{aligned}\quad (5.17)$$

Furthermore, the SNR estimate on the n th subcarrier can be written as (5.4)

$$\hat{\rho}(n) = \frac{1}{N_R} \sum_{r=1}^{N_R} \frac{\sum_{t=1}^{N_T} \hat{M}_{2,p,tr}(n)}{\hat{M}_{2,rz}} - \frac{1}{N_T N_R Q}.\quad (5.18)$$

5.3. Improved MIMO-PS (MIMO-IPS) Estimator

It can be expected that the MIMO-PS estimator performs poorly in the low SNR regime. Similarly to the SISO case, to filter the noise, the estimation of the average noise power can be used to determine an appropriate threshold for the selection of the significant CIR paths. By comparing the average power estimates of the individual CIR paths $|\hat{h}_{tr_p}(k)|^2$ with the threshold λ_r determined by the average noise power estimate $\hat{M}_{2,rz}$ obtained in frequency domain, only the significant CIR paths are selected as inputs to the N -point DFT. The rest of the CIR paths, whose average power estimates are below the threshold, are nulled assuming that they contain only noise samples. Therefore, the CIR for each path prior to the N -point DFT can be written as

$$\hat{h}_{tr}(k) = \begin{cases} \hat{h}_{tr_p}(k), & |\hat{h}_{tr_p}(k)|^2 > \lambda_r \\ 0, & \text{otherwise} \end{cases}.\quad (5.19)$$

The selection of the threshold λ_r is based on the reduction of the mean square error (MSE) of the individual channel estimates. It is shown in [58] that the MSE is reduced when

$$\sigma_{\hat{h}_{tr}}^2(k) > \frac{1}{\rho_{av,r}}, \quad k = 0, \dots, N-1,\quad (5.20)$$

holds, where $\sigma_{\hat{h}_{tr}}^2(k) = \text{E} \{ |h_{tr}(k)|^2 \}$ denote the average power of the k th CIR path. Because only CIR estimates $\hat{h}_{tr_p}(k)$ (5.14) are available, $\sigma_{\hat{h}_{tr_p}}^2(k)$ can be written as

$$\sigma_{\hat{h}_{tr_p}}^2(k) = \frac{\sigma_S^2}{N_T} \sigma_{h_{tr}}^2(k) + \frac{\sigma_{W,r}^2}{Q}.\quad (5.21)$$

By replacing (5.21) in (5.20), it can be derived that MSE is reduced when

$$\sigma_{\hat{h}_{trp}}^2(k) > \left(\frac{1}{N_T} + \frac{1}{Q} \right) \sigma_{W,r}^2 \quad (5.22)$$

holds. The average power of the k th subcarrier $\sigma_{\hat{h}_{trp}}^2(k)$ and the average noise power $\sigma_{W,r}^2$ in (5.22) can be replaced with the available unbiased estimates, $|\hat{h}_{trp}(k)|^2$ and $\hat{M}_{2,rz}$, respectively. Therefore, the appropriate threshold can be derived as

$$|\hat{h}_{trp}(k)|^2 > \left(\frac{1}{N_T} + \frac{1}{Q} \right) \hat{M}_{2,rz} = \lambda_r. \quad (5.23)$$

After significant path selection and DFT, channel estimates $\hat{H}_{tr}(n)$ are obtained using (5.16), while SNR per subcarrier estimates $\hat{\rho}(n)$ are derived from (5.18). Since performed CIR filtering significantly reduces the amount of noise present in channel estimates, the average power estimate can be written as

$$\hat{M}'_{2,trp} = \frac{1}{N} \sum_{n=0}^{N-1} |\hat{H}_{tr}(n)|^2. \quad (5.24)$$

The average SNR estimation at the r th receive antenna is then given by

$$\hat{\rho}'_{av,r} = \frac{\hat{M}'_{2,rp}}{\hat{M}_{2,z}} - \frac{1}{Q}, \quad (5.25)$$

while the estimation of the average SNR yields

$$\hat{\rho}'_{av} = \frac{1}{N_R} \sum_{r=1}^{N_R} \hat{\rho}'_{av,r}. \quad (5.26)$$

5.4. Simulation Results

The performance of the MIMO-PS and MIMO-IPS estimators is evaluated by means of the Monte-Carlo simulations. The parameters of the OFDM system comply with the WiMAX specifications: a 2×2 antenna array, $N = 512$ subcarriers, CP length of 64 samples, and sampling frequency of 7.68MHz (5MHz bandwidth mode), see Appendix B.2. The performance of the estimators is evaluated for four different channel models: AWGN channel and three extended ITU channels given in Appendix A. The number of independent trials is set to $N_t = 100000$ assuring a high confidence level for the estimations. The evaluation of the performance is done in the terms of the normalized MSE (NMSE) of the estimated average SNR values as

$$\text{NMSE}_{av} = \frac{1}{N_t} \sum_{i=1}^{N_t} \left(\frac{\hat{\rho}_{av,i} - \rho_{av}}{\rho_{av}} \right)^2, \quad (5.27)$$

where $\hat{\rho}_{av,i}$ is the estimate of the average SNR in the i th trial and ρ_{av} is the true value. Furthermore, the NMSE of the estimated SNRs per subcarrier is given by

$$\text{NMSE}_{sc} = \frac{1}{N N_t} \sum_{i=1}^{N_t} \sum_{n=0}^{N-1} \left(\frac{\hat{\rho}(n)_i - \rho(n)}{\rho(n)} \right)^2, \quad (5.28)$$

where $\hat{\rho}(n)_i$ is the estimate of $\rho(n)$ in the i th trial.

During the simulation, the MIMO-PS and MIMO-IPS estimators are evaluated for two different numbers of time periodic parts, i.e., $Q = 4$ and 8 . To compare its performance with the Boumard's estimator under the same spectral efficiency conditions, the corresponding versions of the MIMO-PS and MIMO-IPS estimator based on two preambles are also examined. The preamble structure shown in Figure 5.2 can be extended by adding the second preamble at each antenna with an interchanged loaded subcarrier arrangement present at the first preambles. Therefore, SNR estimation at each antenna is achieved by averaging over two preambles such that the performance is improved as shown in Figure 5.7 - Figure 5.10.

Figure 5.3 and Figure 5.4 show the NMSE_{av} as a function of the average SNR for the proposed estimators based on one preamble in AWGN and highly selective ETU channel, respectively. The appropriate performance of the Minimum Mean Square Error (MMSE) estimator, an optimal estimator in an AWGN channel, see [6], is shown as a reference. The MIMO-PS estimator performs identically in both channels, i.e., it is robust to frequency selectivity. Note that the increasing number of identical parts Q brings its performance closer to the MMSE estimator. This behavior can be explained by the fact that more subcarriers are used for the average noise power estimation (5.9) and the transmitted power on the loaded subcarriers is scaled by the Q , thus giving a more accurate estimation in (5.8). Moreover, the accuracy of the MIMO-IPS estimator is better than the one of the MIMO-PS estimator for particular Q values, especially in the low SNR regime. However, this performance improvement caused by the increase of the number of identical parts Q is susceptible to frequency selectivity, i.e., both estimators perform almost identically for $Q = 8$ in the ETU channel.

A similar behavior of the NMSE_{sc} as a function of the SNR in the EPA and ETU channel, is shown in Figure 5.5 and Figure 5.6, respectively. The SNR per subcarrier MIMO-IPS estimator stops to benefit from the increase of Q in high frequency-selective channels due to degrading influence of the interpolation over the nulled subcarriers.

Figure 5.7 and Figure 5.8 compare the NMSE_{av} of the proposed estimators based on two preambles with Boumard's estimator proposed from [8]. The MIMO-PS and MIMO-IPS estimators outperform the Boumard's estimator whose performance is susceptible to frequency selectivity. Furthermore, the performance improvement introduced by the selection of significant CIR paths is particularly noticeable for the NMSE_{sc} vs. SNR curves as shown in Figure 5.9 and Figure 5.10.

The performance of the MIMO-PS and MIMO-IPS estimators can be further improved by combining the average noise power estimation with more sophisticated channel estimation algorithms that use pilot subcarriers within the data symbols.

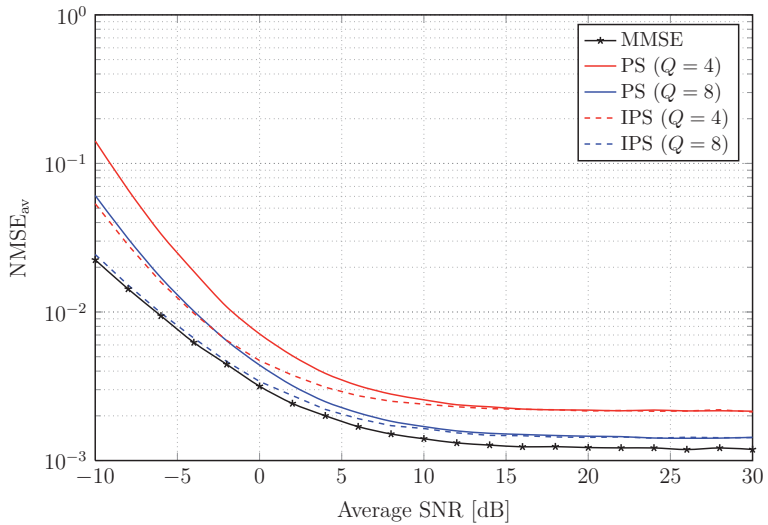


Figure 5.3.: NMSE of the average SNR estimation based on one preamble in AWGN channel.

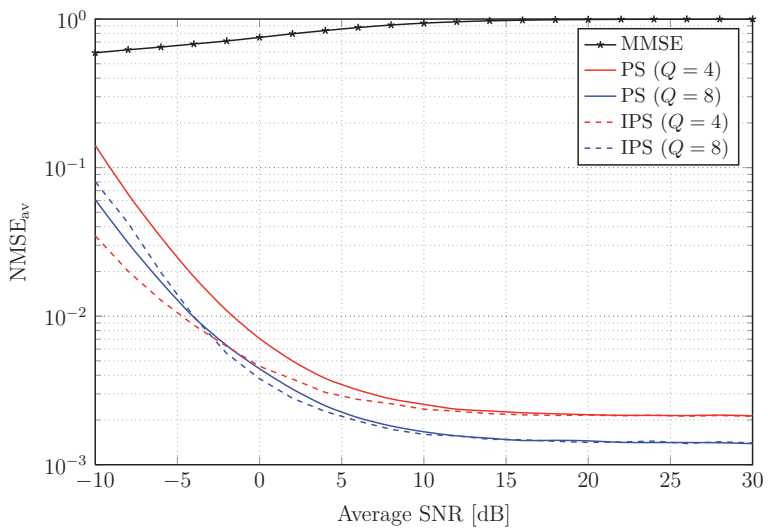


Figure 5.4.: NMSE of the average SNR estimation based on one preamble in the ETU channel.

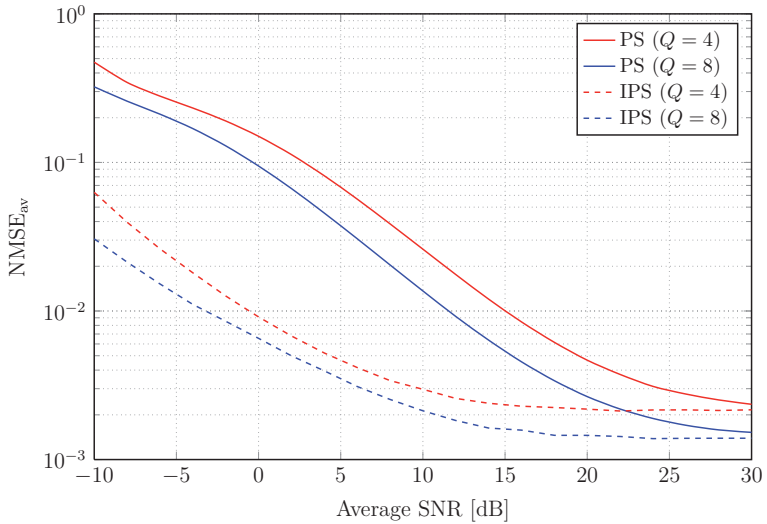


Figure 5.5.: NMSE of the SNR per subcarrier estimation based on one preamble in the EPA channel.

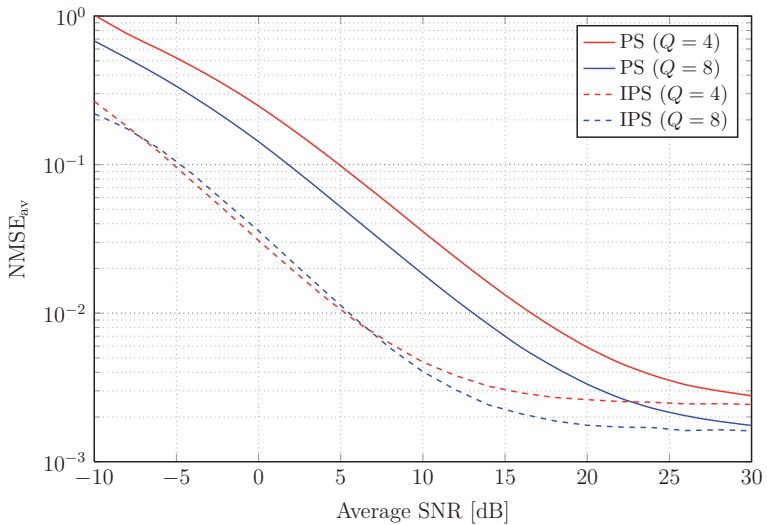


Figure 5.6.: NMSE of the SNR per subcarrier estimation based on one preamble in the ETU channel.

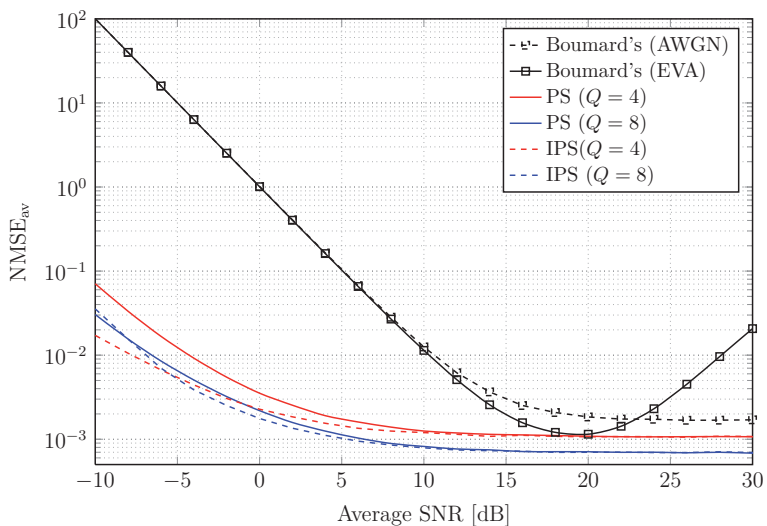


Figure 5.7.: NMSE of the average SNR estimation based on two preambles in the EVA channel.

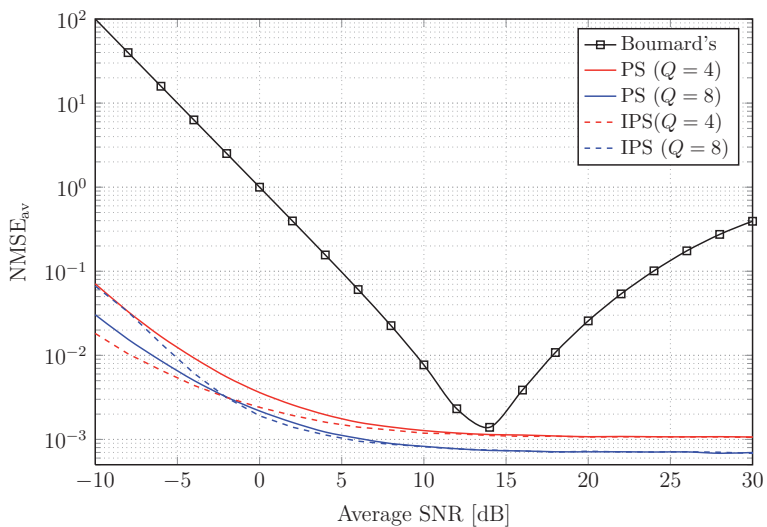


Figure 5.8.: NMSE of the average SNR estimation based on two preambles in the ETU channel.

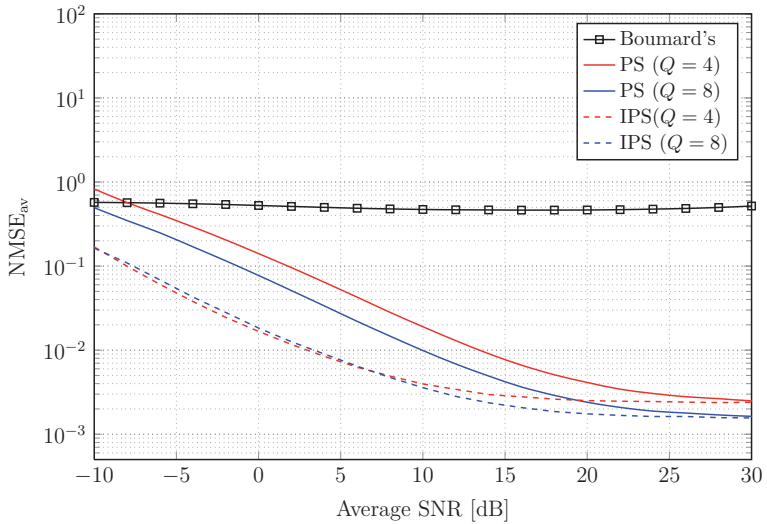


Figure 5.9.: NMSE of the SNR per subcarrier estimation based on two preambles in the EVA channel.

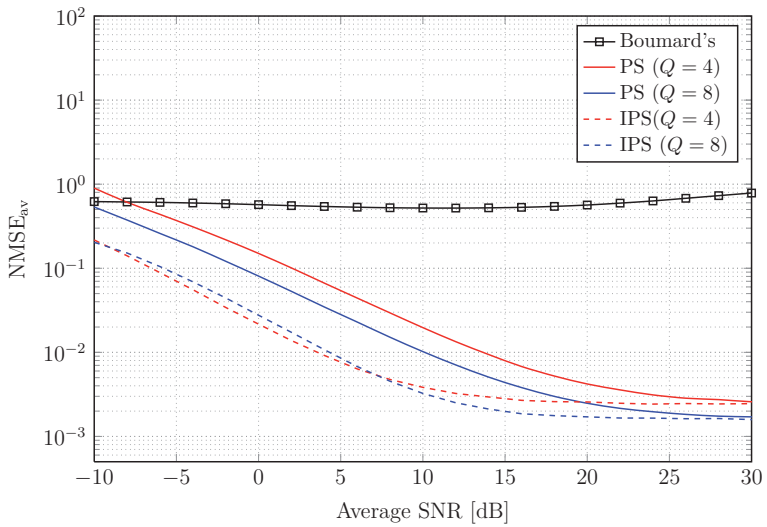


Figure 5.10.: NMSE of the SNR per subcarrier estimation based on two preambles in the ETU channel.

6. Joint Synchronization and Spectrum Characterization in OFDM-based Cognitive Radio Systems

Spectrum efficiency of current wireless systems can be significantly improved by opportunistic sharing of the available frequency band between licensed primary users (PU) and a group of unlicensed secondary users or cognitive radios (CRs) [64]. While monitoring the spectrum of interest, CRs are able to detect the unused portions (*spectrum holes*) and adapt waveform properties according to the dynamically changing environment without introducing harmful interference to the PU. To regulate adaptive cooperative spectrum utilization, the IEEE 802.22 working group initiated the standardization of wireless regional area networks (WRAN) for allowing broadband access in UHF/VHF TV bands between 54 and 862 MHz [65]. The standard, briefly presented in Appendix B.4, also leaves the opportunity for extending spectrum utilization methods within any regulatory regime. Furthermore, due to its flexibility in allocating resources among CRs, OFDM has been shown as a promising candidate for the physical (PHY) layer within the WRAN standard. OFDM is a multicarrier modulation scheme based on division of broadband channel into many narrowband subchannels modulated on different subcarriers. By leaving a set of subchannels unused, OFDM provides a flexible spectral shape that can fill spectral gaps without interfering with the PU.

Standardization efforts for observation, decision, and action of CRs are widely discussed in [65]. One of them is based on Fractional Bandwidth (FBW) usage where the total band is divided into several subbands that can be activated (occupied by CRs) if spectrum sensing indicates the absence of the PUs within them. During the initialization, the OFDM CR receiver first needs to adjust its timing, then to synchronize itself to some appropriate carrier frequency, and, finally, to identify active subbands in order to further process only the subcarriers that belong to them.

After an initial coarse timing estimation, the receiver has to estimate the carrier frequency offset (CFO) that arises due to a potential mismatch between the transmitter and receiver oscillators. In most cases, the CFO may exceed the subcarrier spacing Δf . Therefore, it is customary to divide the CFO into an integer part (integer CFO - ICFO), a multiple of Δf that produces a shift of subcarrier indices, plus a fractional part (fractional CFO - FCFO) that results into interchannel interference (ICI) due to loss of orthogonality among subcarriers. Conventional methods for estimating the fractional offset operate in the time-domain and measure the phase shift between the repetitive parts of dedicated preambles [57]. In contrast, the integer offset is typically estimated in the frequency-domain by loading a known pseudo-noise (PN) sequence over certain subcarriers [66]. This can be extended to mode detection as proposed in [67].

After the acquisition of the carrier frequency the active subbands in an FBW scenario can be reliably identified via a dedicated out-of-band control channel [68]. However, this approach can significantly reduce the bandwidth efficiency, particularly in heavy loaded networks, by increasing the receiver complexity through the need of mutual synchronization among CR receivers. One efficient way to avoid the usage of a control channel is to embed the information of currently used subbands into the structure of data packets. The authors in [67, 68] utilize the synchronization preamble for embedding the information of spectrum usage patterns. Particularly, each CR identifies the FBW mode jointly with the ICFO estimation. However, these methods do not provide any additional characterization of the spectral content that quantifies CR signal quality in active subbands and/or the level of interference in nonactive subbands. Such information can be further exploited for adapting the transmission parameters (bandwidth, coding/data rate, power) to preserve energy and bandwidth efficiency of CR systems. A widely used standard measure of the received signal quality is the signal-to-noise ratio (SNR), as defined in (2.39). Under the FBW scenario, the SNR in active subbands is defined as the ratio of the CR signal power to the noise power. Similarly, the level of interference in nonactive subbands can be characterized by the interference power from the PU signal.

In this chapter, we utilize the time periodic structure of the packet preamble proposed by [57] that allows for the FCFO estimation over a wider CFO range with only one preamble, hence reducing the training symbol overhead. After correcting the FCFO, we modify the method from [67] to exploit the general frequency domain form of the same preamble for joint ICFO estimation and current FBW mode detection. Moreover, we have already shown in [9, 11] that the given preamble structure can be efficiently used for the SNR estimation based on the second order moments of the received preamble samples. The key contribution of this chapter consists in extending our previous work, which leads to a robust and efficient SNR estimation in active subbands and interference power estimation in nonactive subbands under the FBW scenario.

Furthermore, the PU interference is modeled as additive Gaussian noise over subcarriers in nonactive subbands, as proposed in [69]. An additional assumption is that a PU occupies all non active subbands with the same average power and that there is no mutual out-of-band transmission between the PU and CR bands. The results can be easily extended by introducing filtering effects and arbitrary PU occupancy of the deactivated subbands.

Parts of the following results have been presented in [12, 13].

6.1. Fractional Bandwidth (FBW) Scenario

As shown in Figure 6.1, the FBW scenario assumes opportunistic usage of some common bandwidth B where PU signals can appear on a preassigned portion of the band or dynamically change the position within it. After obtaining the information about spectrum occupancy from spectrum sensing, the CR transmitter deactivates (nulls) the subcarriers in the subbands occupied by the PU signals. Moreover, by sensing any change in spectrum occupancy, the proposed CR system can activate previously nulled subbands or null the subbands that are active. As shown in Figure 6.1, the common frequency band B , consisting of N subcarriers, is divided into $M = 8$ subbands, each carrying $N_{BW} = N/M$

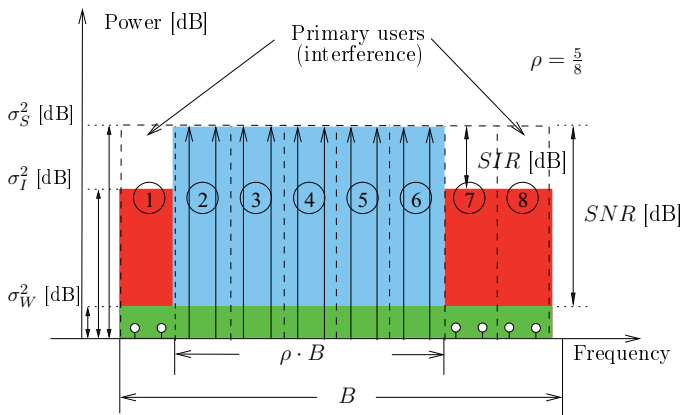


Figure 6.1.: Frequency representation of the considered FBW model.

subcarriers. The total number of activated subbands can vary from 1 to M where only contiguous subbands are allowed to be activated in order to reduce the power leakage in the nulled subbands and mutual interference between PUs and CR [65]. Therefore, in total there are $M_T = \frac{M(M+1)}{2}$ FBW modes with $M_A = 1, 2, \dots, M$ contiguous active subbands. Moreover, *pool allocation* $\rho = M_A/M$ is defined as a parameter that indicates the level of the spectrum utilization of a CR system [70]. In the example shown in Figure 6.1, with $M = 8$ subbands, where a total of $M_T = 36$ FBW modes are supported, currently $M_A = 5$ subbands are active, giving the pool allocation of $\rho = \frac{5}{8} = 0.625$.

The block diagram of a typical CR system with the FBW is shown in Figure 6.2. Given the spectrum sensing results, the CR transmitter loads only the subcarriers of the active subbands while the rest of subcarriers is nulled. Let $C_m(n)$ denote the symbol carried on the n th subcarrier in mode m , for $n = 0, \dots, N-1$, while \mathcal{S}_m is the set of subcarriers belonging to active subbands in the m th mode. Therefore,

$$C_m(n) = \begin{cases} S(n), & n \in \mathcal{S}_m \\ 0, & n \notin \mathcal{S}_m \end{cases}, \quad (6.1)$$

where $\sigma_S^2 = \mathbb{E}\{|S(n)|^2\}$ is the average signal power. Without the loss of generality, we assume that all subcarriers in nonactive subbands are occupied with the interference of equal average power and that there is no interference power leakage to active subbands. The interference on the subcarriers is modeled as a sampled complex zero-mean Gaussian random variable with zero mean and variance σ_I^2 , i.e., $I(n) \sim \mathcal{N}(0, \sigma_I^2)$ [69], thus giving

$$I_m(n) = \begin{cases} 0, & n \in \mathcal{S}_m \\ I(n), & n \notin \mathcal{S}_m \end{cases}. \quad (6.2)$$

Moreover, noise samples are modeled as a complex zero-mean AWGN, $W(n)$, with vari-

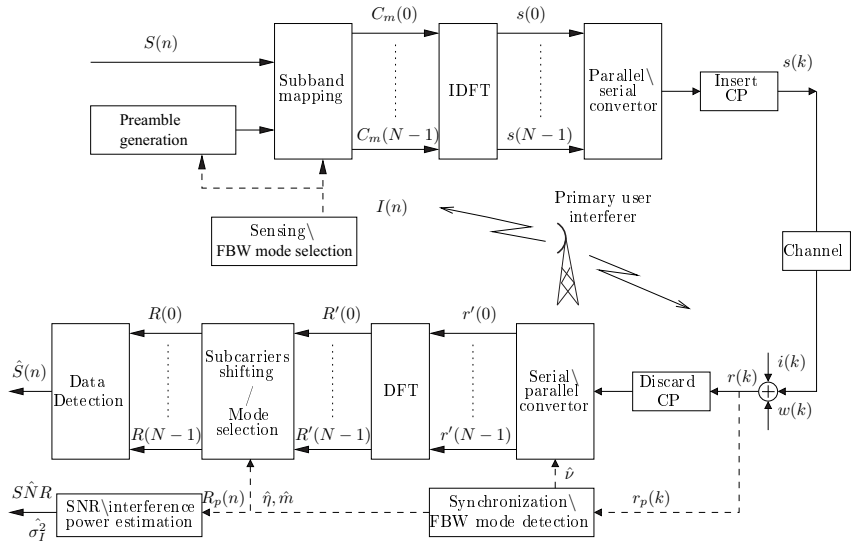


Figure 6.2.: The FBW system model.

ance σ_W^2 , i.e., $W(n) \sim \mathcal{N}(0, \sigma_W^2)$. To simplify the ongoing analysis, without losing generality, we consider an AWGN channel, which is a regular assumption since timing synchronization is performed with sufficiently large cyclic prefix [68]. The spectral content on the subcarriers within the common band then can be written as

$$R(n) = \begin{cases} S(n) + W(n), & n \in \mathcal{S}_m \\ I(n) + W(n), & n \notin \mathcal{S}_m \end{cases}. \quad (6.3)$$

Therefore, we can define the frequency domain average SNR of the received signal in active subbands as

$$SNR = \frac{\sigma_S^2}{\sigma_W^2}. \quad (6.4)$$

Although the desired signal and interference are separated within the common band B , as shown in Figure 6.1, we define the ratio between the average signal power and average interference power as the average signal-to-interference ratio (SIR), denoted as

$$SIR = \frac{\sigma_S^2}{\sigma_I^2}. \quad (6.5)$$

The visual representation of above defined quantities and their relations in the frequency domain are shown in Figure 6.1.

To characterize the received signal in the time domain, we denote N_g as the number of samples in cyclic prefix. At the receiver, the incoming signal after the ADC is

sampled at the rate $f_s = N\Delta f$, where Δf is the subcarrier spacing. Due to the frequency mismatch between the transmitter and receiver oscillator, the frequency f_{LO} of the local oscillator at the CR receiver differs from the received carrier frequency f_c . Let denote $\varepsilon_c = (f_c - f_{LO})/\Delta f$ the CFO normalized to the subcarrier spacing. Assuming the perfect timing synchronization, the received signal in the time domain $r(k)$, for $k = -N_g, \dots, N - 1$, in the presence of the normalized CFO ε_c , is given by

$$\begin{aligned} r(k) &= \frac{e^{j2\pi\varepsilon ck}}{N} \sum_{n=0}^{N-1} R(n)e^{-j2\pi\frac{nk}{N}} \\ &= \frac{e^{j2\pi\varepsilon ck}}{N} \left(\sum_{n \in \mathcal{S}_m} S(n) + \sum_{n \notin \mathcal{S}_m} I(n) \right) e^{-j2\pi\frac{nk}{N}} + \frac{1}{N} \sum_{n=0}^{N-1} W(n)e^{-j2\pi\frac{nk}{N}} \quad (6.6) \\ &= e^{j2\pi\varepsilon ck} \left(s(k) + i(k) \right) + w(k). \end{aligned}$$

We now give the insight into the preamble design issues to facilitate its time and frequency domain structure for the joint CFO synchronization and spectrum occupancy characterization under the FBW scenario.

6.1.1. Preamble Design

In many wireless OFDM systems, transmission is normally organized in frames where a sequence of data symbols is preceded by several preambles of known data used for the synchronization and/or channel estimation purposes. Here, based on the approach taken by the PS and IPS estimators for the average SNR estimation presented in Chapter 4, we use only one preamble proposed by Morelli and Mengali [57]. We utilize the time periodic preamble structure for the FCFO estimation, joint ICFO estimation and mode detection, and, finally, for the SNR and interference power estimation. To cover a wider frequency range, the preamble is divided into Q identical parts, each containing $N_p = N/Q$ samples, as shown in Figure 4.1. It can be seen that such time periodic structure can be created in the frequency domain by loading every Q th subcarrier.

The time domain representation of the preamble having the Q identical parts can be written as

$$s_p(k) = s_p\left(k + q\frac{N}{Q}\right), \quad k = 0, \dots, \frac{N}{Q} - 1, \quad q = 1, \dots, Q - 1.$$

The preamble can be formed in the frequency domain by transmitting a QPSK or PN sequence on every Q th subcarrier in the active subbands, thus giving

$$C_{p,m}(n) = \begin{cases} \sqrt{Q}S_p(n), & n \in \mathcal{S}_{p,m} \\ 0, & n \notin \mathcal{S}_{p,m} \end{cases}, \quad (6.7)$$

where $\mathcal{S}_{p,m}$ presents the set of loaded preamble subcarriers belonging to active subbands of mode m , i.e., $\mathcal{S}_{p,m} \subset \mathcal{S}_m$ while scaling factor \sqrt{Q} is used to ensure the constant average signal energy.

To perform joint ICFO estimation and mode detection using one preamble, the authors in [66, 67] proposed a differential coding structure of loaded subcarriers, which for a given preamble with an arbitrary number of time periodic parts Q can be constructed as

$$S_p(n) = S_p(n - Q) \cdot P_m(n), \quad n \in \mathcal{S}_{p,m} - N_{st,m}. \quad (6.8)$$

Here, $N_{st,m}$ is the index of the first subcarrier of mode m and P_m is the PN sequence used for embedding the information of particular mode m . Prior work in literature [68, 70] emphasized the advantage of using Frank-Zadoff-Chu (FZC) sequences due to their preferable autocorrelation properties and low PAPR behavior in the time domain. Therefore, the FZC sequence used in (6.8) can be accommodated as [70]

$$P_m(n) = (-1)^{m \cdot n/Q} e^{\frac{j\pi mn^2}{\rho_m N Q}}, \quad n \in \mathcal{S}_{p,m}, \quad (6.9)$$

where ρ_m is the pool allocation for the given mode m .

Having this preamble structure, CFO can be decomposed into a fractional part ν that belongs to the interval $(-Q/2, Q/2]$, and an integer part that is a multiple of Q . The normalized CFO is thus given by

$$\varepsilon_c = \nu + \eta Q. \quad (6.10)$$

Clearly, the estimation of η is unnecessary if the maximum value of $|\varepsilon_c|$ is guaranteed to be less than $Q/2$, because, in this case, it yields $\eta = 0$.

6.2. Fractional CFO Estimation

We assume that the initial timing estimation is successfully performed utilizing the sufficiently large cyclic prefix [68]. The next synchronization stage has to correct FCFO utilizing the time domain structure of the received preamble. From (6.6), the received preamble in the time domain in the presence of the normalized frequency offset ε_c can be written as

$$r_p(k) = e^{\frac{j2\pi\varepsilon_c k}{N}} (s_p(k) + i_p(k)) + w_p(k). \quad (6.11)$$

The authors in [57] proposed the best linear unbiased estimator (BLUE) of FCFO that is given by

$$\hat{\nu} = \frac{Q}{2\pi} \sum_{j=1}^{Q/2} w(j) \varphi(j), \quad (6.12)$$

where

$$w(j) = \frac{12(Q-j)(Q-j+1) - 3Q^2}{2Q(Q^2-1)}, \quad (6.13)$$

and $\varphi(j)$ is the angle

$$\varphi(j) = \left[\arg \left\{ \frac{V(j)}{V(j-1)} \right\} \right]_{2\pi}. \quad (6.14)$$

Here, $[x]_{2\pi}$ presents modulo 2π operation and $V(j)$ denotes the correlation of time periodic preamble parts separated by jN/Q samples given by

$$V(j) = \frac{1}{N - jN/Q} \sum_{k=jN/Q}^{N-1} r_p(k) r_p^*(k - j \frac{N}{Q}), \quad 0 \leq j \leq Q/2.$$

After obtaining the FCFO estimate $\hat{\nu}$, the phase corrected preamble samples $r'_p(k)$ can be written as

$$r'_p(k) = r_p(k) e^{-\frac{j2\pi\hat{\nu}k}{N}}. \quad (6.15)$$

6.3. Joint Integer CFO and FBW Mode Estimation

After the perfect FCFO compensation, i.e., $\hat{\nu} = \nu$, the frequency domain form of the phase corrected preamble $R'_p(n) = \text{DFT}_N[r'_p(k)]$ are shifted due to the ICFO presence, thus giving

$$R'_p(n) = \begin{cases} \sqrt{Q}S_p(|n - \eta Q|_N)P_m(|n - \eta Q|_N) + W(n), & n \in \mathcal{S}_{p,m,\eta Q} \\ W(n), & n \in \mathcal{S}_{p,z,\eta Q} \\ I(|n - \eta Q|_N) + W(n), & n \in \mathcal{S}_{p,i,\eta Q} \end{cases},$$

where $|n - \eta Q|_N$ is the value $n - \eta Q$ reduced to the interval $[0, N - 1]$. Here, $\mathcal{S}_{p,m,\eta Q}$ is the set of subcarriers where CR signal is present and that satisfy $\left((n \in \mathcal{S}_{p,m}) \wedge (|n - \eta Q|_N \leq \rho N + N_{st,m} - n) \right) \vee \left((n \notin \mathcal{S}_m) \wedge (|n - \eta Q|_N > \rho N + N_{st,m} - n) \wedge (|n - N_{st,m}|_Q = 0) \right)$. Similarly, $\mathcal{S}_{p,z,\eta Q}$ presents the set of subcarriers with only noise samples for which holds $\left((n \in \mathcal{S}_{z,m}) \wedge (|n - \eta Q|_N \leq \rho N + N_{st,m} - n) \right) \vee \left((n \notin \mathcal{S}_m) \wedge (|n - \eta Q|_N > \rho N + N_{st,m} - n) \wedge (|n - N_{st,m}|_Q \neq 0) \right)$, where $\mathcal{S}_{z,m}$ denote the set of nulled subcarriers that belong to active subbands of mode m , thus $\mathcal{S}_{z,m} = \mathcal{S}_m / \mathcal{S}_{p,m}$. Moreover, $\mathcal{S}_{p,i,\eta Q}$ is the set of subcarriers with the interfering PU signal and that satisfy $\left((n \notin \mathcal{S}_m) \wedge (|n - \eta Q|_N \leq \rho N + N_{st,m} - n) \right) \vee \left((n \in \mathcal{S}_m) \wedge (|n - \eta Q|_N > \rho N + N_{st,m} - n) \right)$.

Utilizing the structure of the appropriately constructed preamble defined in (6.7), the ICFO η and current mode m can be estimated by maximizing the following differential correlation [67, 68]

$$B_m(\hat{\eta}) = \frac{|\sum_{n \in \mathcal{S}_{p,m}} R'_p(n + \eta Q) R_p^{*s}(n + \eta Q + Q) P_m(n + Q)|^2}{(\sum_{n \in \mathcal{S}_{p,m}} |R'_p(n + \eta Q)|^2)^2}, \quad (6.16)$$

which gives estimates

$$(\hat{m}, \hat{\eta}) = \arg \max_{(m, \hat{\eta})} |B_m(\hat{\eta})|^2, \quad (6.17)$$

for $1 \leq m \leq M_T$.

6.4. SNR and Interference Power Estimation

Given the ICFO estimation and mode detection obtained in (6.17), the spectral content characterization can be performed by means of the SNR estimation in active subbands and interference power estimation in nonactive subbands. After shifting the received signal $R'_p(n)$ with the estimated ICFO $\hat{\eta}$, the corrected signal can be written as

$$R_p(n) = R'_p(n + \hat{\eta}Q). \quad (6.18)$$

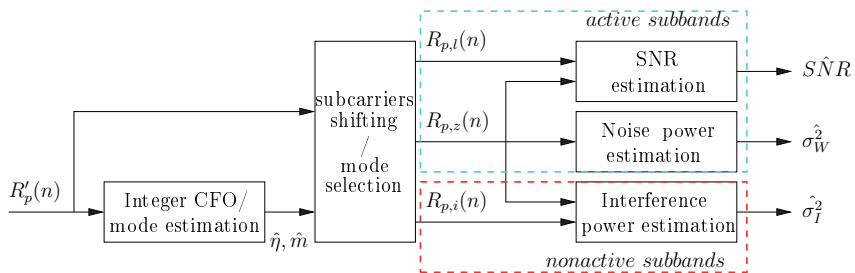


Figure 6.3.: Block diagram of the SNR and interference power estimator.

Assuming the perfect FCFO and ICFO estimation and mode detection, i.e., $\hat{\nu} = \nu$, $\hat{\eta} = \eta$, and $\hat{m} = m$, respectively, the received preamble can be written as

$$R_p(n) = \begin{cases} R_{p,l}(n), & n \in \mathcal{S}_{p,m} \\ R_{p,z}(n), & n \in \mathcal{S}_{z,m} \\ R_{p,i}(n), & n \notin \mathcal{S}_m \end{cases} \quad (6.19)$$

where

$$R_{p,l}(n) = \sqrt{Q}S_p(n)P_m(n) + W(n) \quad (6.20)$$

denote the received signal on the loaded subcarriers of active mode m . Further,

$$R_{p,z}(n) = W(n) \quad (6.21)$$

denote the received signal on the nulled subcarriers of active mode m , and

$$R_{p,i}(n) = I(n) + W(n) \quad (6.22)$$

is the received signal in nonactive subband.

We extend the preamble-based method for the average SNR estimation from Chapter 4 such that the empirical second order moment of the received signal on the loaded subcarriers in active subbands can be expressed as

$$\hat{M}_{2,l} = \frac{Q}{\rho N} \sum_{n \in \mathcal{S}_{p,m}} |R_{p,l}(n)|^2, \quad (6.23)$$

with the expected value $E\{\hat{M}_{2,l}\} = Q\sigma_S^2 + \sigma_W^2$. Similarly, the empirical second order moment of the received signal on the nulled subcarriers in active subbands is given by

$$\hat{M}_{2,z} = \frac{Q}{\rho N(Q-1)} \sum_{n \in \mathcal{S}_{z,m}} |R_{p,z}(n)|^2 \quad (6.24)$$

with the expectation $E\{\hat{M}_{2,z}\} = \sigma_W^2$. Finally, the empirical second order moment of the received signal on subcarriers in nonactive subbands can be written as

$$\hat{M}_{2,i} = \frac{1}{(1-\rho)N} \sum_{n \notin \mathcal{S}_m} |R_{p,i}(n)|^2 \quad (6.25)$$

with the expected value $E\{\hat{M}_{2,i}\} = \sigma_I^2 + \sigma_W^2$.

As shown in [9, 11], the average SNR can be estimated as

$$\begin{aligned} S\hat{N}R &= \frac{1}{Q} \frac{\hat{M}_{2,l} - \hat{M}_{2,z}}{\hat{M}_{2,z}} \\ &= \frac{1}{Q} \left((Q-1) \frac{\sum_{n \in S_{p,m}} |R_{p,l}(n)|^2}{\sum_{n \in S_{z,m}} |R_{p,z}(n)|^2} - 1 \right), \end{aligned} \quad (6.26)$$

where, by the strong law of large numbers, $\hat{M}_{2,l}$ and $\hat{M}_{2,z}$ are strongly consistent unbiased estimators of $Q\sigma_S^2 + \sigma_W^2$ and average noise power σ_W^2 , respectively. Similarly, the interference power σ_I^2 can be estimated as

$$\begin{aligned} \hat{\sigma}_I^2 &= \hat{M}_{2,i} - \hat{M}_{2,z} \\ &= \frac{1}{N} \left(\frac{1}{1-\rho} \sum_{n \notin S_m} |R_{p,i}(n)|^2 - \frac{Q}{\rho(Q-1)} \sum_{n \in S_{z,m}} |R_{p,z}(n)|^2 \right). \end{aligned} \quad (6.27)$$

The block diagram of the proposed estimators is shown in Figure 6.3

6.5. Simulation Results

The performance of the proposed preamble-based joint frequency estimation and spectrum occupancy characterization method in cognitive radio systems under the FBW scenario is evaluated using Monte-Carlo simulation. We assume that timing synchronization is already performed while the CR channel is considered as AWGN, which is a regular assumption because the cyclic prefix is sufficiently large. However, the straightforward extension to other types of channels can be conducted. It is further assumed that the total number of subcarriers is 1024 according to the WRAN (IEEE 802.22) standard [65], see Appendix B.4.

The available band is divided into $M = 8$ subbands, where the lowest mode corresponds to the pool allocation $\rho = 0.125$, while the highest mode $\rho = 1$ corresponds to the absence of the PU when CR occupies the whole band. We consider a different number of time periodic parts, i.e., $Q = 2, 4$, and 8 . Furthermore, the normalized CFO is taken to be $\varepsilon_c = 8.5$, which corresponds to $\nu = 0.5$ and $\eta = 4, 2$, and 1 for $Q = 2, 4$, and 8 , respectively. The accuracy of the FCFO estimation is measured in the terms of the mean square error (MSE), which is defined as $E\{|\hat{\mu} - \mu|^2\}$.

Figure 6.4 shows the performance of the MSE vs. ρ for $Q = 2, 4$, and 8 . The SIR is chosen to be -6 and -10 dB while the SNR is fixed to 6 dB. The MSE decreases with ρ and there are slight variations of the MSE with respect to Q for both SIR values.

The ICFO and mode detection error probabilities, defined as $\Pr(\hat{\eta} \neq \eta)$ and $\Pr(\hat{m} \neq m)$, respectively, are shown in Figure 6.5. Because they are obtained from the joint maximization of differential correlation defined in (6.16), their performance overlap along all considered values of the given parameters. For SIR = -6 dB, the cases when $Q = 4, 8$ perform almost the same and outperform the case when $Q = 2$ while the error probabilities drop below 10^{-3} even for the $\rho = 0.375$. Similarly, for SIR = -10 dB the error probabilities

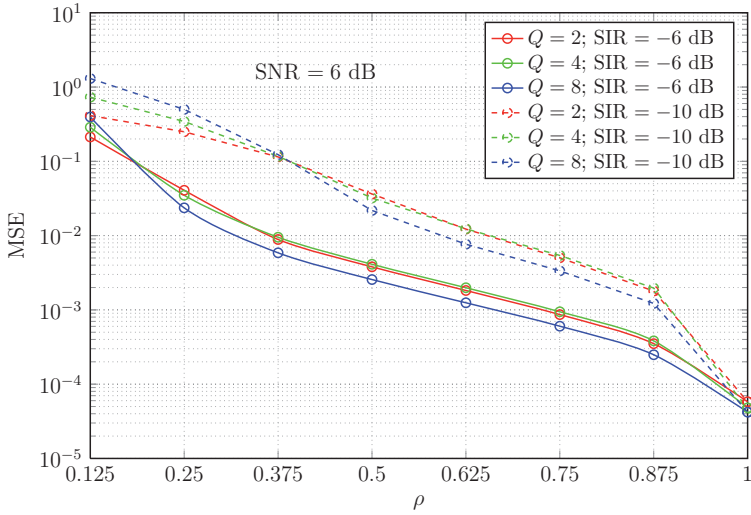


Figure 6.4.: MSE vs. pool allocation for SNR = 6 dB at SIR = -6 dB and -10 dB.

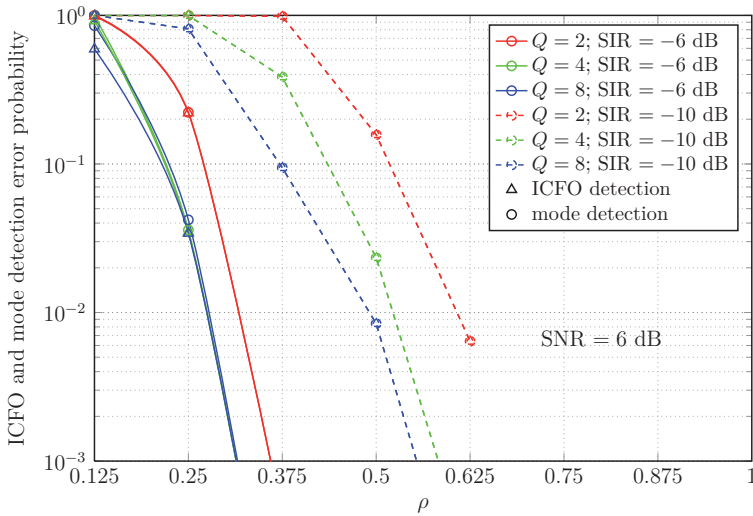


Figure 6.5.: ICFO and mode detection error probability vs. pool allocation for SNR = 6 dB at SIR = -6 dB and -10 dB.

are smaller than 10^{-3} , starting from $\rho = 0.625$ and $\rho = 0.75$ for $Q = 4, 8$ and $Q = 2$, respectively.

The SNR estimation is evaluated in the terms of the normalized MSE, or NMSE(SNR), defined as $E\{(\frac{S\hat{N}R - SNR}{SNR})^2\}$, while $NMSE(\sigma_I^2)$, defined as $E\{(\frac{\hat{\sigma}_I^2 - \sigma_I^2}{\sigma_I^2})^2\}$, is used as the performance measure for the interference power estimation. Figure 6.6 and Figure 6.7 show the NMSE(SNR) vs. ρ for the fixed SNR = 6 dB and SIR = -6 dB and SIR = -10 dB, respectively. Two cases are analyzed here: the first case considers the perfect ICFO estimation and mode detection, while the second case assumes that those estimates are jointly obtained using (6.17). As expected, the increase of Q improves the performance. For SIR = -6 dB the performance of both cases overlaps starting from $\rho = 0.375$, which agrees to the detection error performance depicted in Figure 6.5. Similar behavior can be noticed for SIR = -10 dB.

Figure 6.8 and Figure 6.9 show the $NMSE(\sigma_I^2)$ vs. ρ performance for the same set of parameters which are considered in the SNR estimation analysis. As it is expected, increasing Q improves the performance due to the increased number of available noise samples in active subbands, thus making (6.24) more accurate. Additionally, when ρ increases, there are two opposite effects that influence the performance, because for both SIR values there is a certain value of ρ up to which the $NMSE(\sigma_I^2)$ decreases and continuing to increase afterwards. This can be explained by the change of the number of available samples, which determine the accuracy of the estimates $\hat{M}_{2,i}$ and $\hat{M}_{2,z}$, defined in (6.24) and (6.25), respectively. This value is additionally determined by the actual SIR value and, in contrast to the SNR estimation, is shown to be very sensitive to previously performed ICFO estimation and mode detection.

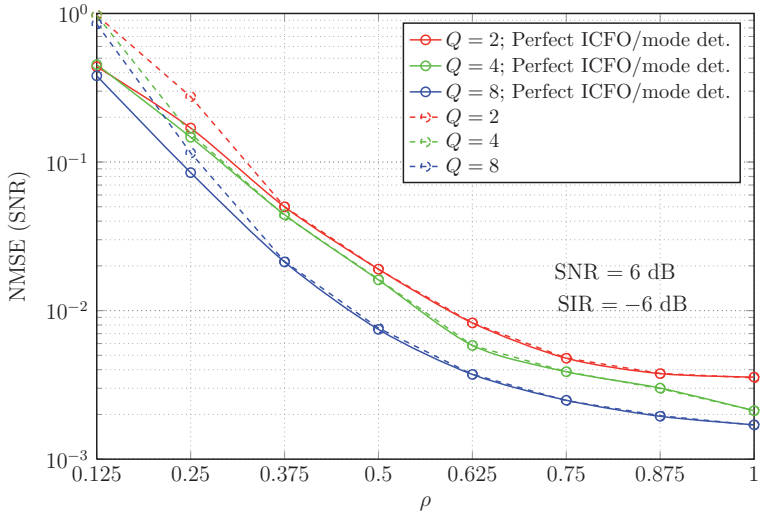


Figure 6.6.: NMSE(SNR) vs. pool allocation for SNR = 6 dB and SIR = -6 dB.

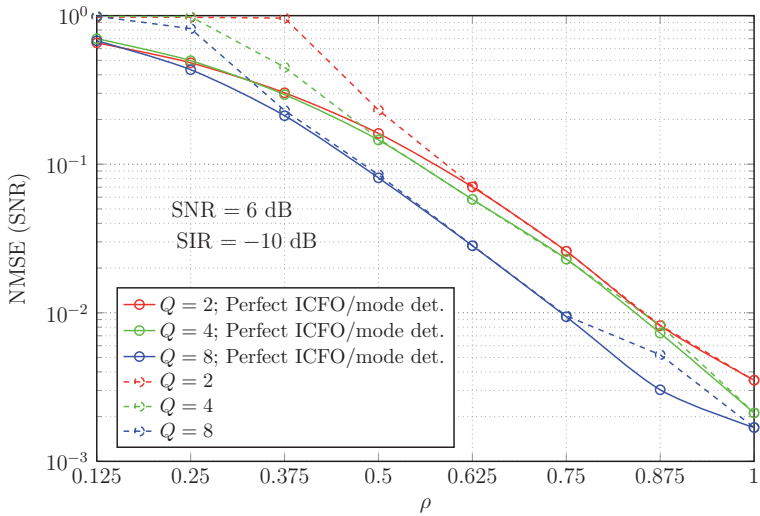
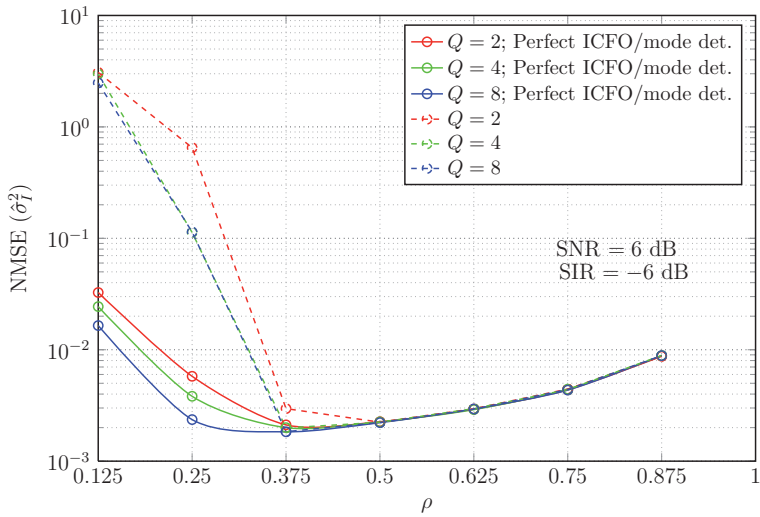
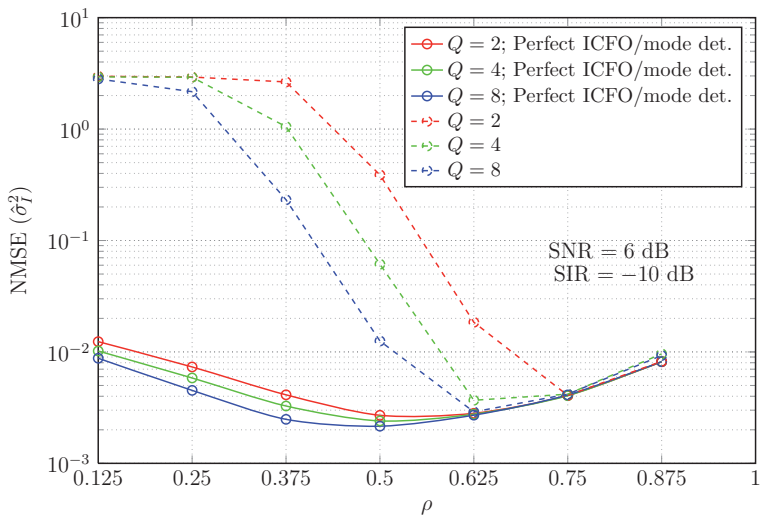


Figure 6.7.: NMSE(SNR) vs. pool allocation for SNR = 6 dB and SIR = -10 dB.

Figure 6.8.: $\text{NMSE}(\hat{\sigma}_I^2)$ vs. pool allocation for $\text{SNR} = 6$ dB and $\text{SIR} = -6$ dB.Figure 6.9.: $\text{NMSE}(\hat{\sigma}_I^2)$ vs. pool allocation for $\text{SNR} = 6$ dB and $\text{SIR} = -10$ dB.

7. Resource Allocation in the Presence of Synchronization Errors

As addressed in Chapter 2, after the initial coarse timing estimation, the receiver has to estimate the carrier frequency offset (CFO), which arises due to the mismatch between the transmitter and receiver oscillators. Synchronization is commonly split into an acquisition stage followed by a tracking phase [41]. Acquisition, also called coarse synchronization, obtains the initial estimates of the synchronization parameters by exploiting the time-domain repetitive structure of a training sequence (preamble) placed at the beginning of the data frame [33, 43, 57, 71]. In this way, the initial CFO is obtained and compensated in the time domain prior to the Discrete Fourier Transform (DFT), thus suppressing the inter-carrier interference (ICI).

However, due to the estimation errors, the received signal may still be corrupted with the residual CFO and sampling frequency offset (SFO) [72]. The residual CFO causes the ICI and constant phase shift over all subcarriers [73, 74], as addressed in Chapter 2. Moreover, the SFO is an additional source of the ICI and introduces the phase drift proportional to the subcarrier index, thereby affecting each subcarrier differently.

The joint tracking of the residual CFO and SFO over OFDM data symbols is required for the compensation of this effects. Most of the tracking algorithms available in the literature utilize the dedicated pilot subcarriers to facilitate the synchronization tasks at the receiver [80]-[81]. The phases of the received pilot subcarriers are first extracted and then averaged over pilot subcarriers and/or over several OFDM symbols to obtain the residual CFO and the phase slope introduced by the SFO.

In this chapter, we investigate a particular synchronization stage implemented within the TIGR framework while focusing on its influence on the OFDM system performance. We address the performance degradation caused by the CFO and SFO compensation through the concept of the SNR loss. Since the final system performance is determined by the variance of the considered estimators, we further derive the rate-power functions that reflect those impairments. Based on this results, we compare the sensitivity of several resource allocation algorithms addressed in Chapter 3 in an imperfectly synchronized OFDM system by means of Monte-Carlo simulation.

Moreover, as discussed in [82, 83], for an imperfectly synchronized system the CFO and SFO affect the accuracy of an SNR estimation method. In this chapter, we further investigate the performance of the PS estimator in the presence of the CFO and SFO and derive the appropriate analytical model. Finally, we analyze the performance of various resource allocation algorithms discussed in Chapter 3 in the case of the imperfect SNR estimation in an OFDM system with synchronization impairments.

7.1. SNR Degradation

The impact of the CFO and SFO on the system performance has been extensively studied in the literature through the introduction of the SNR loss [84, 85]. We present this analysis and focus on the influence of the introduced SNR loss on the performance of the resource allocation algorithms.

As derived in Subsection 2.5.2, according to (2.61), the received signal in the presence of the CFO and SFO is given by

$$R_i(n) = e^{j2\pi i N t \phi_n / N} H(n) C_i(n) f_N(\phi_n) + I_i(n, \varepsilon_c, \varepsilon_s) + W_i(n), \quad (7.1)$$

where the time index $i = 0$ stands for the estimation preamble and is omitted for simplification purposes while $I_i(n, \varepsilon_c, \varepsilon_s)$ in (2.62) accounts for the ICI. Depending on the values for ε_s and ε_c , we consider four different cases that determine the quality of the received signal.

a) The joint presence of the SFO and CFO, i.e., $\varepsilon_s, \varepsilon_c \neq 0$

To quantify the influence of the ICI on the received signal, we assume $E\{|H(n)|^2\} = 1$ and $E\{|C_i(n)|^2\} = 1$. For a large number of subcarriers, the interference term $I_i(n, \varepsilon_c, \varepsilon_s)$ can be reasonably modeled as a circularly symmetric complex zero-mean AWGN with the variance given by

$$\sigma_I^2(n, \varepsilon_c, \varepsilon_s) = E\{|I_i(n, \varepsilon_c, \varepsilon_s)|^2\} = \sigma_S^2 \sum_{\substack{m=-\frac{N}{2} \\ m \neq n}}^{\frac{N}{2}-1} |f_N(\phi_m + m - n)|^2. \quad (7.2)$$

Under the assumption that the identity

$$\sum_{m=-\frac{N}{2}}^{\frac{N}{2}-1} |f_N(\phi_m + m - n)|^2 = 1 \quad (7.3)$$

holds true for all subcarriers independently of ε_c , the interference power (7.2) can be then written as

$$\sigma_I^2(n, \varepsilon_c, \varepsilon_s) = \sigma_S^2 (1 - |f_N(\phi_n)|^2). \quad (7.4)$$

From (2.38), the SNR on the n th subcarrier in the joint presence of the CFO and SFO is defined as the ratio of the signal power attenuated with the factor $|f_N(\phi_n)|^2$ to the power of the joint contribution of the AWGN noise and ICI, which is given by

$$\begin{aligned} \rho_{FO}(n) &= \frac{E\{|H(n)|^2 |C(n)|^2 |f_N(\phi_n)|^2\}}{E\{|I(n, \varepsilon_c, \varepsilon_s) + W(n)|^2\}} \\ &= \frac{\sigma_S^2 E\{|H(n)|^2\} |f_N(\phi_n)|^2}{E\{|I_i(n, \varepsilon_c, \varepsilon_s)|^2\} + E\{|W(n)|^2\}} \\ &= \frac{\rho(n) |f_N(\phi_n)|^2}{1 + \rho_{av}(1 - |f_N(\phi_n)|^2)}, \end{aligned} \quad (7.5)$$

where $\rho(n)$ is the SNR on the n th subcarrier at the ideal transceiver. Using the Taylor series expansion of $|f_N(\phi_n)|^2$ around $\phi_n = 0$, given by [29], it yields

$$\begin{aligned} |f_N(\phi_n)|^2 &\approx 1 - \frac{1}{3}\pi^2\phi_n^2 \\ &\approx 1 - \frac{1}{3}\pi^2(\varepsilon_c + n\varepsilon_s)^2. \end{aligned} \quad (7.6)$$

The expression (7.5) can be then written as

$$\begin{aligned} \rho_{FO}(n) &= \frac{\rho(n) \left(1 - \frac{1}{3}\pi^2(\varepsilon_c + n\varepsilon_s)^2\right)}{1 + \frac{1}{3}\rho_{av}\pi^2(\varepsilon_c + n\varepsilon_s)^2} \\ &\approx \frac{\rho(n)}{1 + \frac{1}{3}\rho_{av}\pi^2(\varepsilon_c + n\varepsilon_s)^2}. \end{aligned} \quad (7.7)$$

The corresponding SNR loss on the n th subcarrier, denoted as $\gamma(n)$, is defined as the ratio of the ideal SNR per subcarrier $\rho(n)$ and the SNR on the n th subcarrier in the presence of the CFO and SFO, which yields

$$\begin{aligned} \gamma_{FO}(n) &= \frac{\rho(n)}{\rho_{FO}(n)} \\ &\approx 1 + \frac{1}{3}\rho_{av}\pi^2(\varepsilon_c + n\varepsilon_s)^2. \end{aligned} \quad (7.8)$$

From (7.8), it can be seen that the SNR loss on the n th subcarrier differs on each subcarrier and is independent on the individual SNR on the n th subcarrier, but depends on the average SNR and the CFO and SFO value. Moreover, the average SNR in the presence of the CFO and SFO can be written as

$$\begin{aligned} \rho_{FO,av} &= \frac{1}{N} \sum_{n=-\frac{N}{2}}^{\frac{N}{2}-1} \rho_{FO}(n) \\ &= \frac{1}{N} \sum_{n=-\frac{N}{2}}^{\frac{N}{2}-1} \frac{\rho(n)}{1 + \frac{1}{3}\rho_{av}\pi^2(\varepsilon_c + n\varepsilon_s)^2}, \end{aligned} \quad (7.9)$$

while the average SNR loss $\gamma_{FO,av}$ is given by

$$\begin{aligned} \gamma_{FO,av} &= \frac{\rho_{av}}{\rho_{FO,av}} \\ &= \frac{N\rho_{av}}{\sum_{n=-\frac{N}{2}}^{\frac{N}{2}-1} \frac{\rho(n)}{1 + \frac{1}{3}\rho_{av}\pi^2(\varepsilon_c + n\varepsilon_s)^2}}. \end{aligned} \quad (7.10)$$

b) SFO is present, no CFO, i.e., $\varepsilon_s \neq 0$, $\varepsilon_c = 0$

Figure 2.11 shows the block scheme of the basic OFDM receiver. It can be seen that the CFO is typically compensated prior to the DFT block assuming the sufficiently wide

frequency range of the CFO estimator. We discuss in the following section that the residual CFO depends on the true SNR and DFT length N . For the large value of N , the residual CFO becomes much lower than the SFO so that it can be neglected in the performance analysis. In the absence of the CFO, i.e., $\varepsilon_c = 0$, for a given SFO ε_s from (2.63), it yields $\phi_n = n\varepsilon_s$. The SNR on the n th subcarrier is then given by

$$\begin{aligned}\rho_{SFO}(n) &= \frac{\rho(n) \left(1 - \frac{1}{3}\pi^2 n^2 \varepsilon_s^2\right)}{1 + \frac{1}{3}\rho_{av}\pi^2 n^2 \varepsilon_s^2} \\ &\approx \frac{\rho(n)}{1 + \frac{1}{3}\rho_{av}\pi^2 n^2 \varepsilon_s^2}.\end{aligned}\quad (7.11)$$

The corresponding SNR loss on the n th subcarrier, denoted as $\gamma_{SFO}(n)$, can be written as

$$\begin{aligned}\gamma_{SFO}(n) &= \frac{\rho(n)}{\rho_{FCFO}(n)} \\ &\approx 1 + \frac{1}{3}\rho_{av}\pi^2 n^2 \varepsilon_s^2.\end{aligned}\quad (7.12)$$

Following the same approach as in (7.9), the average SNR in the presence of the SFO is given by

$$\begin{aligned}\rho_{SFO,av} &= \frac{1}{N} \sum_{n=-\frac{N}{2}}^{\frac{N}{2}-1} \rho_{SFO}(n) \\ &= \frac{1}{N} \sum_{n=-\frac{N}{2}}^{\frac{N}{2}-1} \frac{\rho(n)}{1 + \frac{1}{3}\rho_{av}\pi^2 n^2 \varepsilon_s^2},\end{aligned}\quad (7.13)$$

while the average SNR loss $\gamma_{SFO,av}$ can be written as

$$\begin{aligned}\gamma_{SFO,av} &= \frac{\rho_{av}}{\rho_{SFO,av}} \\ &= \frac{N\rho_{av}}{\sum_{n=-\frac{N}{2}}^{\frac{N}{2}-1} \frac{\rho(n)}{1 + \frac{1}{3}\rho_{av}\pi^2 n^2 \varepsilon_s^2}}.\end{aligned}\quad (7.14)$$

From (7.12), it can be seen that the SNR loss on the n th subcarrier is proportional to the normalized SFO ε_s and to the square of the subcarrier index n . Figure 7.1 shows the average SNR loss of the subcarrier $n = 200$ as a function of ε_s . Each curve represents a particular modulation scheme and corresponds to the real SNR value required to achieve $\text{BER} = 10^{-3}$, given in Table 3.1. There are the two sets of curves: the first set without the marks corresponds to an ideal transceiver with the SFO as the only impairment; the second set with the marks corresponds to a transceiver with the LS channel estimation in the presence of the SFO. Clearly, due to the higher SNR demands for achieving the same BER (see Table 3.1), the impact of the SFO on the SNR loss is more critical for a non-ideal transceiver, e.g., for $\varepsilon_s = 10^{-4}$ (100 ppm), the SNR loss of 16-QAM at the transceiver with the LS channel estimation is approximately 0.4 dB higher compared to the SNR loss at an ideal transceiver, with the same value of the SFO.

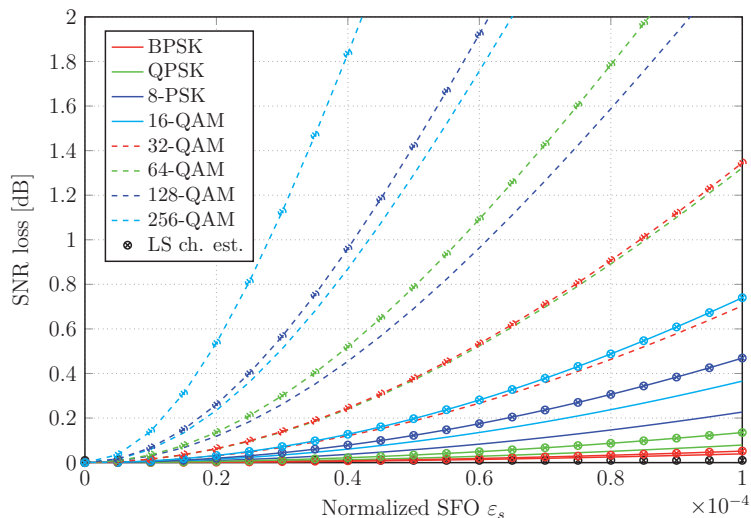


Figure 7.1.: SNR loss vs. normalized SFO ε_s for $\varepsilon_c = 0$ at the subcarrier $n = 200$ in an AWGN channel for $N = 512$ and $\text{BER} = 10^{-3}$.

c) No SFO, the presence of non-integer (fractional) CFO, i.e., $\varepsilon_s = 0$, $\varepsilon_c \notin \mathbb{Z}$

For the academic purposes we now neglect the presence of the SFO and assume that the CFO takes a non-integer value, i.e., $\varepsilon_c \notin \mathbb{Z}$, where \mathbb{Z} is the set of integer numbers. In this case, the power from each individual subcarrier leaks over the adjacent subcarriers resulting in a loss of their mutual orthogonality. In the absence of the SFO, for the given CFO ε_c , from (2.63) it yields $\phi_n = \varepsilon_c$. The SNR on the n th subcarrier can be written as

$$\begin{aligned} \rho_{FCFO}(n) &= \frac{\rho(n) \left(1 - \frac{1}{3}\pi^2 \varepsilon_c^2\right)}{1 + \frac{1}{3}\rho_{av}\pi^2 \varepsilon_c^2} \\ &\approx \frac{\rho(n)}{1 + \frac{1}{3}\rho_{av}\pi^2 \varepsilon_c^2}. \end{aligned} \quad (7.15)$$

The corresponding SNR loss on the n th subcarrier, denoted as $\gamma_{FCFO}(n)$, is given by

$$\begin{aligned} \gamma_{FCFO}(n) &= \frac{\rho(n)}{\rho_{FCFO}(n)} \\ &\approx 1 + \frac{1}{3}\rho_{av}\pi^2 \varepsilon_c^2. \end{aligned} \quad (7.16)$$

The SNR loss is constant among subcarriers and approximately proportional to the square of the normalized CFO ε_c .

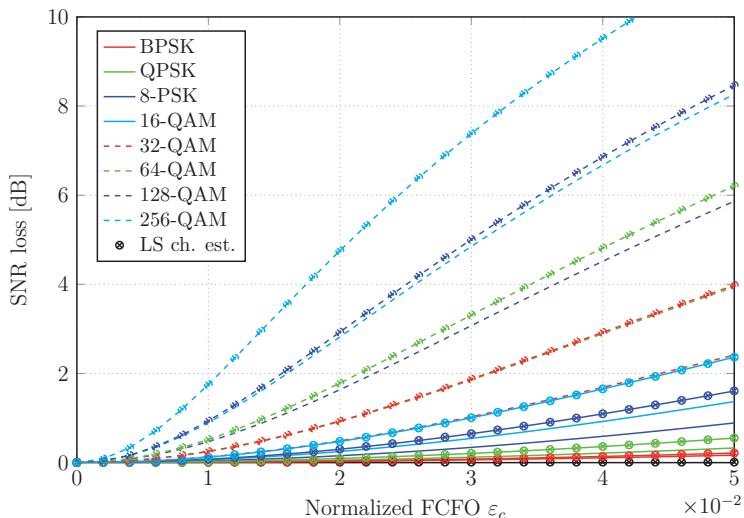


Figure 7.2.: SNR loss vs. normalized CFO ε_c for $\varepsilon_s = 0$ in an AWGN channel for $N = 512$ and $\text{BER} = 10^{-3}$.

The average SNR in the presence of the fractional CFO can be written as

$$\begin{aligned} \rho_{FCFO,av} &= \frac{1}{N} \sum_{n=-\frac{N}{2}}^{\frac{N}{2}-1} \rho_{FCFO}(n) \\ &\approx \frac{\rho_{av}}{1 + \frac{1}{3}\rho_{av}\pi^2\varepsilon_c^2}, \end{aligned} \quad (7.17)$$

while the average SNR loss $\gamma_{FCFO,av}$ is given by

$$\begin{aligned} \gamma_{FCFO,av} &= \frac{\rho_{av}}{\rho_{FCFO,av}} \\ &\approx 1 + \frac{1}{3}\rho_{av}\pi^2\varepsilon_c^2. \end{aligned} \quad (7.18)$$

From (7.16) and (7.18), it can be seen that the SNR loss is constant over subcarriers and is equal to the average SNR loss. Figure 7.2 shows the average SNR loss as a function of ε_c . Similar to the previous case, the impact of the CFO on the SNR loss is more critical for a non-ideal transceiver, e.g., for $\varepsilon_c = 5 \cdot 10^{-2}$, the SNR loss of 64-QAM and 16-QAM at the transceiver with the LS estimation is approximately 2 dB and 1 dB higher compared to the SNR loss at an ideal transceiver, respectively.

d) No SFO, CFO is an integer multiple of Δf , i.e., $\varepsilon_s = 0$, $\varepsilon_c \in \mathbb{Z}$

We now assume that the SFO is absent and that the CFO is an integer multiple of subcarrier spacing Δf , i.e., $\varepsilon_c \in \mathbb{Z}$. Here (2.58) reduces to

$$R_i(n) = e^{j\psi_i} H(|n - \varepsilon_c|_N) C_i(|n - \varepsilon_c|_N) + W_i(n), \quad (7.19)$$

where $|n - \varepsilon_c|_N$ is the value of $n - \varepsilon_c$ reduced to the interval $[0, N - 1]$. This equation indicates that an integer frequency offset preserves the orthogonality among subcarriers and only results into a shift of the subcarrier indexes by the quantity ε_c . The DFT output on the n th subcarrier presents an attenuated and phase-rotated version of $C_i(|n - \varepsilon_c|_N)$ rather than of $C_i(n)$, which results in BER of 0.5. Therefore, in the presence of an integer CFO (ICFO), an appropriate ICFO estimation method has to be applied.

However, several CFO estimation methods from the literature provide a frequency offset estimation range larger than one [57]. Assuming that the transmitter and receiver oscillators operate within this range, the ICFO estimation may be avoided, thus reducing the receiver complexity.

7.2. Estimation of Synchronization Impairments

During the design of TIGR, we assumed a sufficiently long time-periodic preamble such that the robustness of the Schmidl and Cox estimator (SCE) [43] allows for neglecting the residual effects of the symbol timing offset (STO) estimation. Moreover, to compensate the effects of the CFO, we implemented the estimator proposed by Morelli and Mengali in [57] as the best linear unbiased estimator (BLUE) [86, 62]. The advantages of utilizing Morelli's estimator within the TIGR framework are twofolds. At first, it is based on the time periodic structure of preamble that allows for the extension of the estimation range of the normalized CFO from $[-1, 1]$, to $[-\frac{Q}{2}, \frac{Q}{2}]$, where Q is the number of identical parts. The extended estimation range enables us to avoid the integer CFO (ICFO) estimation and thus to reduce the computational complexity of the receiver. Secondly, as it was discussed in Chapter 4, the time periodic preamble structure is also utilized for the design of an effective SNR estimator. In this way, an additional data overhead is avoided while preserving the good performance. We present the theoretical model of the Morelli's CFO estimator, and compare the corresponding analytical expressions with the simulation results regarding its performance. We show that the resulting residual CFO is sufficiently small such that the performance of the PS SNR estimator is not affected.

Furthermore, the presence of the residual CFO and SFO requires joint phase tracking and compensation over the OFDM data symbols. Most of the state-of-the-art methods [45, 72, 76, 87, 88] are based on the processing of the phase difference between the transmitted and received symbols located at the predetermined subcarriers, known as pilot subcarriers. Within the design of the TIGR we implement the linear least square (LLS) estimator proposed by Hwang in [81]. According to the study on the residual CFO and SFO estimators, given in [77], the LLS estimator offers satisfying performance for a sufficiently large number of pilot subcarriers, while preserving the low computational complexity. The implementation advantages are based on the fact that LLS estimator exploits the pilot subcarriers from one OFDM symbol while other estimators are either

based on grid-search methods or utilize the two or more adjacent OFDM symbols to derive one estimate.

7.2.1. CFO Estimation

As given in (2.54), the received preamble in the time domain, in the presence of the CFO ε_c can be written as

$$r(k) = e^{\frac{j2\pi\varepsilon_c k}{N}} y(k) + w(k). \quad (7.20)$$

Here, we assume that $\varepsilon_s = 0$ and an AWGN channel is applied since the performance of the considered estimator is independent of the channel frequency response.

Authors in [57] proposed a BLUE of the CFO given by

$$\hat{\varepsilon}_c = \frac{Q}{2\pi} \sum_{j=1}^{Q/2} \nu(j) \psi(j) \quad (7.21)$$

where

$$\nu(j) = \frac{12(Q-j)(Q-j+1) - 3Q^2}{2Q(Q^2-1)} \quad (7.22)$$

and $\psi(j)$ is the angle

$$\psi(j) = \left[\arg \left\{ \frac{V(j)}{V(j-1)} \right\} \right]_{2\pi}. \quad (7.23)$$

Here $[x]_{2\pi}$ presents the modulo 2π operation and $V(j)$ is the correlation of time periodic preamble parts separated by jN/Q samples given by

$$V(j) = \frac{1}{N - jN/Q} \sum_{k=jN/Q}^{N-1} r(k)r^*(k - j\frac{N}{Q}), \quad 0 \leq j \leq Q/2.$$

After obtaining the CFO estimate $\hat{\varepsilon}_c$, the phase corrected preamble samples $r'(k)$ can be written as

$$r'(k) = r(k)e^{-\frac{j2\pi\hat{\varepsilon}_c k}{N}}. \quad (7.24)$$

However, due to the estimator variance, the residual CFO $\varepsilon'_c = \varepsilon_c - \hat{\varepsilon}_c$ still remains and is given by

$$\text{Var}(\hat{\varepsilon}_c) = \frac{3}{2\pi^2 N(1 - \frac{1}{Q^2})} \frac{1}{\rho_{av}}. \quad (7.25)$$

The estimation variance is independent of the estimated CFO and is determined by the average SNR ρ_{av} and system parameters N and Q . The analytical expressions and simulation results in Figure 7.3 show the variance of the estimated CFO for a different number of identical parts Q . The analytical and simulation curves are overlapping for SNR > 0 dB. The residual normalized CFO ε'_c has a Gaussian distribution with the variance in (7.25), as shown in Figure 7.4. The simulation results match the theoretical curves corresponding to the Gaussian distribution with the given variance.

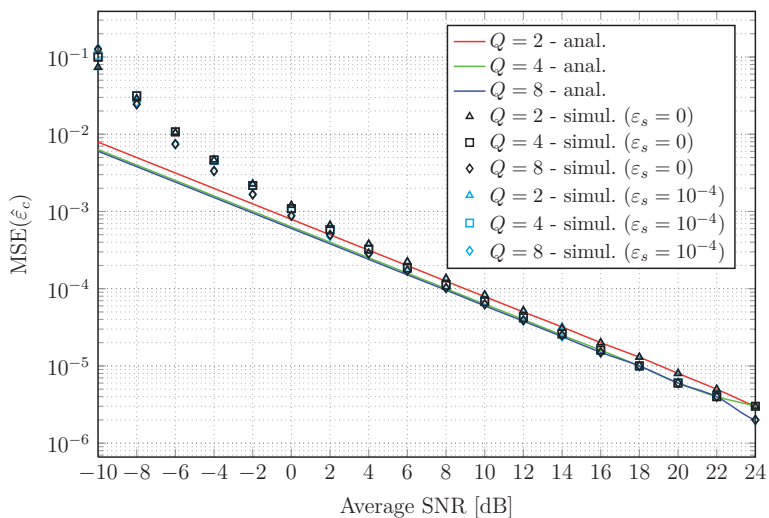


Figure 7.3.: $MSE(\hat{\varepsilon}_c)$ vs. average SNR for $\varepsilon_s = 0$ and 10^{-4} with $Q = 2, 4,$ and 8 .

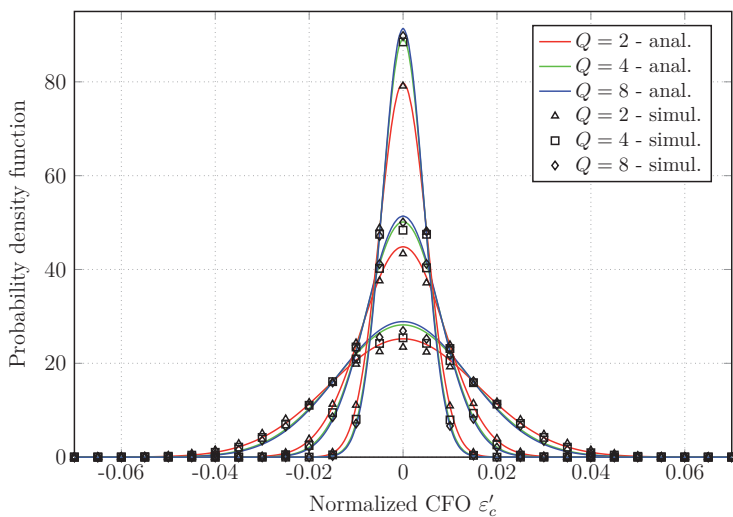


Figure 7.4.: Pdf of the normalized residual CFO ε'_c for SNR = 5, 10, and 15 dB with $Q = 2, 4,$ and 8 .

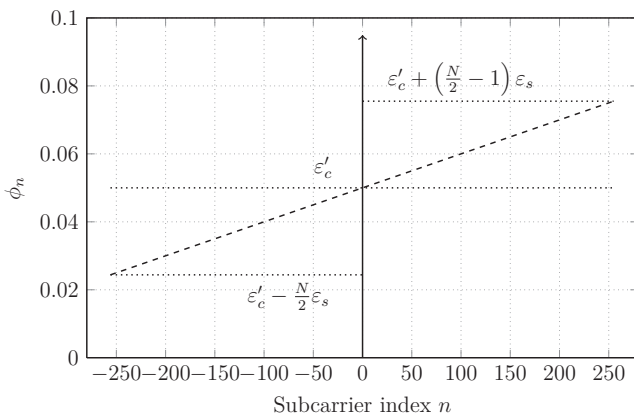
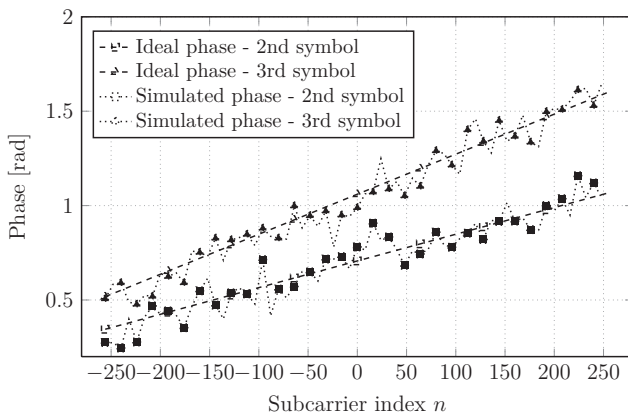
(a) Phase factor ϕ_n originating from the residual CFO and SFO vs. subcarrier index n (b) Phases $2\pi i N_t \phi_n / N$ over subcarriers in two adjacent OFDM symbols

Figure 7.5.: The phase offset over subcarriers originating from the residual CFO $\epsilon_s = 5 \cdot 10^{-2}$ and SFO $\epsilon_s = 10^{-4}$ for $N = 512$ and SNR = 20 dB.

7.2.2. Residual CFO and SFO Compensation

As discussed in the previous subsection, due to the finite variance of the CFO estimator some residual CFO still exists, named $\epsilon'_c = \hat{\epsilon}_c - \epsilon_c$. According to (2.61), the received signal can be written as

$$R_i(n) = e^{j2\pi i N_t \phi_n / N} H(n) C_i(n) f_N(\phi_n) + I_i(n, \epsilon_c, \epsilon_s) + W_i(n), \quad (7.26)$$

Algorithm 5 LLS algorithm for the residual CFO and SFO estimation.

- 1: $\hat{\phi}_{0,n} = 0, \quad n = -\frac{N}{2}, \dots, \frac{N}{2} - 1$
 - 2: **for** $i = 1, \dots, I$ **do**
 - 3: $\tilde{Y}'_i(n) = \tilde{Y}_i(n) \cdot e^{-j\frac{2\pi N_i}{N}\hat{\phi}_{i-1,n}}, \quad n = -\frac{N}{2}, \dots, \frac{N}{2} - 1$
 - 4: $\xi_i(n_p) = \angle\left(\tilde{Y}_i(n_p), C_i(n_p)\right), \quad n_p \in \mathcal{P}$
 - 5: $\hat{\varepsilon}'_c = \frac{N}{2\pi N_i} \frac{\sum_{\mathcal{P}} \xi_i(n_p)}{N_p}$
 - 6: $\hat{\varepsilon}_s = \frac{N}{2\pi N_i} \frac{\sum_{\mathcal{P}} n_p \xi_i(n_p)}{\sum_{\mathcal{P}} n_p^2}$
 - 7: $\hat{\phi}_{i,n} = \hat{\varepsilon}'_c + n\hat{\varepsilon}_s, \quad n = -\frac{N}{2}, \dots, \frac{N}{2} - 1$
 - 8: $Y_i(n) = \tilde{Y}'_i(n) \cdot e^{-j\frac{2\pi N_i}{N}\hat{\phi}_{i,n}}, \quad n = -\frac{N}{2}, \dots, \frac{N}{2} - 1$
 - 9: **end for**
-

where $I_i(n, \varepsilon_c, \varepsilon_s)$ accounts for the ICI on the n th subcarrier in (2.62), and ϕ_n now corresponds to the residual CFO and SFO, i.e., $\phi_n = \varepsilon'_c + n\varepsilon_s$. Assuming the large number of subcarriers, the ICI term $I_i(n, \varepsilon_c, \varepsilon_s)$ can be modeled as a Gaussian random variable, with the variance in (7.2). However, due to the low value of this variance, for the sake of simplicity in the following derivations concerned with the phase tracking, we neglect the ICI term from (7.26), thus yielding

$$R_i(n) = e^{j2\pi i N_i \phi_n / N} \mathcal{H}(n) C_i(n) + W_i(n), \quad (7.27)$$

where $\mathcal{H}(n) = f_n(\phi_n)H(n)$ represents the equivalent channel frequency response at the beginning of the frame. Since this term is independent of the time index i , the phase shift introduced by $f_n(\phi_n)$ is removed by equalization, as discussed in Section 2.6. Assuming the perfect channel estimate $\mathcal{H}(n)$, the received signal in the presence of the residual CFO and SFO after equalization becomes

$$\tilde{Y}_i(n) = \frac{R_i(n)}{\mathcal{H}(n)} = e^{j2\pi i N_i \phi_n / N} C_i(n) + \tilde{W}_i(n), \quad (7.28)$$

where $\tilde{W}_i(n) = W_i(n)/\mathcal{H}(n)$ represent the equalized AWGN samples. As (7.28) suggests, each OFDM symbol still contains the phase shift proportional to $i\phi_n = i(\varepsilon'_c + n\varepsilon_s)$, which is determined by the time index i . Additionally, the phase variations over subcarrier index n are linear, with the slope determined by the symbol index i and normalized SFO ε_s as shown in Figure 7.5a. The implemented LLS phase tracking [81] is based on the fitting of the phases to the best linear line.

Within the frame, each data block contains N_p pilot subcarriers symmetrically located with respect to the DC subcarrier at the pilot subcarrier indexes $\mathcal{P} = \{n_1, n_2, \dots, n_{N_p}\}$. According to (7.28), the received signal at the pilot subcarrier n_p after equalization becomes

$$\tilde{Y}_i(n_p) = \frac{R_i(n_p)}{\mathcal{H}(n_p)} = e^{j2\pi i N_i \phi_{n_p} / N} C_i(n) + \tilde{W}_i(n_p), \quad n_p \in \mathcal{P}. \quad (7.29)$$

Moreover, we assume that the power loaded on the pilot subcarriers $\sigma_P^2 = |C_i(n_p)|^2$ is equal to the average signal power, i.e., $\sigma_P^2 = \sigma_S^2$. In general, as specified by some of the

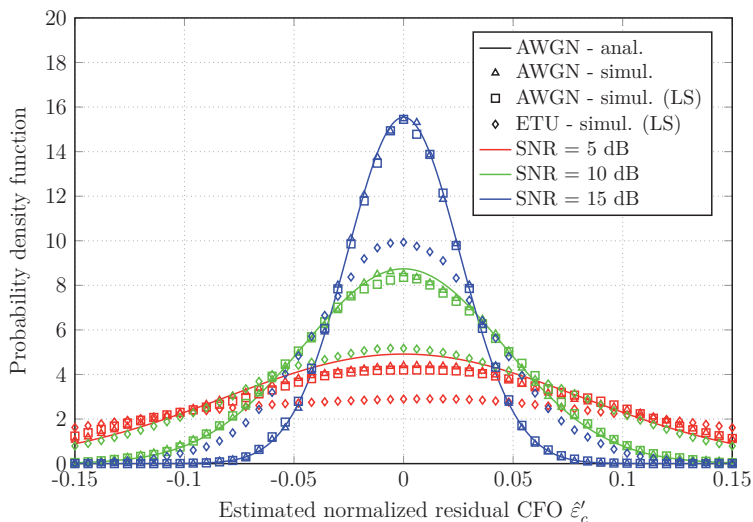


Figure 7.6.: Pdf of the estimated normalized residual CFO $\hat{\epsilon}'_c$ for $\epsilon'_c = 0$, SNR = 5, 10, and 15 dB with $N = 512$ and $N_p = 48$.

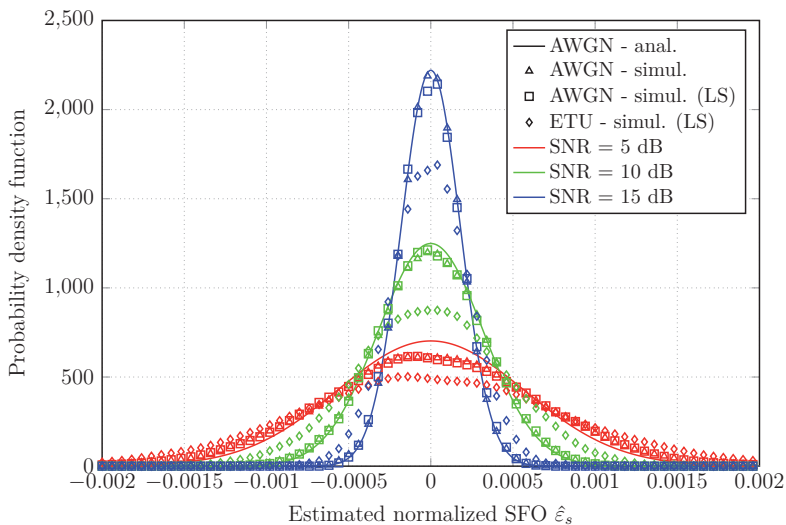


Figure 7.7.: Pdf of the estimated normalized SFO $\hat{\epsilon}_s$ for $\epsilon_s = 0$, SNR = 5, 10, and 15 dB with $N = 512$ and $N_p = 48$.

current wireless standards, the power of the pilot subcarriers are additionally boosted to bring better estimation performance, e.g., in WiMAX the boosting factor is 2.5 dB. The individual steps of the LLS phase tracking are given in Algorithm 5.

The time index $i = 0$ corresponds to the preamble symbol adjacent to the first data symbol. Each symbol is pre-compensated with the phase offset determined from the previous symbol. This allows for reducing the phase ambiguity of the LLS estimate since the slope of the phase increases with the time index i , as shown in Figure 7.5b. Furthermore, in Step 4, $\xi_i(n_p)$ denote the phase difference between the transmitted signal $C_i(n_p)$ and the equalized received signal $\tilde{Y}_i(n_p)$ at the n_p th pilot subcarrier. The LLS algorithm interpolates those phase offsets to calculate the phase drift of each data subcarrier, as given in steps 5-7. The CRBs that correspond to the residual CFO and SFO estimation are derived in [77] as

$$\text{CRB}\{\hat{\varepsilon}'_c\} = \frac{1}{\rho_P N_P} \quad (7.30)$$

and

$$\text{CRB}\{\hat{\varepsilon}_s\} = \frac{1}{\rho_P \sum_{\mathcal{P}} n_p^2}, \quad (7.31)$$

respectively, where $\rho_P = \frac{\sigma_P^2}{\sigma_W^2}$ denotes the average SNR on the pilot subcarriers. We further assume that the average SNR on pilot subcarriers is equal to the average SNR on data subcarriers, i.e., $\rho_P = \rho_{av}$.

The given variances are independent of the estimated residual CFO and SFO and are determined by the average SNR on the pilot subcarriers ρ_P , number of pilot subcarriers N_P , and their positioning within the OFDM symbol. The analytical expressions and simulation results in Figure 7.6 and Figure 7.7 show the pdf of the estimated residual CFO and SFO, respectively, for different SNR values in an AWGN and highly selective Extended Typical Urban (ETU) channel, given in Appendix A. For an AWGN channel the simulation results match the theoretical curves that correspond to the Gaussian distribution of given variance. It is shown that the corresponding estimates stay unbiased but variance increases in an ETU channel due to the frequency selectivity. Figure 7.8 and Figure 7.7 show the MSE of the estimated residual CFO and SFO as a function of the SNR. For SNR values greater than 8 dB, the analytical and simulation curves are overlapping for an AWGN channel, while the SNR loss introduced by the frequency-selective ETU channel stays constant.

The performance of an OFDM system with the considered synchronization stages, i.e., with Morelli's CFO estimation and LLS phase tracking, for $\varepsilon_s = 10^{-4}$ in an AWGN channel is given in Figure 7.10. The related list of SNR values required to achieve BER = 10^{-3} is given in Table 7.1 while corresponding rate-power functions are shown in Figure 7.11. In Section 7.4, they are utilized for the rate adaptive algorithms addressed in Chapter 3.

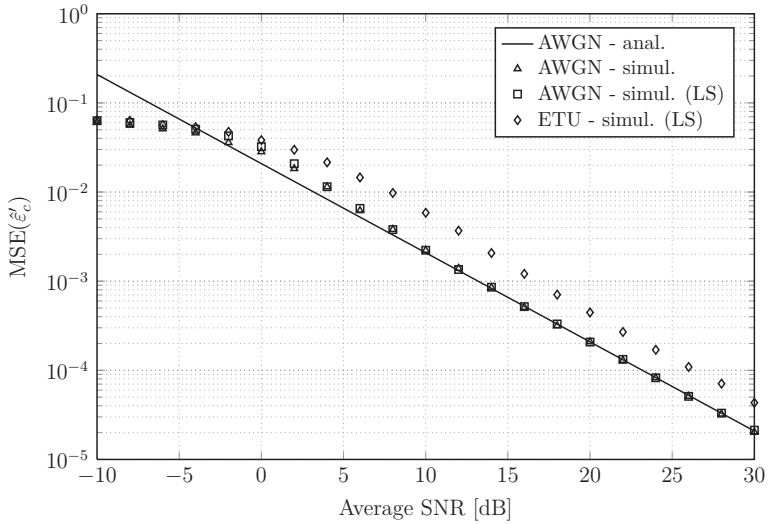


Figure 7.8.: $MSE(\hat{\epsilon}'_c)$ vs. average SNR for $\epsilon_s = 0$ with $N = 512$ and $N_p = 48$.

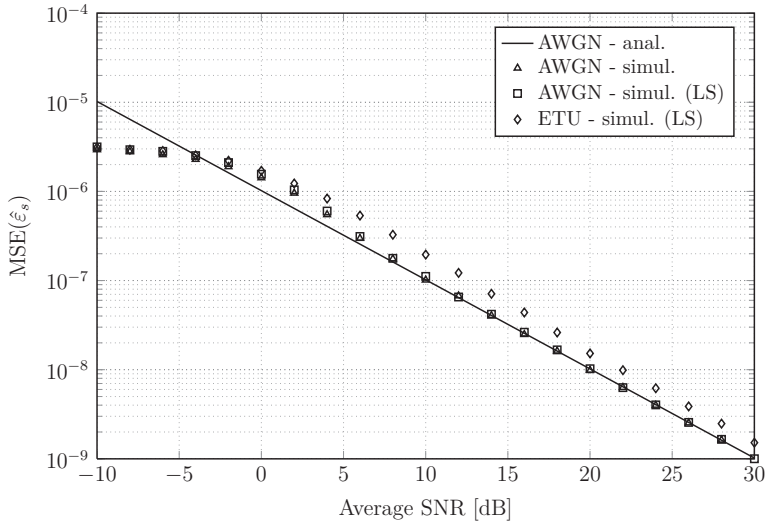


Figure 7.9.: $MSE(\hat{\epsilon}_s)$ vs. average SNR for $\epsilon_s = 0$ with $N = 512$ and $N_p = 48$.

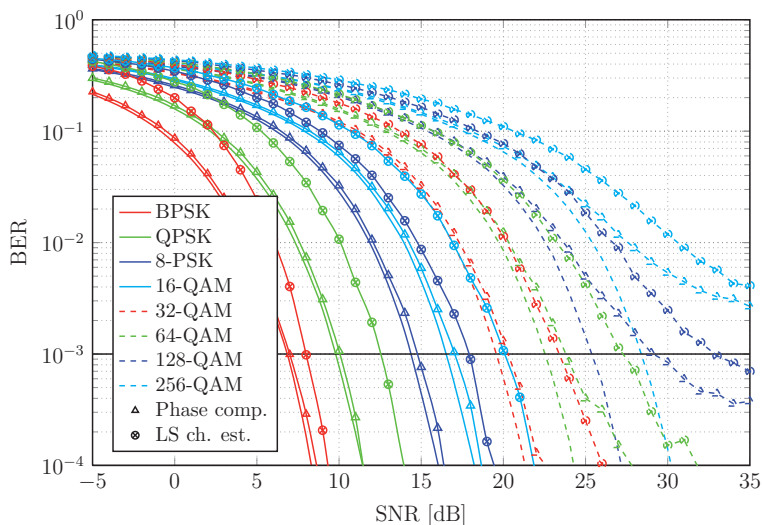


Figure 7.10.: BER performance of an OFDM system with the LLS phase compensation in an AWGN channel for $N = 512$ and $N_P = 48$.

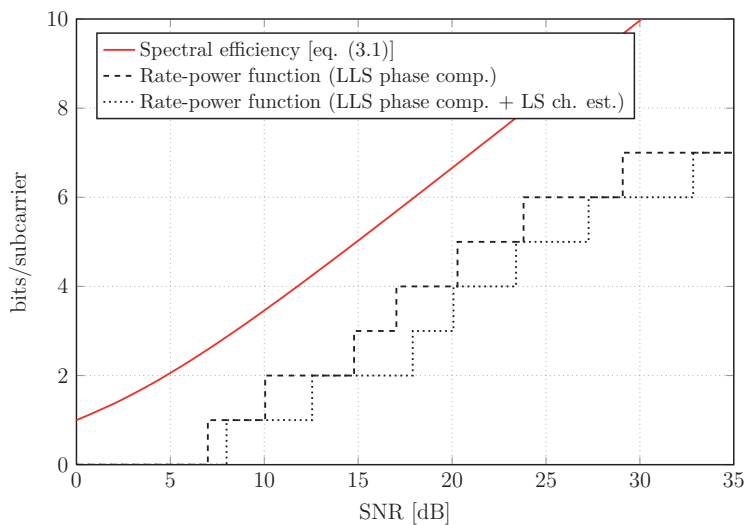


Figure 7.11.: Rate-power function of an OFDM system with the LLS phase compensation for $\text{BER} = 10^{-3}$, $N = 512$, and $N_P = 48$.

Table 7.1.: Required SNR, SNR gap, and SNR margin of an OFDM system with the LLS phase compensation in an AWGN channel for BER = 10^{-3} , $N = 512$, and $N_p = 48$.

Modulation bits r	LLS phase comp. (ideal transc.)			LLS phase comp. (LS ch. est.)		
	Required SNR [dB]	$\Gamma_{r,LLS}$ [dB]	ΔSNR_{LLS} [dB]	Required SNR [dB]	$\Gamma_{r,LLS+LS}$ [dB]	$\Delta\text{SNR}_{LLS+LS}$ [dB]
1	6.99	6.99	0.2	7.99	7.99	1.2
2	10.05	5.27	0.24	12.55	7.78	2.75
3	14.78	6.33	0.37	17.9	9.45	3.49
4	17.03	5.27	0.5	20.07	8.31	3.54
5	20.29	5.38	0.73	23.41	8.49	3.85
6	23.81	5.81	1.25	27.26	9.27	4.72
7	29.09	8.05	3.67	32.83	11.8	7.43
8						

7.3. SNR Estimation in the Presence of Synchronization Errors

The PS estimator, previously discussed in Chapter 4, is based on the second order moments of the preamble samples. It utilizes the presence of the noise samples on the received nulled subcarriers and signal plus noise components on the received loaded subcarriers. In previous sections of this chapter we have shown that the presence of synchronization errors affects the received signal twofold. At first, it introduces the phase shift that rotates the signal constellations, thus requiring for an additional phase compensation. Secondly, the power leakage from adjacent subcarriers causes the ICI.

Concerning the PS estimator, in the presence of the CFO and SFO, the content on the nulled subcarriers is changed such that besides noise components it contains the ICI component originating from the adjacent loaded subcarriers. Write $n = mQ + q$, $m = -\frac{N_p}{2}, \dots, \frac{N_p}{2} - 1$, and $q = 0, \dots, Q - 1$. Having the same notation setting as in Section 4.2, the transmitted signal on the n th subcarrier is given by

$$C(n) = C(mQ + q) = \begin{cases} \sqrt{Q}\sigma_S C_p(mQ), & q = 0 \\ 0, & q = 1, \dots, Q - 1 \end{cases} \quad (7.32)$$

According to (4.17), the received signal on the n th subcarrier in the presence of the CFO and SFO can be written as

$$Y(n) = Y(m + q) = \begin{cases} Y_p(mQ), & q = 0 \\ Y_z(mQ + q), & q = 1, \dots, Q - 1 \end{cases}$$

where

$$Y_p(mQ) = \sqrt{Q}\sigma_S H_p(m)C_p(mQ)f_N(\phi_{mQ}) + I(mQ, \varepsilon_c, \varepsilon_s) + W(mQ) \quad (7.33)$$

is the received signal on the loaded subcarriers, and

$$Y_z(mQ + q) = I(mQ + q, \varepsilon_c, \varepsilon_s) + W(mQ + q). \quad (7.34)$$

is the received signal on the nulled subcarriers. Here, $I(mQ, \varepsilon_c, \varepsilon_s)$ denotes the ICI on the n th subcarrier given by

$$I(mQ, \varepsilon_c, \varepsilon_s) = \sqrt{Q} \sigma_S \sum_{\substack{l=-\frac{N_p}{2}, \\ l \neq m}}^{\frac{N_p}{2}-1} H_p(lQ) C_p(lQ) f_N(\phi_{lQ} + (l-m)Q), \quad (7.35)$$

where $f_N(\cdot)$ is given in (2.59). Moreover, ϕ_{mQ} presents the degradation effect of the joint contribution of the CFO and SFO in (2.63) as $\phi_{mQ} \approx \varepsilon_c + mQ \cdot \varepsilon_s$. From (7.34), it can be seen that the received signal on the nulled subcarriers contains both the noise component and ICI originating from the adjacent loaded subcarriers.

The estimation of the average SNR in the presence of the CFO and SFO, according to (4.23), is given by

$$\hat{\rho}_{FO,av} = \frac{1}{Q} \left(\frac{\hat{M}_{FO,2,p}}{\hat{M}_{FO,2,z}} - 1 \right), \quad (7.36)$$

where $\hat{M}_{FO,2,p}$ and $\hat{M}_{FO,2,z}$ denote the empirical second-order moments of the received signal on loaded and nulled subcarriers, respectively. Therefore, by substituting (7.33) in (4.20), the empirical second-order moment of the received signal on the loaded subcarriers becomes

$$\hat{M}_{FO,2,p} = \frac{1}{N_p} \sum_{m=-\frac{N_p}{2}}^{\frac{N_p}{2}-1} |Y_p(mQ)|^2. \quad (7.37)$$

Its expected value can be written as

$$\begin{aligned} E \{ \hat{M}_{FO,2,p} \} &= \frac{1}{N_p} E \left\{ \sum_{m=-\frac{N_p}{2}}^{\frac{N_p}{2}-1} |Y_p(mQ)|^2 \right\} \\ &= \frac{1}{N_p} \sum_{m=-\frac{N_p}{2}}^{\frac{N_p}{2}-1} E \{ |Y_p(mQ)|^2 \} \\ &= \frac{Q\sigma_S^2}{N_p} \sum_{m=-\frac{N_p}{2}}^{\frac{N_p}{2}-1} E \{ |H_p(mQ)|^2 |f_N(\phi_{mQ})|^2 \} \\ &+ \frac{Q\sigma_S^2}{N_p} \sum_{m=-\frac{N_p}{2}}^{\frac{N_p}{2}-1} \sum_{\substack{l=-\frac{N_p}{2}, \\ l \neq m}}^{\frac{N_p}{2}-1} E \{ |H_p(lQ)|^2 |f_N(\phi_{lQ} + (l-m)Q)|^2 \} + \frac{\sigma_W^2}{N_p} \sum_{m=-\frac{N_p}{2}}^{\frac{N_p}{2}-1} E \{ |W(mQ)|^2 \} \\ &= \frac{Q\sigma_S^2}{N_p} \sum_{m=-\frac{N_p}{2}}^{\frac{N_p}{2}-1} \sum_{l=-\frac{N_p}{2}}^{\frac{N_p}{2}-1} E \{ |H_p(lQ)|^2 |f_N(\phi_{lQ} + (l-m)Q)|^2 \} + \frac{\sigma_W^2}{N_p} \sum_{m=-\frac{N_p}{2}}^{\frac{N_p}{2}-1} E \{ |W(mQ)|^2 \} \\ &= Q\sigma_S^2 \psi(Q) + \sigma_W^2, \end{aligned} \quad (7.38)$$

where $\psi(Q)$ denotes the contribution from the loaded subcarriers mutually separated by $Q - 1$ subcarriers given by

$$\psi(Q) = \sum_{l=-\frac{N_p}{2}}^{\frac{N_p}{2}-1} |f_N(\phi_{lQ} + (l-m)Q)|^2. \quad (7.39)$$

Similarly, by substituting (7.34) in (4.22), the empirical second-order moment of the received signal on the nulled subcarriers

$$\hat{M}_{FO,2,z} = \frac{1}{(Q-1)N_p} \sum_{m=-\frac{N_p}{2}}^{\frac{N_p}{2}-1} \sum_{q=1}^{Q-1} |Y_z(mQ+q)|^2 \quad (7.40)$$

has expectation

$$\begin{aligned} E\{\hat{M}_{FO,2,z}\} &= \frac{1}{(Q-1)N_p} E\left\{ \sum_{m=-\frac{N_p}{2}}^{\frac{N_p}{2}-1} \sum_{q=1}^{Q-1} |Y_z(mQ+q)|^2 \right\} \\ &= \frac{1}{(Q-1)N_p} \sum_{m=-\frac{N_p}{2}}^{\frac{N_p}{2}-1} \sum_{q=1}^{Q-1} E\{|Y_z(mQ+q)|^2\} \\ &= \frac{1}{(Q-1)N_p} \sum_{m=-\frac{N_p}{2}}^{\frac{N_p}{2}-1} \sum_{q=1}^{Q-1} E\{|I(mQ+q)|^2\} + \frac{1}{(Q-1)N_p} \sum_{m=-\frac{N_p}{2}}^{\frac{N_p}{2}-1} \sum_{q=1}^{Q-1} E\{|W(mQ+q)|^2\} \\ &= \frac{Q\sigma_S^2}{(Q-1)N_p} \sum_{m=-\frac{N_p}{2}}^{\frac{N_p}{2}-1} \sum_{q=1}^{Q-1} \sum_{l=-\frac{N_p}{2}}^{\frac{N_p}{2}-1} E\{|H_p(lQ)|^2\} |f_N(\phi_{lQ} + (l-m)Q - q)|^2 \\ &\quad + \frac{1}{(Q-1)N_p} \sum_{m=-\frac{N_p}{2}}^{\frac{N_p}{2}-1} \sum_{q=1}^{Q-1} \sigma_W^2 \\ &= \frac{Q\sigma_S^2}{Q-1} (1 - \psi(Q)) + \sigma_W^2, \end{aligned} \quad (7.41)$$

where, using (7.39), it yields

$$\begin{aligned} \sum_{q=1}^{Q-1} \sum_{l=-\frac{N_p}{2}}^{\frac{N_p}{2}-1} E\{|H_p(lQ)|^2\} |f_N(\phi_{lQ} + (l-m)Q - q)|^2 &= \sum_{q=0}^{Q-1} \sum_{l=-\frac{N_p}{2}}^{\frac{N_p}{2}-1} |f_N(\phi_{lQ} + (l-m)Q - q)|^2 \\ &\quad - \sum_{l=-\frac{N_p}{2}}^{\frac{N_p}{2}-1} |f_N(\phi_{lQ} + (l-m)Q)|^2 \\ &= 1 - \psi(Q). \end{aligned} \quad (7.42)$$

Inserting (7.37) and (7.40) in (7.36) yields

$$\begin{aligned}
\hat{\rho}_{FO,av} &= \frac{1}{Q} \left(\frac{\hat{M}_{FO,2,p} - \hat{M}_{FO,2,z}}{\hat{M}_{FO,2,z}} \right) \\
&= \frac{1}{Q} \left(\frac{Q\sigma_S^2\psi(Q) + \sigma_W^2 - \frac{Q\sigma_S^2}{Q-1}(1-\psi(Q)) + \sigma_W^2}{\frac{Q\sigma_S^2}{Q-1}(1-\psi(Q)) + \sigma_W^2} \right) \\
&= \frac{\frac{\sigma_S^2}{\sigma_W^2}(\psi(Q) - \frac{1-\psi(Q)}{Q-1})}{1 + \frac{\sigma_S^2}{\sigma_W^2} \frac{Q}{Q-1}(1-\psi(Q))} \\
&= \frac{\frac{Q}{Q-1}(\psi(Q) - \frac{1}{Q})\rho_{av}}{1 + \frac{Q}{Q-1}(1-\psi(Q))\rho_{av}},
\end{aligned} \tag{7.43}$$

where $\rho_{av} = \frac{\sigma_S^2}{\sigma_W^2}$ is the ideal average SNR defined in (2.39).

To estimate the SNR per subcarrier from (4.30), the channel estimates in the presence of the CFO and SFO after the N -point DFT can be written as (4.28)

$$\hat{H}_{FO}(n) = \sigma_S H(n) f_n(\phi_n) + I(n) + \frac{\sigma_W}{\sqrt{Q}}(n) \tilde{W}(n), \quad -\frac{N}{2} \leq n \leq \frac{N}{2} - 1, \tag{7.44}$$

where $I(n)$ accounts for the ICI on n th subcarrier and is given by

$$I(n) = \sqrt{Q} \sigma_S \sum_{\substack{l=-\frac{N}{2}, \\ l \neq n}}^{\frac{N}{2}-1} H(l) C(l) f_N(\phi_l + (l-n)). \tag{7.45}$$

Similarly to (7.38), the expectation of the empirical second order moment $|\hat{H}_{FO}(n)|^2$ can be written as

$$\begin{aligned}
E \{ \hat{M}_{FO,2,p}(n) \} &= E \{ |\hat{H}_{FO}(n)|^2 \} \\
&= \sigma_S^2 E \{ |H(n)|^2 \} |f_N(\phi_n)|^2 + \sigma_S^2 \sum_{\substack{l=-\frac{N}{2}, \\ l \neq n}}^{\frac{N}{2}-1} E \{ |H(n)|^2 \} |f_N(\phi_l + (l-n))|^2 \\
&\quad + \frac{1}{Q} E \{ |\tilde{W}(n)|^2 \} \\
&\approx \sigma_S^2 E \{ |H(n)|^2 \} |f_N(\phi_n)|^2 + \sigma_S^2 (1 - |f_N(\phi_n)|^2) + \frac{\sigma_W^2}{Q}.
\end{aligned} \tag{7.46}$$

As given in (4.30), by using the noise power estimates from (7.40), the SNR estimate on the n th subcarrier becomes

$$\begin{aligned}
 \hat{\rho}_{FO}(n) &= \frac{\hat{M}_{FO,2,p}(n)}{\hat{M}_{FO,2,z}} - \frac{1}{Q} \\
 &= \frac{\sigma_S^2 E\{|H(n)|^2\} |f_N(\phi_n)|^2 + \sigma_S^2(1 - |f_N(\phi_n)|^2) + \frac{\sigma_W^2}{Q}}{\frac{Q\sigma_S^2}{Q-1}(1 - \psi(Q)) + \sigma_W^2} - \frac{1}{Q} \\
 &= \frac{\frac{\sigma_S^2}{\sigma_W^2} E\{|H(n)|^2\} |f_N(\phi_n)|^2 + \frac{\sigma_S^2}{\sigma_W^2}(1 - |f_N(\phi_n)|^2) + \frac{1}{Q} - \frac{1}{Q} - \frac{\sigma_S^2}{\sigma_W^2} \frac{1}{Q-1}(1 - \psi(Q))}{1 + \frac{\sigma_S^2}{\sigma_W^2} \frac{Q}{Q-1}(1 - \psi(Q))} \\
 &= \frac{|f_N(\phi_n)|^2 \rho(n) + \left(\frac{1}{Q-1}(Q - 2 + \psi(Q)) - |f_N(\phi_n)|^2\right) \rho_{av}}{1 + \frac{Q}{Q-1}(1 - \psi(Q)) \rho_{av}},
 \end{aligned} \tag{7.47}$$

where $\rho(n) = \frac{\sigma_S^2 E\{|H(n)|^2\}}{\sigma_W^2} = \rho_{av} \cdot E\{|H(n)|^2\}$ is the ideal SNR on the n th subcarrier, defined in (2.38).

7.3.1. Numerical Results

We investigate the impact of synchronization errors on the performance of the PS estimator. Both the average SNR and SNR per subcarrier estimation are considered. The performance for a different number of preamble identical parts, i.e., $Q = 2, 4$, and 8 , is compared with the real SNR in the presence of the CFO and SFO while the ideal SNR value (of an ideal transceiver) is given as a reference. The investigated system comply with the WiMAX specifications: $N = 256$ subcarriers, CP length of 32 samples, and 3.5 MHz bandwidth mode, see Appendix B.2.

Figure 7.12 shows the average SNR estimate for $\varepsilon_c = 5 \cdot 10^{-2}$ and $\varepsilon_s = 10^{-4}$ in an AWGN channel. The simulation results agree with the analytical expression in (7.43). The estimated value of the average SNR approaches the real average SNR value as Q increases. Figure 7.13 shows the mean of the average SNR estimation in the presence of the Morelli's estimator with the residual CFO ε'_c and SFO $\varepsilon_s = 10^{-4}$. Because the CFO estimation is performed prior to the DFT, ε'_c is normally zero-mean distributed with the variance in (7.25). The real SNR curves obtained from (7.9) for a different number of preamble identical parts, i.e., $Q = 2, 4$, and 8 , are almost identical because the corresponding variances of ε'_c perform closely as shown in Figure 7.3. As Q increases, the estimated SNR is approaching the real SNR value.

Figures 7.14, 7.15, and 7.17 show that the PS SNR per subcarrier estimation in the presence of the SFO does not follow the slope of the real affected SNR, due to the ICI originating from the adjacent subcarriers. However, for small SFO values, as one present in the USRP, i.e., up to 10^{-4} , Figure 7.15 shows that those degradations are negligible, such that the PS SNR estimation bias to the real SNR per subcarrier value is negligible. It is further shown in Figure 7.16 that the PS SNR per subcarrier estimation in the absence of the SFO approaches the real SNR values and that the simulation results agree with the analytical expression in (7.47).

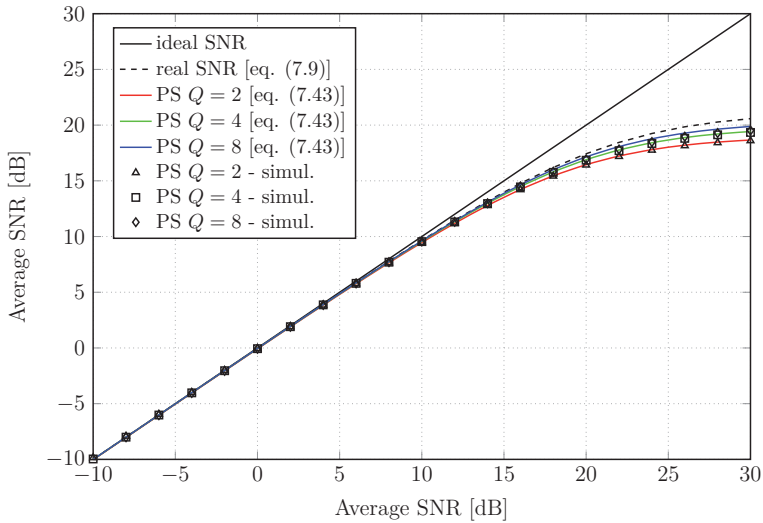


Figure 7.12.: Average SNR for $\varepsilon_c = 5 \cdot 10^{-2}$, $\varepsilon_s = 10^{-4}$, and $N = 256$ with $Q = 2, 4,$ and 8 .

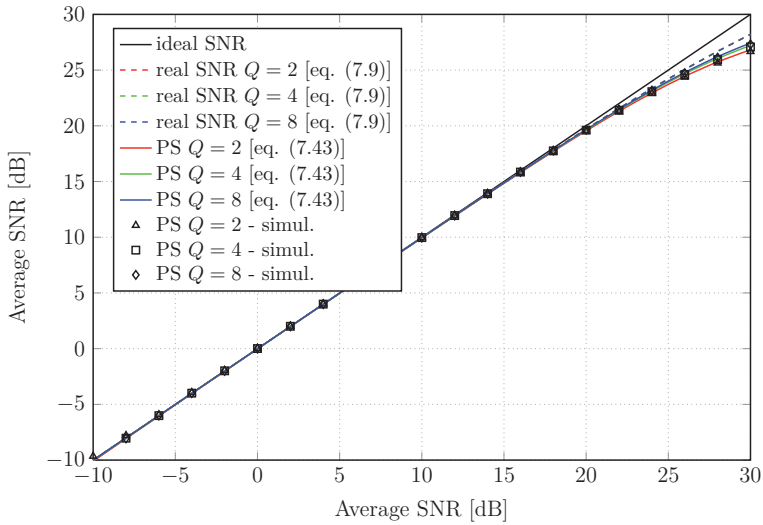


Figure 7.13.: Average SNR in the presence of ε'_c for $\varepsilon_s = 2 \cdot 10^{-4}$ and $N = 256$ with $Q = 2, 4,$ and 8 .

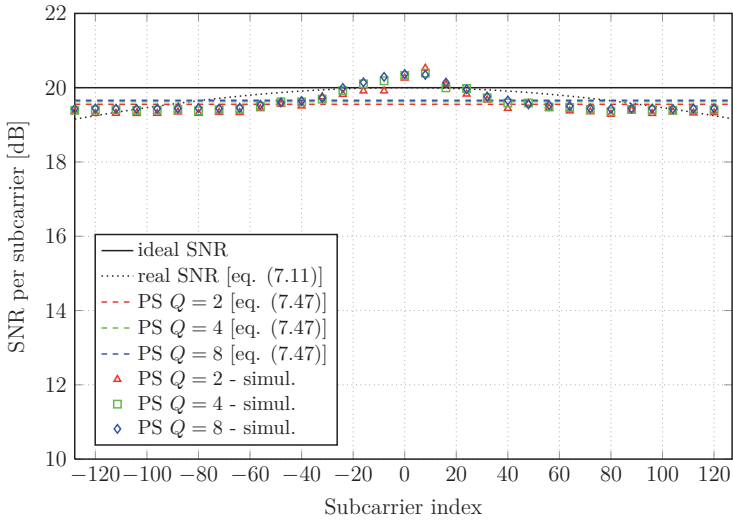


Figure 7.14.: SNR per subcarrier for $\rho_{av} = 20$ dB, $\varepsilon_c = 0$, and $\varepsilon_s = 2 \cdot 10^{-4}$ with $Q = 2, 4$, and 8 .

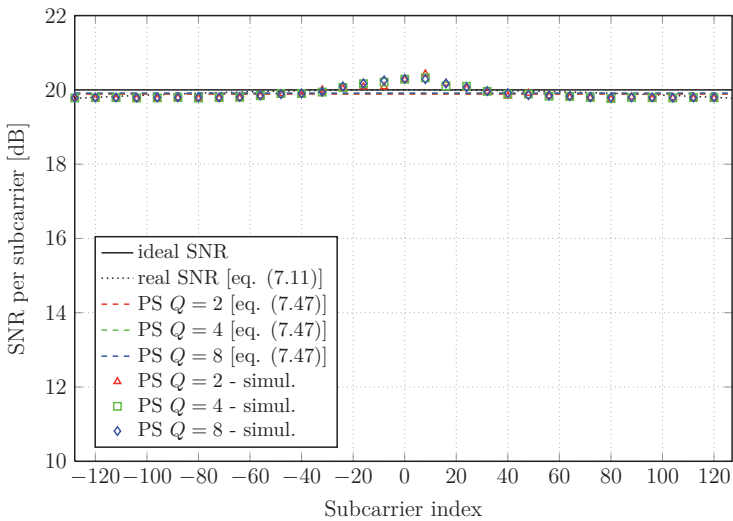


Figure 7.15.: SNR per subcarrier for $\rho_{av} = 20$ dB, $\varepsilon_c = 0$, and $\varepsilon_s = 10^{-4}$ with $Q = 2, 4$, and 8 .

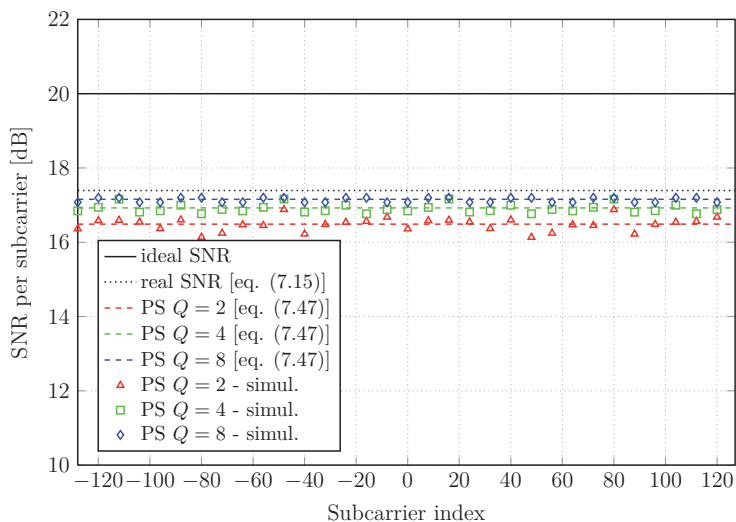


Figure 7.16.: SNR per subcarrier for $\rho_{av} = 20$ dB, $\varepsilon_c = 2 \cdot 10^{-2}$, and $\varepsilon_s = 0$ with $Q = 2, 4$, and 8 .

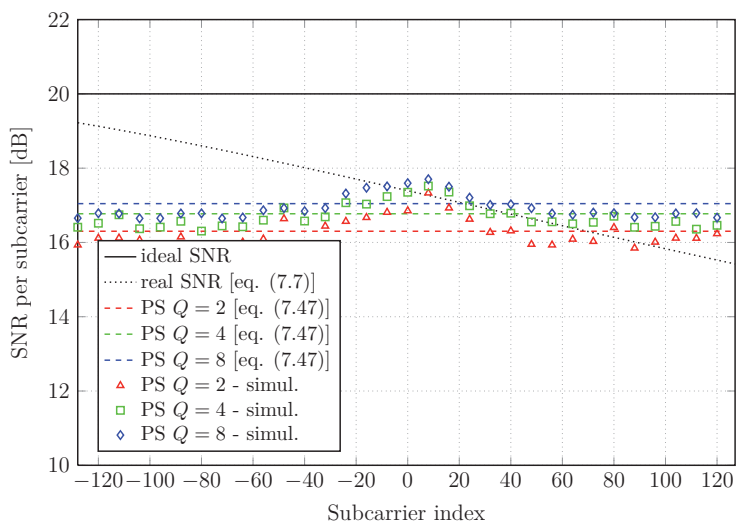


Figure 7.17.: SNR per subcarrier for $\rho_{av} = 20$ dB, $\varepsilon_c = 5 \cdot 10^{-2}$, and $\varepsilon_s = 2 \cdot 10^{-4}$ with $Q = 2, 4$, and 8 .

7.4. Resource Allocation in the Presence of Receiver Imperfections

In this section, we investigate by means of simulation study the performance of the Levin-Campello (LC) and Uniform power (UP) rate adaptive algorithms discussed in Chapter 3 for an receiver with the PS SNR estimator. The simulation environment is compatible with the WiMAX PHY standard specification, given in Appendix B.2. The system parameters used in the simulation are taken from WiMAX 5 MHz mode having the total of $N = 512$ subcarriers, where $N_u = 384$ subcarriers are used for data transmission. Furthermore, the CP length is 64 samples with the sampling frequency of 7.68 MHz (5 MHz bandwidth mode). We evaluate the performance for the required BER= 10^{-3} in a highly selective ETU channel, given in Appendix A.

We consider two general cases. The first case assumes an ideal transceiver, while the second case includes the presence of the LS channel estimation. Figure 7.18 shows that the increased SNR estimation variance at low SNR values favors the higher data rate which results in the decreased rate decrement to water-filling. However, this introduces the violation of the BER requirement. Figure 7.19 shows that the BER of the UP algorithm is preserved below the required BER of 10^{-3} while its achieved rate is independent of the number of identical parts Q in the synchronization preamble. On contrary, the LC algorithm is highly sensitive to Q , especially in low SNR region. The performance of the system utilizing the PS estimator with $Q = 8$ can be considered acceptable, thus offering low BER variations for operating SNR values.

We further analyze the performance of the considered rate adaptive algorithms for a receiver with the PS SNR estimator and synchronization stage that includes Morelli's CFO estimator and LLS phase tracking. Figure 7.20 and Figure 7.21 show that the LC algorithm is more robust to the presence of the SFO. In the high SNR region, the ICI causes the performance deterioration while the required BER is preserved. Moreover, the UP algorithm experiences the large increase of the BER.

Figure 7.22 and Figure 7.23 compare several rate adaptive algorithms addressed in Chapter 3 in the presence of the considered synchronization stage and $\varepsilon_s = 20$ ppm. While the UP and SB methods experience either constant or decreasing BER with the increasing SNR, the BER related to the LC algorithm constantly decreases, while offering the highest data rate. In Chapter 8, we extend this analysis by comparing the simulation results with the experimental measurements obtained by using the TIGR framework.

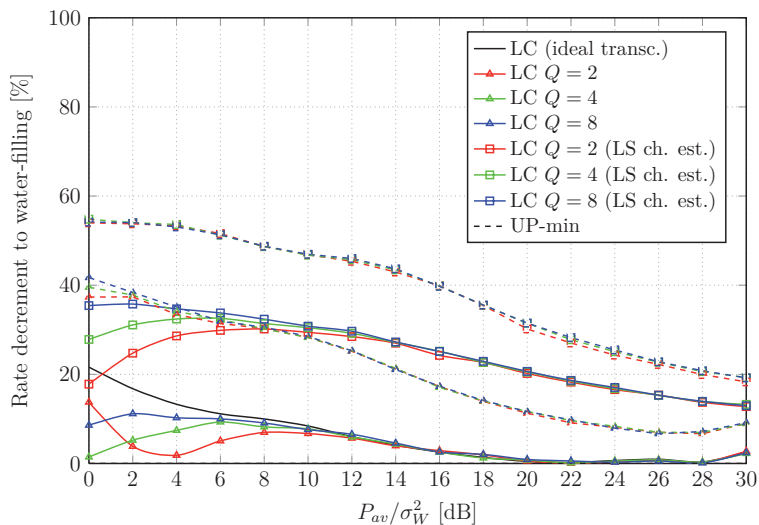


Figure 7.18.: Rate decrement to water-filling vs. SNR for an OFDM transceiver with the PS SNR estimation in the ETU channel for $\text{BER} = 10^{-3}$.

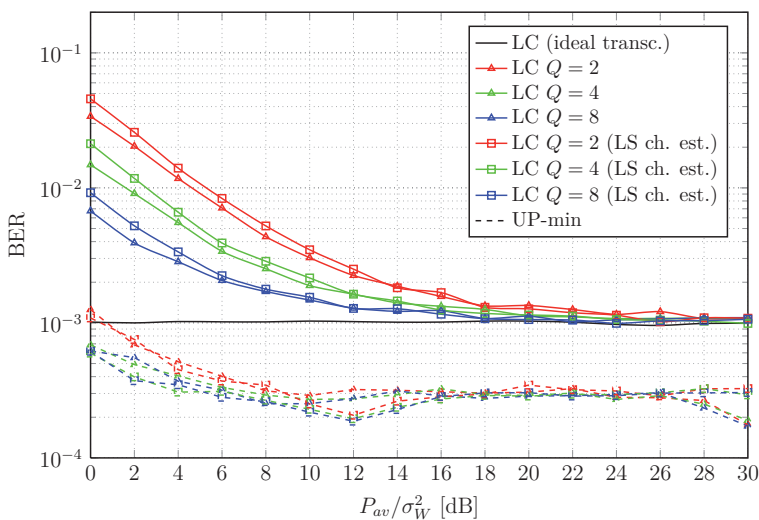


Figure 7.19.: BER vs. SNR for an OFDM transceiver with the PS SNR estimation in the ETU channel for $\text{BER} = 10^{-3}$.

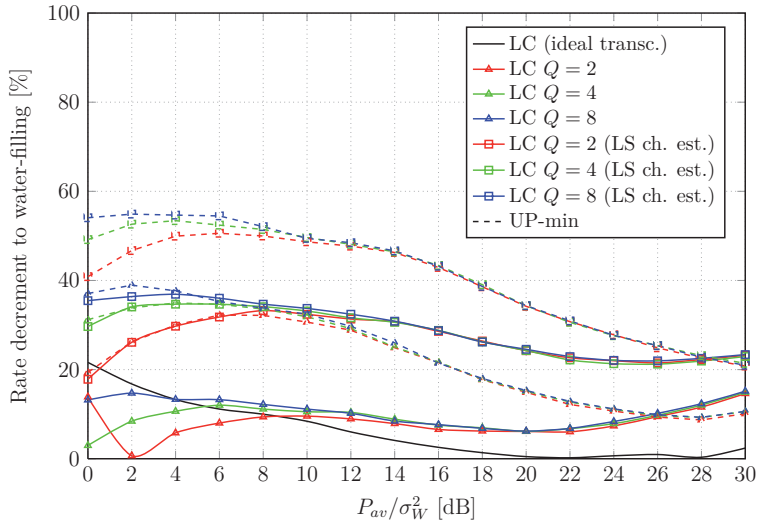


Figure 7.20.: Rate decrement to water-filling vs. SNR for an OFDM transceiver with the PS SNR estimation and LLS phase compensation in the ETU channel for $\text{BER} = 10^{-3}$.

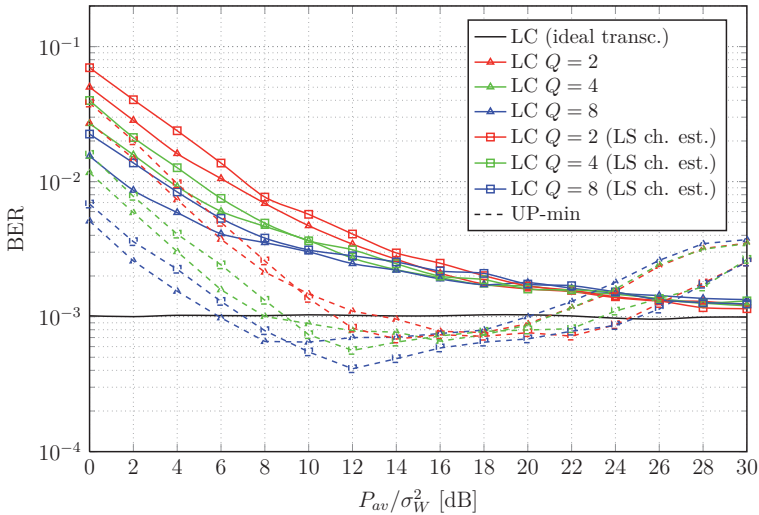


Figure 7.21.: BER vs. SNR for an OFDM transceiver with the PS SNR estimation and LLS phase compensation in the ETU channel for $\text{BER} = 10^{-3}$.

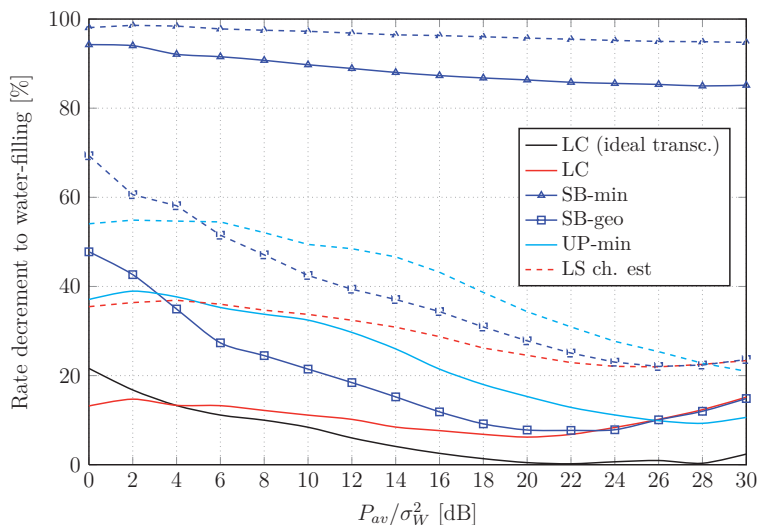


Figure 7.22.: Rate decrement to water-filling vs. SNR for an OFDM transceiver with the PS SNR estimation with $Q = 8$ and LLS phase compensation in the ETU channel for $\text{BER} = 10^{-3}$.

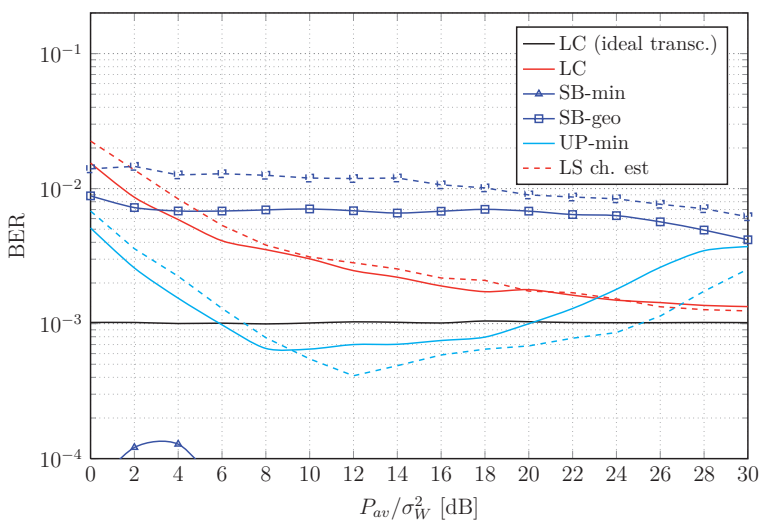


Figure 7.23.: BER vs. SNR for an OFDM transceiver with the PS SNR estimation with $Q = 8$ and LLS phase compensation in the ETU channel for $\text{BER} = 10^{-3}$.

8. Implementing Adaptive OFDM by Software Defined Radio

Optimal utilization of radio resources (bandwidth, transmit power) in multicarrier systems becomes very challenging due to the coexistence of various wireless standards within the same frequency band. The investigation and assessment of information theoretic concepts for wireless resource management in real-world scenarios requires flexible testbeds with a wide range of reconfigurable parameters. These functionalities are currently offered only by Software Defined Radio (SDR) technology based on general purpose reprogrammable hardware. Using the SDR concept we developed TIGR (Theoretische Informationstechnik GNU Radio), a modular, SDR based reconfigurable framework that allows for an adaptive OFDM transmission with a large set of adaptable parameters for different radio scenarios. Developed at the Institute for Theoretical Information Technology (TI) at RWTH University in Germany, TIGR is based on the GNU Radio framework [89], a free and open source software toolkit based on hybrid C++/Python programming model that provides a library of signal processing blocks for developing communication systems and conducting experiments in different radio environments. The GNU Radio runs in real time and can be interfaced with the RF hardware, thus allowing for a transition from the experimentation to the deployment within the same framework.

We start with a general introduction to the SDR. Rather than presenting architectural issues and in-depth conceptual analysis of the SDR, we focus on the basic ideas and SDR adaptivity capabilities as well as on potential implementation issues. A more complete coverage of the subject with a comprehensive list of references in the field can be found in [90, 91, 92]. Moreover, the advantages of the SDR and the corresponding hardware limitations are discussed. We further provide an overview of the GNU Radio, which is used as the basis for TIGR and give the insight into the basic architectural features considering the hardware and software specifications.

The corresponding system model and basic TIGR functionalities are described, while different components of the system are individually introduced. Finally, we conduct a measurement campaign to investigate several rate adaptive allocation algorithms addressed in Chapter 3 and compare their performance with the simulation results. Similarly to the simulation study, we utilize the concept of the SNR gap discussed in Chapter 3. Based on BER measurements, for each modulation scheme we determine the required SNR for achieving a given BER constraint. Due to the more “conservative“ rate-power functions caused by the performance degradation in a real RF environment, the achieved data rates are lower compared to the simulation results. The achieved BER violates the required constraints in the low SNR region, mostly due to the finite variance of the SNR estimator discussed in Chapter 7.

Parts of the following results have been presented at international conferences, see [14, 18, 15, 16].

8.1. The Basics of Software Defined Radios

An SDR is a radio system that is built entirely or in large parts in a software running on a general purpose computer. It allows for the additional flexibility not available in commercial hardware. Adaptivity can be realized by moving the signal processing into the software domain such that certain functions can be performed on-the-fly by executing the corresponding software routines. Moreover, new functionalities can be easily included by software updates, hence without the need for a hardware modification.

This means that instead of using analog circuits or a specialized digital signal processor (DSP) to receive the radio signal, the digitized signals are processed by architecture independent high level software running on a general purpose processor (GPP). The term "radio" refers to any device that transmits and/or receives radio waves. While most modern radios contain the firmware written in a certain programming language, the important distinction of the SDR is its general design irrespective to a specific chip or platform. It is therefore possible to reuse its code across different underlying architectures [93].

Ideally, besides a computer, the only required hardware is an antenna, an analog-to-digital converter (ADC) at the receiver, and a digital-to-analog converter (DAC) at the transmitter. An ideal SDR thus looks as depicted in Figure 8.1. At the receiver, a transmitted radio signal is picked up by an antenna, and then fed into an ADC for sampling. Once digitized, the signal is sent to a general purpose computer (e.g. an embedded PC) for further processing. The transmitter looks very similar, except that the signal is sent in the reverse direction, and a DAC is used instead of an ADC. The complete transceiver may share the processing unit and the antenna between the receiver and transmitter.

While this concept is very simple and extremely versatile, it is not practical due to limitations of a real hardware. However, various solutions have been suggested to overcome these problems. Some of signal manipulation can be performed by hardware while processors of different types, such as field programmable gate arrays (FPGA), DSP, and general purpose processors (GPP) can handle other parts of the signal processing. A quick look at different hardware limitations is given below. For better readability, only the receiving side is discussed. The transmitting side is subject to analogous limitations.

- *Analog-Digital Converters:* The ultimate idea of the SDR is to move ADC/DAC as close as possible to the antenna such that all signal processing can be done in the digital domain. However, to implement this concept, the requirements of the ADC and DAC far exceed practical capabilities such as the sampling rate, dynamic range and bandwidth [94]. To digitize an analog RF signal at least requires sampling rate that is determined by the Nyquist frequency. The high sampling rate requires the higher resolution, which influences the dynamic range of the receiver. As each additional bit doubles the resolution of the sampled input voltage, the dynamic range can be roughly estimated as $R = 6 \text{ dB} \times n$ where R is the dynamic range and n is the number of bits in the ADC. As ADCs used for the SDR usually have a resolution of less than 16 bits, it is important to filter out the strong interfering signals, such as signals from mobile phones, before the wideband ADC. This is usually done in the RF frontend.

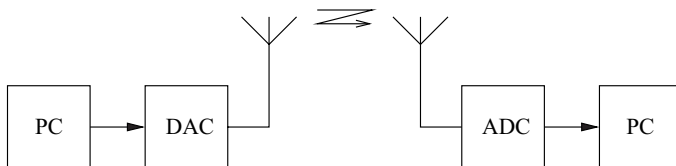


Figure 8.1.: Ideal SDR transmission.

- *Bus Speed:* Another problem lies in getting the data from the ADC to the computer. For any practical bus, there is a maximum for possible data rate limiting the product of the sample rate and resolution of the samples. The speed of common buses in commodity PCs ranges from a few Mbps to several Gbps. As an example, the PCI 2.2 bus has a theoretical maximum speed of 4256 Mbps.
- *Performance of the Processing Unit:* For a real-time processing, the performance of the CPU and sample rate limit the number of mathematical operations that can be performed per sample, as samples must be processed on-line. In practice, this means that fast CPUs, smart programming, and possibly parallelization are required. Parallelization brings two major benefits. At first, it allows for simultaneous operation of the transmitter and receiver. Secondly, by segmenting the data stream into the blocks of samples, different tasks such as synchronization, (de)modulation, and (de)coding can be processed in parallel on different processing units. However, if those are insufficient, a compromise must be found to use a suboptimal but faster signal processing algorithms.
- *Latency:* Since general purpose computers are not designed for real-time applications, a rather high latency can occur in practical SDRs. While latency is not much of an issue in transmit-only or receive-only applications, many wireless standards, such as WLAN or LTE, require precise timing and are therefore very difficult to implement in an SDR.

Because of the use of general purpose processing units, an implementation of a given wireless application in an SDR usually requires more power and occupies more space than a hardware radio with analog filtering and a dedicated signal processor. Because an SDR contains more complex components than a hardware radio, it will likely be more expensive.

Nevertheless, the SDR concept carries the flexibility of software over to the radio world and introduce a number of interesting possibilities. For example, SDR could allow its user to load a different configuration depending on whether the user wants to listen to a broadcast transmission, place a phone call, or determine the position via GPS. The development cycle for the signal processing software in SDR is much shorter and cost-effective over designing and producing special purpose hardware such as application specific integrated circuit (ASIC). Moreover, the reusability of the software between processors allows for an easy porting with minimal required modification. While portability is the major advantage in GPP-based SDR systems, it is not fully possible in the FPGA-based SDR architectures with low level hardware description languages, such as Verilog or VHDL.

Since the same hardware can be used for a variety of applications, a great reuse of resources is possible. Another interesting application field of SDR is cognitive radio [95, 96], a communication concept where different radio devices are aware of their RF environment and accordingly adapt themselves to changes in the environment. By doing so, a cognitive radio can use both the RF spectrum and its own energy resources more efficiently. As a cognitive radio requires a very high degree of flexibility, the concept of SDR presents a basis for its practical realization.

8.2. GNU Radio Architecture

GNU Radio is an open source, free software toolkit for building the SDRs [89]. It is designed to run on personal computers (PC) and combined with the minimal hardware allows the construction of simple software radios [93]. The project was started in early 2000 by Eric Blossom and has evolved into a mature software infrastructure that is used by a large community of developers. It is licensed under the GNU General Public License (GPL), thus anyone is allowed to use, copy, and modify the GNU Radio without limits, provided that extensions are made available under the same license. While the GNU Radio was initially started on a Linux platform, it now supports various Windows, Mac OS, Unix platforms.

The GNU Radio architecture consists of two software components [97]. The first component is the set of numerous building blocks representing C++ [98, 99] implementations of digital signal processing routines such as (de)modulation, filtering, (de)coding, and I/O operations. The second component is a framework to control the data flow among blocks. Implemented as a Python script it enables easy reconfiguration and control of various system functionalities and parameters. More insight into Python is given in [100]. By “wiring” together the signal processing C++ blocks, an user can create an SDR, similar to connecting physical RF building blocks to create a hardware radio.

An RF interface for the GNU Radio architecture is realized by Universal Software Radio Peripheral (USRP) boards, a general purpose RF hardware, which performs computationally intensive operations such as filtering, up- and down-conversion controlled through a robust application programming interface (API) provided by the GNU Radio. Each USRP device provides an independent transmit and receive channel capable of full duplex operation in some hardware configurations. A host PC connected to an USRP acts as a software-defined radio with host-based digital signal processing. For the experimental performance evaluation of TIGR in a real RF environment we use USRP1 and USRP2 boards equipped with the RFX2400 daughterboards.

The Hardware - USRP

Despite some differences in characteristics and specifications among various models, all USRP devices have the same general architecture shown in Figure 8.2. The RF frontend, mixers, filters, oscillators, and amplifiers at the receive chain are used to translate a signal from the RF domain to the complex baseband or IF signals. The baseband or IF signals are sampled by the ADCs, and the digital samples are further processed into an FPGA. The FPGA performs digital downconversion, which includes fine-frequency tuning and

Table 8.1.: USRP1 and USRP2 comparison [89].

	USRP1	USRP2
Photo		
Interface	USB 2.0	Gigabit Ethernet
FPGA	Altera EP1C12	Xilinx Spartan 3-2000
RF bandwidth to/from host	8 MHz @ 16 bits - 32 MB/s	25 MHz @ 16 bits 100 MB/s
ADC samples	12-bit, 64 MS/s	14-bit, 100 MS/s
DAC samples	14-bit, 128 MS/s	16-bit, 400 MS/s
Daughterboard capacity	2 Tx, 2 Rx	1 Tx, 1 Rx
SRAM	None	1 Megabyte
Power	6 V, 3 A	6 V, 3 A

several decimation filters. After the decimation, raw samples or other data are streamed to a host computer through the host interface. The reverse process applies to the transmit chain [101].

The comparison of the main characteristics between the USRP1 and USRP2 board is given in Table 8.1 [102]. At the receive chain, the USRP1 has four high-speed 12-bit ADCs with the sampling rate of 64 MS/s, which allows for digitization of a 32 MHz wide band (100 MHz using bandpass sampling) [96]. The transmit chain has four 14-bit DACs with the clock frequency of 128 MS/s and the useful output frequency range from DC to about 50 MHz [89]. Four input and four output channels with the real sampling are paired up to two inputs and two outputs with the complex (IQ) sampling and further connected to an Altera Cyclone EP1C12 FPGA. More about IQ sampling can be found in [103]. The FPGA further reduces data rates for the USB 2.0 and is connected to the computer via a Cypress FX2 USB 2.0 interface chip. Both the FPGA circuitry and USB microcontroller are programmable over the USB 2.0 bus.

The USRP2 board is released in 2008 and presents an evolution of the USRP1 board. It contains a Xilinx Spartan 3-2000 FPGA connected to a host computer via the Gigabit Ethernet (GbE) port. The USRP2 also features a Secure Digital (SD) card reader used for loading the firmware. The receive chain has a dual 14-bit ADC LTC2284 chip used at the sampling rate of 100 MS/s. At the transmit chain, a dual 16-bit DAC AD9777 chip fed with clock frequency of 100 Ms/s produces 400 MS/s based analog output based on

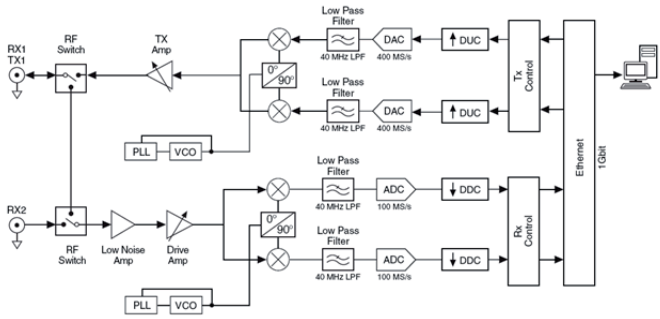


Figure 8.2.: General USRP Architecture - USRP2 [101].

a selectable interpolation rate ($2x/4x/8x$) [89]. The transmit and receive chains operate independently but share a common internal 10-MHz reference clock with the nominal accuracy of 10 ppm from which local oscillator (LO) is derived. Timing and frequency between two USRPs can be synchronized using the MIMO expansion port, which also acts as an Ethernet switch allowing a pair of USRPs to share a single GbE connection. The 10-MHz reference clock and pulse per second (PPS) SMA connectors on the front of the USRP enable an external frequency reference and timing synchronization to supplement the internal reference clock for greater frequency accuracy or to provide synchronization among a larger numbers of devices.

Two important operations inside the FPGA are digital downconversion (DDC) at the receive chain and digital upconversion (DUC) at the transmit chain. Because the data rate of the digitized IF signal at the output of an ADC is too high for further processing on the GPP, it has to be decimated. The DDC shown in Figure 8.3 performs two actions. First, it downconverts the signal from the IF to the baseband. The complex input IF signal is multiplied by the constant IF exponential signal such that the resulting complex signal is centered at 0 Hz. Secondly, the DDC decimates the signal such that the decimated data rate is adapted to the rates of the USB 2.0 or GbE port reasonable for the GPP computing capability. The DDC can be treated as a low-pass filter followed by a downsampler. The decimation is performed by a four stage cascaded integrator-comb (CIC) filter, a high performance filter using only adders and delays [103]. The CIC can decimate in the ranges [1,128] and [4,512] for the USRP1 and USRP2, respectively. To finally obtain the best possible spectral shaping and to reject out-of-band signals, there is a 31-tap half-band filter (HBF) cascaded to the DDC. The USRP2 additionally has another 7 tap HBF filter that decimates by the two. The standard FPGA configuration implements two complete DDCs. There is also an image with four DDCs but without half band filters, which allows one, two, or four separate RX channels, which are interleaved. The USRP can operate in full duplex mode such that the multiple channels must be the same rate while the combined rate must not exceed 32 MB/s or 100 MB/s for USRP1 and USRP2, respectively.

At the transmit chain, the baseband signal from the USB 2.0 or GbE port has to be upconverted to the IF band, i.e., to be adjusted to the clocking rate of the DACs. The

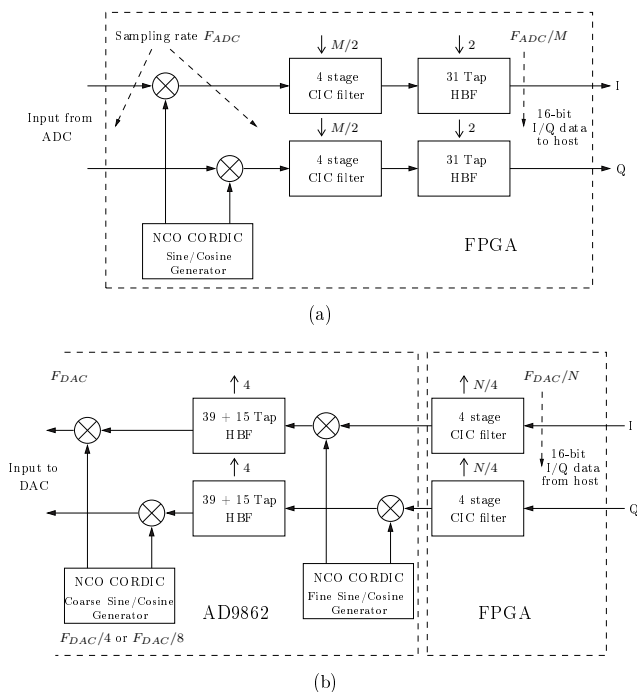


Figure 8.3.: The digital downconversion (a) and upconversion (b) at the USRP [89].

procedure is reversal to the receiver chain. The input IF signal is first interpolated by the CIC filters in the FPGA. The signal is further interpolated by a factor of four using HBF filters and upconverted to the IF. In contrast to decimation, HBF filters and digital upconversion are implemented in the AD9862 DAC chip, not in the FPGA, as shown in Figure 8.3.

The Hardware - RFX2400 Daughterboard

The major part of analog processing is performed in a daughterboard, which is connected to the USRP via the SMA connectors. It has a heterodyne structure containing an RF filter to circumvent the out-of-band transmission, a low noise amplifier (LNA), a mixer to translate the signal from RF to intermediate frequency (IF), an IF filter, and an IF amplifier. The complete list of daughterboards provided by Ettus Research is given in [101]. For our experimentation we have chosen the RFX2400 daughterboard, a transceiver board operating in full duplex mode in 2.4-2.5 GHz ISM band. The main features of the RFX2400 are:

- Frequency range 2.4-2.483 GHz

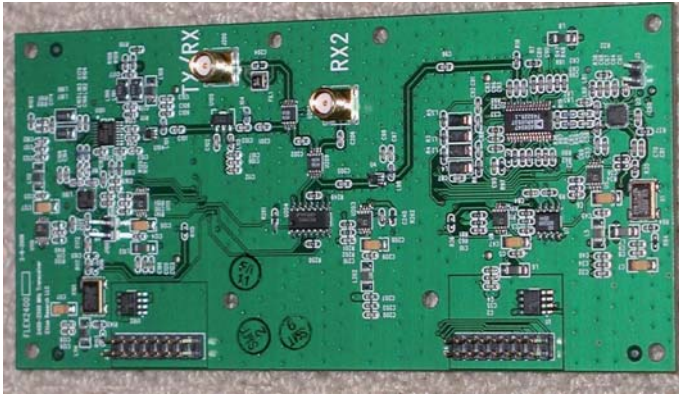


Figure 8.4.: RFX2400 daughterboard.

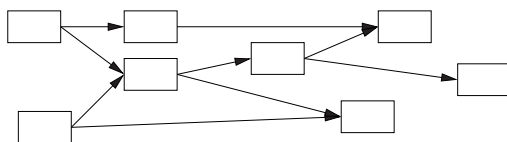
- Maximal transmit power 50 mW (17 dBm)
- Independent local oscillators for the Tx and Rx chains
- Noise figure 8 dB
- Adjustable transmit power controllable from the GNU Radio.

As shown in Figure 8.4, the RFX2400 daughterboard has two SMA connectors allowing for the two independent RF sections. The connector TX/RX has access to the output of the DAC for the transmit chain and to the input of the ADC for the receive chain, while the connector RX accesses only the input of the ADC for the receive chain.

The Software - Gnu Radio Framework

A data flow among different blocks is abstracted by a *flow graph*, a directed acyclic graph where the vertices corresponds to the GNU Radio blocks and edges are data streams as shown in Figure 8.5. Generally, the GNU Radio blocks shown in Figure 8.6 operate on continuous data streams. Most of the blocks have a set of input and/or output ports, and therefore they consume data from the input streams and generate data for their output streams. Special blocks called sources and sinks either only consume or only produce data, respectively. Examples of sources and sinks are blocks that read and write, respectively, from the USRP receive ports, sockets, and file descriptors. Each block has an input and output signature (IO signatures), which defines the minimum and maximum number of input and output streams, respectively, as well as the size of the data type on the corresponding stream. The supported types are:

- **c** - complex interleaved floats (8 byte each)
- **f** - floats (4 byte)
- **s** - short integers (2 byte)
- **b** - byte integers (1 byte).

Figure 8.5.: An example of a *flow graph*.

Each block defines a *general_work()* function that operates on its input to produce the output streams. To help the scheduler decide when to call the work function, blocks also provide a *forecast()* function that returns the system runtime, the number of required input items required to produce a number of output items, and how many output items a block can produce given a number of the input items. At the runtime, the blocks inform the system how many input (output) items they have consumed (produced). The blocks may consume data on each input stream at a different rate, but all of the output streams have to produce data at the same rate. The input and output streams of a block have the associated buffers. Each input stream has a read buffer, from which the block reads data for further processing. Similarly, after processing, a block writes data to the appropriate write buffers of its output streams. The data buffers are used to implement the edges in the flow graph: the input buffers for a particular block are at the same time the output buffers of the upstream block in the flow graph. The GNU Radio buffers are single writer, multiple reader FIFO (First In First Out) buffers.

Several blocks are connected in Python forming a flow graph using the *connect* function that specifies how the output stream(s) of a processing block connects to the input stream of one or more downstream blocks. The flow graph mechanism then automatically builds the flow graph; the details of this process are hidden from the user. A key function performed during the construction of a flow graph is the allocation of data buffers to connect the neighboring blocks. The buffer allocation algorithm considers the input and output block sizes and the relative rate at which blocks consume and produce items on their input and output streams. Once the buffers have been allocated, they are connected with the input and output streams of the appropriate block.

Several blocks can also be combined in a new block, named *hierarchical* block as shown in Figure 8.7. Hierarchical blocks are implemented in Python and together with other blocks can be combined into a new hierarchical block. Input and output ports of hierarchical blocks have the same constraints as those of terminal blocks.

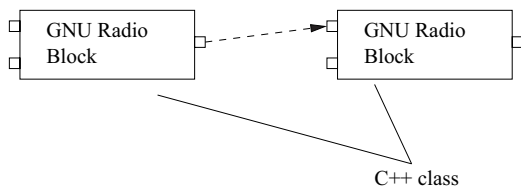


Figure 8.6.: GNU Radio blocks.

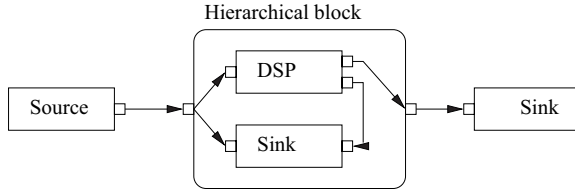


Figure 8.7.: An example of a flow graph with a *hierarchical* block.

The GNU Radio scheduler executes the graph that was built by the flow graph mechanism. During the execution, the scheduler queries each individual block for its input requirements and uses the abovementioned forecast functions to determine how much data the block can consume from its available input. If sufficient data is available in the input buffers, the scheduler calls the work function within a block. If a block has insufficient input, the scheduler simply moves on to the next block in the graph. The skipped blocks will be executed later, when more input data become available. The scheduler is designed to operate on a continuous data stream.

8.2.1. An Example: Wireless Channel Simulation

It will be shown how a model for a static wireless channel can be implemented as a GNU Radio hierarchical block. The channel is affected by the multipath propagation, frequency offset, and additive noise. Figure 8.8 shows a model with internal blocks and the corresponding ports [104].

The multipath effects are modeled using a FIR-filter for which the complex filter coefficients are taken from an arbitrary channel model, e.g., Rayleigh channel model. The signal from an input port is derived to the corresponding GNU Radio block *gr.fir_filter_ccc*. The suffix *ccc* denotes that the input stream, output stream, and filter coefficients are of complex data type.

According to (2.53), the frequency offset is modeled as a sine wave with the fixed frequency and is multiplied with the incoming signal. The corresponding GNU radio blocks are the complex sine signal source *gr.sig_source_c* and the multiplier with complex inputs and outputs *gr.multiply_cc*. Finally, the complex additive Gaussian noise generated by *gr.noise_source_c* is added to the incoming signal in the *gr.add_cc* block and the result is directed to the output port.

The initial parameters of a given hierarchical block, named *simple_channel*, are the additive noise standard deviation, frequency offset normalized to the subcarrier spacing,

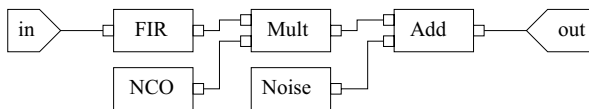


Figure 8.8.: Wireless communication channel simulation model.

Program 1 Python script for the simulation of a wireless communication channel.

```
class simple_channel(gr.hier_block2):
    def __init__(self, noise_rms, frequency_offset, channel_coefficients):
        gr.hier_block2.__init__(self, "simple_channel", # Blocktype Identifier
            gr.io_signature(1,1,gr.sizeof_gr_complex), # incoming
            gr.io_signature(1,1,gr.sizeof_gr_complex)) # outgoing

        # for example channel_coefficients = [0.5+0.1j, 0.2-0.01j]
        multipath_sim = gr.fir_filter_ccc(1, channel_coefficients)

        # frequency_offset normalized to subcarrier spacing
        # amplitude = 1.0, DC offset = 0.0
        offset_src = gr.sig_source_c(1, gr.GR_SIN_WAVE, frequency_offset, 1.0, 0.0)
        mix = gr.multiply_cc()

        # noise_rms -> var(noise) = noise_rms**2
        noise_src = gr.noise_source_c(gr.GR_GAUSSIAN, noise_rms/sqrt(2))
        add_noise = gr.add_cc()

        # describe signal paths
        self.connect(self, multipath_sim)          # incoming port
        self.connect(multipath_sim, (mix,0))
        self.connect(offset_src, (mix,1))
        self.connect(mix, (noise_add,0))
        self.connect(noise_src, (noise_add,1))
        self.connect(noise_add, self)            # outgoing port
```

and complex FIR-filter coefficients. The IO signatures of the input and output ports are identical; there is minimum one port and maximum one port for both input and output. At the runtime, internal blocks are initialized and connected to the flow graph. The corresponding Python script is shown above.

8.3. TIGR System Overview

The system diagram of the TIGR framework is shown in Figure 8.9. The transmitter and receiver nodes are composed of a host commodity computer and a general purpose RF hardware (USRP)[101]. The baseband signal processing at the host computer is implemented in the GNU Radio framework, while the USRP performs computationally intensive operations such as filtering, up- and downconversion controlled through a robust application programming interface (API) provided by the GNU Radio. The communication between the transmit and receive node is organized as a reconfigurable continuous one-way transmission of OFDM symbol frames. As shown in Table 8.2, input configuration parameters are divided into two sets. The set of static parameters containing FFT size, the number of subchannels, frame size, etc., is initialized at the beginning of the

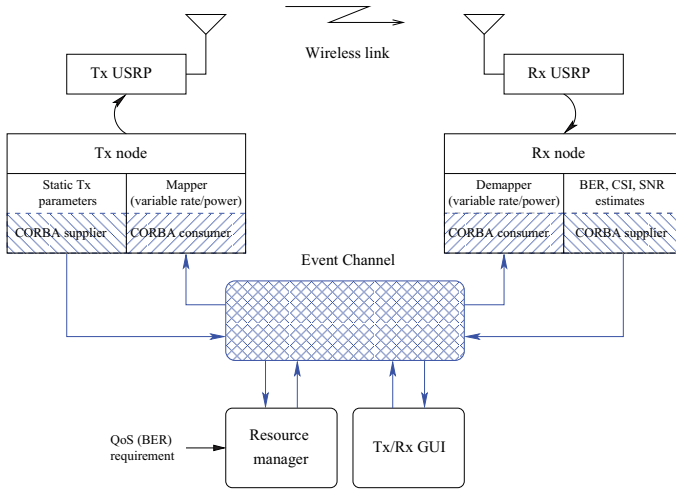


Figure 8.9.: The system overview.

transmission and is known to both nodes. The set of dynamic parameters, which are reconfigurable at runtime includes the total transmit power, carrier frequency, and allocated power/rate over subcarriers. The TIGR OFDM frame structure is shown in Figure 8.10. The sequence of ten data symbols is preceded with two preambles (one synchronization preamble and one preamble used for the channel estimation) and one ID symbol used for the synchronization.

Each frame contains an unique ID associated with the current parameter settings. The decoded ID enables the receiver to perform a parameter lookup necessary for demapping. The forwarding of meta information to the receiver is implemented by the Common Object Request Broker Architecture (CORBA) communication library [105] over the Ethernet. Moreover, the ID is utilized both at the transmitter and receiver to determine the random bit sequence used for BER calculation.

The transmission parameters such as carrier frequency, transmission power, and power/bit loading on the subcarriers, can be reconfigured on-the-fly. The Graphical User Interface (GUI) is further used to observe the impact of these changes on the received signal by showing estimated SNR, normalized channel state information, carrier frequency offset (CFO), and measured BER.

Moreover, TIGR can operate in two modes: the first mode assumes the RF transmission where the transmitter and receiver are interfaced with the USRPs; the second is the simulation mode where the transmitter and receiver “communicate” over an emulated channel, without the RF interface (USRPs). This allows for the exclusion of unwanted distortions caused by the hardware, but also for system evaluation in the presence of various controllable channel and hardware impairments, such as CFO, sampling frequency offset (SFO), additive noise, interference, and multipath propagation. An example of a simulated channel is shown in Figure 8.11.

Table 8.2.: TIGR OFDM symbol parameters.

Bandwidth (<i>static</i>)	Variable, up to 8 MHz
FFT length (<i>static</i>)	64 – 1024
Frame length (<i>static</i>)	Variable
Carrier frequency (<i>dynamic</i>)	2400 – 2483 MHz
Modulations (<i>dynamic</i>)	BPSK, QPSK, 8-PSK, 16-QAM, 32-QAM, 64-QAM, 128-QAM, 256-QAM
Power (<i>dynamic</i>)	Up to 20 mW

Signal processing blocks are implemented as C++ classes and connected in a directed acyclic graph forming a flow graph in Python. Flow graphs are implemented as Python scripts that take care of communication among signal processing blocks. The most of the used signal processing blocks within TIGR are developed at the TI and are further referred with the prefix *ofdm_*, while CORBA blocks have the prefix *corba_*. The blocks from the standard GNU Radio library are usually prefixed as *gr_*.

8.3.1. CORBA Integration

The backbone of the system is realized over the local Ethernet network by the CORBA event service, a distributed communication model that allows an application to send an event that will be received by any number of objects located in different logical and/or physical entities. The typical communication model through an *event channel* is shown in Figure 8.12. The estimated parameters that indicate link quality (average S(I)NR, CSI, and BER) and current static transmitter's parameters are supplied as CORBA events

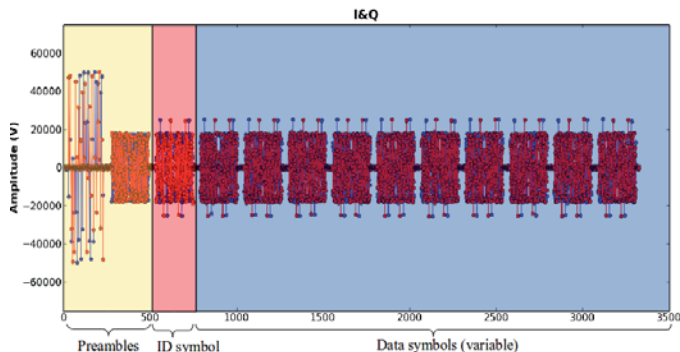


Figure 8.10.: Frame structure.

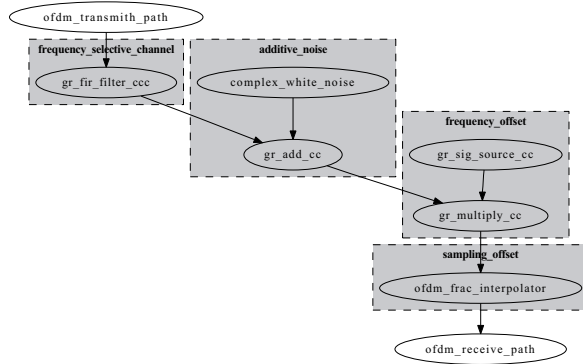


Figure 8.11.: Simulation channel between the transmit and receive chain.

to an event channel, which allows other components (consumers) within the system to register their interests in events.

From a supplier’s perspective, the event channel appears as a single consumer, while from a consumer’s perspective, the event channel appears as a single supplier. In this way, suppliers and consumers are decoupled where any number of suppliers can issue events to any number of consumers while using a single event channel.

As shown in Figure 8.9, the estimated parameters that indicate a link quality are supplied to an event channel from the GNU Radio flow graph using CORBA suppliers implemented as a GNU Radio sink block. At the GUI, a CORBA consumer provide the corresponding events to the GUI objects. In this way, the transceiver system can run independently of the GUI activity since CORBA consumers make no assumptions on the number of connected CORBA suppliers.

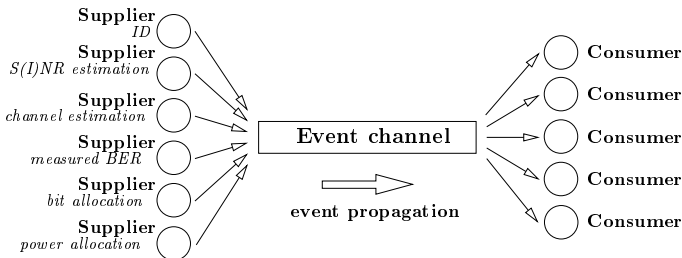


Figure 8.12.: Communication model through an event channel.

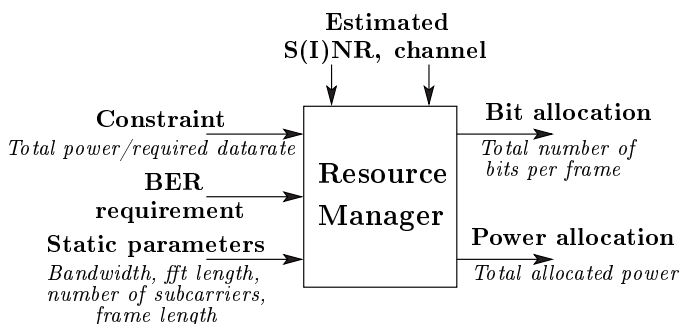


Figure 8.13.: Resource manager.

8.3.2. Resource Manager

The central control unit that determines the optimal input transmission parameters for given requirements is *resource manager*, whose basic functionalities are depicted in Figure 8.13. Controlled by the interactive GUI it consumes the supplied events forwarded from an event channel, performs the allocation in an optimal manner, and supplies new transmission parameters, i.e., the total transmit power and power/rate per subchannel (rate and power allocation), which are finally consumed by other components within the system. The current stage of the TIGR framework implements resource manager as a Python class, thus allowing for flexible design of different scenarios, such as grouping of subcarriers in subbands in the presence of weak frequency-selective channels or enabling an opportunistic use of available spectrum through Dynamic Spectrum Access (DSA).

8.3.3. Graphical User Interface (GUI)

The Graphical User Interface (GUI), facilitating the demonstration, is developed in the Qt/C++ framework. The simplicity, high modularity, and rich collection of Qt GUI widgets allow for fast prototyping of the interactive GUI elements. The transmitter's GUI contains the static transmission parameters and current allocation of rate and power over subchannels as shown in Figure 8.14. The receiver's GUI, depicted in Figure 8.15, dynamically shows estimated signal parameters (average $S(I)NR$, CSI, BER, and a scatterplot of the specified subcarrier) and contains interactive interface for controlling of transmitted power and allocation strategy in the resource manager. This further allows for on-the-fly configuration of the number of allocation subbands in resource allocation, given the certain constraints and requirements. For example, TIGR can be reconfigured from per subcarrier allocation based on the SNR measurements [15] to per subband allocation in DSA environment based on the SINR measurements [16].



Figure 8.14.: The transmitter's GUI.

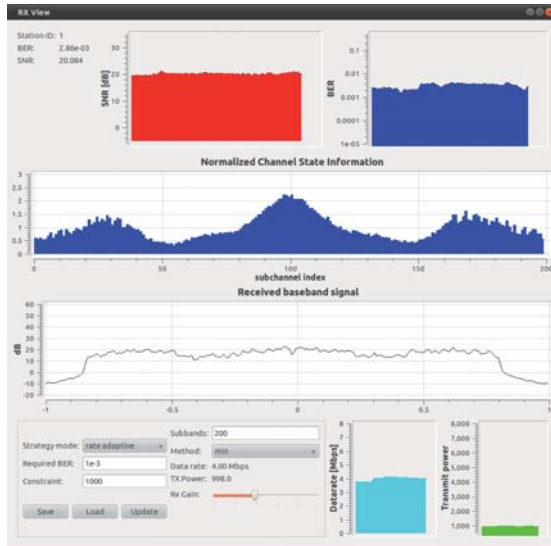


Figure 8.15.: The receiver's GUI with an interactive control interface.

8.3.4. The Transmitter

The flow graph of the TIGR OFDM transmitter is shown in Figure 8.16. The transmitter is controlled by the *corba_tx_control* Python hierarchical block. It contains the *corba_C++* blocks that represent wrappers for CORBA consumers. The control of the whole adaptation starts from the *corba_id_src* block that consumes an ID (implemented as a simple counter) from the event channel. Every time when an ID is changed it "triggers" the other CORBA blocks to consume events from the event channel. The ID is also encoded with the repetition code while being included in the frame after the preambles, as shown in Figure 8.10. Whenever the ID is changed at its input, the *corba_bitmap_src* block connects to an event channel, consumes the event that contains the bit allocation vector, and, finally, forwards this vector to the *ofdm_generic_mapper* block. Similarly, *corba_bitcount_source_src_si* consumes the bit allocation and, for the given frame size, calculates the number of bits which will be transmitted within one frame. For the bit allocation vector $\mathbf{r} = [r_1 \ r_2 \ \dots \ r_{N_u}]$, where N_u is the number of loaded subcarriers, the total number of transmitted bits within the frame containing N_{pl} payload OFDM symbols is given by

$$r_{frame} = N_{pl} \sum_{n=1}^{N_u} r_n. \quad (8.1)$$

The *ofdm_reference_data_source_id* block reads r_{frame} bits from the stored random data file and supplies them to *ofdm_stream_controlled_mux_b*, which further multiplexes it with the encoded ID, thus forming a data payload part of the frame. The output of *ofdm_stream_controlled_mux_b* is forwarded to the *ofdm_generic_mapper_bcv* block that actually performs mapping of the incoming bits to the complex signals. This block is triggered once for each frame and performs the mapping according to the output of *corba_bitmap_src*, which is a CORBA consumer block that receives the bit allocation from the event channel and forwards it to the *ofdm_generic_mapper_bcv* block.

The ID OFDM symbol is always BPSK modulated to provide the robust and safe signaling communication to the receiver. Following the mapper, the signal is derived to the *corba_power_allocator* block that loads on individual or grouped subcarriers the power allocation vector consumed from the event channel. The data stream is further forwarded to the standard OFDM transmit chain. Firstly, *ofdm_pilot_subcarrier_inserter* inserts stored vector of pilot subcarriers into the each data OFDM symbol. Currently, a static configuration of 8 pilot subcarriers is supported, but in general TIGR allows for inserting an arbitrary number of pilots depending on the FFT length and number of available data subcarriers. Furthermore, before the FFT block, each data symbol is padded with the zeros at the edges forming the guard bands to avoid an out-of band transmission due to the high sidelobes. To circumvent unwanted DC and low-frequency components generated by the receiver's frontend [41], the two subcarriers in the middle are also nulled.

The number of nulled DC and side subcarriers is also reconfigurable and is defined at the initialization of the transmitter and receiver script. The zero padded OFDM data symbol, shown in Figure 8.17, with the DFT length of 256, having 200 data subcarriers, two nulled DC subcarriers, eight pilot subcarriers and 23 nulled subcarriers at the both edges, is derived to the IFFT block taken from the standard GNU Radio library. After the IFFT, the time domain signal is forwarded to the *ofdm_frame_mux* block that prepends

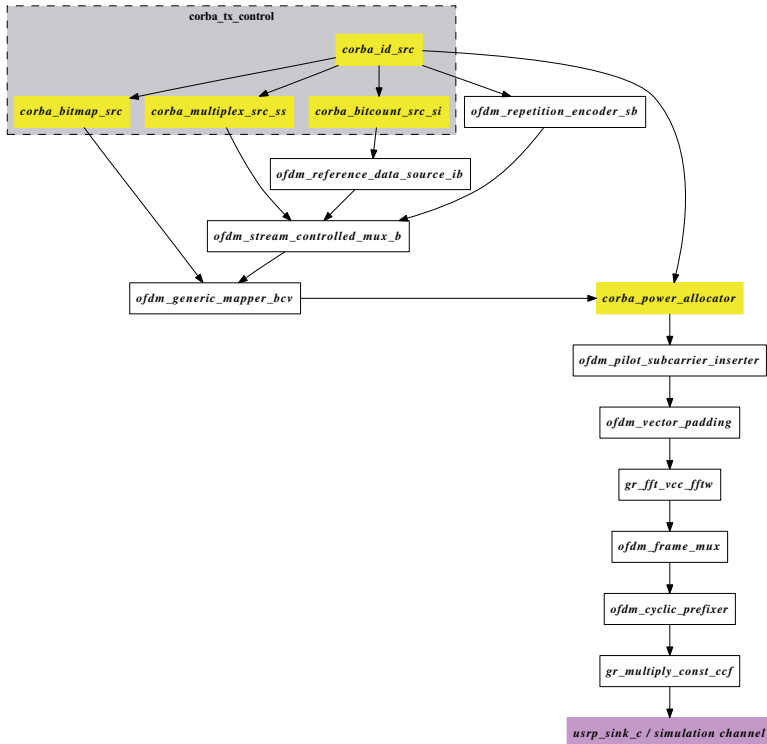


Figure 8.16.: The flow graph of the TIGR OFDM transmitter.

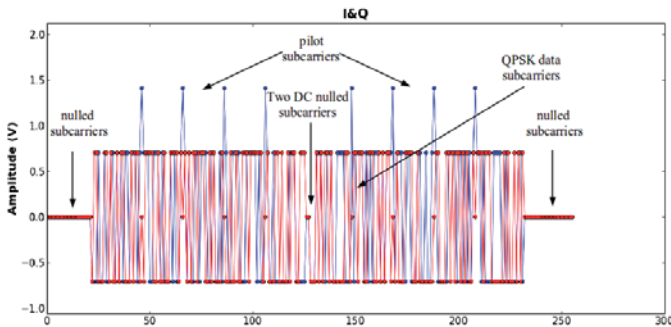


Figure 8.17.: Frequency domain representation of the QPSK modulated OFDM data symbol.

two predefined and prestored preambles. Furthermore, to protect against multipath propagation causing intersymbol interference (ISI), a cyclic prefix (CP) is prepended to each symbol in the frame. The complex OFDM baseband signal is then scaled with the complex amplitude and derived either to the simulation channel or to the USRP where is further upconverted through the DUC and DAC and, finally transmitted to the RF channel the using the RFX2400 daughterboards.

8.3.5. The Receiver

The flow graph of the TIGR receiver is shown in Figure 8.18 containing an incoming complex baseband data stream originating either from a simulation channel or from an USRP (the downconverted signal after the DDC). It is clear that the receive chain has higher computational complexity compared to the transmitter, due to the synchronization and data acquisition required for the decoding of the transmitted signal. In general, besides the receiver chain, TIGR also allows for a simultaneous observation of the spectral content by deriving the incoming complex data stream to the power spectral density (PSD) analyzer whose output is supplied to an event channel and consumed at the receiver's GUI as shown in Figure 8.15.

Timing Synchronization

The first synchronization stage at the receive chain has to actually identify the beginning of an OFDM frame. The implemented frame detection is a slightly modified version of Schmidl & Cox timing estimator [43], which is based on the autocorrelation of the incoming sample stream. Due to the time periodic structure of the first preamble, by detecting the pick of the timing metric, a timing trigger (the start of the each OFDM frame) is created. The resulted timing metric taken as a screenshot from the TIGR GUI is shown in Figure 8.19. The exact timing trigger is located within the plateau, which is induced by a CP insertion. For further information on experimentation with different timing synchronization algorithms in GNU Radio, readers are referred to [106]. The time periodic structure of the first preamble is created in the frequency domain by inserting seven zeros between the loaded subcarriers. In such a way, every eight subcarrier is loaded, which is exploited for the PS SNR estimation proposed in Chapter 4, while the time-domain representation has eight identical parts utilized for the Morelli's CFO estimation method addressed in Section 7.2. The `ofdm_time_sync` block produces two output streams, denoted 0 and 1: the output 0 is the time synchronized complex data stream; the output 1 is the frame (timing) trigger.

CFO Synchronization

After the initial timing estimation, the receiver has to estimate the carrier frequency offset (CFO) caused by the mismatch between the transmitter and receiver oscillator. It is customary to divide the CFO into an integer part (ICFO), a multiple of subcarrier spacing, which produces a shift of subcarrier indexes, plus a fractional part (FCFO), which results into the inter-carrier interference (ICI) due to the loss of the orthogonality among

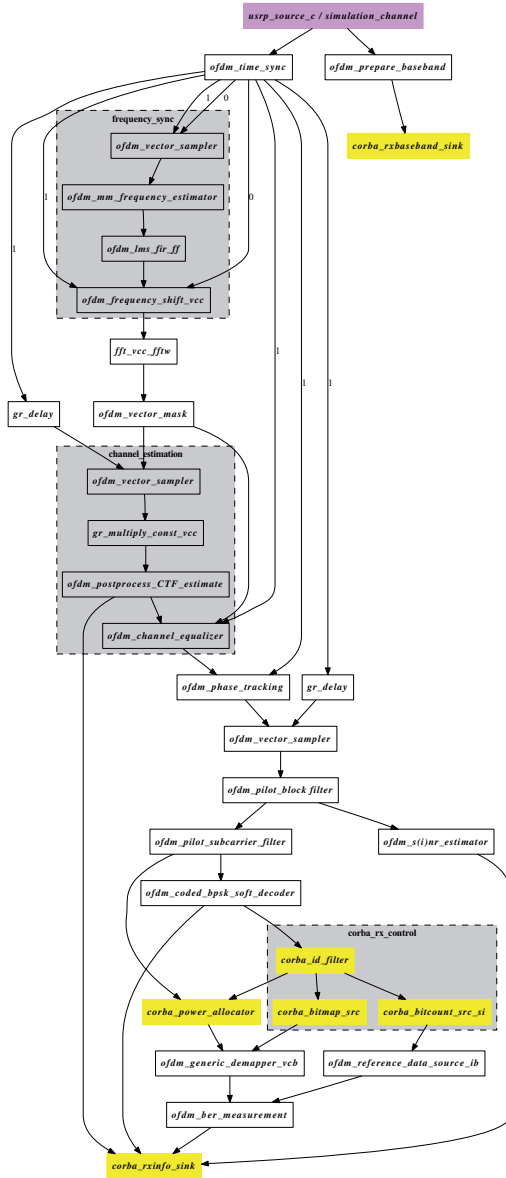


Figure 8.18.: The flow graph of the TIGR OFDM receiver.

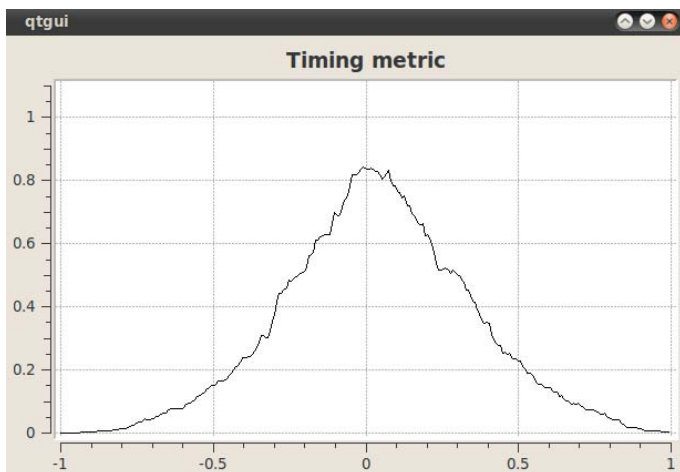


Figure 8.19.: The Schmidl & Cox timing metric for SNR = 10 dB.

the subcarriers. All standard designs of the receiver chain assume the initial stage for the fine frequency synchronization (FCFO estimation based on the autocorrelation of the input stream in the time domain), while the stage for the ICFO estimation is performed after the FFT and is based on the correlation of the frequency-domain structure of used preamble(s). However, to circumvent an additional increase of the receiver complexity and leave the ICFO estimation out, we implement the Morelli's method for the CFO estimation [57].

The Morelli's method extends the acquisition range of the CFO by increasing the number of time periodic parts. During the TIGR implementation, based on the experimental investigation, we choose the number of periodic parts to be eight, thus allowing for the CFO acquisition in the range of $(-4, +4]$ subcarrier spacings Δf . This is shown to be sufficient for the signal bandwidths (2 – 8 MHz) used during the experimentation with the USRPs. The structure of the synchronization preamble is shown in Figure 8.20. The estimated CFO is further filtered and, finally, the phase of each time domain sample is corrected. Nevertheless, as discussed in Section 7.2, there is still a residual CFO and SFO that have to be corrected. The more detailed discussion and the corresponding mathematical model on phase correction and its performance is given in Chapter 7.

Channel Estimation

After the CFO estimation, the next step is the transition from the time to the frequency domain, which is done by the FFT block. To compensate any amplitude and/or phase noise introduced by the wireless channel, an equalization needs to be performed by means of the least square (LS) estimation previously discussed in Section 2.6. The received second preamble is multiplied with the stored conjugated replica of the transmitted version, thus giving the channel frequency response. The

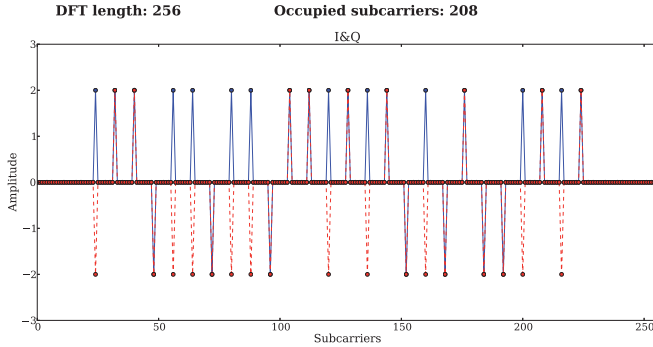


Figure 8.20.: The synchronization preamble logged at the TIGR transmitter. Every 8th subcarrier is loaded with a QPSK symbol.

ofdm_postprocess_CTF_estimate block produces two output streams. The first output is further derived to the *ofdm_channel_equalizer* block. The second output stream contains the squared magnitude of the channel frequency response, which is supplied to an event channel. In such a way, it may be further consumed at the resource manager as the input for a resource allocation algorithm or may be shown at the GUI as depicted in Figure 8.15.

Phase Tracking

Due to the residual CFO and SFO caused by different sampling times of transmitter and receiver, an additional phase correction is performed in the *ofdm_phase_tracking* block based on the phase tracking of pilot subcarriers inserted within the data payload OFDM symbols. The detailed description of the linear least square (LLS) phase tracking algorithm [81] is given in Section 7.2.

Demodulation

Furthermore, to extract only the data symbols (including the ID symbol), preambles and pilot subcarriers are removed in *ofdm_pilot_block_filter* and *pilot_subcarrier_filter*, respectively. Based on the synchronization preamble, the SNR or SINR estimation is performed to provide an information about signal quality to the resource manager. The implemented PS SNR estimation algorithm is proposed in Chapter 4.

After deallocating the power on data subcarriers in the CORBA controlled *corba_power_allocator* block, the demapping of complex samples to a bitstream is performed in *ofdm_generic_demapper_vcb* according to the bitmap allocation consumed from the event channel in *corba_bitmap_src*, in a similar way as at the transmitter. To measure the BER, data from the identical random file as the one stored at the transmitter is derived to the *ofdm_ber_measurement* block that performs BER measurement and supplies it to the event channel. The S(I)NR estimation, channel estimation, BER

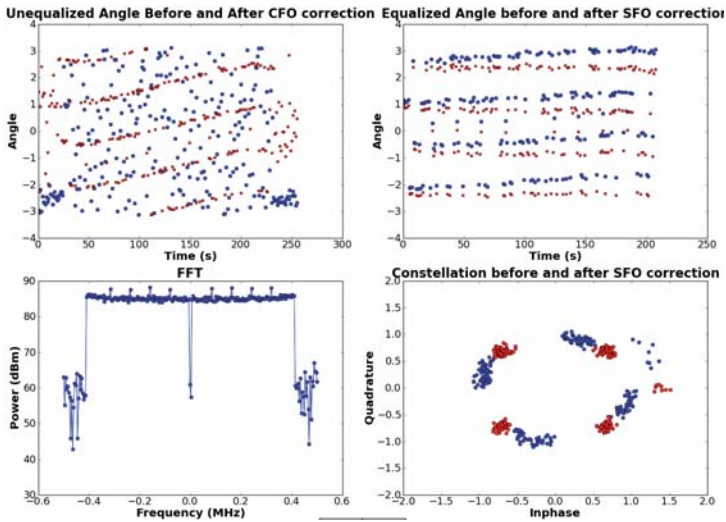


Figure 8.21.: The TIGR receiver performance for the QPSK signal in the simulated channel at SNR = 25 dB, $\epsilon_c = 2.5$, and $\epsilon_s = 20$ ppm.

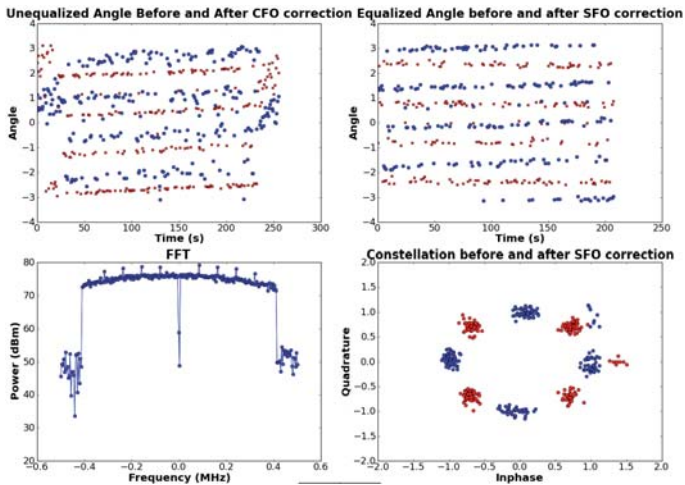


Figure 8.22.: TIGR receiver performance for the QPSK signal with the estimated SNR = 25 dB in an RF channel with 2.45 GHz carrier frequency and 1 MHz bandwidth.

measurements, and current ID block are finally derived to the *corba_rx_info_sink* block, which supplies them to an event channel.

We further investigate the TIGR receiver performance in a simulated AWGN channel with the QPSK modulated subcarriers for SNR $\rho_{av} = 25$ dB, CFO $\varepsilon_c = 2.5$, and SFO $\varepsilon_s = 20$ ppm. Using modified plotting tool available in a standard GNU Radio distribution, the corresponding results are shown in Figure 8.21. The spectrum (PSD) of the received signal is depicted in the bottom left corner. The upper left plot shows the phase of the received data samples before (blue) and after (red) frequency synchronization performed on the time domain signals. The effects of the residual CFO and SFO are still present in the received samples inducing a linear phase increase over the subcarriers, as shown in upper right plot. This plot depicts the input (blue) and the output (red) streams of the *ofdm_phase_tracking* block showing the effect of phase tracking based on the pilot subcarriers. The corresponding constellation plot in bottom right shows the corrected phase shift of data symbols in the I/Q plane prior to deriving to the demapper.

The performance of the TIGR receiver in a real RF environment is shown in Figure 8.22. The RF link between two nodes equipped with the USRP1s operates at the carrier frequency of 2.45 GHz having the bandwidth of 1 MHz. The transmit amplitude is adjusted such that the estimated SNR at the receiver is 25 dB. Similarly to the simulation results, Figure 8.22 shows the effects of the CFO and SFO as well as the effects of their compensation at the TIGR receiver.

8.4. Experimental Results

We conduct a series of measurements using the TIGR framework to investigate the performance of several rate adaptive algorithms in a real RF link. The OFDM symbol parameters assume the DFT length $N = 256$ and $N_u = 208$ occupied subcarriers containing the eight pilot subcarriers used for the phase tracking and 200 data subcarriers,

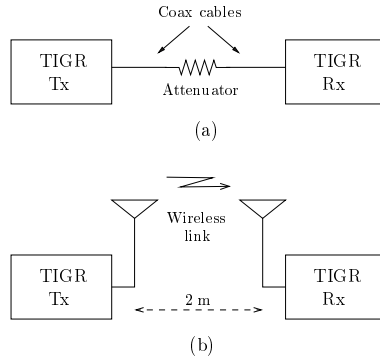


Figure 8.23.: Two RF experimentation scenarios: (a) Connection over coaxial cable with an attenuator - Wired link; (b) Wireless link.

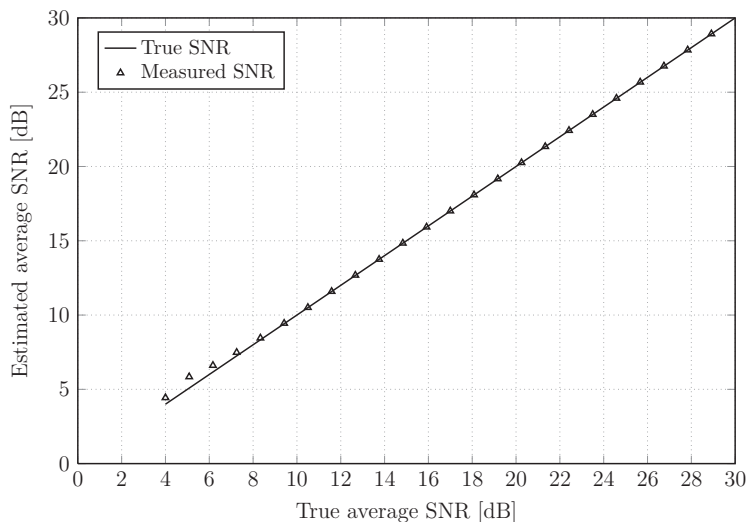


Figure 8.24.: Estimated vs. true average SNR.

as shown in Figure 8.17. The synchronization preamble has $Q = 8$ identical parts as depicted in Figure 8.20. The communication between the transmit and receive node is organized as a reconfigurable continuous one-way transmission of OFDM symbol frames. The frame structure is shown in Figure 8.10 and represents a sequence of ten data symbols preceded with two preambles (one synchronization preamble and one preamble used for the channel estimation) and one ID symbol used for the synchronization. The easy reconfigurable back-end and control mechanisms of the TIGR framework allows for the on-the-fly monitoring of the measurement result at the receiver GUI shown in Figure 8.15.

We consider two experimental RF scenarios shown in Figure 8.23. First, the transmitter and receiver nodes (composed of a host commodity computer and an USRP) are connected via an RF cable and an attenuator as shown in Figure 8.23a. The *wired link* between two nodes excludes the impact of a wireless RF channel and includes only the effects of the hardware components neglecting the potential effects caused by the RF cable. In this way, the wired link emulates a static, frequency-flat SNR propagation environment, which we use to determine the rate power function for a real RF environment. The second scenario assumes the *wireless link* between two nodes equipped with omnidirectional antennas and spaced two meters apart, which we use for the experimental evaluation of the rate adaptive transmission. During the RF experimentation we use one pair of USRP1s and one pair of USRP2s equipped with the RFX2400 daughterboards. Each measurement is performed using the carrier frequency of 2.48 GHz, which belongs to the IEEE 802.11 Channel 14. Since Wireless LAN devices in Europe and North America are prohibited to operate in this channel, we avoid the potential interference to an RF link between two USRPs.

Prior to performing the actual measurements, we have conducted several calibration steps. First, because an accurate SNR estimate represents the crucial input parameter

to many allocation methods, we need to validate the performance of the PS estimator in the TIGR framework. As discussed in Section 8.3, TIGR can operate in the simulation mode where the transmitter and receiver are connected via an artificial channel with the controllable noise power. The performance of the estimated vs. true average SNR in the simulated ETU channel is shown in Figure 8.24. The PS estimator implemented in the TIGR framework provides an unbiased estimate over a large SNR range in the absence of any hardware impairment.

Moreover, when using the USRP boards equipped with the RFX2400 daughterboard as an RF interface, the only controllable parameter that determines the transmit power is the digital amplitude assigned from the GNU radio software. The next calibration step is to investigate how the change of the digital amplitude influences the SNR of the received signal in an RF link. For both pairs of USRP boards we measure the SNR performance as a function of the digital transmit amplitude. We set the receiver gain to 30 dB since it provides the best SNR value given the received power [107]. This is performed by using the TIGR control mechanism where a specially designed resource manager automatically changes the transmit amplitude every 30 seconds while logging to the file the measured SNR and the corresponding transmit amplitude.

The measurement results that correspond to a pair of USRP1 boards for signal bandwidths of 1 MHz and 2 MHz are shown in Figure 8.25. For each value of the signal bandwidth, we investigate four cases: one case assumes the wireless link shown in Figure 8.23b while other three cases assume the wired links with 20 dB, 30 dB, and 40 dB attenuators, as shown in Figure 8.23a. The wireless link experiences the similar SNR conditions as the wired link having a 40 dB attenuator. As expected, the corresponding curves for different bandwidths differ approximately 3 dB. It is shown that the received SNR stops increasing after reaching the digital amplitude value of 12000. For further experimental investigation with the pair of USRP1s we choose a bandwidth of 1 MHz and use a wired link with 40 dB attenuation for the derivation of the rate power function. The received SNR range between 7 dB and 29 dB is achieved by changing the transmit amplitude from 400 to 12000.

Similarly, the corresponding measurement results for a pair of USRP2 boards using the signal bandwidths of 2.5 MHz and 5 MHz are shown in Figure 8.26. The x-axis corresponds to the digital amplitude range of $[0,1]$. In this case, the wireless link experiences similar SNR conditions as the wired link having a 30 dB attenuator. Here, the signal with the bandwidth of 5 MHz achieves at most THE SNR of 27 dB, while the 2.5 MHz signal reaches 29 dB in a wireless link. For further investigation with the USRP2s we choose a bandwidth of 2.5 MHz and a wired link with 30 dB attenuation for the derivation of the rate power function. In these cases, the received SNR range between 7 dB and 29 dB is achieved by changing the transmit amplitude from 0.005 to 0.3.

8.4.1. TIGR Receiver Performance

SNR Estimation

Furthermore, we investigate the performance of the PS estimator in a real RF environment in terms of the normalized variance of the measured average SNR. This measure is equivalent to the normalized mean square error (NMSE) given in (4.68), which is considered

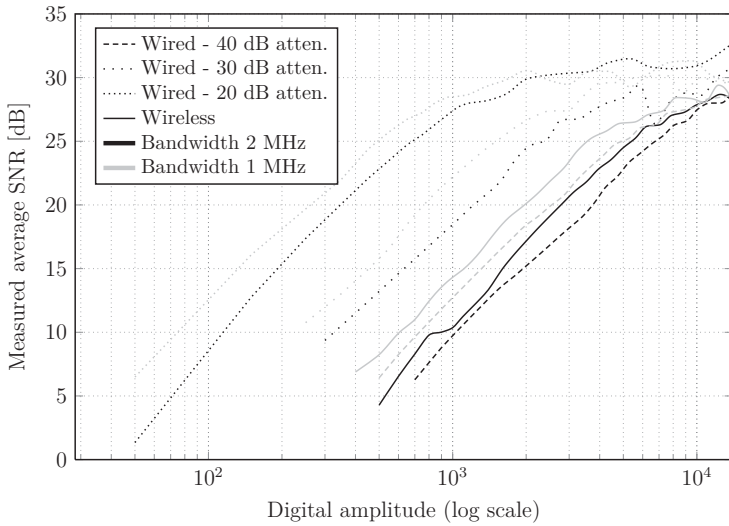


Figure 8.25.: Estimated SNR vs. digital amplitude for the USRP1.

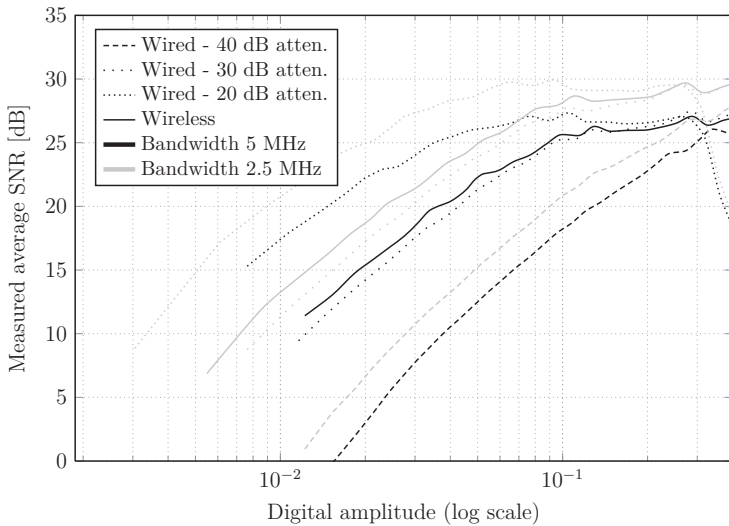


Figure 8.26.: Estimated SNR vs. digital amplitude for the USRP2.

as a performance metric for the Matlab simulations performed in Section 4.2. However, in contrast to the simulation, the true SNR is not available for an RF channel. Assuming the unbiased estimator, the mean value of the measured SNR can approximate its true value, such that the normalized variance is a good approximation of the NMSE.

Figure 8.27 shows the measurement results for the normalized variances as a function of the measured average SNR. The results correspond to several investigated scenarios in a real RF environment (using a pair USRP1 and USRP2 boards both in wired and wireless links) as well as to the simulation results obtained from the Matlab and TIGR. While both simulation models assume an AWGN channel, the TIGR simulation includes the complete transceiver chain containing all synchronization stages, while the Matlab simulation corresponds to an ideal transceiver. The simulation results shows that as SNR increases, the normalized variance obtained from the TIGR simulation is approaching the Matlab simulation curve and becomes identical to it for the SNR higher than 22 dB. In the investigated RF scenarios for SNR values below 10 dB the normalized variances of the PS estimator are substantially high, which is caused by the estimation variance of the synchronization stage in the low SNR region. While the particular USRP pair performs similarly for the wired and wireless links, the USRP1 pair provides better performance than the pair of USRP2 boards. Moreover, as SNR increases, the normalized variance is increasing starting from 22 dB and 18 dB for a pair of USRP1s and USRP2s, respectively. This can be explained by the presence of the residual CFO and SFO, which are theoretically discussed in Chapter 7.

Figure 8.28 shows the probability density function (pdf) of the measured average SNR in several investigated RF scenarios as well as the analytical result given in (4.53) for the true SNR = 10 dB. Here, for the measurement results, the “true SNR” corresponds to the measured average SNR ≈ 10 dB. The TIGR simulation results agree with the derived analytical model. Moreover, the pdf of the measured average SNR is characterized with the increased variance for the investigated RF scenarios.

CFO Estimation

The next step of the calibration process is to investigate the performance of the TIGR synchronization stages. We firstly consider the performance of the CFO estimator in a real RF environment and observe the long term CFO variations due to the environmental changes and inherent offsets between different oscillators. The performance of the CFO estimator is affected by the real-world degradations, such as voltage fluctuations, phase noise, and variable SNR.

Figure 8.29 shows the measured normalized CFO over the period of one hour for a pair of USRP1s and a pair of USRP2s. For each pair of boards, the transmitter and receiver node are connected via an RF cable and a 30 dB attenuator as shown in Figure 8.23a. The transmitter and receiver daughterboards operate independently, each with its own local oscillator to generate an RF carrier frequency. The output of the *ofdm_mm_frequency_estimator* block from the receiver flow graph shown in Figure 8.18 is logged to the file in the receiver PC at the beginning of each frame. The mean values of the collected measured CFO estimates are shown in Figure 8.29.

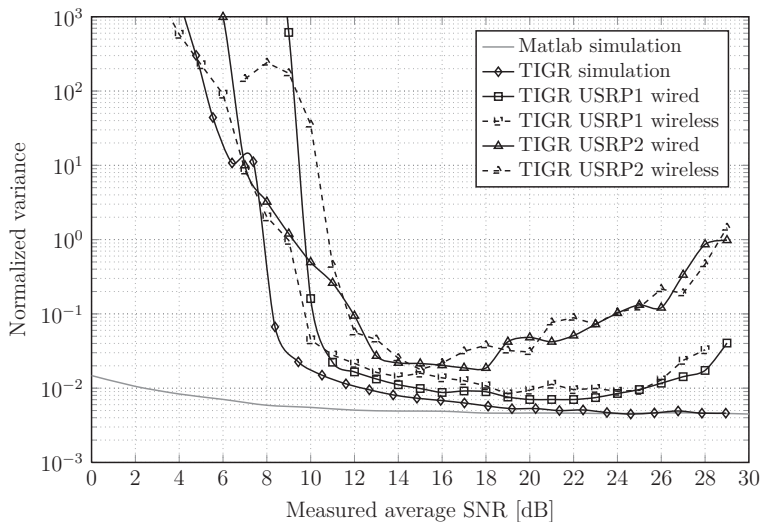
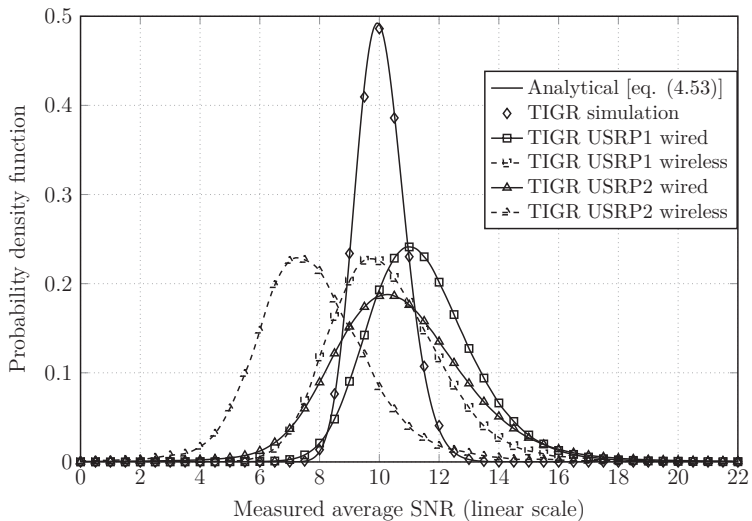


Figure 8.27.: Normalized variance vs. measured average SNR.

Figure 8.28.: Pdf of the average PS SNR estimation in TIGR for the measured average SNR ≈ 10 dB.

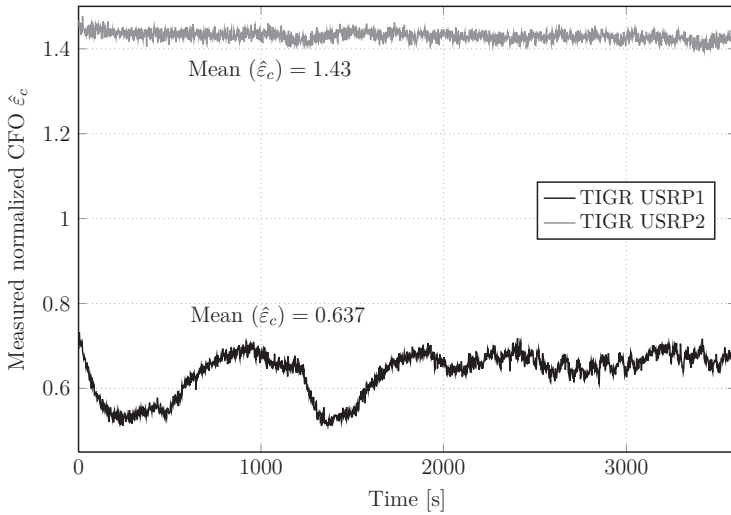


Figure 8.29.: Measured normalized CFO over the period of one hour; The measured average SNR ≈ 10 dB.

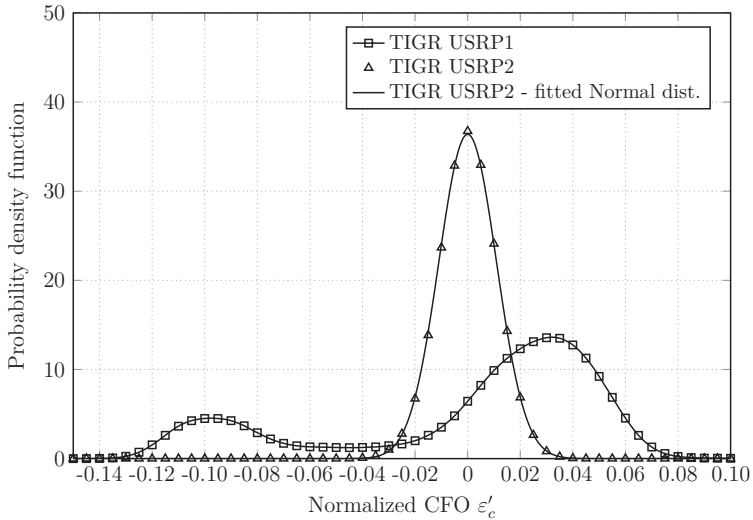


Figure 8.30.: Pdf of the normalized residual CFO $\epsilon'_c = \hat{\epsilon}_c - \text{Mean}(\hat{\epsilon}_c)$ measured over the period of one hour; The measured average SNR ≈ 10 dB.

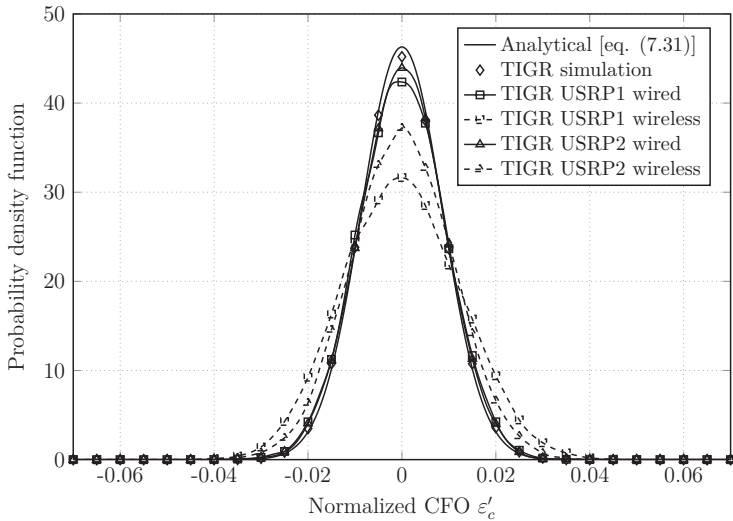


Figure 8.31.: Pdf of the normalized residual CFO $\epsilon'_c = \hat{\epsilon}_c - \text{Mean}(\hat{\epsilon}_c)$ measured over the period of two seconds; The measured average SNR ≈ 10 dB.

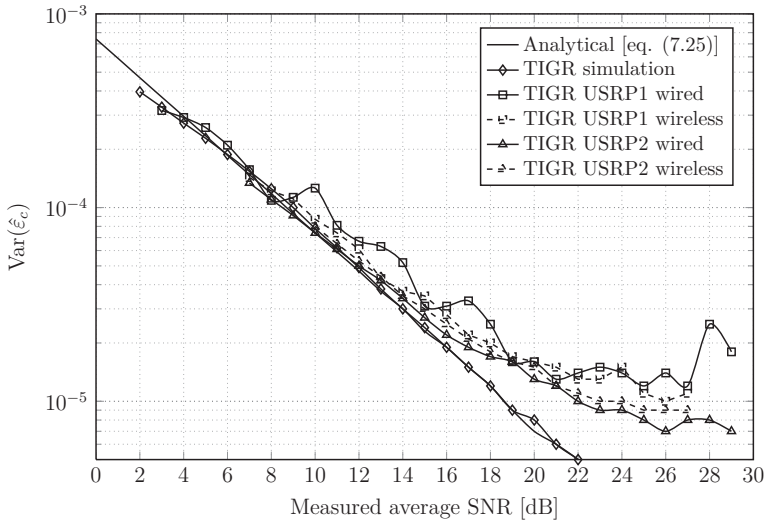


Figure 8.32.: $\text{Var}(\hat{\epsilon}_c)$ vs. measured average SNR.

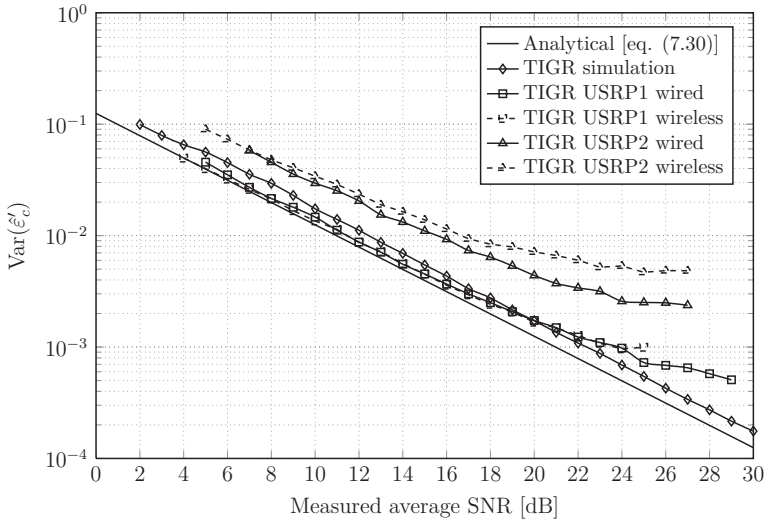
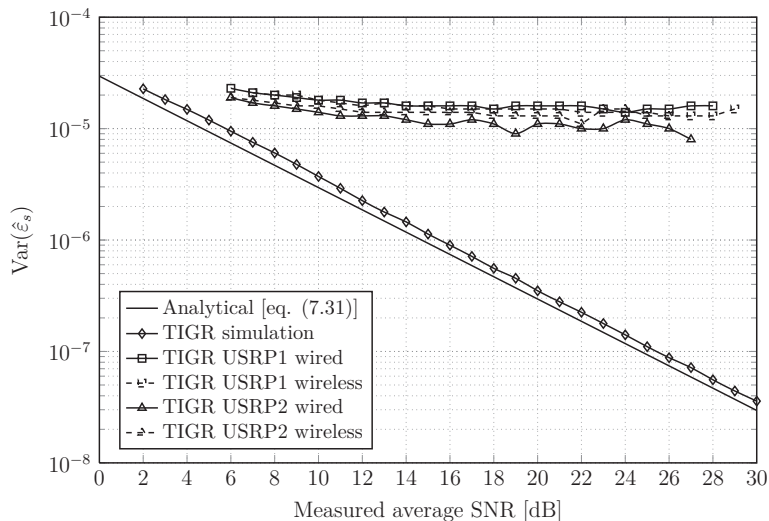


Figure 8.33.: $\text{Var}(\hat{\epsilon}'_c)$ vs. measured average SNR.

The CFO variation over time between the two USRP1 boards is higher compared to the CFO variation associated with the USRP2 boards. The corresponding pdfs are shown in Figure 8.30. The shape of the pdf indicates that the measured CFO between the two USRP1 boards can not be characterized by a simple distribution. In contrast, the pdf of the measured CFO for the pair of USRP2 boards can be fitted to the Gaussian curve determined by the corresponding empirical mean and standard deviation.

As shown, the CFO varies over time and temperature. However, it can be assumed that the frequency offset is constant during the frame, whose duration is less than 5 ms in our system settings. Since the CFO is extracted at the beginning of each frame, the addressed time and temperature variations can be accurately tracked. The pdfs of the short term CFO measurements over the period of two seconds are shown in Figure 8.31. The results obtained from the TIGR simulation fit well with the Normal distribution while the measurements taken in a real RF environment are characterized with the increased variance.

Figure 8.32 shows the variance of the measured CFO as a function of the measured average SNR. For this measurement campaign, the resource manager is configured to change the transmitted amplitude in a given range every 30 seconds and log the measured CFO in a file. The TIGR simulation results fit well with the analytical variance given in 7.25. However, the measurement results follow the analytical curve closely up to the SNR of 14 dB and then start to reach the performance floor, which is caused by the presence of the SFO. The transceiver using a pair of USRP2s performs slightly better than the transceiver with the USRP1 boards.

Figure 8.34.: $\text{Var}(\hat{\epsilon}_s)$ vs. measured average SNR.

Phase Tracking

We further investigate the performance of the phase tracking at the TIGR receiver chain. Similarly as for the CFO estimation, the specially configured resource manager changes the transmitted amplitude in a given range every 30 seconds and log the residual CFO and SFO outputs of the *ofdm_phase_tracking* block for each OFDM symbol. The variance of the measured residual CFO and measured SFO as a function of the measured SNR is shown in Figure 8.33 and Figure 8.34, respectively. In both cases, the measurements obtained from the TIGR simulation perform closely to the analytical curves. However, the results related to the measured SFO in a real RF environment reach the floor already in the low SNR region.

8.4.2. Resource Allocation Performance

To further analyze the performance of rate adaptive algorithms in a real RF environment using the TIGR framework we need to determine the corresponding rate-power function, which maps the performance of a particular modulation to the required SNR under the given BER condition. As the first step, we investigate the BER vs. SNR simulation performance of the TIGR framework in an AWGN channel excluding all potential hardware impairments. Figure 8.35 shows this performance for three different cases. The first case corresponds to the mapper/demapper performance that excludes other transceiver stages, i.e., it assumes an ideal transceiver. The second case considers the performance of TIGR including channel estimation in the absence of synchronization stages. And, finally, the third case corresponds to the whole TIGR transceiver chain. As a benchmark we use the

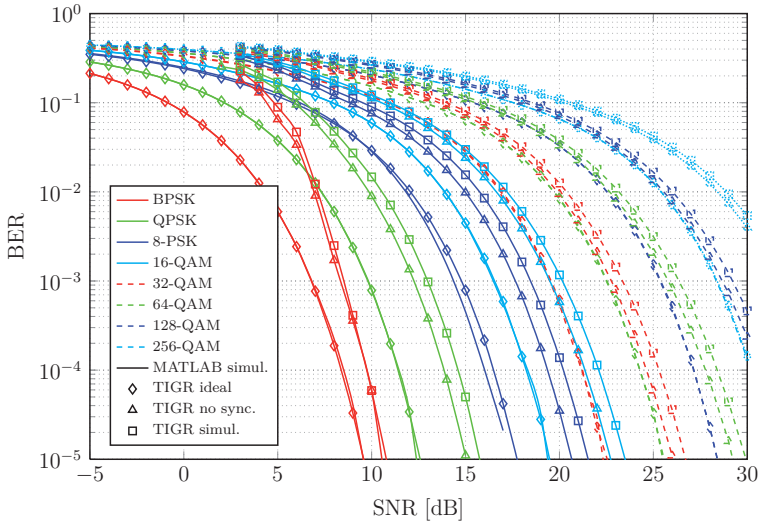


Figure 8.35.: BER vs. SNR performance of the TIGR transceiver in the simulation environment.

results obtained from the Matlab simulation of an ideal transceiver. The results show that an ideal TIGR transceiver performs identically to the corresponding Matlab simulation model. As expected, the implemented LS channel estimation in TIGR introduces a SNR loss that varies between 3 and 4 dB for a particular modulation scheme. Moreover, starting from QPSK up to 256-QAM there is an additional loss around 0.8 dB introduced by the finite variance of the synchronization stages (CFO estimator and phase tracking).

We further investigate the BER performance for a pair of the USRP1 boards. Due to the implementation issues, the transmitted signal bandwidth is 1 MHz. The two RF scenarios are considered, as shown in Figure 8.23. At first, we evaluate the performance of the wired link, where the USRPs are connected via a coaxial cable and a 40 dB attenuator to include only the effects of hardware components, thereby excluding the influence of a wireless channel and neglecting the potential effects caused by an RF cable. Secondly, the BER vs. SNR performance of the wireless link is investigated using omnidirectional antennas spaced two meters apart. The obtained results together with the TIGR simulation performance are shown in Figure 8.36. The TIGR receiver performs almost identically in a wired and a wireless link due to the small bandwidth of the transmitted signal, which prevents multipath effects. Based on the measured BER performance shown in Figure 8.36, the corresponding rate-power function for $\text{BER} = 10^{-3}$ is depicted in Figure 8.37 together with the Shannon spectral efficiency given in (3.1). The results show that the residual phase offset in a real RF environment precludes the two highest modulation schemes, 128-QAM and 256-QAM, from achieving the BER of 10^{-3} within the operating SNR range.

Figure 8.38 and Figure 8.39 show the experimental results obtained from the measurement campaign where several resource allocation algorithms are investigated in a real RF

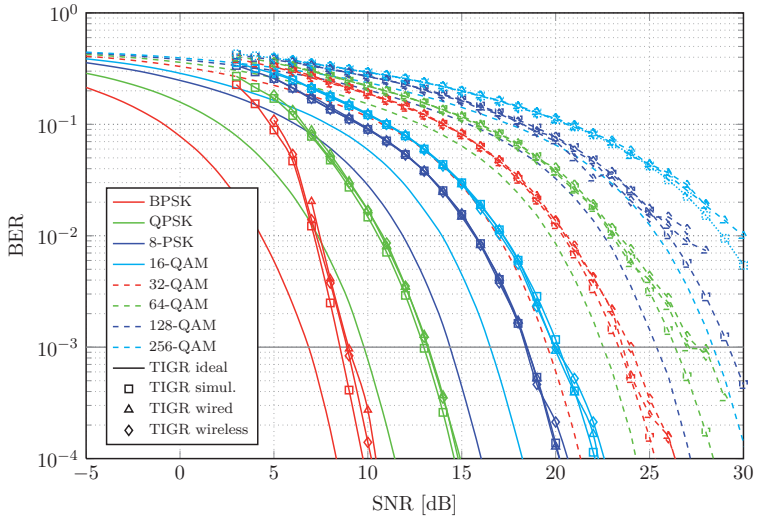


Figure 8.36.: BER vs. SNR performance of the TIGR transceiver with USRP1 boards for the bandwidth of 1 MHz.

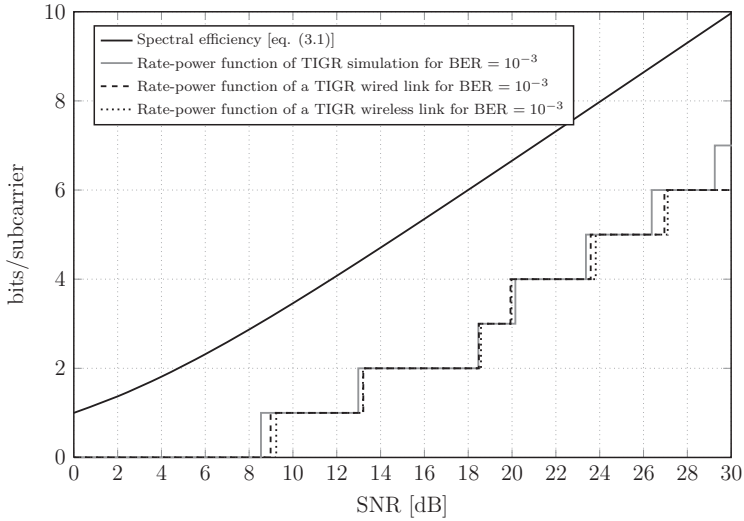


Figure 8.37.: Rate-power function of the TIGR transceiver with USRP1 boards for the bandwidth of 1 MHz and $BER = 10^{-3}$.

Table 8.3.: Rate-power function, SNR gap, and SNR margin of the TIGR transceiver with USRP1 boards for the bandwidth of 1 MHz and BER = 10^{-3} .

Modulation bits r	TIGR		
	Required SNR [dB]	$\Gamma_{r,GR}$ [dB]	ΔSNR_{GR} [dB]
1	9.24	9.24	2.45
2	13.2	8.43	3.39
3	18.58	10.13	4.17
4	19.97	8.21	3.43
5	23.82	8.91	4.25
6	27.1	9.11	4.55
7			
8			

environment. The OFDM signal parameters are given at the beginning of the section while the corresponding rate-power function shown in Figure 8.37 is used to determine the required SNR values to achieve BER = 10^{-3} , see Table 8.3. We consider the Levin-Campello (LC) algorithm, Subband allocation with the eight subbands using geometric SNR mean as the measure of the subband quality (SB-geo), and Uniform power (UP) rate adaptive allocation in an wireless link using a pair of USRP1 boards equipped with omnidirectional antennas spaced two meters apart. Due to the narrowband nature of the wireless channel, grouping the subcarriers in subbands does not affect the achieved rate due to the large coherence bandwidth. This results in almost identical performance for the LC and SB-geo algorithms, while the UP algorithm performs approximately 3 dB worse. The corresponding measured BER values perform similarly. Although the high variance of the BER measurement causes the instability of the measured BER for values less than 10^{-3} , the main tendency of the BER performance is easily noticeable in Figure 8.39.

Furthermore, Figure 8.40 shows the measured BER performance for a pair of the USRP2 boards. The transmitted signal bandwidth is 2.5 MHz. We consider the same two RF scenarios shown in Figure 8.23 as for a pair of the USRP1s. The TIGR simulation performance is used as a benchmark. In contrast to the previous case that assumes the USRP1 boards, the TIGR performance in a real RF environment with the USRP2 boards with the transmitted signal of 2.5 MHz bandwidth is worse than the simulation results obtained from the simulation. However, the TIGR receiver performs almost identically in a wired and a wireless link because the signal bandwidth of 2.5 MHz is still insufficiently large to introduce multipath effects. Based on the measured BER performance shown in Figure 8.40, the corresponding rate-power function for BER = 10^{-3} is depicted in Figure 8.41 together with the Shannon spectral efficiency in (3.1). The corresponding SNR values required to achieve BER = 10^{-3} are given in Table 8.4. The results show that the residual phase offset in a real RF environment precludes the highest modulation scheme, 256-QAM, from achieving the BER of 10^{-3} within the operating SNR range.

Moreover, to compare the performance of the TIGR transceiver in a wireless RF environment with the Matlab simulation results discussed in Chapter 7, the ETU channel with parameters given in Appendix A is “emulated”. This is achieved by the convolution of the output signal of the transmit chain with the considered channel impulse response. The resulted signal is further forwarded to the USRP2 such that the transmitted narrow-

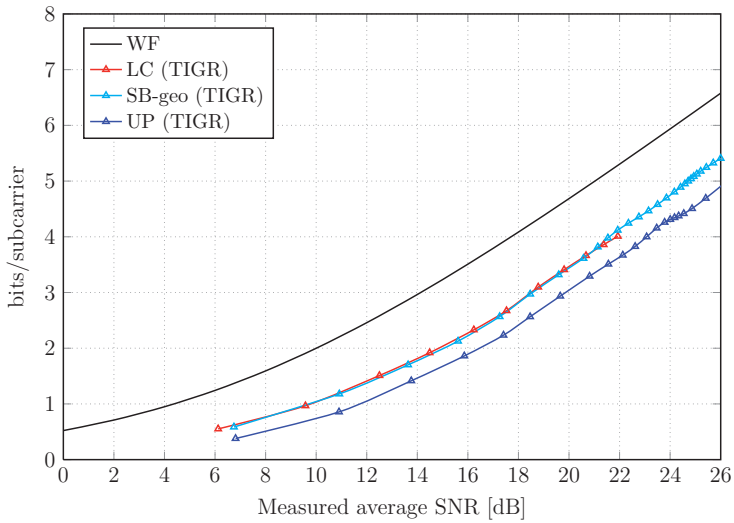


Figure 8.38.: Number of bits per subcarrier vs. SNR for BER= 10^{-3} ; Wireless RF channel; USRP1 boards; Bandwidth 1 MHz.

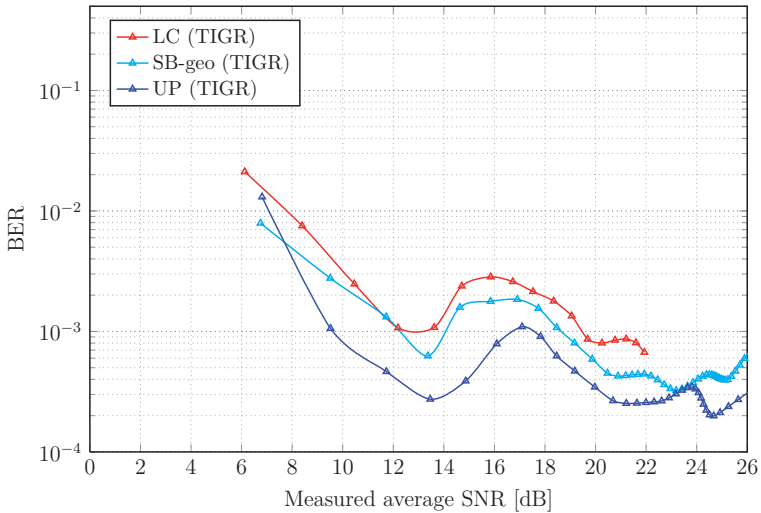


Figure 8.39.: BER vs. SNR for BER= 10^{-3} in TIGR; Wireless RF channel; USRP1 boards; Bandwidth 1 MHz.

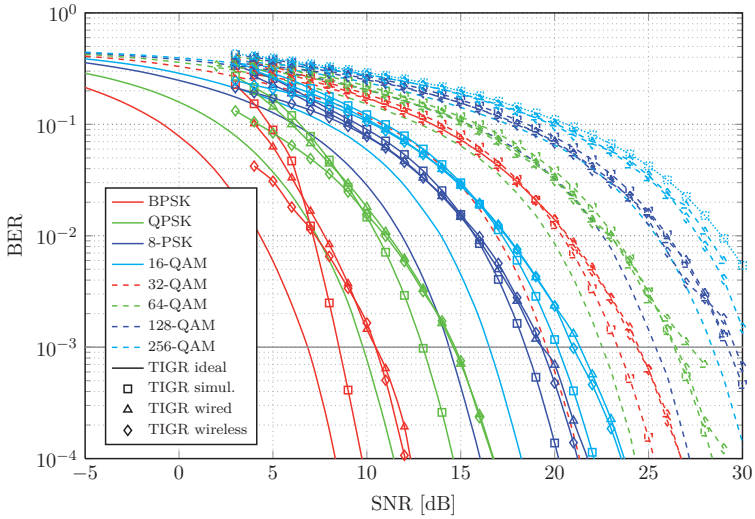


Figure 8.40.: BER vs. SNR performance of the TIGR transceiver with USRP2 boards for the bandwidth of 2.5 MHz.

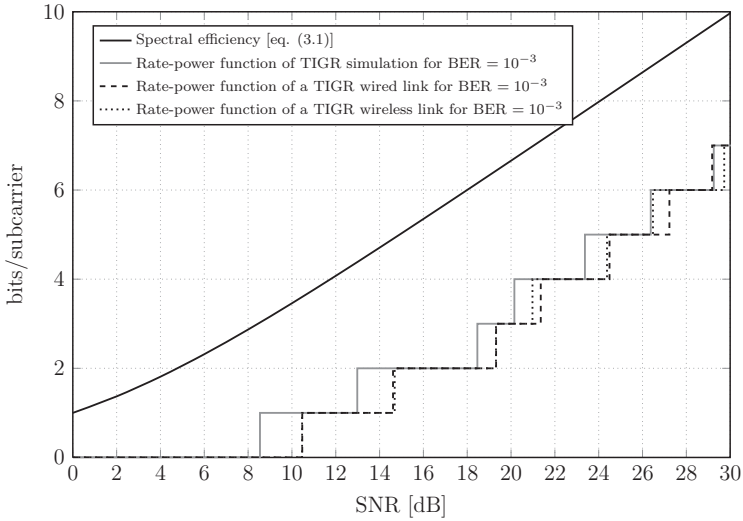


Figure 8.41.: Rate-power function of the TIGR transceiver with USRP2 boards for the bandwidth of 2.5 MHz and $BER = 10^{-3}$.

Table 8.4.: Rate-power function, SNR gap, and SNR margin of the TIGR transceiver with USRP2 boards for the bandwidth of 2.5 MHz and $\text{BER} = 10^{-3}$.

Modulation bits r	TIGR		
	Required SNR [dB]	$T_{r,GR}$ [dB]	ΔSNR_{GR} [dB]
1	10.46	10.46	3.67
2	14.69	9.92	4.89
3	19.31	10.86	4.9
4	20.98	9.22	4.44
5	24.38	9.47	4.82
6	26.48	8.48	3.93
7	29.73	8.69	4.32
8			

band signal of 2.5 MHz “becomes” frequency-selective, allowing us to investigate the joint influence of the time dispersive channel and hardware impairments to the performance of the TIGR transceiver.

Figure 8.42 shows the bits per subcarrier vs. measured average SNR performance for several rate adaptive allocation algorithms, including the LC, SB-geo allocation with the eight subbands, and UP methods. Three different transmission scenarios are investigated. The first scenario assumes a TIGR transceiver using a pair of USRP2 boards equipped with omnidirectional antennas spaced two meters apart in the wireless “emulated” ETU RF channel. The second scenario corresponds to the TIGR simulation including the ETU channel. The third scenario presents the simulation results obtained from the Matlab transceiver model with the same synchronization stage as the one implemented in TIGR including the additional presence of the normalized SFO $\varepsilon_s = 20$ ppm, which corresponds to the specifications of the USRP boards.. Finally, the optimal water-filling (WF) continuous rate allocation is given as a benchmark. The SB-geo and LC allocation still perform closely as in the previously investigated case with the USRP1 boards and 1 MHz signal. Moreover, due to conservative strategy of keeping the transmitted amplitude constant over all subcarriers, the UP allocation achieves lower rate compared to other two methods. The investigated methods achieve lower rates in a real RF environment compared to the simulation scenario due to the higher SNR requirements to support the particular modulation scheme given the $\text{BER} = 10^{-3}$ constraint, as shown in Table 8.4.

It can be also concluded that the concept of SNR gap provides a good strategy in the operating SNR range. As shown in Figure 8.43, starting from the minimum SNR = 10.46 dB that allows for the transmission (of a BPSK modulated signal), the investigated methods violate the BER constraint just slightly even in the presence of a relatively large SNR estimation variance in the high SNR region shown in Fig 8.27. However, the large performance gap between the optimal WF solution and investigated algorithms, shown in Figure 8.42, may be further decreased by implementing more advanced channel estimation scheme or more accurate synchronization methods, which comes at the cost of increased computational complexity. Software profiling of the GNU Radio transceiver, introduced in Appendix D, gives the insight into the computational complexity of each individual signal processing block. This provides a good starting point for the future development of the TIGR framework and improvement of the overall transceiver performance.

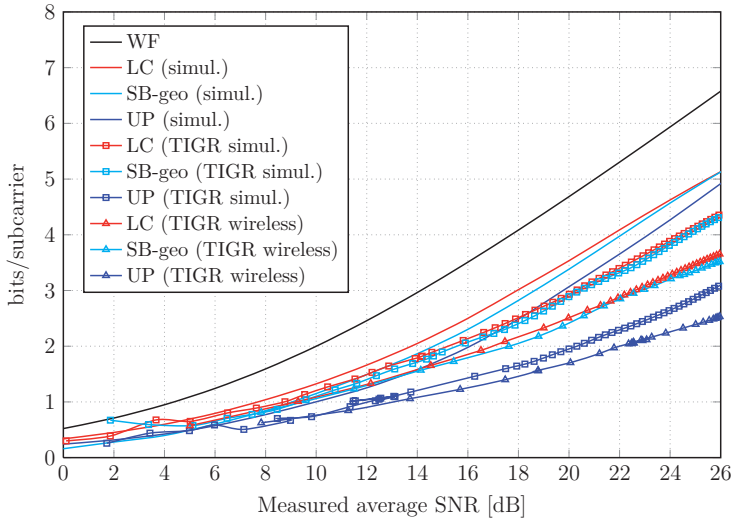


Figure 8.42.: Number of bits per subcarrier vs. SNR for BER= 10^{-3} ; Wireless “emulated” RF channel; USRP2 boards; Bandwidth 2.5 MHz.

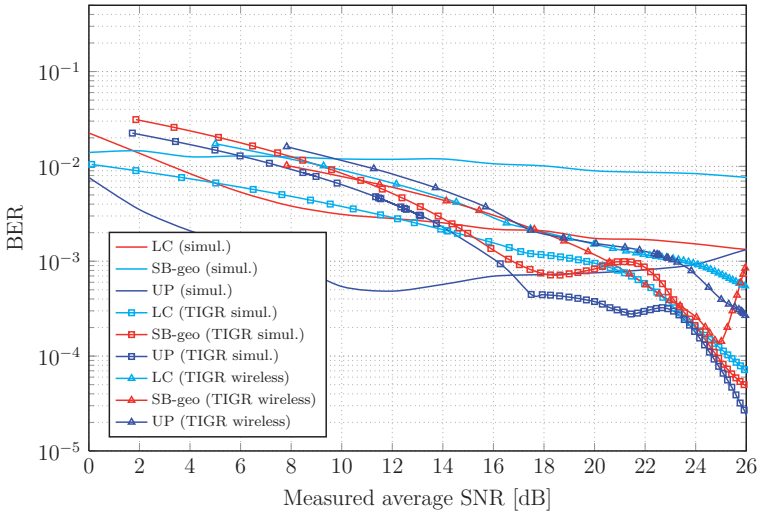


Figure 8.43.: BER vs. SNR for BER= 10^{-3} in TIGR; Wireless “emulated” RF channel; USRP2 boards; Bandwidth 2.5 MHz.

9. Conclusions

9.1. Summary

Optimal utilization of radio resources (bandwidth, transmit power) in multicarrier systems becomes very challenging due to the coexistence of various wireless standards within the same frequency band. The investigation of theoretical concepts for wireless resource management in a real RF environment requires flexible testbeds with a wide range of reconfigurable parameters. To bridge the gap between the theoretical investigations and real world scenarios we have developed a highly reconfigurable SDR framework, named TIGR.

In this thesis, we have proposed novel methods and presented new results concerning the performance evaluation of an adaptive OFDM system in a wireless RF environment. First, we have developed an efficient algorithm for the SNR estimation. It has been noticed that existing methods for SNR estimation performs poorly in a frequency-selective channel. The proposed algorithm outperforms the existing solutions and provides a reliable SNR estimate required for many resource allocation algorithms.

Initially proposed for SISO systems, the SNR estimator has been further extended to a MIMO scenario, thus enabling for future expansion of the TIGR framework. Moreover, we have shown that the properly adjusted preamble structure can be applied for the joint synchronization and spectrum characterization in OFDM-based cognitive radio systems.

Furthermore, we have conducted a simulation study investigating the influence of hardware impairments on the performance of rate adaptive allocation methods. Several resource allocation algorithms, characterized with different computational complexity and sensitivity to hardware imperfections, have been considered. The presence of the estimation noise is introduced through the concept of SNR loss assuming the individual SNR gap for each modulation scheme. While most of the current research work assumes the constant gap approximation due to decreased computational complexity, it has been shown that this assumption introduces performance degradations and violation of the constraints that become even more critical in the presence of synchronization errors. The simulation results are compared to the measurements obtained in a real RF environment using the implemented testbed.

The results show the applicability of modeled hardware imperfections and robustness of the proposed SNR estimator to the design of efficient resource allocation algorithms. Finally, through the extensive measurement campaign in a real RF environment, we have demonstrated that the TIGR framework can be utilized for further experiments related to this area.

9.2. Outlook

TIGR supports for continuous capacity achieving OFDM transmission with the optimal rate and power allocation over subchannels for given system constraints. The developed framework extends the PHY layer functionalities of the current wireless standards by offering control and feedback mechanisms for easy reconfiguration of transmission parameters. This allows for the evaluation of different communication strategies in either simulation or RF scenarios. However, additional experimental evaluation in different indoor conditions is required in order to get a larger insight into the capability of the TIGR framework

The current efforts are focused on the profiling of the transmitter/receiver execution in order to optimize the signal processing code, thus allowing for higher bandwidths and implementing more efficient algorithms. Additionally, TIGR is close to support an additional feature of fully adaptive Coded OFDM (COFDM), which enables the joint coding and rate allocation. This brings the framework capabilities closer to the current wireless standards (WiMAX, LTE). The work on MIMO implementation has been conducted and some initial results are derived. Available flexibility further allows for the integration of some advanced communication features, such as an implementation of cyclostationary signatures [18, 19, 20] and filterbank multicarrier techniques in order to support additional cognitive radio scenarios.

A. Simulation Setup

The extended ITU channel models adopted by LTE are used for simulations in this thesis. They are based on ITU channel models further modified for the large bandwidth scenarios supporting up to 25 MHz bandwidth [26]. The power delay profiles of Extended Pedestrian A (EPA), Extended Vehicular A (EVA), and Extended Typical Urban (ETU) are listed in Table A.1.

Table A.1.: Extended ITU channel models adopted in LTE.

Path number	EPA		EVA		ETU	
	Delay	Average relative power	Delay	Average relative power	Delay	Average relative power
l	τ_l (ns)	Ω_l (dB)	τ_l (ns)	Ω_l (dB)	τ_l (ns)	Ω_l (dB)
1	0	0	0	0	0	-1
2	30	-1	30	-1.5	50	-1
3	70	-2	150	-1.4	120	-1
4	80	-3	310	-3.6	200	0
5	110	-8	370	-0.6	230	0
6	190	-17.2	710	-9.1	500	0
7	410	-20.8	1090	-7	1600	-3
8			1730	-12	2300	-5
9			2510	-16.9	5000	-7

The corresponding RMS delay spreads τ_{RMS} , derived in (2.4), are listed in Table A.2.

Table A.2.: RMS delay spreads τ_{RMS} for extended ITU channel models.

Category	Channel model	RMS delay spread τ_{RMS} (ns)
Low delay spread	EPA	43
Medium delay spread	EVA	357
High delay spread	ETU	991

The adopted Doppler frequencies 5, 70, 300, and 1000 Hz correspond to pedestrian/vehicular speeds of 2, 30, 120, and 350 km/h, respectively, for the carrier frequency of 2.7 GHz.

B. OFDM Based Wireless Standards

We provide a brief overview of the current wireless standards based on OFDM technology with the corresponding system parameters. It includes a discussion on available practical modulation and coding schemes.

B.1. Wireless LAN (IEEE 802.11 Series of Standards)

The first communication standard that adopted OFDM transmission for broadband connectivity was Digital Subscriber Line (DSL). It has been shown that DSL is an efficient solution for the last-mile connection over the existing Public Switched Telephone Network (PSTN) primarily used to carry voice communication between 300 and 3400 Hz. DSL operates over the twisted pair copper wire in a higher frequency band, reaching up to 30 MHz and achieving up to 200 Mbps in the recent implementations. Due to the very stable channel behavior, such high data rates are enabled by the adaptive modulation per sub-carrier without the significant signaling loss. In particular, the SNR estimates obtained during the sufficiently long initialization phase stay valid until the end of the transmission. The initially proposed algorithms for the adaptive subcarrier allocation [2, 3] were designed for DSL systems.

However, a DSL signal undergoes strong attenuation over the distance requiring for a repeater on every few kilometers. An increased need for the mobility, while keeping broadband connectivity, furthermore resulted in the development of the Wireless LAN (WLAN) standard. WLAN establishes connection between wireless stations, such as PCs, notebooks and handhelds, and the access point connected to DSL or Ethernet. This offers broadband connectivity to either fixed wireless users or pedestrian users. WLAN operates in unlicensed frequency bands, such as ISM bands at 900 MHz, 2.4 GHz, and 5.8 GHz, as well as in the Unlicensed National Information Infrastructure (U-NII) band at 5 GHz.

The standardization of WLAN was performed within the 802.11 framework. The first version IEEE 802.11b based on Direct Sequence Spread Spectrum (DSSS) is introduced in 1999 and utilized 83.5 MHz spectrum in the 2.4 GHz ISM band, while offering the data rates up to 11 Mbps within the range of 100 m. However, it became clear that further throughput could not be increased by using the single carrier transmission, due to the distorting influence of multipath spread for the short symbol durations. Therefore, IEEE 802.11a was introduced in 1999 as the first wireless standard to use OFDM modulation. IEEE 802.11a specifies communication in the 5.4 GHz U-NII band over 20 MHz bandwidth with the FFT length of 64 with 48 data subcarriers. Various modulation and coding schemes (MCS) were defined to provide scalable data rates from 6 up to 54 Mbps within less than 100 m range. In 2003, IEEE 802.11g was introduced as an extension of IEEE

Table B.1.: IEEE 802.11 system parameters.

Parameters	Specification
Frequency band [GHz]	2.4, 3.6 (USA), 4.9 (USA), 5
Bandwidth [MHz]	20, 40 (IEEE 802.11n)
Subcarrier spacing [kHz]	312.5
Payload modulation	BPSK, QPSK, 16-QAM, 64-QAM
FEC	Convolutional coding (1/2 binary convolutional coder with constraint length 7 and puncturing modes in Table B.2)
Transmit EIRP [W]	0.1 – 1, regulated by domestic agencies
FFT size	64
Number of data subcarriers	48, 52 (IEEE 802.11n)
Number of pilot subcarriers	4, 6 (optional)
Number of null/guardband subcarriers	12, 10 (IEEE 802.11n)
Symbol duration [μ s]	4
CP length	1/4, 1/8 (optional)
Multiple access	CSMA/CA
Duplexing	TDD

802.11a in the 2.4 GHz ISM band while preserving the same design and offering backward compatibility with IEEE 802.11b. These systems, although attended to support high data rates, lack a MAC protocol with Quality of Service (QoS) requirements, later introduced in the IEEE 802.11e amendment. In 2007, IEEE released a comprehensive specification named IEEE Std 802.11-2007, which included the amendments of groups a, b, e, g, h, i, and j.

The latest specification, named IEEE 802.11n is ratified in 2009. The main technical advancement of IEEE 802.11n is the introduction of MIMO technology with different MCS and multi-antenna configurations. It includes from 1 to 4 spatial streams, supporting the data rates from 6.5 up to 289 Mbps in 20 MHz channels. Moreover, the bonding of two 20 MHz channels into the one having 40 MHz bandwidth, the increased number of data subcarriers from 48 to 52, and reduced length of cyclic prefix from 800 ns to 400 ns allow for higher data rates (up to 600 Mbps).

In Europe, the standardization efforts for WLAN service based on OFDM technology were ratified in 2000, when European Telecommunications Standards Institute (ETSI) issued HiperLAN/2. Due to cheaper production costs and market acceptance of products specified for the IEEE 802.11 series of standards, HiperLAN/2 have never received a wide commercial implementation. However, much of the work on HiperLAN/2 has survived in the PHY specification of IEEE 802.11a, which is nearly identical to the PHY of HiperLAN/2. Since IEEE 802.11 series of standards only defines PHY and MAC layers, the Wi-Fi Alliance was formed as a nonprofit industry association. The main goal of the Wi-Fi Alliance is to enhance the user experience by defining the networking layer and to contribute to testing and certification programs. The success of the WLAN has enforced

Table B.2.: Modulation and coding rates for IEEE 802.11a/g with 6 MHz channel and CP length of 1/16.

PHY mode	Modulation	Coding rate	Data rate [Mbps]	Spectral efficiency [bits/s/Hz]
1	BPSK	1/2	6	0.3
2	BPSK	3/4	9	0.45
3	QPSK	1/2	12	0.6
4	QPSK	3/4	18	0.9
5	16-QAM	1/2	24	1.2
6	16-QAM	3/4	36	1.8
7	64-QAM	2/3	48	2.4
8	64-QAM	3/4	54	2.70
8 ¹	64-QAM	5/6	65	3.25

the development of broadband wireless connectivity characterized by more mobility and guaranteed QoS.

The values of key parameters for the IEEE 802.11 series of standards are given in Table B.1. The supported modulation and coding rates are shown in Table B.2.

B.2. WiMAX (IEEE 802.16 Series of Standards)

The very successful deployment of OFDM based IEEE 802.11a/g networks led to the new wireless technologies for Broadband Wireless Access (BWA), which should reduce operational costs and infrastructural demands required by the DSL and cable modem. The IEEE 802.11 series of standards are characterized with the limited performance in severe multipath environments with multi-user requirements, as well as with the lack of mechanisms to regulate multi-user network interoperability. Therefore, the IEEE 802.16 Working Group initiated the standardization activities for BWA based on the OFDM technology. In 2003, the IEEE 802.16a version is completed, specifying PHY and MAC layers. It was replaced by the IEEE 802.16-2004 standard (fixed WiMAX profile) with the operating band of 2 – 11 GHz, which further formed a basis for fixed WiMAX solutions. In 2005, the IEEE 802.16e-2005 amendment (mobile WiMAX profile), based on scalable OFDMA, is ratified to introduce the enhancement for high-speed mobile environments. The corresponding system parameters are given in Table B.3. Since the IEEE 802.16 series of standards specify only PHY and MAC layers functionalities, the industry-led WiMAX Forum created guidelines for the network architectures and protocols including the certification and interoperability with the other networks.

¹Added to the IEEE 802.11n amendment, while Mode 2 is removed. Additionally, MIMO functionality supports 1-4 spatial streams, thus giving in total 32 modes.

Table B.3.: IEEE 802.16 system parameters.

Parameters	IEEE 802.16-2004		IEEE 802.16e-2005		
Frequency band [GHz]	2 – 11, regulated by domestic regulations				
Bandwidth [MHz]	3.5	1.25	5	10	20
Sampling rate	8/7	28/25	28/25	28/25	28/25
FFT size	256	128	512	1024	2048
Subcarrier spacing [kHz]	15.63		10.9375		
Payload modulation	BPSK, QPSK, 16-QAM, 64-QAM				
FEC	Convolutional coding at rates 1/2, 2/3, 3/4, 5/6 (optional LDPC, BTC, CTC)				
Transmit EIRP [W]	0.1 – 1, regulated by domestic agencies				
Number of data subcarriers	192	96	384	768	1536
Number of pilot subcarriers	8	12	48	96	192
Number of null/guardband subcarriers	56	20	80	160	320
Number of subbands	4	2	8	16	32
Number of data subcarriers in subband	48				
Symbol duration [μ s]	72		102.9		
CP length	1/8, (optional 1/4, 1/16, 1/32)				
Multiple access	OFDMA				
Duplexing	TDD, FDD				
Number of OFDM symbols in 5 ms frame	69		48		

Mobile WiMAX has been also seen as the main candidate for the 4G mobile networks, due to the presence of several features that outperform the data throughput of common 3G standards, such as Evolution-Data Optimized (EV-DO) and High Speed Packet Access (HSPA). These capacity achieving features are: scalable OFDMA, Adaptive Modulation and Coding (AMC), Time Division Duplexing (TDD), MIMO technology, Hybrid-ARQ, fast frequency-selective scheduling, fractional frequency use, and bandwidth efficient handover. The peak data rate is 74 Mbps in the 20 MHz channel. The main technical advancement of WiMAX is a scalable PHY architecture that allows for easy scalability of data rate by changing the FFT length based on the available channel bandwidth. The system parameters of the IEEE 802.16 series of standards for different channel bandwidths are shown in Table B.3.

WiMAX supports a number of modulation and forward error correction (FEC) coding schemes and allows their change per user and per frame basis according to the channel conditions. The FEC coding based on convolutional codes is mandatory, while convolutional codes are combined with an outer Reed-Solomon code in the downlink. Turbo codes and low-density parity check (LDPC) codes are optionally supported giving in total 52 combinations of modulation and coding schemes. AMC is an effective mechanism to maximize throughput in a time-varying channel. The adaptation algorithm typically calls for the use of the highest modulation and coding scheme that can be supported by the SINR ratio of the particular user.

²Used for pilot subcarriers and for data modulation only in IEEE 802.16-2004.

Table B.4.: Modulation and mandatory coding rates for the IEEE 802.16 series of standards.

PHY mode	Modulation	Coding rate
0	BPSK ²	1/2
1	QPSK	1/2
2	QPSK	3/4
3	16-QAM	1/2
4	16-QAM	3/4
5	64-QAM	1/2
6	64-QAM	2/3
7	64-QAM	3/4

IEEE 802.16-2004 and IEEE 802.16e-2005 support both the time division duplexing (TDD) and frequency division duplexing (FDD), as well as a half-duplex FDD, which allows for a low-cost system implementation. TDD is favored by a majority of implementations because of its advantages, such as flexibility in choosing uplink-to-downlink data rate ratios, ability to exploit channel reciprocity, and less complex transceiver design. All initial WiMAX profiles are based on TDD, except two fixed WiMAX profiles in the 3.5 GHz band.

In Mobile WiMAX, both uplink and downlink resource allocations are controlled by a scheduler in the base station. Capacity is shared among multiple users on a demand basis using a burst TDM scheme. By using the OFDMA-PHY mode, multiplexing is additionally done in the frequency dimension, by allocating the different subsets of OFDM subcarriers to different users. Resources may be also allocated in the spatial domain by using the optional advanced antenna systems (AAS). The standard allows for the resource allocation in time, frequency, and space, enabled by a flexible mechanism to convey the signaling information on a frame-by-frame basis.

Data and pilot subcarriers can be grouped into subbands that represent the smallest unit for data allocation. The concept of grouping into subbands is used in the uplink of IEEE 802.16-2004 and both in the uplink and downlink of IEEE 802.16e-2005. In the downlink, the base station allocates subbands to different users based on their data requirements and channel conditions. The lower modulation schemes are allocated to the users with poor channel quality, while higher modulation schemes are allocated to the users with high SNR values. In the uplink, the users can be grouped into subbands only if the base station acknowledges that it is capable of decoding corresponding subbands. This type of multiple access scheme is called orthogonal frequency division multiple access (OFDMA). Each subband contains either distributed subcarrier permutation (FUSC and PUSC modes) or adjacent (contiguous) subcarrier permutation (AMC).

In distributed subcarrier permutation, the subcarriers are partitioned into the groups of contiguous subcarriers, where each subband consists of one subcarrier from each of

these groups either in uniform or in random way. The subchannels formed by the distributed subcarriers provide higher frequency diversity, which is particularly useful for mobile applications. WiMAX defines several grouping schemes based on the distributed subcarriers both for the uplink and downlink. One of them, named partial usage of subcarriers (PUSC), is mandatory for all mobile WiMAX implementations.

In contrast, the AMC permutation mode assumes that all subcarriers of a particular subband are adjacent to each other. Although frequency diversity is lost to a large extent, the exploitation of multiuser diversity is easier. Multiuser diversity provides the significant improvement in overall system capacity because, at any given time, a subband is allocated to the user with the highest SNR (capacity) in that subband. In this subcarrier permutation, nine adjacent (eight data and one pilot) subcarriers are used to form a bin. Four adjacent bins in the frequency domain constitute a band. An AMC subband consists of six contiguous bins from the same band. Thus, an AMC subband can consist of one bin over six consecutive symbols, two consecutive bins over three consecutive symbols, or three consecutive bins over two consecutive symbols. In general, the contiguous subbands are more suited for fixed and low-mobility applications.

Each subcarrier permutation defines a slot structure, which is a basic building block of an OFDMA frame. Each slot starts with the preamble, utilized for the synchronization. The preamble and pilot subcarriers are BPSK modulated having the power boosted 2.5 dB above the average power value specified by the other modulations.

B.3. LTE

The increased capacity due to robustness to multipath effects offered by OFDM technology was one of the main reasons for the wide acceptance of WLAN and the subsequent introduction of the WiMAX technology. The Third Generation Partnership Project (3GPP), formed by Global System for Mobile communications (GSM) and consisting of several standardization groups from different regions worldwide, utilized the IP-based OFDMA technology within the Long Term Evolution (LTE) project. The main goal of LTE was to accommodate increasing data rate demands and new multimedia applications in the 4G mobile networks.

The objectives of LTE were to address higher throughput, increase base station capacity, reduce latency, enable full mobility, and to include a radio interface PHY layer supporting wireless bandwidth up to 20 MHz with new transmission schemes and advanced multiantenna technologies. Additionally, LTE was supposed to target some of the weak points of the other OFDM-based wireless standards and to preserve compatibility with the legacy infrastructure.

In December 2008, the Release 8 of the 3GPP standard was ratified, where LTE Radio Access Modes, transmission bandwidth, and peak data rates are defined. The following Release 9 introduced the Self-Organizing Networks (SON) and Multimedia Broadcast/Multicast Service (MBMS) features. The Release 10, also known as LTE Advanced (LTE-A), released in March 2011, introduced the spectrum aggregation of non-contiguous channels up to 100 MHz together with MIMO enhancements, with up to 4 layers for uplink spatial streams and up to 8 downlink spatial streams. Moreover, the new features included

Table B.5.: Downlink LTE system parameters.

Parameters		Specification					
Frequency band [GHz]		0.8 – 2.62, regulated by domestic regulations					
Bandwidth [MHz]		1.25	2.5	5	10	15	20
Sampling frequency [MHz]		1.92	3.84	7.68	15.36	23.04	30.72
FFT size		128	256	512	1024	1536	2048
Subcarrier spacing [kHz]		15					
Payload modulation		QPSK, 16-QAM, 64-QAM, (optional OFDM/OQAM)					
FEC		Turbo or Convolutional coding with rate 1/3, rate matching (optional LDPC, BTC, CTC)					
BS Transmit EIRP [dBm]		45 – 48, regulated by domestic regulations					
UE Transmit EIRP [dBm]		23 ± 2, minimum power –40, off power –50					
Number of data subcarriers		60	150	250	500	750	1000
Number of pilot subcarriers		12	30	50	100	150	200
Number of null/guardband subcarriers		56	86	212	424	636	848
Frame duration [ms]		10					
Slots per frame		20					
OFDM symbols per slot (short/long CP)		7/6					
OFDM symbols duration (short/long CP) [μ s]		71.3 × 6. 71.9 × 1/83.3					
Short CP length (μ s/samples)		(5.21/10) × 1, (46.9/9) × 6	(5.21/20) × 1, (46.9/18) × 6	(5.21/40) × 1, (46.9/36) × 6	(5.21/180) × 1, (46.9/72) × 6	(5.21/120) × 1, (46.9/108) × 6	(5.21/160) × 1, (46.9/144) × 6
Long CP length (μ s/samples)		16.67/32 × 6	16.67/64 × 6	16.67/128 × 6	16.67/256 × 6	16.67/384 × 6	16.67/512 × 6
Number of RB		6	15	25	50	75	100
Number of RB per frame		120	300	500	1000	1500	2000
MIMO configurations		Downlink: 1 × 1, 1 × 2, 2 × 2, 4 × 4 Uplink: 1 × 1, 1 × 2					
Multiple access		OFDMA					
Duplexing		TDD, FDD					

the relay techniques to increase the coverage and data rate, and coordinated multipoint transmission to reduce the inter-cell interference and improve the signal strength.

Similar to WiMAX, LTE allows for TDD and FDD, while the scalable OFDM enables efficient spectrum utilization. The supported transmission bandwidths and the other system parameters are shown in Table B.5. LTE also utilizes OFDMA for a multiple access scheme in the downlink. The basic allocation unit assigned by the scheduler at the base station is a physical resource block (PRB), which consists of 12 adjacent (10 data and 2 pilot) subcarriers within one slot. Two CP lengths are supported: the first CP length is 1/4 of the useful symbol duration or 4.687 μ s and is used for the communication

Table B.6.: Modulation and mandatory coding rates for LTE.

PHY mode	Modulation	Coding rate /1024
1	QPSK	78
2	QPSK	120
3	QPSK	193
4	QPSK	308
5	QPSK	449
6	QPSK	602
7	16-QAM	378
8	16-QAM	490
9	16-QAM	616
10	64-QAM	466
11	64-QAM	567
12	64-QAM	666
13	64-QAM	772
14	64-QAM	873
15	64-QAM	948

with large delay spreads; the second CP length is $1/16$ or $16.67 \mu\text{s}$ and is used for the communication characterized with low delay spreads (for distances up to 5 km). Because the slot duration is fixed to 0.5 ms, the longer CP allows for 6 symbols per slot, while shorter CP allows for 7 symbols per slot with the first CP extended to $5.2 \mu\text{s}$. The generic radio frame consists of 20 slots with maximum information block size of 6144 bits. The supported modulation schemes and FEC coding rates are given in Table B.6.

For the LTE uplink, Single Carrier Frequency Division Multiple Access (SC-FDMA) is used as a multiple access technique. Although it is still based on the OFDMA technology, SC-FDMA is mainly introduced due to the low peak to average power ratio (PAPR) characteristic, which is a critical issue for the power consumption at the user equipment (UE). While PAPR is not a problem for the base station, it is unacceptable for the mobile unit. As a result, SC-FDMA combines the low PAPR offered by single-carrier systems with the multipath interference resilience and flexible subcarrier frequency allocation provided by the OFDM. The peak downlink and uplink data rates for the 20 MHz channel bandwidth are 326 and 86 Mbps, respectively. Furthermore, by utilizing the spectrum aggregation up to 100 MHz, the achievable peak rates are 1 Gbps and 500 Mbps for downlink and uplink, respectively.

B.4. WRAN (IEEE 802.22 Standard)

In November 1994, IEEE formed the 802.22 Working Group for the Wireless Regional Area Networks (WRAN). The specific task of the IEEE 802.22 standard was to intro-

Table B.7.: IEEE 802.22 system parameters.

Parameters	Specification	Remark
Frequency range	54 – 862 MHz	
Bandwidth [MHz]	6, 7, 8	Accommodated to TV channelization of different regulatory domains
Sampling rate [MHz]	6.856, 8, 9.136	
Subcarrier spacing [kHz]	3.348, 3.906, 4.46	
Payload modulation	QPSK, 16-QAM, 64-QAM	BPSK used for preambles, pilots and CDMA modes
FEC	Convolutional coding (1/2 binary convolutional coder with constraint length 7 and puncturing modes in Table B.8)	Optional FEC modes (CTC, SBTC, LDPC)
Transmit EIRP	4 W maximum for CPEs	4 W maximum for BSs in the USA but may vary in other regulatory domains
Multiple access	OFDMA	
FFT size	2048	
Number of guard subcarriers	368 (184,1,183)	
Number of used subcarriers	1680	
Number of data subcarriers	1440	
Number of pilot subcarriers	240	
CP length	1/4, 1/8, 1/16, 1/32	
Multiple access	OFDMA	
Duplexing	TDD	

duce PHY and MAC regulations based on cognitive radio techniques, to allow for the non-interfering sharing of geographically unused spectrum allocated to the licensed TV broadcast service. The cognitive radio features comprise the channel sensing, detection of spatially or temporally unused portions of the spectrum (spectrum holes or white spaces), adjustment of operating frequencies, and transmit control. Those actions must be performed dynamically such that harmful interference to the licensed transmissions is avoided.

In contrast to WiMAX, IEEE 802.22 targets the WRAN over the UHF/VHF TV bands between 54 and 862 MHz in rural and remote areas of typically 17-30 km in radius (up to the maximum of 100 km) from a base station (BS). Each BS serves up to 255 fixed units of customer premises equipment (CPE) with the outdoor directional antennas located

Table B.8.: Modulation and coding rates for IEEE 802.22 with 6 MHz channel and CP length of 1/16.

PHY mode	Modulation	Coding rate	Data rate [Mbps]	Spectral efficiency [bits/s/Hz]
1	BPSK	Uncoded	4.54	0.76
2	QPSK	1/2, repetition 4	1.13	0.19
3	QPSK	1/2, repetition 3	1.51	0.25
4	QPSK	1/2, repetition 2	2.27	0.38
5	QPSK	1/2	4.54	0.76
6	QPSK	2/3	6.05	1.01
7	QPSK	3/4	6.81	1.13
8	QPSK	4/5	7.56	1.26
9	16-QAM	1/2	9.08	1.51
10	16-QAM	2/3	12.10	2.01
11	16-QAM	3/4	13.61	2.27
12	16-QAM	4/5	15.13	2.52
13	64-QAM	1/2	13.61	2.27
14	64-QAM	2/3	18.15	3.03
15	64-QAM	3/4	20.42	3.40
16	64-QAM	4/5	22.69	3.78

at nominally 10 m above ground level. The data rate requirement at the edge of the coverage area is 1.5 Mbps in the downlink and 384 kbps in the uplink, available in 50% of the locations and 99.9% of the time, to provide a reliable connection where it is possible. Due to the extended coverage offered by the UHF/VHF TV bands, the choice of the PHY technology should be robust to the longer multipath excess delays up to 37 μ s. Therefore, OFDM has been chosen for PHY in the WRAN standard. Additionally, OFDM provides a flexible spectral shape that fills spectral gaps without interfering with the licensed systems and allows for adaptive modulation.

The IEEE 802.22 PHY specification and its key parameters are summarized in Table B.7. It can be noticed that MIMO technology is not supported due to the large physical size of antennas in this low frequency band. Moreover, TDD is the only duplexing mode currently supported, while the specification of FDD is expected in a future amendment to the standard. To achieve trade-off between data rate and robustness, depending on channel quality and interference condition, IEEE 802.22 defines 16 combinations of three modulations (QPSK, 16-QAM, 64-QAM) and 4 coding rates (1/2, 2/3, 3/4, 5/6), obtained by puncturing the output of the convolutional coder. The first 4 modes are used for control signaling while the rest of the modes are used for the data transmission. The corresponding parameters are given in Table B.7, where data rates and spectral efficiencies correspond to the 6 MHz channel and CP length of 1/16.

The elementary unit for resource allocation is the subchannel, which consists of 28 (24 data + 4 pilot) subcarriers. There are total of 60 subchannels in each OFDM symbol.

C. The Impact of the Constant Gap Assumption

A majority of published work on resource allocation in OFDM systems assumes the constant SNR gap for all considered M-QAM constellations. The most commonly used constant gap value is given as $\Gamma = \Gamma_{r_n} = -1.5/\ln(5 \cdot \text{BER})$, $r_n \in \{1, \dots, M\}$ as derived in [108]. Because Γ depends only on the required BER, the expression for the incremental power on the n th subcarrier in (3.20) can be simplified as

$$\Delta P_{r_n}(n) = \begin{cases} \frac{\Gamma}{G(n)}, & r_n = \beta \\ \frac{\Gamma}{G(n)} 2^{r_n} (1 - 2^{-\beta}) & r_n > \beta \end{cases} \quad (\text{C.1})$$

Having the granularity of one bit, i.e., $\beta = 1$, the incremental power becomes

$$\Delta P_{r_n}(n) = \begin{cases} \frac{\Gamma}{G(n)}, & r_n = 1 \\ \frac{\Gamma}{G(n)} 2^{r_n-1} & r_n > 1 \end{cases} \quad (\text{C.2})$$

Our simulation results indicate that for the LC algorithm the constant SNR gap slightly reduces data rate compared to the assumption of individual SNR gaps. However, the constant SNR gap introduces BER violations at low SNR values and BER improvements in the high SNR region as shown in Figure C.1 and Figure C.2. In our performance analysis in Chapters 3, 7, and 8 we avoid the concept of constant gap and assume that each modulation scheme is characterized with the individual SNR gap.

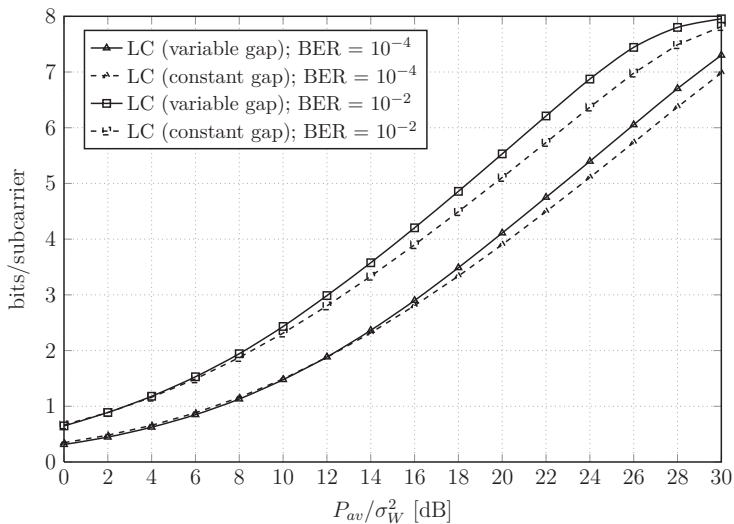


Figure C.1.: Number of bits per subcarrier vs. average SNR in the EVA channel.

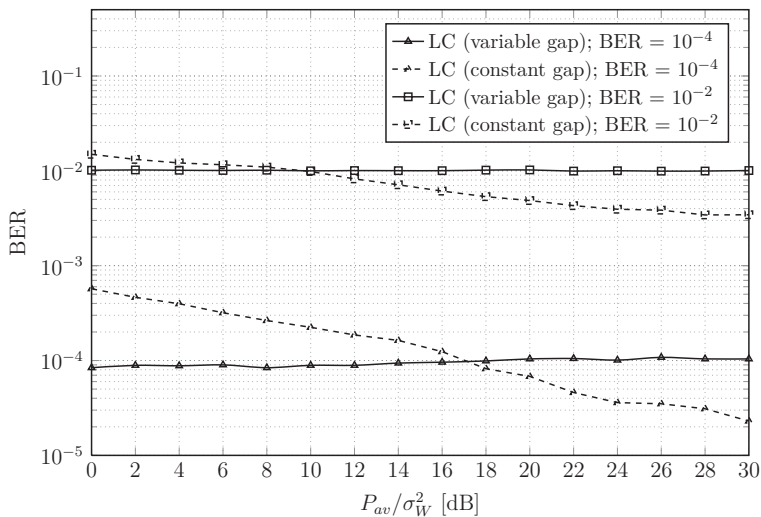


Figure C.2.: BER vs. average SNR in the EVA channel.

D. The TIGR Transceiver Benchmark

As addressed in Section 8.2, the TIGR framework is based on the GNU Radio software architecture where signal processing blocks are implemented as a C++ class while Python connects several blocks into a flow graph. Each GNU Radio block has a few callable functions that perform different parts of the signal processing. The important issue in the design of any software defined radio (SDR) is to investigate the software performance on different platforms. Therefore, to analyze the performance of the signal processing blocks utilized by the TIGR framework we conduct several benchmarking tests.

We profile the TIGR transceiver by using the *gr-benchmark* [109], a new tool for characterizing the software radio performance on different architectures platforms. The *gr-benchmark* is available as an out-of-tree GNU Radio repository and further allows for waveform level performance measurement. A number of specific tests is given in the form of the Python based GNU Radio waveform test modules. A test definition given as a parametrized Javascript Object Notation (JSON) description runs the particular test in a module for a specific number of data items and number of iterations while recording execution time and runtime spent in each instantiated block of the flow graph [110].

First, we investigate the performance of the generic mapper and generic demapper for different modulation schemes at the transmitter and receiver, respectively. We compare their performance on two different machines: a desktop PC with i7-960 CPU @ 3.20 GHz and a Lenovo X220 Thinkpad notebook with i7-2620M CPU @ 2.70 GHz. While the performance of other processing blocks is affected only by the symbol (sampling) rate, the computational complexity of the mapper and demapper additionally depends on the

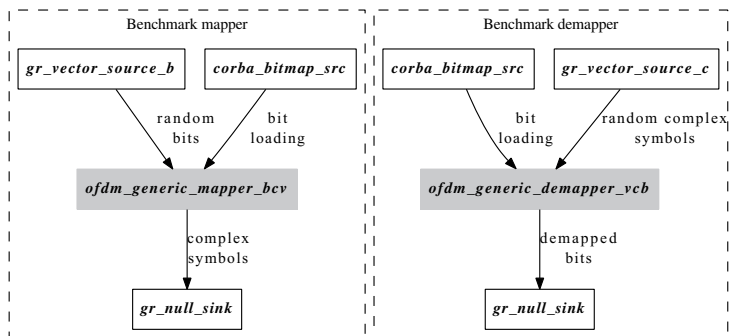


Figure D.1.: Benchmark flow graph for the TIGR mapper and demapper.

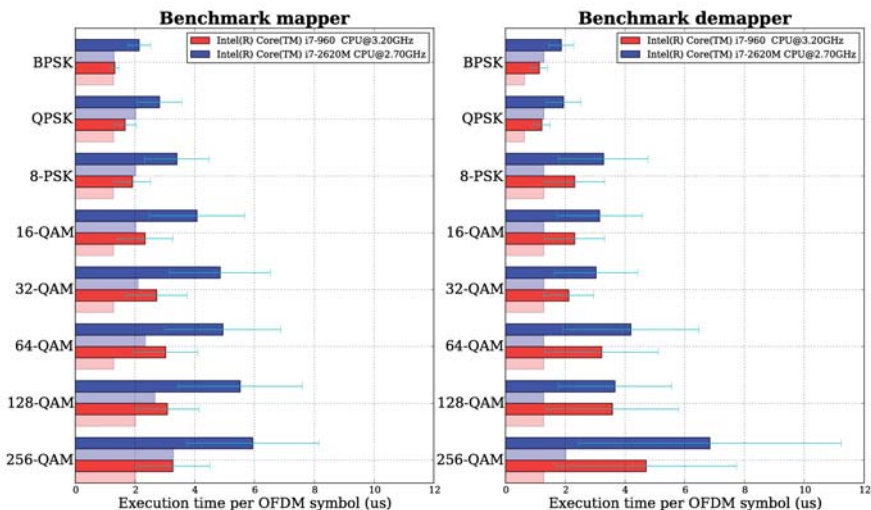


Figure D.2.: Performance comparison of the mapper/demapper block for different modulations available in TIGR.

particular bit loading vector given at the input. The GNU Radio flow graphs of the mapper and demapper benchmark tests are shown in Figure D.1.

In the mapper benchmark, the *gr_vector_source_b* block produces the random bits that are derived to the *ofdm_generic_mapper_bcv* block, while *corba_bitmap_source* provides the bit loading vector defining the particular modulation scheme on each sub-carrier at the mapper. For each modulation scheme, *gr_vector_source_b* generates the number of random bits required by the mapper to produce 100000 OFDM symbols. The higher the modulation scheme, the more bits are supplied to the mapper. Similarly, for the demapper benchmark, the *gr_vector_source_c* produces 100000 complex OFDM symbols supplied to the *ofdm_generic_demapper_bcv* block, while *corba_bitmap_source* provides the bit loading vector. The outputs of the mapper and demapper are derived to the *gr_null_sink* block to flush the generated complex symbols and demapped bits, respectively. However, the execution time of one simulation run may depend on the particular value of random bits as well as on the operating system factors. The simulation is thus run 100 times and the average execution time that mapper/demapper spends to generate/decode one OFDM symbol is used as a statistic to measure the performance, as shown in Figure D.2. The execution times that correspond to the shortest simulation runs (the light bars), as well as the corresponding standard deviation of the execution times are also depicted.

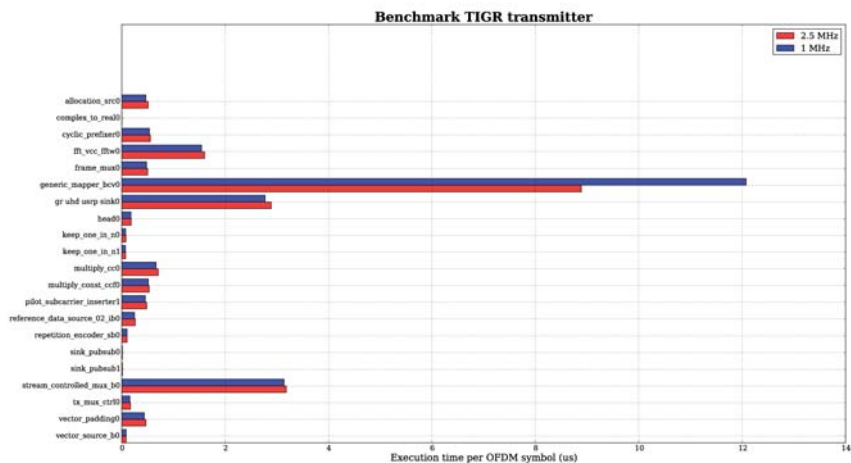


Figure D.3.: Execution times for the TIGR transmitter.

As expected, the BPSK modulation requires the least computational effort while the computational footprint increases with the number of constellation points. For the mapper, the average execution time for a notebook with an i7-2620M processor is nearly doubled compared to the performance of a desktop PC with an i7-960 processor. However, it is shown that the performance difference between two machines decreases in the demapper benchmark.

Furthermore, we profile the transmitter and receiver to analyze the execution times of different GNU Radio blocks within the TIGR transceiver. We also investigate the influence of the signal bandwidth (sampling rate) on the performance of the individual block. The benchmark is performed at the desktop PCs with an i7-960 CPU @ 3.20 GHz by transmitting/receiving the signals with the bandwidths of 1 MHz and 2.5 MHz via a USRP2 board. The 10000 OFDM frames are generated. The frame structure is shown in Figure 8.10 and represents a sequence of ten data symbols preceded with two preambles (one synchronization preamble and one preamble used for channel estimation) and one ID symbol used for the synchronization. The data subcarriers carry 16-QAM modulated complex symbols.

Figure D.3 shows that the mapper has the biggest computational footprint compared to other blocks at the transmitter. Since symbol bandwidth determines the number of bits transmitted during a given period, the demapper spends more time to generate one 1MHz symbol then for producing one 2.5MHz symbol.

At the receiver, the `gr_uhd_usrp_source` block experiences the longest execution time as shown in Figure D.4. Since the source block receives samples from the USRP and writes them to a stream further processed in the GNU Radio flow graph, the long execution time is caused by the buffering of the incoming samples from the USRP.

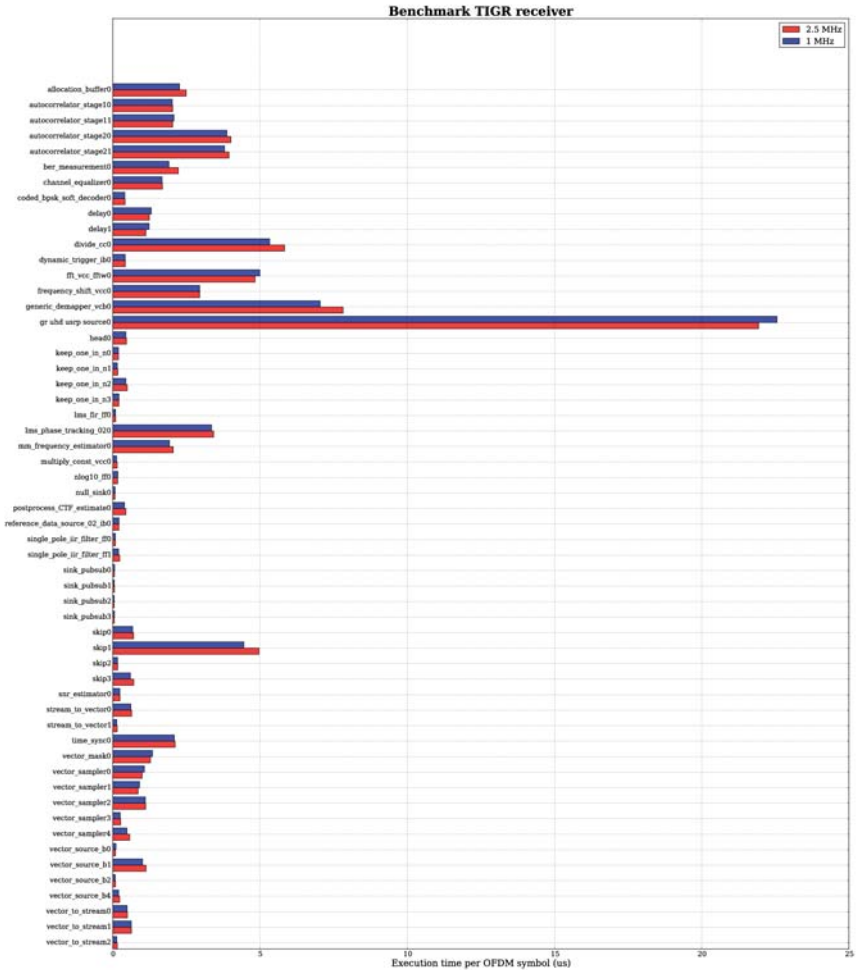


Figure D.4.: Execution times for the TIGR receiver.

The second largest computational effort at the receiver is associated with the timing synchronization consisting of five blocks: four autocorrelation blocks for generating the timing metrics and one *gr_time_sync* block that performs the peak detection. The timing synchronization is the initial processing stage at the receiver, i.e., the incoming samples from the USRP are firstly processed to find the correct beginning of an OFDM frame. Thus, the further reduction of the overall receiver complexity can be achieved by moving the timing synchronization into the FPGA at the USRP board.

Acronyms

3GPP	Third Generation Partnership Project
AAS	Advanced Antenna Systems
ADC	Analog-to-Digital Converter
AMC	Adaptive Modulation and Coding
API	Application Programming Interface
ARQ	Automatic Repeat Request
ASIC	Application Specific Integrated Circuit
AWGN	Additive White Gaussian Noise
BER	Bit Error Rate
BLUE	Best Linear Unbiased Estimator
BPSK	Binary Phase Shift Keying
BS	Base Station
BWA	Broadband Wireless Access
CFO	Carrier Frequency Offset
CFR	Channel Frequency Response
CIC	Cascaded Integrator-Comb
CIR	Channel Impulse Response
CNR	Channel-to-Noise Ratio
CORBA	Common Object Request Broker Architecture
CP	Cyclic Prefix
CPU	Central Processing Unit
CRB	Cramer-Rao Bound
DAC	Digital-to-Analog Converter
DDC	Digital Downconversion
DECT	Digital Enhanced Cordless Telecommunications
DFT	Discrete Fourier Transform
DSA	Dynamic Spectrum Access
DSL	Digital Subscriber Line
DSSS	Direct Sequence Spread Spectrum

DUC	Digital Upconversion
EPA	Extended Pedestrian A Channel Model
ERF	Error Function
ERFC	Complementary Error Function
ETSI	European Telecommunications Standards Institute
ETU	Extended Typical Urban Channel Model
EVA	Extended Vehicular A Channel Model
EV-DO	Evolution-Data Optimized
FBW	Fractional Bandwidth
FCFO	Fractional Carrier Frequency Offset
FDD	Frequency Division Duplexing
FEC	Forward Error Correction
FFT	Fast Fourier Transform
FIFO	First In First Out
FPGA	Field Programmable Gate Array
FUSC	Full Usage of Subcarriers
FZC	Frank-Zadoff-Chu
GbE	Gigabit Ethernet
GPL	General Public License
GPP	General Purpose Processor
GPS	Global Positioning System
GSM	Global System for Mobile Communications, orig. Groupe Spécial Mobile
GUI	Graphical User Interface
HBF	Half-Band Filter
HSPA	High Speed Packet Access
ICFO	Integer Carrier Frequency Offset
ICI	Inter-carrier Interference
IDFT	Inverse Discrete Fourier Transform
IF	Intermediate Frequency
IFFT	Inverse Fast Fourier Transform
IPS	Improved Periodic Sequence Estimator
ISI	Inter-symbol Interference
JSON	Javascript Object Notation
LDPC	Low Density Parity Check
LLS	Linear Least Square

LNA	Low Noise Amplifier
LO	Local Oscillator
LOS	Line-Of-Sight
LS	Least Square
LTE	Long Term Evolution
LTE-A	Long Term Evolution Advanced
MAC	Media Access Control
MBMS	Multimedia Broadcast/Multicast Service
MCS	Modulation and Coding Scheme
MIMO	Multiple Input Multiple Output
MMSE	Minimum Mean Square Error
M-PSK	Multiple Phase Shift Keying
NCO	Numerically Controlled Oscillator
NCRB	Normalized Cramer-Rao Bound
OFDM	Orthogonal Frequency Division Multiplexing
OFDMA	Orthogonal Frequency Division Multiple Access
PAPR	Peak-to-Average Power Ratio
PCI	Peripheral Component Interconnect
PDF	Probability Density Function
PDP	Power Delay Profile
PHY	Physical Layer
PPS	Pulse Per Second
PS	Periodic Sequence Estimator
PSD	Power Spectral Density
PSK	Phase Shift Keying
PSTN	Public Switched Telephone Network
PUSC	Partial Usage of Subcarriers
QAM	Quadrature Amplitude Modulation
QoS	Quality of Service
QPSK	Quadrature Phase Shift Keying
RF	Radio Frequency
SB	Subband Resource Allocation
SC-FDMA	Single Carrier Frequency Division Multiple Access
SD	Secure Digital
SDR	Software Defined Radio

SER	Symbol Error Rate
SFO	Sampling Frequency Offset
SIR	Signal-to-Interference Ratio
SISO	Single Input Single Output
SMA	SubMiniature Version A
SNR	Signal-to-Noise Ratio
SON	Self-Organizing Networks
STO	Symbol Timing Offset
TDD	Time Division Duplexing
UE	User Equipment
U-NII	Unlicensed National Information Infrastructure
UP	Uniform Power Allocation
USRP	Universal Software Radio Peripheral
VC	Virtual Subcarriers
WiMAX	Worldwide Interoperability for Microwave Access
WLAN	Wireless Local Area Network
WMAN	Wireless Metropolitan Area Network
WRAN	Wireless Regional Area Network
ZF	Zero Forcing
ZP	Zero Padding

Notations

Symbols for General Purpose

$*$	Convolution operation.
\otimes	Circular convolution operation.
$(\cdot)^*$	Complex conjugate.
$(\cdot)_N$	Modulo N .
$E(X)$	Expectation value of X .
$R(X)$	Autocorrelation of X .
$\text{Var}(X)$	Variance of X .
$B(u, v)$	Beta function.
$I_a(u)$	Modified Bessel function of the first kind of the order a .
$J_0(u)$	Bessel function of the first kind of the order 0.
$\mathcal{L}(\lambda_{\mathcal{L}})$	Lagrange function.
$Q(x)$	Q function.
$\text{erfc}(x)$	Inverse error function.
$\Gamma(u)$	Gamma function.
P	Noncentral chi-squared random variable.
V	Noncentral F random variable.
Z	Central chi-squared random variable.
$\lambda_{\mathcal{L}}$	Lagrange multiplier.
$F_{\nu_p, \nu_z}(\lambda)$	Noncentral F -distribution with with ν_p numerator and ν_z denominator degrees of freedom and noncentrality parameter λ .
$\chi_{\nu_p, \lambda}^2$	Noncentral chi-squared distribution with ν_p degrees of freedom and noncentrality parameter λ .
$\chi_{\nu_z}^2$	Central chi-squared distribution with ν_z degrees of freedom.

\mathbb{N}, \mathbb{N}_0 Set of natural numbers and natural numbers including zero, respectively.

\mathbb{Z} Set of integer numbers.

Symbols for SISO OFDM Systems

B Signal bandwidth, p. 7.

B_c Coherence bandwidth, p. 7.

C Capacity, p. 34.

$C_i(n)$ Transmitted complex data symbol on the n th subcarrier in the i th OFDM symbol, p. 15.

$\tilde{C}_i(n)$ Equalized complex data symbol on the n th subcarrier in the i th OFDM symbol, p. 29.

$C_p(n)$ Transmitted complex data symbol on the n th subcarrier of the preamble, p. 29.

$G(n)$ CNR of the n th subcarrier, p. 36.

$H(f)$ Channel frequency response, p. 6.

$H(f, t)$ Time-variant channel frequency response, p. 5.

$H(n)$ Channel frequency response on the n th subcarrier, p. 17.

$\hat{H}(n)$ Estimated channel frequency response on the n th subcarrier, p. 29.

$I_i(n, \varepsilon_c, \varepsilon_s)$ ICI on the n th subcarrier caused by the normalized CFO ε_c and normalized SFO ε_s , p. 27.

K Modulation dependent scaling factor, p. 21.

L Number of received signal paths (length of the channel impulse response), p. 5.

$\hat{M}_{2,p}$ Empirical second order moment of the received signal on the loaded subcarriers, p. 55.

$\hat{M}'_{2,p}$ Empirical second order moment of the received signal on the loaded subcarriers (IPS estimator), p. 74.

$\hat{M}_{2,p}(n)$ Empirical second order moment of the received signal on the n th loaded subcarrier, p. 57.

$\hat{M}_{2,z}$ Empirical second order moment of the received signal on the nulled subcarriers, p. 55.

N Number of subcarriers (subchannels), p. 12.

N_g Number of samples in the guard interval, p. 14.

N_p	Number of loaded subcarriers of the preamble, p. 54.
N_{pl}	Number of data symbols in the frame, p. 149.
N_t	Total number of samples in OFDM symbol, p. 14.
N_u	Number of occupied subcarriers, p. 149.
N_z	Number of nulled subcarriers of the preamble, p. 54.
$P(n)$	Power allocated on the n th subcarrier, p. 36.
$P^*(n)$	Optimal power allocated on the n th subcarrier, p. 37.
P_{av}	Average transmit power, p. 44.
$P_D(\tau)$	Power delay profile, p. 6.
$P_{r_n}(n)$	Required power for transmitting r bits over the n th subcarrier, p. 39.
P_{tot}	Total available power, p. 37.
Q	Number of identical parts in the synchronization preamble, p. 54.
$R_i(n)$	Received complex data symbol on the n th subcarrier in the I th OFDM symbol in the presence of synchronization impairments, p. 26.
$S_D(f)$	Doppler spectrum, p. 10.
T_c	Coherence time, p. 10.
T_g	Guard interval duration, p. 15.
T_s	Sampling time, p. 12.
T'_s	Mismatched sampling time at the receiver, p. 23.
T_{sym}	OFDM symbol duration, p. 12.
$W_i(n)$	Complex noise samples on the n th subcarrier in the i th OFDM symbol, p. 17.
$Y_i(n)$	Received complex symbol on the n th subcarrier in the i th OFDM symbol, p. 17.
$\tilde{Y}_i(n)$	Received complex symbol on the n th subcarrier in the i th OFDM symbol after equalization in the presence of the residual CFO and SFO, p. 115.
$Y_p(n)$	Received complex symbol on the n th loaded subcarrier of the preamble, p. 54.
$Y_z(n)$	Received complex symbol on the n th nulled subcarrier of the preamble, p. 54.

c	Spectral efficiency, p. 34.
$c(k)$	Discrete-time domain representation of the transmitted OFDM symbol, p. 16.
$c(t)$	Continuous-time domain representation of the transmitted OFDM symbol, p. 16.
Δf	Subchannel bandwidth (subcarrier spacing), p. 12.
f_c	Carrier frequency, p. 23.
f_D	Maximum Doppler frequency, p. 10.
f_d	Frequency offset, p. 23.
f_{LO}	Local oscillator frequency, p. 23.
$f_N(x)$	Auxiliary function, p. 27.
f_n	Subcarrier frequency, p. 12.
f_s	Sampling rate, p. 12.
f'_s	Mismatched sampling rate at the receiver, p. 23.
$g(t)$	Pulse shape, p. 19.
$h(k)$	Discrete-time channel impulse response, p. 16.
$\hat{h}(k)$	Estimated channel impulse response prior to the DFT, p. 56.
$\hat{h}_p(k)$	Estimated channel impulse response after the IDFT, p. 56.
$h(\tau)$	Channel impulse response, p. 6.
$h(\tau, t)$	Time-variant channel impulse response, p. 5.
i	OFDM symbol time index, p. 15.
k	Time index, p. 15.
Δk	Timing offset, p. 24.
m	Subcarrier index in the ICI term, p. 28.
n	Subcarrier index, p. 15.
r	Data rate, p. 34.
\mathbf{r}	Bit distribution vector, p. 39.
r^{WF}	Data rate achieved by the water-filling algorithm, p. 44.

$r(k)$	Discrete-time domain representation of the received OFDM symbol in the presence of synchronization impairments, p. 23.
r_{frame}	Total number of transmitted bits within the frame, p. 149.
$w(k)$	Time domain representation of complex noise samples , p. 16.
$y(k)$	Discrete-time domain representation of the received OFDM symbol, p. 16.
Γ	Constant SNR gap, p. 35.
Γ_r	SNR gap for the modulation r , p. 34.
Γ_{r_n}	SNR gap for the modulation r on the n th subcarrier, p. 39.
$\Omega(l)$	Expectation value of the received power associated with the l th multipath component, p. 6.
β	Information granularity, p. 39.
$\gamma_{FCFO}(n)$	SNR loss on the n th subcarrier in the presence of the CFO, p. 109.
$\gamma_{FCFO,av}$	Average SNR loss in the presence of FCFO, p. 110.
$\gamma_{FO}(n)$	SNR loss on the n th subcarrier in the presence of the CFO and SFO, p. 107.
$\gamma_{FO,av}$	Average SNR loss in the presence of the CFO and SFO, p. 107.
$\gamma_{SFO}(n)$	SNR loss on the n th subcarrier in the presence of the SFO, p. 108.
$\gamma_{SFO,av}$	Average SNR loss in the presence of the SFO, p. 108.
ϕ_m	Phase shift at the m th subcarrier, p. 28.
$\hat{\phi}_{i,n}$	Estimated phase offset on the n th subcarrier in the i th OFDM symbol, p. 115.
$\rho(n)$	SNR per subcarrier, p. 18.
$\hat{\rho}(n)$	Estimated SNR on the n th subcarrier, p. 57.
ρ_{av}	Average SNR, p. 18.
$\hat{\rho}_{av}$	Estimated average SNR, p. 56.
$\hat{\rho}'_{av}$	Estimated average SNR (IPS estimator), p. 74.
$\hat{\rho}_{av,Bou}$	Estimated average SNR (Boumard's estimator), p. 51.
$\hat{\rho}_{av,i}$	Estimated average SNR in the i th simulation trial, p. 65.
$\hat{\rho}_{av,MMSE}$	Estimated average SNR (MMSE estimator), p. 51.

$\hat{\rho}_{av, Ren I}$	Estimated average SNR (Ren's I Estimator), p. 52.
$\hat{\rho}_{av, Ren II}$	Estimated average SNR (Ren's II Estimator), p. 53.
$\rho_{FCFO}(n)$	SNR on the n th subcarrier in the presence of the CFO, p. 109.
$\rho_{FCFO, av}$	Average SNR in the presence of FCFO, p. 110.
$\rho_{FO}(n)$	SNR on the n th subcarrier in the presence of the CFO and SFO, p. 106.
$\rho_{FO, av}$	Average SNR in the presence of the CFO and SFO, p. 107.
$\hat{\rho}_i(n)$	Estimated SNR per subcarrier in the i th simulation trial, p. 65.
ρ_P	Average SNR on the pilot subcarriers, p. 117.
$\rho_{SFO}(n)$	SNR on the n th subcarrier in the presence of the SFO, p. 108.
$\rho_{SFO, av}$	Average SNR in the presence of the SFO, p. 108.
$\sigma_h^2(k)$	Average power of the k th CIR path, p. 73.
$\sigma_{h_p}^2(k)$	Estimated average power of the k th CIR path after the IDFT, p. 73.
$\sigma_I^2(n, \varepsilon_c, \varepsilon_s)$	ICI power on the n th subcarrier caused by the normalized CFO ε_c and normalized SFO ε_s , p. 106.
σ_P^2	Average power on the pilot subcarriers, p. 117.
σ_S^2	Average signal power, p. 15.
$\hat{\sigma}_{S, Bou}^2$	Estimated average power (Boumard's estimator), p. 51.
$\hat{\sigma}_{S, MMSE}^2$	Estimated average power (MMSE estimator), p. 51.
$\hat{\sigma}_{S, Ren I}^2$	Estimated average power (Ren's I Estimator), p. 52.
$\hat{\sigma}_{S, Ren II}^2$	Estimated average power (Ren's II Estimator), p. 53.
σ_W^2	Average noise power, p. 16.
$\hat{\sigma}_{W, Bou}^2$	Estimated noise power (Boumard's estimator), p. 51.
$\hat{\sigma}_{W, MMSE}^2$	Estimated noise power (MMSE estimator), p. 51.
$\hat{\sigma}_{W, Ren I}^2$	Estimated noise power (Ren's I Estimator), p. 52.
$\hat{\sigma}_{W, Ren II}^2$	Estimated noise power (Ren's II Estimator), p. 53.
τ_{RMS}	Root mean square delay spread, p. 6.
θ_0	Constant phase, p. 19.
ε_c	Normalized CFO, p. 24.

ε_s	Normalized SFO, p. 23.
φ_i	Phase offset of the i th OFDM symbol, p. 27.
$\xi_i(n_p)$	Phase offset on the n_p th pilot subcarrier in the i th OFDM symbol, p. 115.

Additional Symbols for MIMO OFDM Systems

$C_t(i, n)$	Complex data symbol on the n th subcarrier in the i th OFDM symbol at the t th transmit antenna, p. 79.
$C_{tp}(m_t)$	Complex data symbol on the m_t th subcarrier of the preamble at the t th transmit antenna, p. 81.
$H_{tr}(i, n)$	Channel frequency response on the n th subcarrier in the i th OFDM symbol between the t th transmit and r th receive antenna, p. 80.
$\hat{H}_{tr}(n)$	Estimated channel frequency response on the n th subcarrier between the t th transmit and r th receive antenna, p. 84.
$\hat{M}_{2,p,tr}(n)$	Empirical second order moment of the received signal on the n th loaded subcarrier between the t th transmit and r th receive antenna, p. 84.
$\hat{M}_{2,rz}$	Empirical second order moment of the nulled signal on the loaded subcarriers at the r th receive antenna, p. 83.
\hat{M}_{2,tr_p}	Empirical second order moment of the received signal on the loaded subcarriers at the r th receive antenna originating from the t th transmit antenna, p. 83.
\hat{M}'_{2,tr_p}	Empirical second order moment of the received signal on the loaded subcarriers at the r th receive antenna originating from the t th transmit antenna (MIMO-IPS estimator), p. 85.
N_R	Number of receive antennas, p. 79.
N_T	Number of transmit antennas, p. 79.
$W_r(i, n)$	Complex noise samples on the n th subcarrier in the i th preamble at the r th receive antenna, p. 80.
$Y_r(i, n)$	Received complex data symbol on the n th subcarrier in the i th preamble at the r th receive antenna, p. 80.
$Y_{rz}(n)$	Received complex symbol on the n th nulled subcarrier of the preamble at the r th receive antenna, p. 81.
$Y_{tr_p}(n)$	Received complex symbol on the n th loaded subcarrier of the preamble at the r th receive antenna originating from the t th transmit antenna, p. 81.

$\hat{h}_{tr}(k)$	Estimated channel impulse response between the t th transmit and r th receive antenna prior to the DFT, p. 83.
$\hat{h}_{tr_p}(k)$	Estimated channel impulse response between the t th transmit and r th receive antenna after the IDFT, p. 83.
m_t	Index of loaded preamble subcarriers at the t th transmit antenna, p. 81.
$\rho_{av,r}$	Average SNR at the r th receive antenna, p. 80.
$\hat{\rho}_{av,r}$	Estimated average SNR at the r th receive antenna, p. 83.
$\hat{\rho}'_{av,r}$	Estimated average SNR at the r th receive antenna (MIMO-IPS estimator), p. 85.
$\sigma_{h_{tr}}^2(k)$	Average power of the k th CIR path (between the t th transmit and r th receive antenna, p. 84.
$\sigma_{h_{tr_p}}^2(k)$	Estimated average power of the k th CIR path between the t th transmit and r th receive antenna after the IDFT, p. 84.
$\sigma_{S,t}^2$	Average signal power at the t th transmit antenna, p. 79.
$\sigma_{W,r}$	Average noise power at the r th receive antenna, p. 80.

Additional Symbols for Cognitive Radio OFDM Systems

$C_m(n)$	Transmitted complex data symbol on the n th subcarrier in the m th mode, p. 93.
$C_{p,m}(n)$	Transmitted complex data symbol on the n th subcarrier of the preamble in the m th mode, p. 95.
$I(n)$	Interference on the n th subcarrier, p. 93.
$I_m(n)$	Interference on the n th subcarrier in the m th mode, p. 93.
$\hat{M}_{2,i}$	Empirical second order moment of the received signal on the subcarriers in nonactive subbands, p. 98.
$\hat{M}_{2,l}$	Empirical second order moment of the received signal on the loaded subcarriers in active subbands, p. 98.
$\hat{M}_{2,z}$	Empirical second order moment of the received signal on the nulled subcarriers in active subbands, p. 98.
M_A	Number of active subbands, p. 93.
M_T	Number of FBW modes, p. 93.
$N_{st,m}$	Index of the first subcarrier in the m th mode, p. 95.
$P_m(n)$	Frank-Zadoff-Chu sequence on the n th subcarrier in the m th mode, p. 95.

$R(n)$	Received complex symbol on the n th subcarrier, p. 94.
$R_p(n)$	Received complex symbol on the n th subcarrier of the preamble after the ICFO correction, p. 97.
$R'_p(n)$	Received complex symbol on the n th subcarrier of the preamble after the FCFO correction, p. 97.
$R_{p,i}(n)$	Received complex symbol on the n th subcarrier of the preamble in non-active subbands, p. 98.
$R_{p,l}(n)$	Received complex symbol on the n th loaded subcarrier of the preamble in active subbands, p. 98.
$R_{p,z}(n)$	Received complex symbol on the n th nulled subcarrier of the preamble in active subbands, p. 98.
$S(n)$	Transmitted complex data symbol on the n th subcarrier, p. 93.
\mathcal{S}_m	Set of subcarriers belonging to active subbands in the m th mode, p. 93.
$S_p(n)$	Transmitted complex data symbol on the n th subcarrier of the preamble, p. 95.
$\mathcal{S}_{p,m}$	Set of loaded subcarriers of the preamble belonging to active subbands in the m th mode, p. 95.
$\mathcal{S}_{z,m}$	Set of nulled subcarriers of the preamble belonging to active subbands in the m th mode, p. 97.
$i(k)$	Time domain representation of the interference signal, p. 95.
m	Index of FBW modes, p. 93.
\hat{m}	Estimated mode index m , p. 97.
$r_p(k)$	Time domain representation of the received preamble, p. 96.
$r'_p(k)$	Time domain representation of the received preamble after the FCFO correction, p. 96.
$s(k)$	Time domain representation of the transmitted OFDM signal, p. 95.
$s_p(k)$	Time domain representation of the transmitted preamble, p. 95.
η	Integer CFO (ICFO), p. 96.
$\hat{\eta}$	Estimated ICFO, p. 97.
ν	Fractional CFO (FCFO), p. 96.
$\hat{\nu}$	Estimated FCFO, p. 96.
σ_I^2	Interference power, p. 93.
$\hat{\sigma}_I^2$	Estimated interference power, p. 99.

Bibliography

- [1] Y. G. Li and G. L. Stüber, *Orthogonal Frequency Division Multiplexing for Wireless Communications*. Springer, 2006.
- [2] P. Chow, J. Cioffi, and J. Bingham, “A practical discrete multitone transceiver loading algorithm for data transmission over spectrally shaped channels,” *IEEE Transactions on Communications*, vol. 43, no. 234, pp. 773–775, Februar 1995.
- [3] J. Campello, “Practical bit loading for DMT,” in *Proceedings: IEEE International Conference on Communications (ICC’99)*, vol. 2, 1999, pp. 801–805.
- [4] Z. Han and K. Liu, *Resource Allocation for Wireless Networks: Basics, Techniques, and Applications*. Cambridge University Press, 2008.
- [5] H. Liu and G. Li, *OFDM-Based Broadband Wireless Networks: Design and Optimization*. Wiley, 2005.
- [6] D. Athanasios and G. Kalivas, “SNR estimation for low bit rate OFDM systems in AWGN channel,” in *Proceedings: IEEE International Conference on Networking, International Conference on Systems and International Conference on Mobile Communications and Learning Technologies, (ICN/ICONS/MCL’06)*, 2006, pp. 198–198.
- [7] G. Ren, Y. Chang, and H. Zhang, “SNR estimation algorithm based on the preamble for wireless OFDM systems,” *Science in China Series F: Information Sciences*, vol. 51, no. 7, pp. 965–974, July 2008.
- [8] S. Boumard, “Novel noise variance and SNR estimation algorithm for wireless MIMO OFDM systems,” in *Proceedings: IEEE Global Telecommunications Conference (GLOBECOM’03)*, vol. 3, 2003, pp. 1330–1334.
- [9] M. Zivkovic and R. Mathar, “Preamble-based SNR estimation in frequency selective channels for wireless OFDM systems,” in *Proceedings: IEEE Vehicular Technology Conference (VTC’09 Spring)*, April 2009.
- [10] —, “Preamble-based SNR estimation algorithm for wireless MIMO OFDM systems,” in *Proceedings: IEEE International Symposium on Wireless Communication Systems (ISWCS’09)*, September 2009, pp. 96–100.
- [11] —, “An improved preamble-based SNR estimation algorithm for OFDM systems,” in *Proceedings: IEEE International Symposium on Personal Indoor and Mobile Radio Communications (PIMRC’10)*, September 2010, pp. 172–176.
- [12] —, “Performance evaluation of timing synchronization in OFDM-based cognitive radio systems,” in *Proceedings: IEEE Vehicular Technology Conference (VTC’11 Fall)*, September 2011.

- [13] —, “Joint frequency synchronization and spectrum occupancy characterization in OFDM-based cognitive radio systems,” in *Proceedings: IEEE Global Telecommunications Conference (GLOBECOM'11)*, December 2011.
- [14] —, “Design issues and performance evaluation of a SDR-based reconfigurable framework for adaptive OFDM transmission,” in *Proceedings: ACM International Workshop on Wireless Network Testbeds, Experimental Evaluation and Characterization (WiNTECH'11)*. New York, NY, USA: ACM, 2011, pp. 75–82.
- [15] M. Zivkovic, D. Auras, and R. Mathar, “Reconfigurable framework for adaptive OFDM transmission,” in *Proceedings: ACM International Workshop on Wireless Network Testbeds, Experimental Evaluation and Characterization (WiNTECH'09)*. New York, NY, USA: ACM, 2009, pp. 91–92.
- [16] —, “OFDM-based dynamic spectrum access,” in *Proceedings: IEEE Symposium on New Frontiers in Dynamic Spectrum (DySPAN'10)*, April 2010.
- [17] M. Zivkovic, C. Liu, and R. Mathar, “Implementation of OFDM power allocation strategy in GNU radio framework,” in *Proceedings: 5th Karlsruhe Workshop on Software Radios*, Karlsruhe, Germany, March 2008, pp. 111–116.
- [18] M. Zivkovic, J. Schmitz, and R. Mathar, “Acquisition and identification of OFDM signals using cyclostationary signatures,” in *Proceedings: ACM International Workshop on Wireless Network Testbeds, Experimental Evaluation and Characterization (WiNTECH'11)*. New York, NY, USA: ACM, 2011, pp. 91–92.
- [19] J. Schmitz, M. Zivkovic, and R. Mathar, “Extended cyclostationary signatures for OFDM-based cognitive radio,” in *Proceedings: 7th Karlsruhe Workshop on Software Radios*, Karlsruhe, Germany, March 2012, pp. 124–130.
- [20] —, “Extended cyclostationary signatures for OFDM in the presence of hardware imperfections,” *Frequenz-Journal of RF-Engineering and Telecommunications*, vol. 66, no. 9-10, pp. 293–302, September 2012.
- [21] D. Bielefeld, G. Fabek, M. Zivkovic, and R. Mathar, “Energy efficient ultra-wideband signaling for cooperative spectrum sensing in cognitive radio,” in *Proceedings: IEEE Vehicular Technology Conference (VTC'11 Spring)*, May 2011.
- [22] —, “Optimization of cooperative spectrum sensing and implementation on software defined radios,” in *Proceedings: International Workshop on Cognitive Radio and Advanced Spectrum Management (CogART'10)*, November 2010.
- [23] R. Mathar, A. Schmeink, and M. Zivkovic, “Optimum discrete signaling over channels with arbitrary noise distribution,” in *Proceedings: IEEE International Conference on Signal Processing and Communication Systems (ICSPCS'08)*, December 2008.
- [24] R. Mathar and M. Zivkovic, “How to position n transmitter-receiver pairs in $n-1$ dimensions such that each can use half of the channel with zero interference from the others,” in *Proceedings: IEEE Global Telecommunications Conference (GLOBECOM'09)*, December 2009.
- [25] M.-O. Pun, M. Morelli, and C. C. J. Kuo, *Multi-Carrier Techniques For Broadband Wireless Communications: A Signal Processing Perspectives*. London, England, UK: Imperial College Press, 2007.

- [26] T. Sorensen, P. Mogensen, and F. Frederiksen, "Extension of the ITU channel models for wideband OFDM systems," in *Proceedings: IEEE Vehicular Technology Conference (VTC'05 Fall)*, vol. 1, September 2005, pp. 392–396.
- [27] G. L. Stüber, *Principles of Mobile Communication*, 3rd ed. Springer Publishing Company, Incorporated, 2011.
- [28] W. Lee, *Mobile Cellular Telecommunications Systems*, ser. Electronic engineering series. McGraw-Hill, 1989.
- [29] M. Abramowitz and I. Stegun, *Handbook of mathematical functions with formulas, graphs, and mathematical tables*, ser. Applied mathematics series. U.S. Govt. Print. Off., 1964, no. Bd. 55,Nr. 1972.
- [30] W. Jakes, *Microwave mobile communications*, ser. IEEE Press classic reissue. IEEE Press, 1974.
- [31] B. Saltzberg, "Performance of an efficient parallel data transmission system," *IEEE Transactions on Communication Technology*, vol. 15, no. 6, pp. 805–811, December 1967.
- [32] S. Weinstein and P. Ebert, "Data transmission by frequency-division multiplexing using the discrete fourier transform," *IEEE Transactions on Communication Technology*, vol. 19, no. 5, pp. 628–634, October 1971.
- [33] J.-J. Van De Beek, M. Sandell, and P. Börjesson, "ML estimation of time and frequency offset in OFDM systems," *IEEE Transactions on Signal Processing*, vol. 45, pp. 1800–1805, July 1997.
- [34] H. Yano, O. Takyu, T. Fujii, and T. Ohtsuki, "Low complexity cyclostationary feature detection method to compensate cyclostationarity-degradation by guard interval insertion," in *Proceedings: ICST Conference on Cognitive Radio Oriented Wireless Networks and Communications (CROWNCOM'11)*, 2011, pp. 51–55.
- [35] A. Bahai, B. Saltzberg, and M. Ergen, *Multi-Carrier Digital Communications: Theory and Applications of OFDM*, ser. Information Technology: Transmission, Processing and Storage. Springer, 2004.
- [36] Y. Li and G. L. Stüber, *Orthogonal Frequency Division Multiplexing for Wireless Communications (Signals and Communication Technology)*. Secaucus, NJ, USA: Springer-Verlag New York, Inc., 2006.
- [37] T. J. Roupheal, *RF and Digital Signal Processing for Software-Defined Radio: A Multi-Standard Multi-Mode Approach*. Newton, MA, USA: Newnes, 2008.
- [38] A. Goldsmith, *Wireless Communications*. New York, NY, USA: Cambridge University Press, 2005.
- [39] J. Proakis, *Digital Communications*. McGraw-Hill Higher Education, 2001.
- [40] M. Ergen, *Mobile Broadband - Including WiMAX and LTE*. Springer, 2009.
- [41] T. Chiueh, P. Tsai, and I. Lai, *Baseband Receiver Design for Wireless MIMO-OFDM Communications*. Wiley, 2012.
- [42] M. Speth, S. Fechtel, G. Fock, and H. Meyr, "Optimum receiver design for wireless broad-band systems using OFDM, part I," *IEEE Transactions on Communications*, vol. 47, no. 11, pp. 1668–1677, November 1999.

- [43] T. Schmidl and D. Cox, "Robust frequency and timing synchronization for OFDM," *IEEE Transactions on Communications*, vol. 45, no. 12, pp. 1613–1621, December 1997.
- [44] M. Speth, F. Classen, and H. Meyr, "Frame synchronization of OFDM systems in frequency selective fading channels," in *Proceedings: IEEE Vehicular Technology Conference (VTC'97)*, vol. 3, May 1997, pp. 1807–1811.
- [45] C. Oberli, "ML-based tracking algorithms for MIMO-OFDM," *IEEE Transactions on Wireless Communications*, vol. 6, no. 7, pp. 2630–2639, July 2007.
- [46] O. Edfors, M. Sandell, J.-J. Van De Beek, S. K. Wilson, and P. O. Börjesson, "Analysis of DFT-based channel estimators for OFDM," *Wireless Personal Communications*, vol. 12, no. 1, pp. 55–70, 2000.
- [47] O. Edfors, M. Sandell, J. J. Van De Beek, S. K. Wilson, and P. O. Börjesson, "OFDM channel estimation by singular value decomposition," *IEEE Transactions on Communications*, vol. 46, no. 7, pp. 931–939, 1998.
- [48] J.-J. van de Beek, O. Edfors, M. Sandell, S. Wilson, and P. Ola Börjesson, "On channel estimation in OFDM systems," in *Proceedings: IEEE Vehicular Technology Conference (VTC'95)*, vol. 2, 1995, pp. 815–819.
- [49] S. Coleri, M. Ergen, A. Puri, and A. Bahai, "Channel estimation techniques based on pilot arrangement in OFDM systems," *IEEE Transactions on Broadcasting*, vol. 48, no. 3, pp. 223–229, 2002.
- [50] R. G. Gallager, *Information Theory and Reliable Communication*. New York, NY, USA: John Wiley & Sons, Inc., 1968.
- [51] T. M. Cover and J. A. Thomas, *Elements of information theory*. John Wiley and Sons, Inc., 1991.
- [52] C. E. Shannon, "A mathematical theory of communication," *Bell Systems Technical Journal*, vol. 27, pp. 379–423, 623–656, 1948.
- [53] S. Boyd and L. Vandenberghe, *Convex optimization*. New York: Cambridge University Press, 2004. [Online]. Available: <http://www.stanford.edu/~boyd/cvxbook/>
- [54] W. Yu and J. Cioffi, "Constant-power waterfilling: performance bound and low-complexity implementation," *IEEE Transactions on Communications*, vol. 54, no. 1, pp. 23–28, 2006.
- [55] Y. Zhang and C. Leung, "Subchannel power-loading schemes in multiuser OFDM systems," *IEEE Transactions on Vehicular Technology*, vol. 58, no. 9, pp. 5341–5347, 2009.
- [56] D. Pauluzzi and N. Beaulieu, "A comparison of SNR estimation techniques for the AWGN channel," *IEEE Transactions on Communications*, vol. 48, no. 10, pp. 1681–1691, October 2000.
- [57] M. Morelli and U. Mengali, "An improved frequency offset estimator for OFDM applications," *IEEE Communications Letters*, vol. 3, no. 3, pp. 75–77, March 1999.
- [58] Y. Kang, K. Kim, and H. Park, "Efficient DFT-based channel estimation for OFDM systems on multipath channels," *IET Communications*, vol. 1, no. 2, pp. 197–202, April 2007.

- [59] G. Ren, H. Zhang, and Y. Chang, "SNR estimation algorithm based on the preamble for OFDM systems in frequency selective channels," *IEEE Transactions on Communications*, vol. 57, no. 8, pp. 2230–2234, August 2009.
- [60] M. Morelli, C.-C. Kuo, and M.-O. Pun, "Synchronization techniques for orthogonal frequency division multiple access (OFDMA): A tutorial review," *Proceedings of the IEEE*, vol. 95, no. 7, pp. 1394–1427, July 2007.
- [61] S. M. Kay, *Fundamentals of Statistical Signal Processing: Detection Theory*. Englewood Cliffs, NJ: Prentice Hall, 1998.
- [62] J. Melsa and D. Cohn, *Decision and estimation theory*, ser. McGraw-Hill series in electrical engineering: Communications and information theory. McGraw-Hill, 1978.
- [63] N. Alagha, "Cramer-Rao bounds of SNR estimates for BPSK and QPSK modulated signals," *IEEE Communications Letters*, vol. 5, no. 1, pp. 10–12, Januar 2001.
- [64] I. Mitola, J. and J. Maguire, G.Q., "Cognitive radio: making software radios more personal," *IEEE Personal Communications*, vol. 6, no. 4, pp. 13–18, August 1999.
- [65] J. Benko, S.-Y. Chang, and Y.-C. Cheong, "Draft PHY/MAC specification for IEEE 802.22," IEEE 802.22-06/0069r1, Tech. Rep., 2006.
- [66] Y. H. Kim, I. Song, S. Yoon, and S. R. Park, "An efficient frequency offset estimator for OFDM systems and its performance characteristics," *IEEE Transactions on Vehicular Technology*, vol. 50, no. 5, pp. 1307–1312, September 2001.
- [67] J. Y. Won, H. G. Kang, Y. H. Kim, I. Song, and M. S. Song, "Fractional bandwidth mode detection and synchronization for OFDM-based cognitive radio systems," in *Proceedings: IEEE Vehicular Technology Conference (VTC'08 Spring)*, 2008, pp. 1599–1603.
- [68] S. Feng, H. Zheng, H. Wang, J. Liu, and P. Zhang, "Preamble design for non-contiguous spectrum usage in cognitive radio networks," in *Proceedings: IEEE Wireless Communications and Networking Conference (WCNC'09)*, 2009.
- [69] T. Yucek and H. Arslan, "MMSE noise plus interference power estimation in adaptive OFDM systems," *IEEE Transactions on Vehicular Technology*, vol. 56, no. 6, pp. 3857–3863, November 2007.
- [70] M. Krondorf, T.-J. Liang, and G. Fettweis, "On synchronization of opportunistic radio OFDM systems," in *Proceedings: IEEE Vehicular Technology Conference (VTC'08 Fall)*, September 2008, pp. 1686–1690.
- [71] P. H. Moose, "A technique for orthogonal frequency division multiplexing frequency offset correction," *IEEE Transactions on Communications*, vol. 42, no. 10, pp. 2908–2914, October 1994.
- [72] M. Speth, S. Fechtel, G. Fock, and H. Meyr, "Optimum receiver design for OFDM-based broadband transmission, part II, a case study," *IEEE Transactions on Communications*, vol. 49, no. 4, pp. 571–578, 2001.
- [73] J. Armstrong, "Analysis of new and existing methods of reducing intercarrier interference due to carrier frequency offset in OFDM," *IEEE Transactions on Communications*, vol. 47, no. 3, pp. 365–369, March 1999.

- [74] K. Sathananthan and C. Tellambura, "Probability of error calculation of OFDM systems with frequency offset," *IEEE Transactions on Communications*, vol. 49, no. 11, pp. 1884–1888, November 2001.
- [75] S.-Y. Liu and J.-W. Chong, "A study of joint tracking algorithms of carrier frequency offset and sampling clock offset for OFDM-based WLANs," in *Proceedings: IEEE International Conference on Communications, Circuits and Systems and West Sino Expositions*, vol. 1, June 2002, pp. 109–113.
- [76] P.-Y. Tsai, H.-Y. Kang, and T.-D. Chiueh, "Joint weighted least squares estimation of frequency and timing offset for OFDM systems over fading channels," in *Proceedings: IEEE Vehicular Technology Conference (VTC'03 Spring)*, vol. 4, April 2003, pp. 2543–2547.
- [77] M. Morelli and M. Moretti, "Fine carrier and sampling frequency synchronization in OFDM systems," *IEEE Transactions on Wireless Communications*, vol. 9, no. 4, pp. 1514–1524, 2010.
- [78] M. Sliskovic, "Carrier and sampling frequency offset estimation and correction in multicarrier systems," in *Proceedings: IEEE Global Telecommunications Conference (GLOBECOM'01)*, vol. 1, 2001, pp. 285–289.
- [79] A. Coulson, "Maximum likelihood synchronization for OFDM using a pilot symbol: algorithms," *IEEE Journal on Selected Areas in Communications*, vol. 19, no. 12, pp. 2486–2494, December 2001.
- [80] —, "Maximum likelihood synchronization for OFDM using a pilot symbol: analysis," *IEEE Journal on Selected Areas in Communications*, vol. 19, no. 12, pp. 2495–2503, December 2001.
- [81] I. ho Hwang, H.-S. Lee, and K. woo Kang, "Frequency and timing period offset estimation technique for OFDM systems," *Electronics Letters*, vol. 34, no. 6, pp. 520–521, March 1998.
- [82] W.-C. Huang, C.-P. Li, and H.-J. Li, "An investigation into the noise variance and the SNR estimators in imperfectly-synchronized OFDM systems," *IEEE Transactions on Wireless Communications*, vol. 9, no. 3, pp. 1159–1167, March 2010.
- [83] T. Summers and S. Wilson, "SNR mismatch and online estimation in turbo decoding," *IEEE Transactions on Communications*, vol. 46, no. 4, pp. 421–423, April 1998.
- [84] T. Pollet, M. Van Bladel, and M. Moeneclaey, "BER sensitivity of OFDM systems to carrier frequency offset and Wiener phase noise," *IEEE Transactions on Communications*, vol. 43, no. 234, pp. 191–193, Februar 1995.
- [85] T. Pollet, P. Spruyt, and M. Moeneclaey, "The BER performance of OFDM systems using non-synchronized sampling," in *Proceedings: IEEE Global Telecommunications Conference (GLOBECOM'94)*, vol. 1, November 1994, pp. 253–257.
- [86] S. M. Kay, *Fundamentals of Statistical Signal Processing: Estimation theory*. Upper Saddle River, NJ, USA: Prentice-Hall, Inc., 1993.
- [87] K. Akita, R. Sakata, and K. Sato, "A phase compensation scheme using feedback control for IEEE 802.11a receiver," in *Proceedings: IEEE Vehicular Technology Conference (VTC'04 Fall)*, vol. 7, 2004, pp. 4789–4793.

- [88] J.-M. Wu and C.-H. Chou, "Baseband sampling clock frequency synchronization for WiMAX systems," in *Institute of Communications Engineering National Tsing Hua University Hsinchu, Taiwan - Internal Publication*, 2005.
- [89] "GNU Radio." [Online]. Available: <http://gnuradio.org/redmine/projects/gnuradio>
- [90] J. Mitola, *Software radio architecture*. John Wiley & Sons, Inc., 2000.
- [91] J. Reed, *Software radio: a modern approach to radio engineering*. Prentice Hall PTR, 2002.
- [92] W. Tuttlebee, *Software Defined Radio: Enabling Technologies*, ser. Wiley Series in Software Radio. Wiley, 2003.
- [93] A. Mueller, *DAB, Software Receiver Implementation*. ETH Zurich: Semester Thesis, 2008.
- [94] B. Le, T. Rondeau, J. Reed, and C. Bostian, "Analog-to-digital converters: A review of the past, present, and future," *IEEE Signal Processing Magazine*, vol. 22, no. 6, pp. 69–77, November 2005.
- [95] J. I. Mitola, *Cognitive Radio Architecture: The Engineering Foundations of Radio XML*. New York, NY USA: Wiley-Interscience, 2006.
- [96] A. Wyglinski, M. Nekovee, and T. Hou, *Cognitive Radio Communications and Networks: Principles and Practice*. Elsevier Science, 2009.
- [97] P. Balister and J. H. Reed, "USRP hardware and software description," *Chameleonic Radio: Technical Memo No. 9*. [Online]. Available: http://www.ece.vt.edu/swe/chamrad/crdocs/CRTM09_060727_USRP.pdf
- [98] S. Meyers, *Effektiv C++ programmieren*. Addison Wesley, 1998.
- [99] —, *Mehr Effektiv C++ programmieren*. Addison Wesley, 1999.
- [100] A. Martelli, *Python in a Nutshell. A Desktop Quick Reference*, 1st ed. O'Reilly & Associates, 2003.
- [101] "USRP." [Online]. Available: <http://www.ettus.com>
- [102] D. T. Nguyen, *Implementation of OFDM systems using GNU Radio and USRP*. School of Electrical, Computer and Telecommunications Engineering, University of Wollongong, 2013. [Online]. Available: <http://ro.uow.edu.au/theses/3977/>
- [103] R. Lyons, *Understanding Digital Signal Processing*, ser. Prentice-Hall accounting series. Pearson Education, 2010.
- [104] D. Auras, *GNU Radio Implementierungen zur Synchronisierung von OFDM-Systemen*. RWTH Aachen: Studienarbeit, 2009.
- [105] "Object Management Group." [Online]. Available: <http://www.omg.org/>
- [106] T. Rondeau, M. Ettus, and R. McGwier, "Open source transparency for OFDM experimentation," in *Proceedings: Software Defined Radio Forum Technical Conference*, 2008.
- [107] G. Berardinelli, P. Zetterberg, O. Tonelli, A. Cattoni, T. Sorensen, and P. Mogenssen, "An SDR architecture for OFDM transmission over USRP2 boards," in *Proceedings: Forty Fifth Asilomar Conference on Signals, Systems and Computers (ASILOMAR'11)*, November 2011, pp. 965–969.

-
- [108] A. Goldsmith and S.-G. Chua, “Variable-rate variable-power MQAM for fading channels,” *IEEE Transactions on Communications*, vol. 45, no. 10, pp. 1218–1230, 1997.
 - [109] “gr-benchmark.” [Online]. Available: <http://github.org/osh/gr-benchmark>
 - [110] T. J.O’Shea and T. W. Rondeau, “A universal GNU radio performance benchmarking suite,” in *Proceedings: 8th Karlsruhe Workshop on Software Radios*, Karlsruhe, Germany, March 2014, pp. 6–11.

Curriculum Vitae

Milan Zivkovic

Aug. 17, 1978	born in Nis, Serbia (former Socialist Federal Republic of Yugoslavia)
Sep. 1985 - Jun. 1993	Primary School "IX srpska udarna brigada", Bor, Serbia
Sep. 1993 - Jun. 1997	Natural Sciences and Mathematics High School "Bora Stankovic", Bor, Serbia
Jun. 1997	High School Diploma (Abitur)
Oct. 1997 - Jul. 2002	Communications Engineering Faculty of Electronic Engineering University of Nis, Serbia
Jul. 08, 2002	Diploma of Electrical Engineering (Dipl.-Ing.) (Best Graduate Award)
Oct. 2002 - Apr. 2006	Master Studies in Telecommunications Faculty of Electronic Engineering University of Nis, Serbia
Oct. 2002 - Apr. 2006	Serbian Ministry of Science, Technology and Development research assistantship at Faculty of Electronic Engineering University of Nis, Serbia
Mar. 2005 - Oct. 2005	Military Service, Nis, Serbia
Apr. 21, 2006	Master of Science Electrical Engineer
Sep. 2006 - Aug. 2009	German Research Foundation (DFG) doctoral fellowship in Graduate School "Software for Mobile Communication Systems"
From Sep. 2009	Research Assistant Institute for Theoretical Information Technology RWTH Aachen University, Germany